

NASA CR-135128
R76-104

LASER-HEATED ROCKET THRUSTER

(NASA-CR-135128) LASER-HEATED ROCKET
THRUSTER Final Report, Jun. 1975 - Jun.
1976 (Rocketdyne) 187 p HC A09/MF A01

N77-24188

CSCL 21H

G3/20

Unclas
29100

by

J. M. Shoji

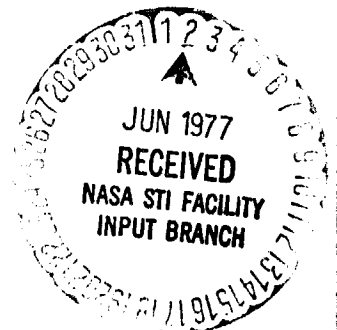
Rocketdyne Division
Rockwell International
Canoga Park, CA 91304

Prepared for

National Aeronautics and Space Administration
NASA Lewis Research Center

Contract NAS3-19728

MAY 1977



FOREWORD

This technical report presents the results of the Laser-Heated Rocket Thruster Program. The analysis, design and fabrication were conducted by Rocketdyne Division, Rockwell International, during the period 27 June 1975 to 2 July 1976 as part of National Aeronautics and Space Administration, Lewis Research Center, Contract NAS3-19728. The 10kw experimental hardware was shipped to NASA-LeRC.

The NASA-LeRC Project Manager was Mr. S. Cohen and the Rocketdyne Program Manager was Dr. S. V. Gunn.

ACKNOWLEDGEMENTS

The work presented on this volume represents the concerted effort and expertise of Physical Sciences Inc., and many members of the Rocketdyne organization. Contributions of major significance were made by the following Rocketdyne personnel:

V. R. Larson	-	Program Management
K. W. Spiegel	-	Thruster Design and Hardware Fabrication
C. E. Greninger	-	Optics
G. D. Simpson	-	Plasma Initiation
J. L. Hillman	-	Thruster Design
J. Nozzi	-	Thrust Stand Design
J. J. Ciana	-	Optical Train Design
C. Lamorte	-	Optical Train Design

TABLE OF CONTENTS

SUMMARY.	1
INTRODUCTION.	4
CONCLUSIONS	7
TASK I: ANALYSIS AND DESIGN	9
Performance Analysis	9
Plasma Analysis	37
Flow Analysis	61
Cooling Analysis	90
Conceptual Design & Analysis	119
Optical Train Analysis	121
10-kw Experimental Hardware Design	146
5000-kw Design Configuration	169
TASK II: FABRICATION	175
10-kw Thruster	175
10-kw Thrust Stand	185
REFERENCES	187

ILLUSTRATIONS

1. Stationary Plasma with Ricirculating Chamber Flow Pattern	2
2. Flowing Plasma with Continuous Chamber Flow	2
3. Laser Heated Rocket Thruster	3
4. Theoretical Equilibrium Vacuum Specific Impulse Variation with Carbon Concentration and Chamber Temperature ($\epsilon = 40:1$)	11
5. Theoretical Equilibrium Specific Impulse Variation with Carbon Concentration and Chamber Temperature ($P_{\text{exit}} = 1.014 \times 10^5 \text{ N/M}^2$ or 14.7 psia)	12
6. Influence of Area Ratio on Theoretical Equilibrium Vacuum Specific Impulse ($T_{\text{chamber}} = 5555.6 \text{ K}$ or 10,000 R)	13
7. Theoretical Equilibrium Vacuum Specific Impulse Variation with Chamber Temperature and Carbon Concentration ($\epsilon = 40:1$)	14
8. Theoretical Equilibrium Specific Impulse Variation with Chamber Temperature and Carbon Concentration ($P_{\text{exit}} = 1.014 \times 10^5 \text{ N/M}^2$ or 14.7 psia)	15
9. Theoretical Equilibrium Vacuum Specific Variation with Chamber Temperature for Pure H_2 ($\epsilon = 40:1$)	16
10. Vacuum Specific Impulse Differential (Equilibrium and Frozen) Variation with Carbon Concentration and Chamber Temperature ($\epsilon = 40$)	18
11. Specific Impulse Differential (Equilibrium and Frozen) Variation with Carbon Concentration and Chamber Temperature ($P_{\text{exit}} = 1.014 \times 10^5 \text{ N/M}^2$ or 14.7 psia)	19
12. Theoretical Frozen Specific Impulse Variation with Carbon Concentration and Chamber Temperature ($P_{\text{exit}} = 1.014 \times 10^5 \text{ N/M}^2$ or 14.7 psia)	20

13. Theoretical Frozen Specific Impulse Variation with Chamber Temperature and Carbon Concentration ($P_{\text{exit}} = 1.014 \times 10^5 \text{ N/M}^2$ or 14.7 psia)	21
14. Theoretical Equilibrium Specific Impulse Variation with Cesium and Carbon Concentration ($T_{\text{chamber}} = 3888.9\text{K}$ or 7000 R)	22
15. Specific Impulse Difference (Equilibrium and Frozen) Variation with Cesium and Carbon Concentration ($T_{\text{chamber}} = 3888.9 \text{ K}$ or 7000 R)	23
16. Hydrogen - Carbon Gas Composition ($T_{\text{chamber}} = 3888.9 \text{ K}$ $C_c = 0.20$)	24
17. Performance Loss Mechanisms	26
18. Influence of Upstream Throat Radius of Curvature on Flow Expansion Rate	28
19. Typical Nozzle Contour	29
20. Equilibrium Throat Gamma	30
21. Inverse Bremsstrahlung Absorption Coefficient for Hydrogen Plasma vs Temperature and Pressure, $\lambda = 10.6 \mu\text{m}$	38
22. $10.6 \mu\text{m}$ Absorption Coefficient, $C_s = 0.005$, $H = 0.995$ Mole Fraction	39
23. Volume Absorption Coefficient for Carbon	42
24. Laser-Heated Rocket Thruster - - Continuous Flow Plasma Concept	43
25. Laser Supported Combustion (LSD) Wave Velocity Variation with Laser Intensity	45
26. Plasma Inlet Velocity Variation with Laser Intensity and Plasma Temperature	46
27. Plasma Inlet Flow Velocity Determination	47

28.	Plasma Throat Area-to-Inlet Area Ratio Variation with Laser Intensity	48
29.	Plasma Throat Area-to-Inlet Area Ratio Variation with Inlet Area	49
30.	Static Pressure and Absorption Coefficient Distributions for 10-KW Power Input	51
31.	Static Temperature Distribution for 10-KW Power Plant .	52
32.	10-KW Thruster Plasma Core Dimensions	53
33.	5000-KW Chamber Plasma Core Dimensions	54
34.	10-KW Plasma Arc Initiating Candidate Power Systems . .	58
35.	Electron Density, Current and Temperature Variation with Time for an Arc Initiated Hydrogen Breakdown (Ref. 3)	59
36.	Selected 10-KW Chamber Plasma Arc Initiating Power System (Series Injection Triggered Spark Gap)	60
37.	Laser Heated Rocket Chamber Sizing	62
38.	Streamtube Heat Balance Schematic	63
39.	Streamtube Heat Balance	64
40.	Hot-Gas Flowrate Variation with Gas Temperature and Carbon Concentration (10-KW Configuration)	66
41.	Chamber Throat Radius Variation With Gas Temperature and Carbon Concentration (10-KW Chamber)	67
42.	Convective Heat Flux Variation with Boundary Layer Edge Temperature (10-KW Chamber)	68
43.	Hydrogen-Carbon Thermal Conductivity Variation with Temperature and Carbon Concentration	69
44.	Average Conductive Heat Flux Variation with Boundary Layer Edge Temperature (10-KW Chamber)	70

45.	Temperature Profiles from Conduction Analysis (10-KW Chamber)	71
46.	Determination of Absorbed Heat Flux and Boundary Layer Edge Temperature	73
47.	10-KW Water-Cooled Chamber	75
48.	10-KW Chamber Flow Recirculation Patterns	76
49.	Hot-Gas Flowrate Variation with Gas Temperature and Carbon Concentration (5000 KW Configuration)	78
50.	Chamber Throat Radius Variation with Gas Temperature and Carbon Concentration (5000 KW Chamber)	79
51.	Convective Heat Flux Variation with Boundary Layer Edge Temperature (5000 KW Chamber)	80
52.	Average Conductive Heat Flux Variation with Boundary Layer Edge Temperature (5000 KW Chamber)	81
53.	5000-KW Chamber Contour	84
54.	Schematic of Candidate Gas-Solid Mixers	87
55.	Typical Test Setup of Feed System	89
56.	10-KW Water-Cooled Chamber Cooling Capability	91
57.	Predicted 10-KW Water-Cooled Chamber Wall Temperature Distribution at Peak Heat Flux Location ($V_{H_2O} = 15.24$ m/sec or 50 ft/sec)	93
58.	Predicted 10-KW Water-Cooled Chamber Wall Temperature Distribution at Peak Heat Flux Location ($V_{H_2O} =$ 30.48 m/sec or 100 ft/sec)	94
59.	10-KW Chamber Arc Initiating Electrode Insulator Wall Temperature Distribution (Water Cooling Only)	95
60.	10-KW Chamber Arc Initiating Insulator Wall Temperature Distribution (Water and H_2 Cooling)	96

61.	10-KW Heat Sink Chamber with Graphite Inserts	98
62.	10-KW Uncooled Chamber - Temperature History at X = -2.54 cm (-1.0 in.)	99
63.	10-KW Uncooled Chamber - Temperature History at X = 0.0 cm with Variation in Inner Radius	100
64.	10-KW Uncooled Chamber Thermal Analysis (Copper Only) .	102
65.	10-KW Uncooled Chamber-Plasma Viewing Window	103
66.	10-KW Chamber Plasma Viewing Window Temperature History - Calcium Fluoride	105
67.	10-KW Chamber Plasma Viewing Window Temperature History - Fused Quartz	106
68.	10-KW Uncooled Chamber - Chamber Temperature History with Graphite Insert at X = -2.54 cm (-1.0 in.)	108
69.	10-KW Uncooled Chamber Thermal Analysis (Copper Chamber with Graphite Insert)	109
70.	Chamber/Nozzle Cooling Circuits	110
71.	5000 KW Chamber Nozzle Maximum Tube Gas-Side Wall Temperature and Minimum Tube Diameter Parametric Data	112
72.	5000 KW Chamber Nozzle Tube Dimensions	113
73.	5000 KW Chamber Tube Gas-Side Wall Temperatures	114
74.	5000-KW Chamber Combustor Channel Dimensions	116
75.	5000-KW Chamber Combustor Wall Temperature Distribution	117
76.	5000 KW Chamber Combustor Coolant Mach Number Distribution	118
77.	10-KW CO ₂ Laser Configuration	122
78.	10-KW CO ₂ Laser Configuration (Magnification = 2.0) . .	124

79.	10-KW CO ₂ Laser Relative Intensity Distribution (Output Beam Magnification = 2.0)	125 125
80.	10-KW CO ₂ Laser Relative Phase Angle Distribution (Output Beam Magnification = 2.0)	126 126
81.	10-KW Optical Train Concepts	128
82.	10-KW Experimental Hardware Optical Train (Laser Beam Output Magnification = 1.523)	129
83.	10-KW Experimental Hardware Optical Train (Laser Output Beam Magnification = 2.0)	131
84.	10-KW Laser Heated Rocket Thruster Test Apparatus (Laser Output Beam Magnification = 2.0)	132
85.	10-KW Laser-Heated Rocket Test Apparatus (Laser Output Beam Magnification = 1.523)	133
86.	10-KW Chamber - Laser Window Intensity Distribution . .	135
87.	10-KW Chamber Window Temperature Distribution After 60 Seconds	136
88.	10-KW Chamber Window Steady-State Temperature Distribution	137
89.	10-KW Optical Train Assembly (M = 2.0)	139/140
90.	10-KW Optical Train Assembly (M = 1.523)	141/142
91.	Typical Space Vehicle Installations	143
92.	5000-KW Optical Train Concepts	144
93.	Laser Beam-To-Optical Train Envelope Limitations . . .	145
94.	10-KW Water-Cooled Chamber Assembly and Detail . . .	149/150
95.	10-KW Thruster Assembly	153/154
96.	Uncooled Chamber Assembly	155/156
97.	10-KW Heat Sink Chamber Thermocouple Installation .	157/158
98.	10-KW Heat Sink Chamber-Graphite Insert	159/160

99.	10-KW Heat Sink Chamber - Typical Plasma Viewing Window Installation	161/162
100.	10-KW Chamber Injector Assembly.	163/164
101.	10-KW Chamber Thrust Stand Assembly	167/168
102.	5000-KW Chamber Configuration (Multiple Carbon Seeded Flow Injection)	171/172
103.	5000-KW Chamber Configuration (Single Carbon Seeded Flow Injection)	173/174
104.	10-KW Water-Cooled Chamber - Liners, Structural Shell and Ignitor Flanges	176
105.	10-KW Water-Cooled Chamber	177
106.	10-KW Water-Cooled Chamber Assembly	179
107.	10-KW Thruster Ignitor Components	180
108.	10-KW Thruster Ignitor Assembly	181
109.	10-KW Uncooled Chamber	182
110.	10-KW Uncooled Chamber Assembly.	183
111.	10-KW Thruster Injector Components	184
112.	10-KW Thrust Stand	186

TABLES

1.	Carbon-Hydrogen Reaction Set	32
2.	Third Body Efficiencies	32
3.	10-KW Chamber Performance	33
4.	5000-KW Chamber Performance	36
5.	10-KW Chamber Dimensions	74
6.	5000-KW Chamber Dimensions	83
7.	Powder Feed Units	86
8.	Plasma Viewing Window Materials	104

SUMMARY

Conceptually the laser-heated rocket may employ one of two methods of operation which are illustrated in Fig. 1 and 2. The first concept has a stationary plasma with a recirculating chamber flow. The second concept utilizes a focused beam with a flowing plasma and a continuous chamber flow without recirculation. The final concept selected in this program was a combination of the two concepts. The selected concept used a focused beam with a flowing plasma and recirculating flow pattern upstream of the plasma and continuous flow in the region of the plasma.

In this program, analysis and design of the 10-kw experimental thruster was performed in Task I. Physical Sciences, Inc. defined the plasma core size and through flow (stable plasma) and heat transfer influences the $3.45 \times 10^5 \text{ N/M}^2$ (50 psia) chamber pressure 10-kw thruster was sized for sea level operation. The throat diameter of this chamber was 0.1168 cm (0.0468 inch) and the main hydrogen injector was 8.89 cm (3.5 inches) upstream of the throat with a 11.43 cm (4.5 inch) distance from the 4.445 cm (1.75 inch) diameter zinc selenide window to the throat. The igniter (plasma arc initiating electrode mechanism) with retracting tungsten electrodes is located 2.54 cm (1-inch) upstream of the throat. With the predicted peak heat flux of 2519 watts/cm^2 ($15.4 \text{ Btu/in.}^2 \text{ sec}$), the water-cooled chamber would allow steady state operation with a 1.7 to 2.3 margin on burnout heat flux. This could be accomplished without carbon seed and therefore to avoid the potential throat plugging problem, pure hydrogen was selected as the propellant.

Although the plasma size was predicted with the most sophisticated analytical techniques available, a possibility exists that the plasma size may be significantly larger than predicted. If this occurred in the water-cooled chamber, the walls of the chamber would overheat. Therefore, an uncooled chamber which could handle a plasma up to four times the predicted diameter was designed. The thrust stand was designed to accommodate either the water-

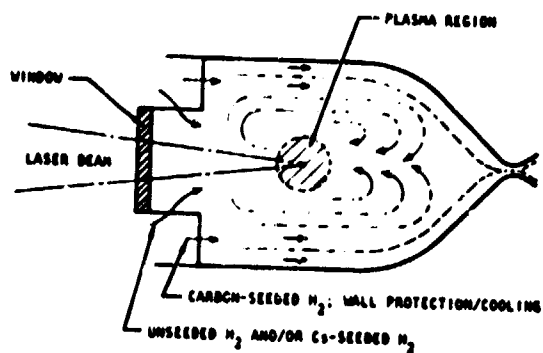


Figure 1. Stationary Plasma With Recirculating Chamber Flow Pattern

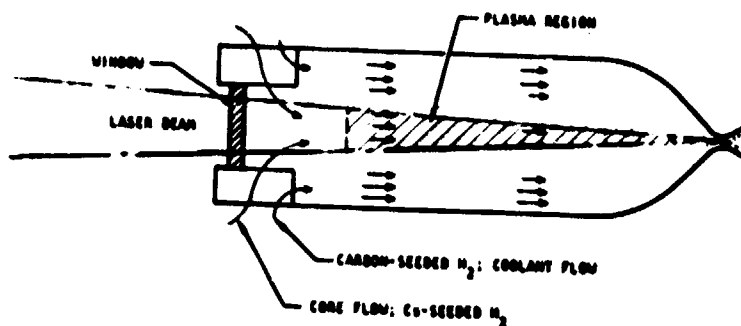


Figure 2. Flowing Plasma With Continuous Chamber Flow Pattern

cooled or uncooled chamber using a balance beam concept with a load cell to measure thrust.

Using methods similar to the JANNAF (Joint Army, Navy, NASA, Air Force) rocket thrust chamber performance methodology, the predicted specific impulse for the 10-kw thruster was $1232.5 \text{ lb}_f \text{ sec/lb}_m$.

The 10-kw thruster component designs prepared in Task 7 were fabricated which included the water-cooled chamber, uncooled chamber, injector, igniters, and thrust stand.

Detail design evaluation of several optical train configurations for the 10-kw experimental thruster were considered and a pointer cassegrain was selected. Beam propagation and chamber window thermal analyses were performed. Detailed drawings of the recommended optical train design were prepared and sent to the NASA-LeRC Project Manager.

The conceptual evaluation of the 5000-kw chamber for space application revealed that carbon seeding was necessary to reduce the plasma radiation heat input. To accomplish this, the radiation absorption layer must have a significantly lower velocity than the primary hot gas. Perhaps the best method of introducing the carbon seeded hydrogen gas is to use multi-injection ports. Using current rocket engine technology, a chamber with zirconium-copper, channel wall cooled combustor and tubular nozzle regeneratively cooled with hydrogen was designed for a 40-to-1 area ratio nozzle. The predicted vacuum specific impulse was $1363.3 \text{ lb}_f \text{ sec/lb}_m$.

An optical train analysis of the 5000-kw configuration resulted in a 90-degree orientation on the incoming laser beam and the line of thrust to provide the optimum beam receiving flexibility.

INTRODUCTION

With the development of laser energy progressing as rapidly as it is, the possibility of beamed energy transmission becomes closer to reality with more efficient beam generation. One of the more promising uses of laser energy is the NASA-LeRC laser-heated rocket thruster where laser energy is beamed to a space vehicle from a ground, air, or space generating station. An optical train on the vehicle receives the beam and focuses it within the thruster through a solid window. As shown in Fig. 3, the absorption of the laser radiation is to occur via inverse bremsstrahlung and form a high temperature plasma within the flowing propellant. The propellant for this application is hydrogen possibly with a 5-micron carbon seed. The carbon seed provides a radiation absorption layer to aid in the cooling of the chamber wall. This concept also employs an electric arc to initiate propellant gas ionization. The attractive features of the laser-heated rocket are:

1. Energy transfer from a ground or space laser energy generating station where weight constraints are not limiting to a weight-critical space vehicle.
2. Potential of 1000 to 2500 $\text{lb}_f\text{sec}/\text{lb}_m$ specific impulse with increase in vehicle payloads.

A twelve-month program was performed for NASA-LeRC by Rocketdyne as the prime contractor and Physical Sciences, Inc., as a subcontractor. A space vehicle application using 5000-kw input laser power was conceptually evaluated, and a detailed evaluation and fabrication of a 10-kw experimental thruster was completed. The objectives of this program were to:

- (1) perform design and analysis of a 5000-kw laser heated rocket thruster;
- (2) design a 10-kw configuration through scaling and design analysis; and
- (3) fabricate and deliver 10-kw experimental hardware (thrust chamber assembly, thrust stand, and plasma initiation system).

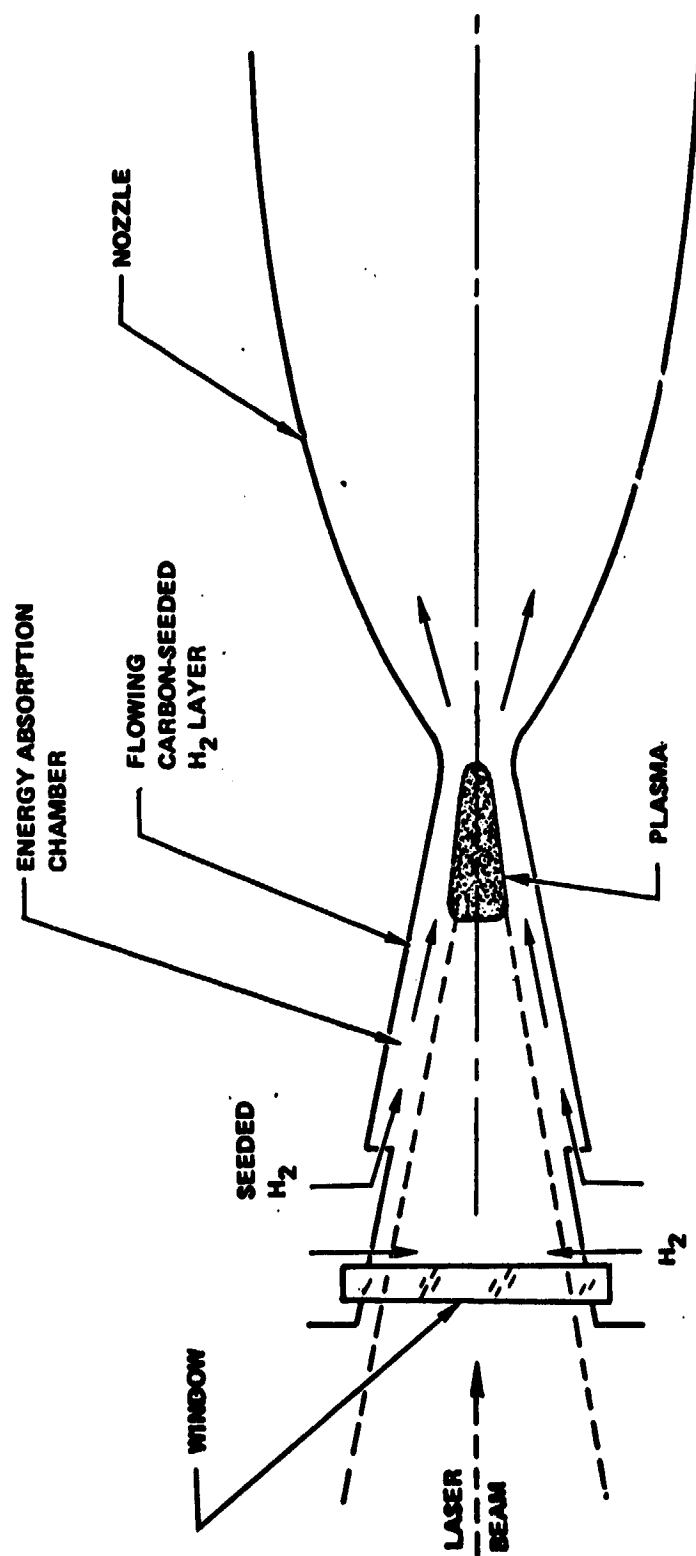


FIGURE 3. LASER HEATED ROCKET THRUSTER

The program was divided into two technical tasks and one reporting task.
Task I was to provide design and analysis of the 5000-kw and 10-kw designs.
The fabrication of the 10-kw experimental hardware was to be performed in
Task II.

CONCLUSIONS

The overall conclusions of the analysis tasks performed in this program included:

1. Delivered specific impulses exceeding 1200 $\text{lb}_f\text{sec/lbm}$ are attainable based on predictions.
2. Low laser input power results in small chamber sizes
 - a. Carbon seed in hydrogen does not significantly influence plasma size.
3. 10-kw thruster was adequately cooled using water forced convection cooling without carbon seeding.
4. 10-kw thruster zinc selenide window was adequately cooled (433 K or 319 F maximum temperature) using 10-percent of the hydrogen flow as window film coolant.
5. For the 5000-kw regeneratively-cooled thruster, a carbon seeded hydrogen layer is required to aid in cooling the chamber wall in the plasma region.
 - a. Low seed gas velocity-to-hot gas velocity ratios are required.
6. 10-kw Optical Train
 - a. For minimum blur circle size at focus, a single transverse mode laser output beam is required.

7. The unique low cost concept of using an uncooled copper chamber with graphite inserts will allow the experimental evaluation of different internal chamber contours.
8. The flowing plasma concept evaluated for both the 10-kw and 5000-kw configurations combine the convective and radiative heat fluxes in the chamber throat. Perhaps a stationary plasma concept which would only have the convective heat flux in the throat should be evaluated for advantages over the flowing plasma concept.
9. More detail evaluation of the 5000-kw configuration should be performed which would include a detailed analysis of the carbon seeded hydrogen flow injection, plasma initiation, optical train cooling, and the engine system (mounting of the thrust chamber and optical train to the vehicle).

TASK I: ANALYSIS AND DESIGN

This task consists of six analysis subtasks and two design subtasks. The analysis subtasks defined the laser-heated rocket chamber configuration, size, performance, cooling and optical train requirements for the 10-kw and 5000-kw configurations. The two design subtasks provided the design layouts of the two configurations and provided detail design drawings for the fabrication of the 10-kw experimental hardware. Also, detail design drawings of the optical train for the 10-kw thruster were performed as part of the optical train analysis.

PERFORMANCE ANALYSIS

Theoretical Performance

Theoretical performance levels which enable the assessment of a rocket thruster's performance potential are chemical equilibrium or shifting, and frozen values. Chemical equilibrium represents an upper limit in achievable performance and is the reference condition used in JANNAF performance methodology. All applicable thruster performance losses are subtracted from the equilibrium value to determine the delivered value. For chemical equilibrium, the propellant is assumed to maintain chemical equilibrium (i.e., chemical species continually change) as it progresses through the throat and the nozzle expansion. In actuality, the nozzle flow has finite reaction rates and does not occur instantaneous as assumed in the chemical equilibrium value. For frozen data, the gas composition is fixed at that in the combustion chamber and represents a lower performance limit.

To predict the delivered specific impulse of the 5000-kw (40:1 area ratio) and the 10-kw ($P_{\text{exit}} = 1.014 \times 10^5 \text{ N/M}^2$ or 14.78 psia) designs, parametric theoretical specific impulse data for various chamber gas temperatures, carbon concentrations, and cesium concentrations were generated for a chamber pressure of $3.45 \times 10^5 \text{ N/M}^2$ or 50 psia. Both equilibrium and frozen data were obtained. Since if carbon is used it will be injected as a solid and may or may not chemically react with the hydrogen, the influence of non-reacting and reacting carbon was evaluated.

For the hydrogen-carbon mixture, the addition of the high molecular weight carbon degrades the theoretical equilibrium specific impulse as shown in Fig. 4 and 5. This degradation becomes greater at the higher chamber temperatures due to the greater amount of dissociated hydrogen at these temperatures.

Also shown in Fig. 4 and 5, the non-reacting or solid carbon state resulted in a $70\text{-lb}_f\text{-sec/lbm}$ (approximately 5 percent) lower specific impulse than if the carbon is assumed vaporized and reacting at an average chamber temperature of 5555.6 K ($10,000\text{ R}$) and for the 40:1 area ratio. However, at high temperatures (3888.9 K or 7000 R and above), the carbon has been theorized to vaporize and react with hydrogen and no longer remain as a solid. Therefore, more realistically the maximum specific impulse difference between solid (non-reacting) carbon and reacting carbon will be less than $30\text{ lb}_f\text{/sec/lbm}$ (2 percent) at 3888.9 K .

Comparing Fig. 4 (40:1 area ratio) and Fig. 5 ($P_{\text{exit}} = 1.014 \times 10^5\text{ N/M}^2$ or 14.7 psia), the lower area ratio condition resulted in a 30-percent lower theoretical specific impulse. The influence of nozzle area ratio is shown in Fig. 6. A specific impulse increase of approximately 7 percent can be achieved with an increase in area ratio from 40 to 200. The carbon concentration is denoted by C_c which represents the weight fraction.

For the 5000-kw design to achieve a vacuum specific impulse greater than a $1000\text{-lb}_f\text{-sec/lbm}$, the average chamber gas temperature will have to exceed 3333.3 K (6000 R) as shown in Fig. 7. The increase in the slope of the specific impulse versus temperature curve above 2777.8 K (5000 R) is the result of a significant increase in dissociated hydrogen at these temperatures (Fig. 7 and 8). For pure hydrogen, this theoretical equilibrium vacuum specific impulse variation with temperature up to $15,000\text{ K}$ ($27,000\text{ R}$) is presented in Fig. 9.

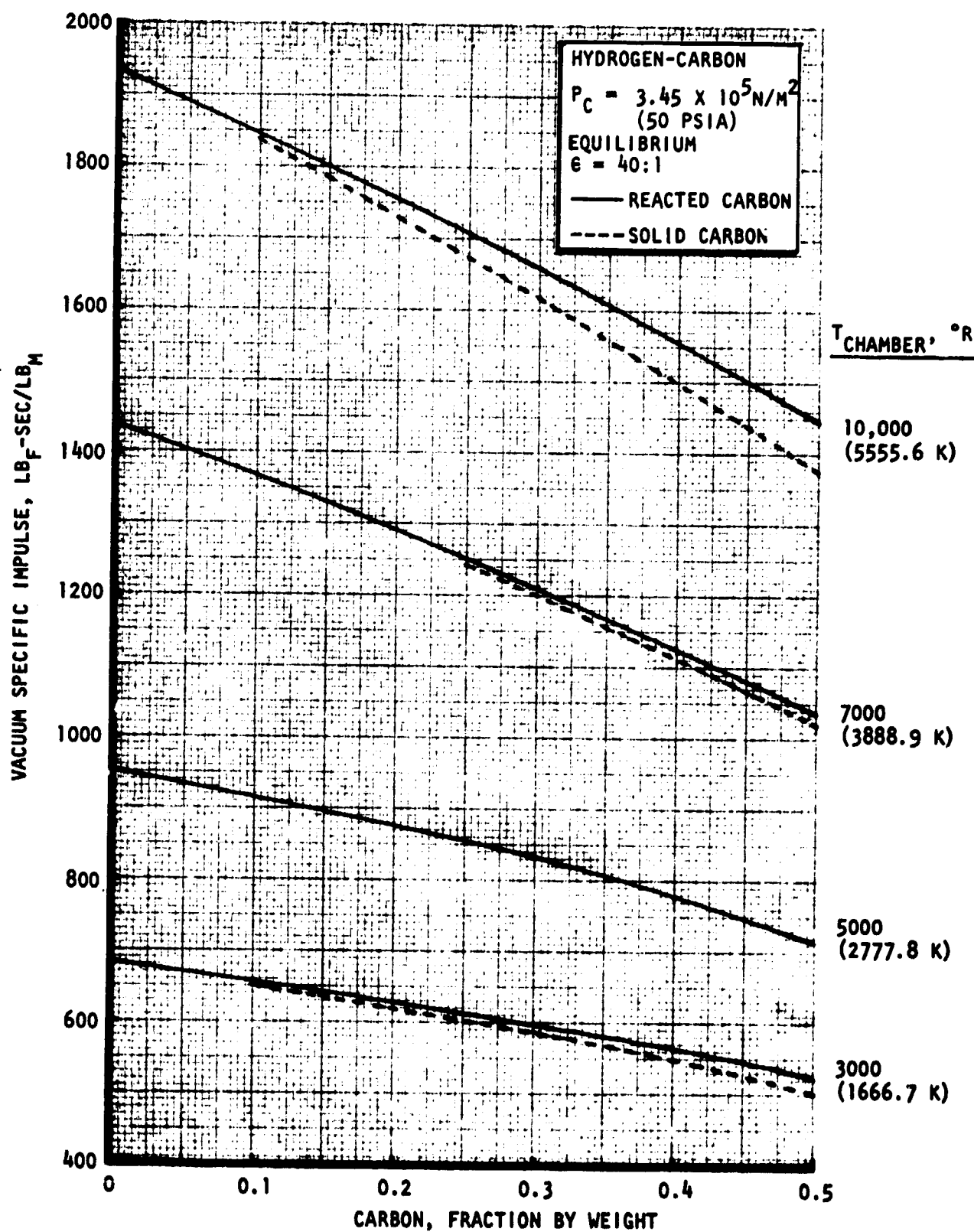


Figure 4. Theoretical Equilibrium Vacuum Specific Impulse Variation with Carbon Concentration and Chamber Temperature ($\epsilon = 40:1$)

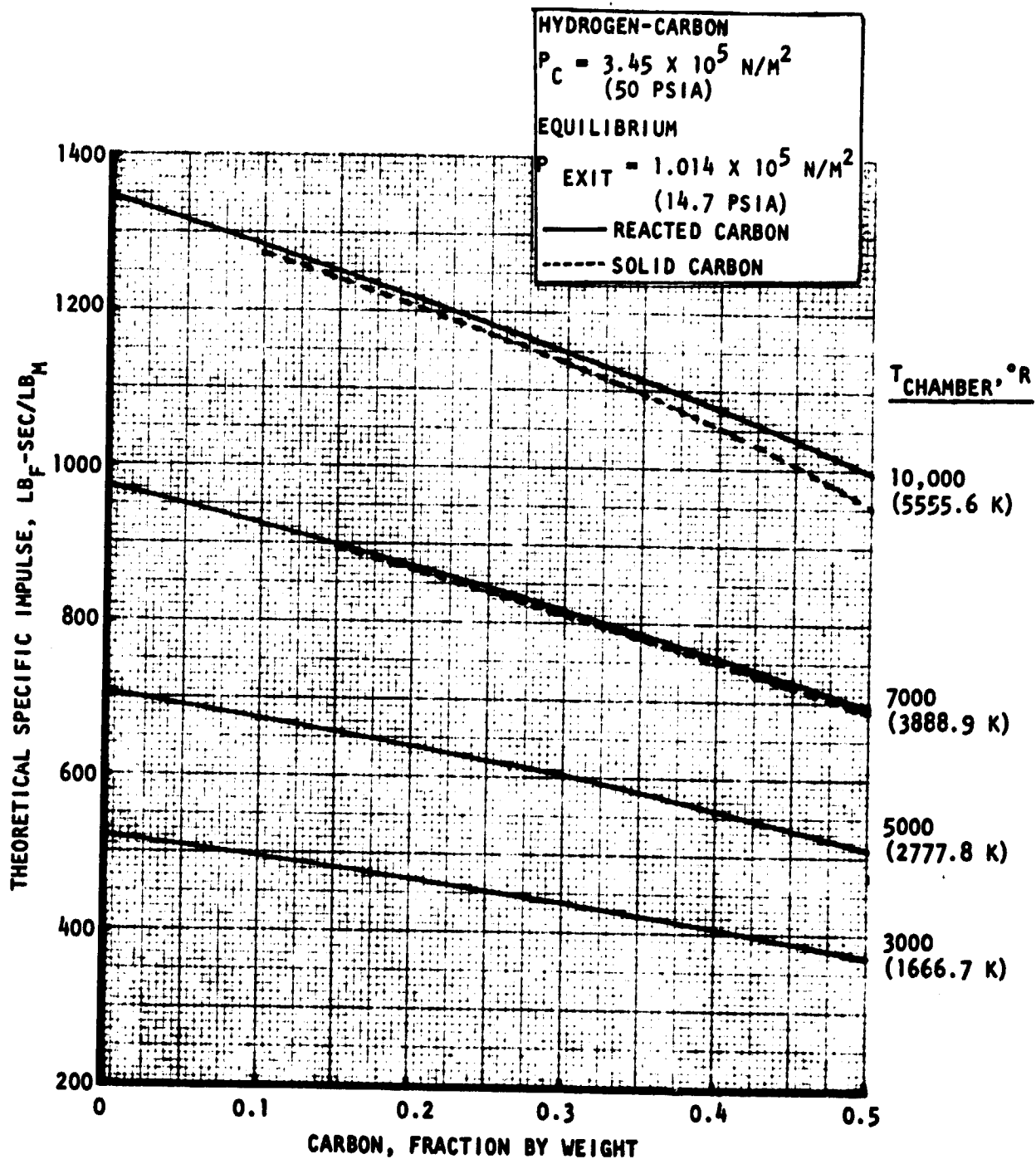


Figure 5. Theoretical Equilibrium Specific Impulse Variation with Carbon Concentration and Chamber Temperature
 $P_{\text{exit}} = 1.014 \times 10^5 \text{ N/M}^2$ or 14.7 psia)

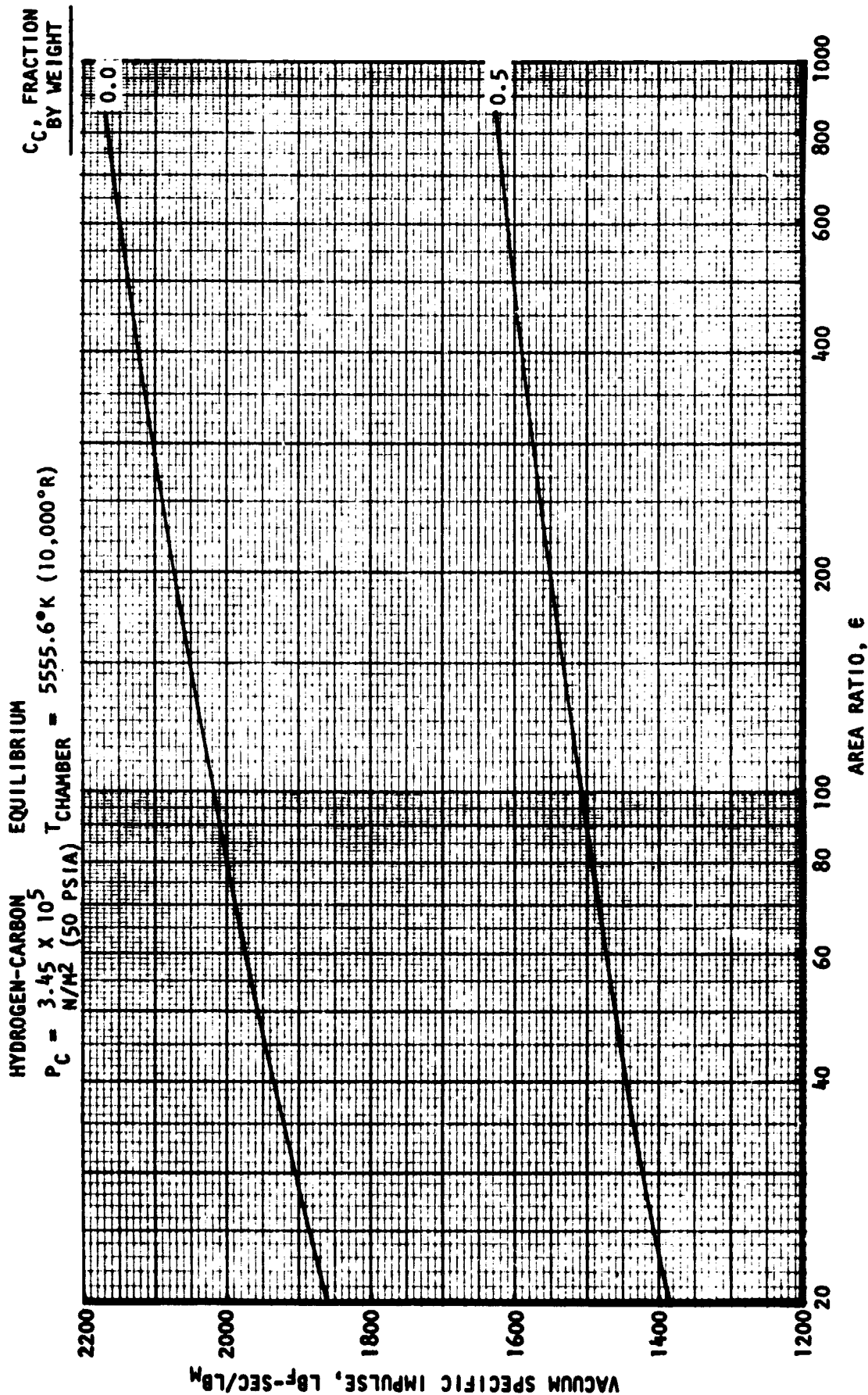


Figure 6. Influence of Area Ratio on Theoretical Equilibrium Vacuum Specific Impulse ($T_{chamber} = 5555.6^\circ\text{K}$ or $10,000^\circ\text{R}$)

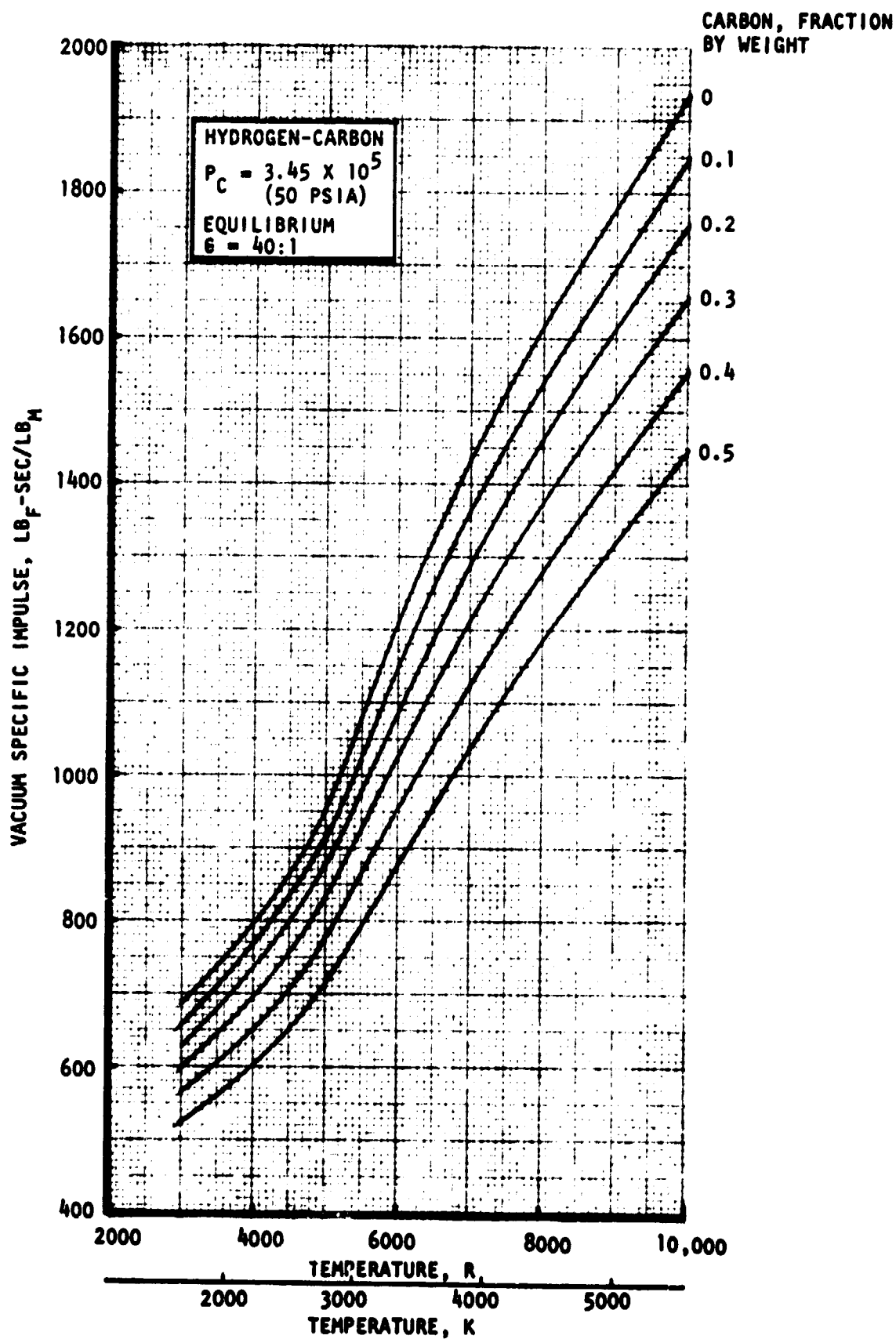


Figure 7. Theoretical Equilibrium Vacuum Specific Impulse Variation with Chamber Temperature and Carbon Concentration ($G = 40:1$)

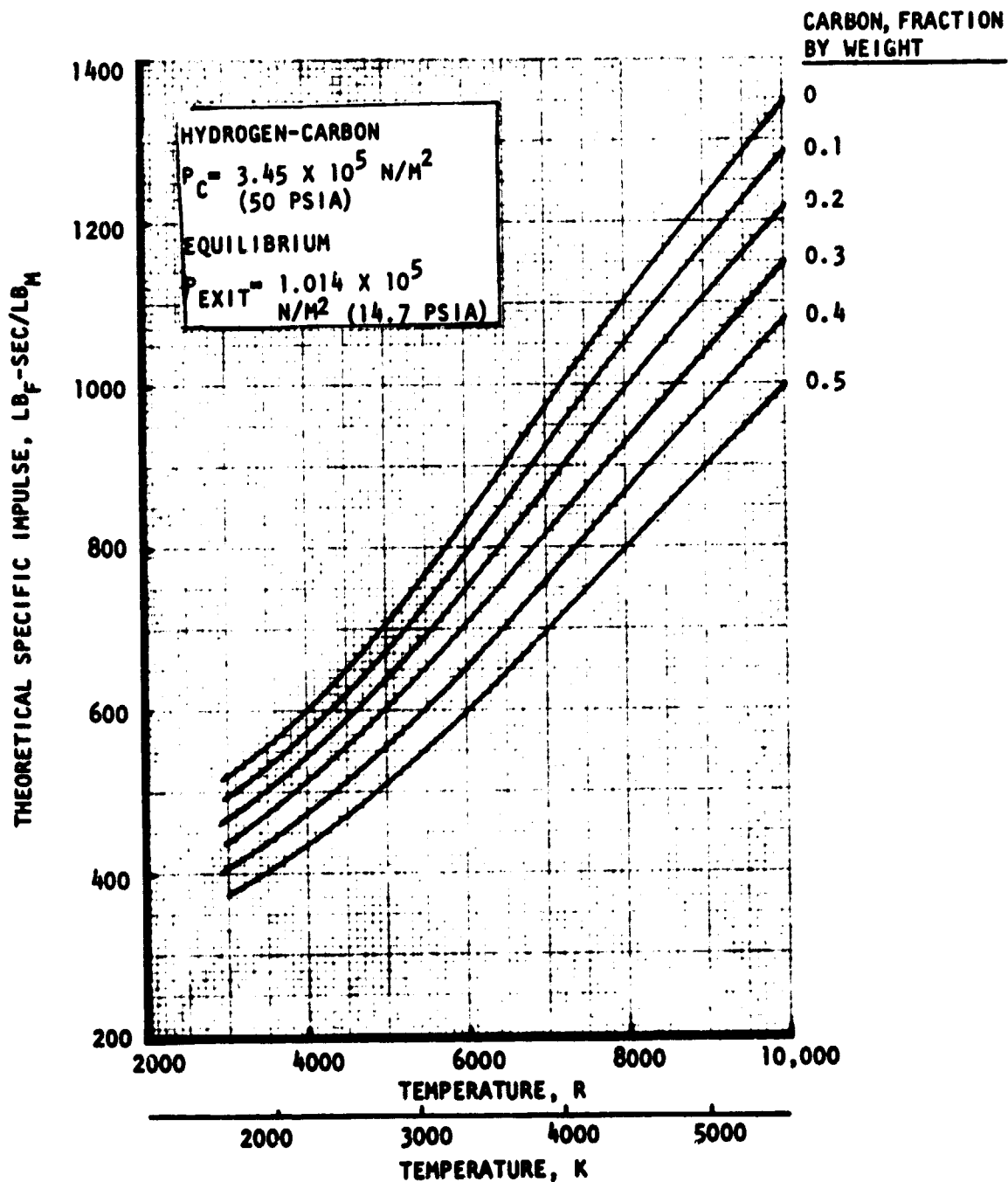


Figure 8. Theoretical Equilibrium Specific Impulse Variation with Chamber Temperature and Carbon Concentration ($P_{\text{exit}} = 1.014 \times 10^5 \text{ N/m}^2$ or 14.7 psia)

PURE HYDROGEN

$P_c = 3.45 \times 10^5 \text{ N/M}^2$ (50 PSIA)

EQUILIBRIUM

$\epsilon = 40:1$

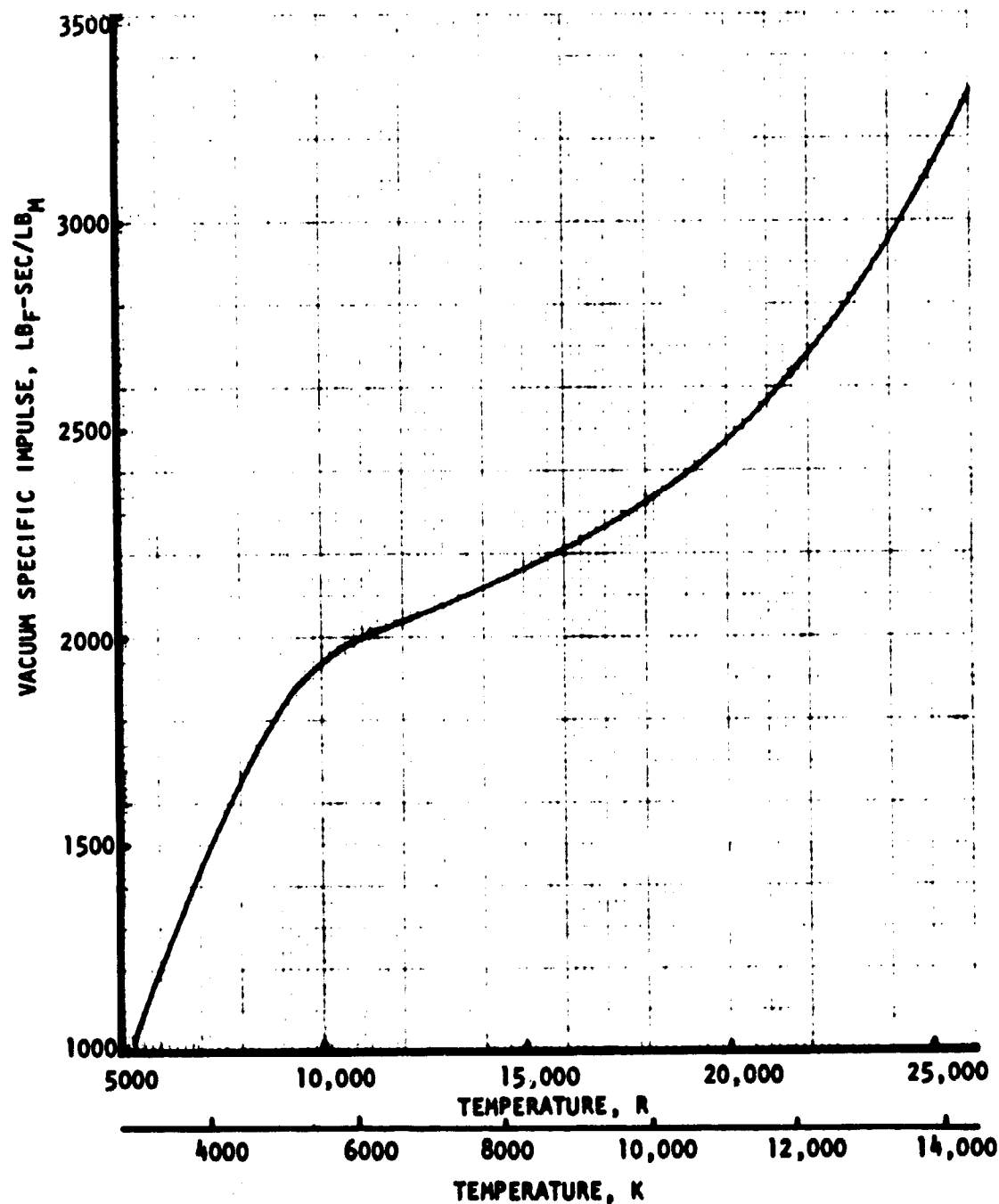


Figure 9. Theoretical Equilibrium Vacuum Specific Impulse Variation with Chamber Temperature for Pure H_2 ($\epsilon = 40:1$)

The difference between equilibrium and frozen specific impulse is presented in Fig. 10 and 11 as a function of chamber temperature and carbon concentration. This difference represents the potential reaction kinetic loss which is dependent on the propellant conditions (chamber pressure, temperature, and carbon concentration), chamber size, and nozzle area ratio. The lower area ratio (approximately 1.2:1) of the 10-kw design tends to lower kinetic losses.

However, the small size of this design will increase the kinetic loss. Therefore, the frozen specific impulse variation with chamber temperature and carbon concentration was presented in Fig. 12 and 13 for an ambient exit pressure. As shown in Fig. 10 and 11, the difference between equilibrium and frozen specific impulse decreased with increase in carbon concentration.

The addition of cesium to the hydrogen-carbon mixture can enhance the plasma formation and initiation. The influence of adding cesium to the hydrogen-carbon gas at a chamber temperature of 3888.9 K (7000 R) is shown in Fig. 14 and 15. Similarly, for the carbon the addition of cesium tends to decrease the theoretical specific impulse and the difference between equilibrium and frozen values.

Typical equilibrium gas composition distributions with the carbon reacting are presented in Fig. 16. The distribution starts at the injector and progresses downstream to the nozzle exit (40:1 area ratio). As shown in Fig. 16, the majority of the gas is composed of H and H_2 . The recombination of H to H_2 in the nozzle is evidenced by the decrease in H and the increase in H_2 . Also, the equilibrium condition predicts the formation of carbon at an area ratio of 12.5:1. However, it is anticipated that the reaction rate of forming solid carbon is so slow that solid carbon will not form.

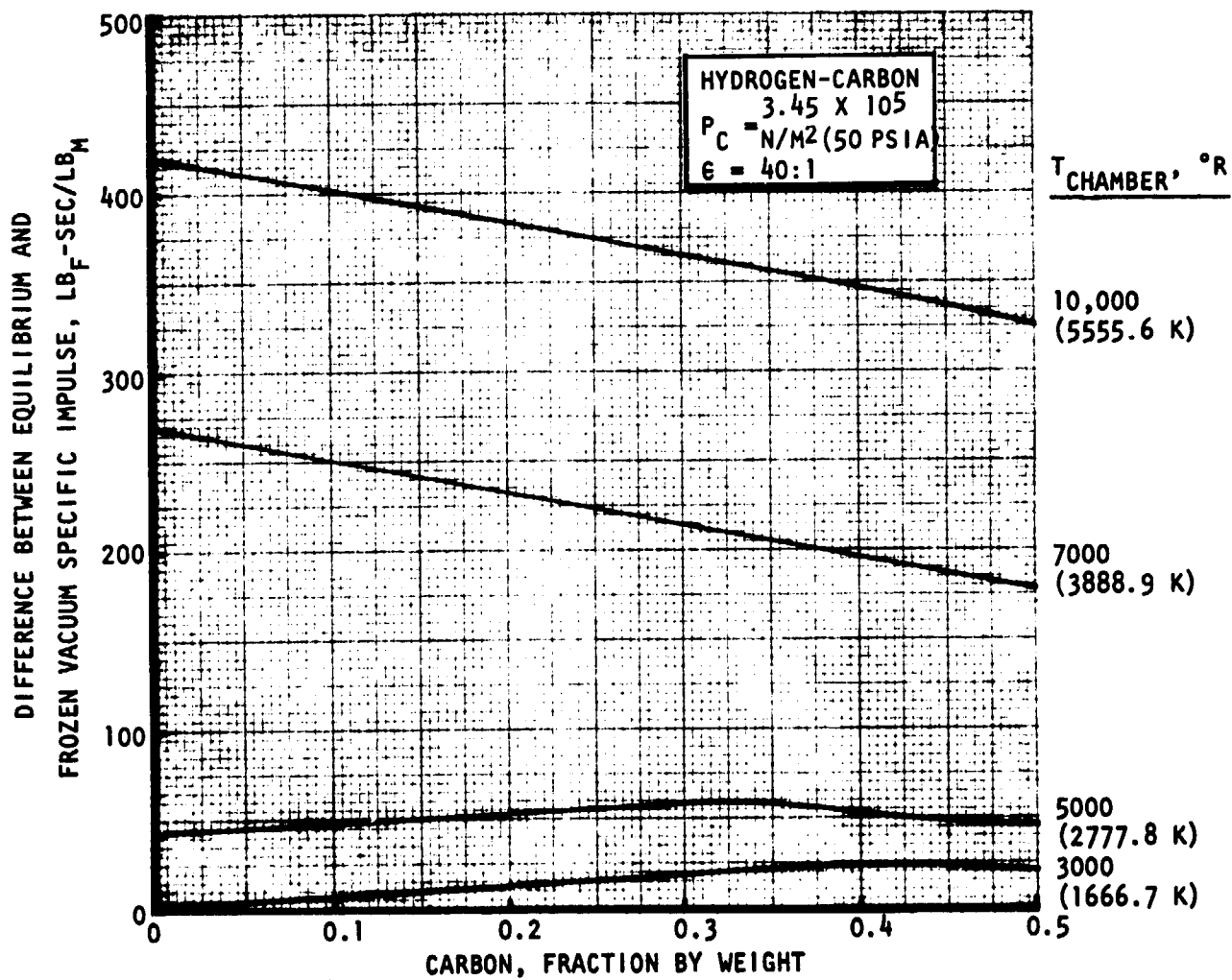


Figure 10 Vacuum Specific Impulse Differential (Equilibrium and Frozen)
 Variation with Carbon Concentration and Chamber
 Temperature ($\epsilon = 40:1$)

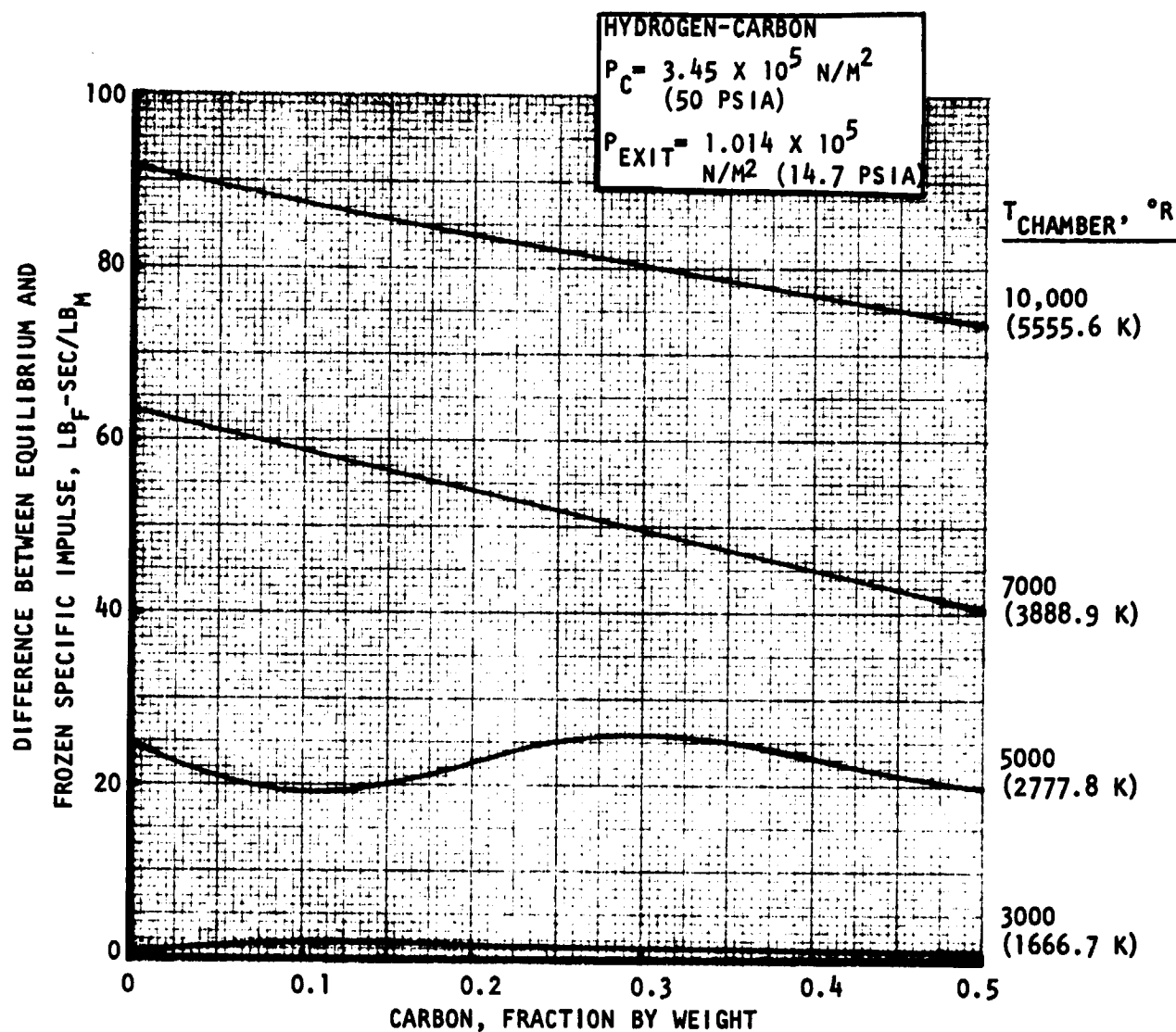


Figure 11. Specific Impulse Differential (Equilibrium and Frozen)
 Variation with Carbon Concentration and Chamber
 Temperature ($P_{exit} = 1.014 \times 10^5 \text{ N/M}^2$ or 14.7 PSIA)

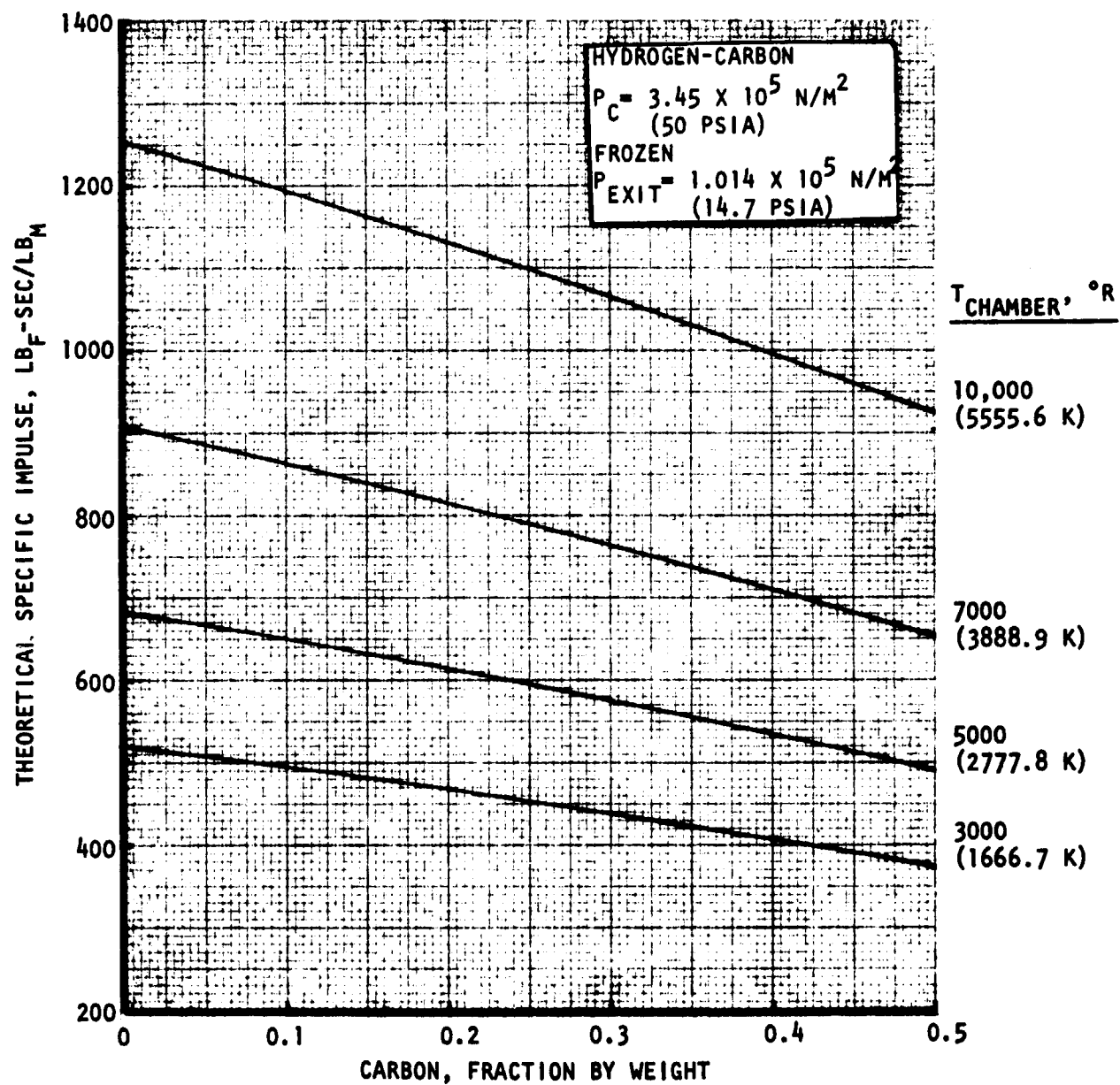


Figure 12. Theoretical Frozen Specific Impulse Variation with Carbon Concentration and Chamber Temperature
 $(P_{\text{exit}} = 1.014 \times 10^5 \text{ N/m}^2 \text{ or } 14.7 \text{ PSIA})$

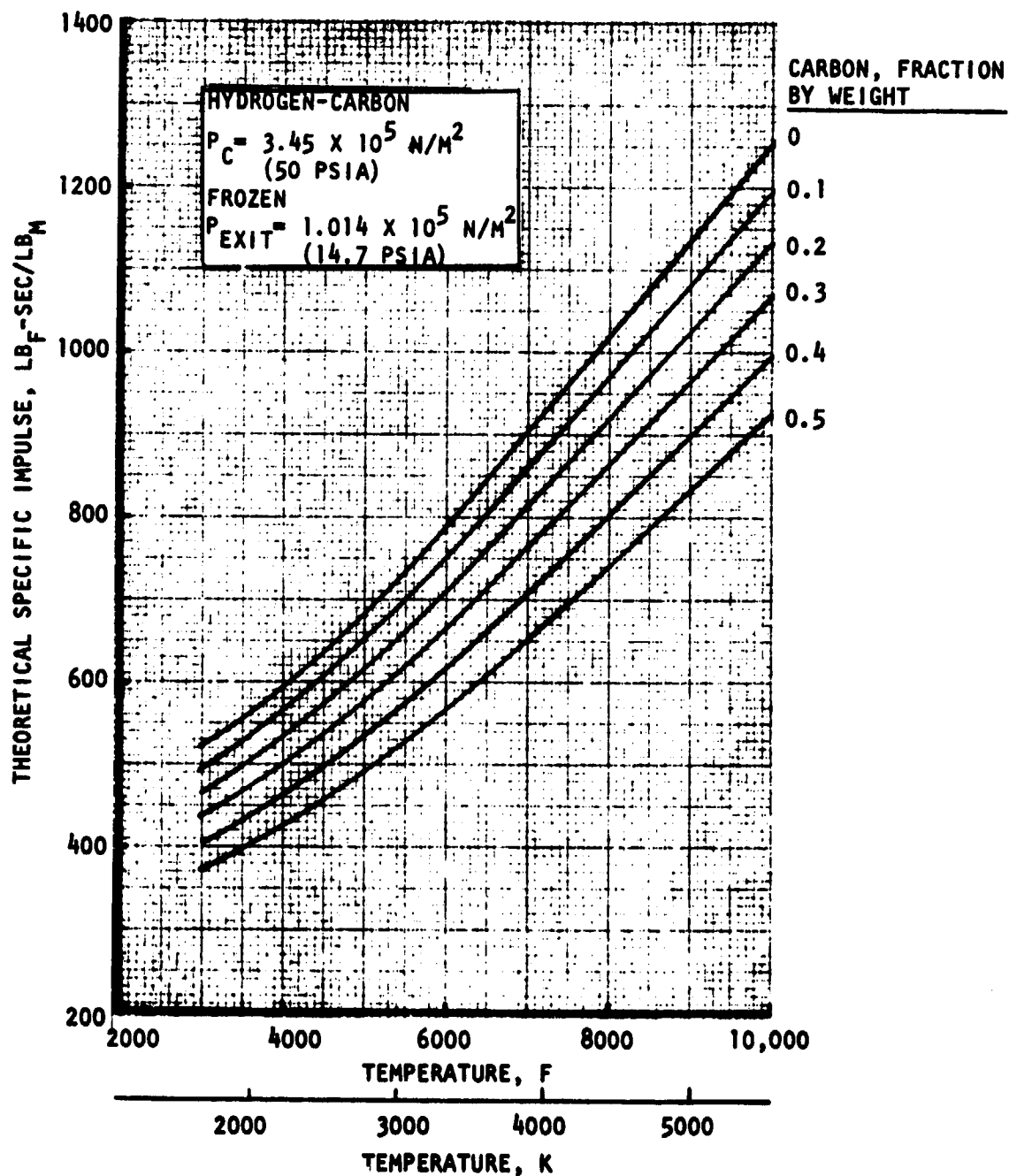


Figure 13. Theoretical Frozen Specific Impulse Variation with Chamber Temperature and Carbon Concentration ($P_{exit} = 1.014 \times 10^5 \text{ N/M}^2$ or 14.7 PSIA)

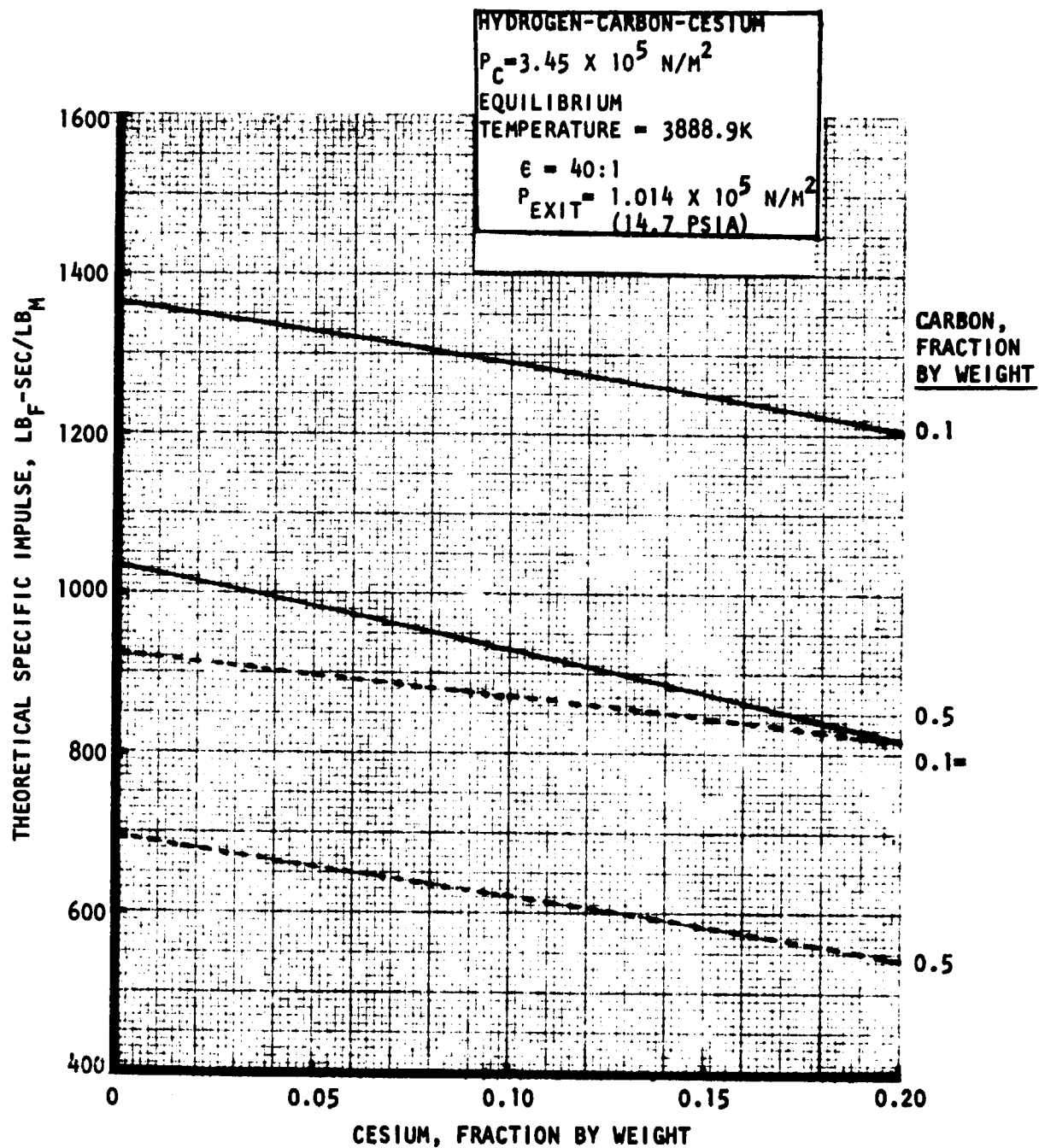


Figure 14. Theoretical Equilibrium Specific Impulse Variation with Cesium and Carbon Concentration ($T_{chamber} = 3888.9K$ or 7000 R)

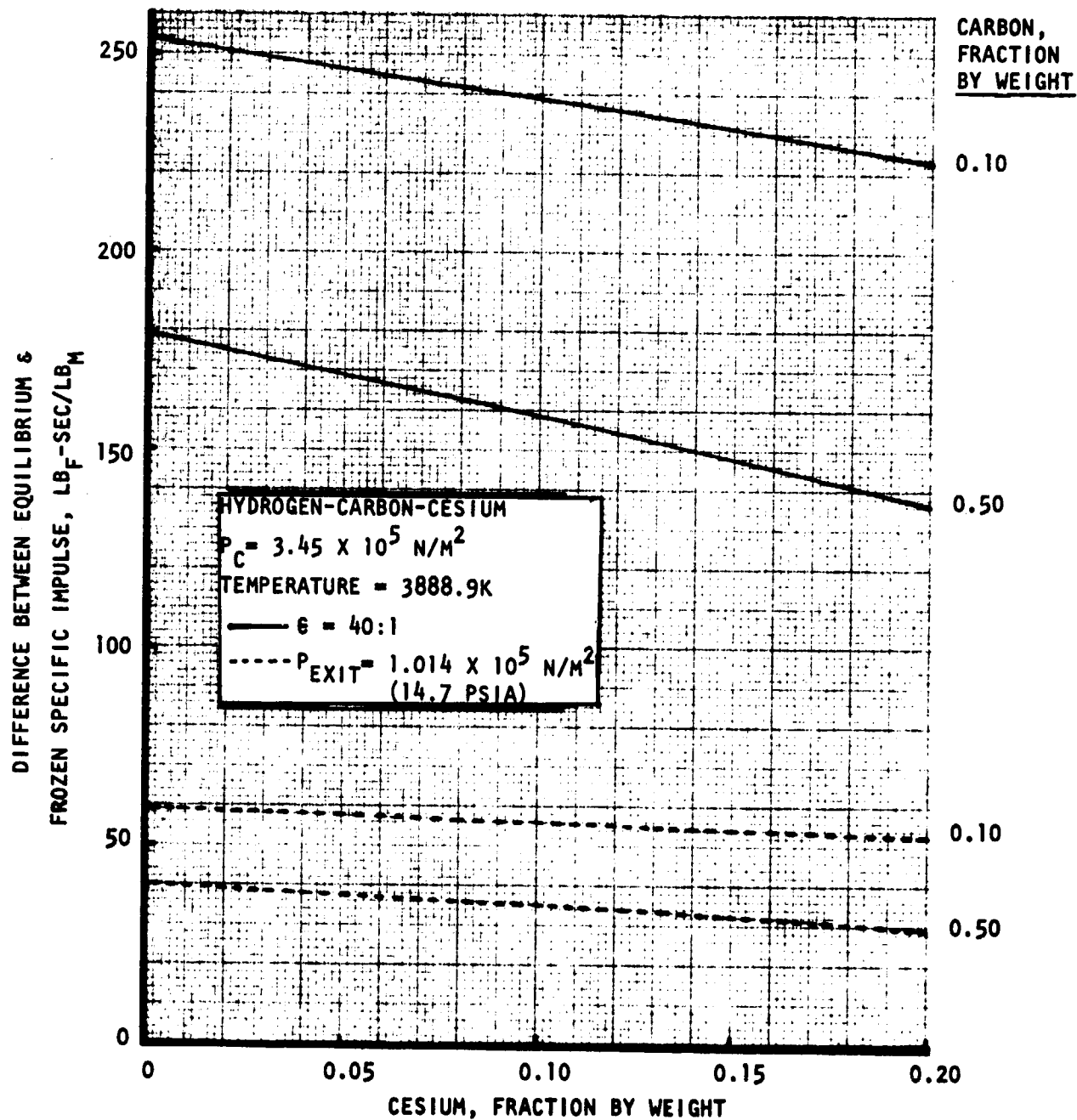


Figure 15. Specific Impulse Difference (Equilibrium and Frozen)
Variation with Cesium and Carbon Concentration
($T_{\text{chamber}} = 3888.9 \text{ K}$ or 7000° R)

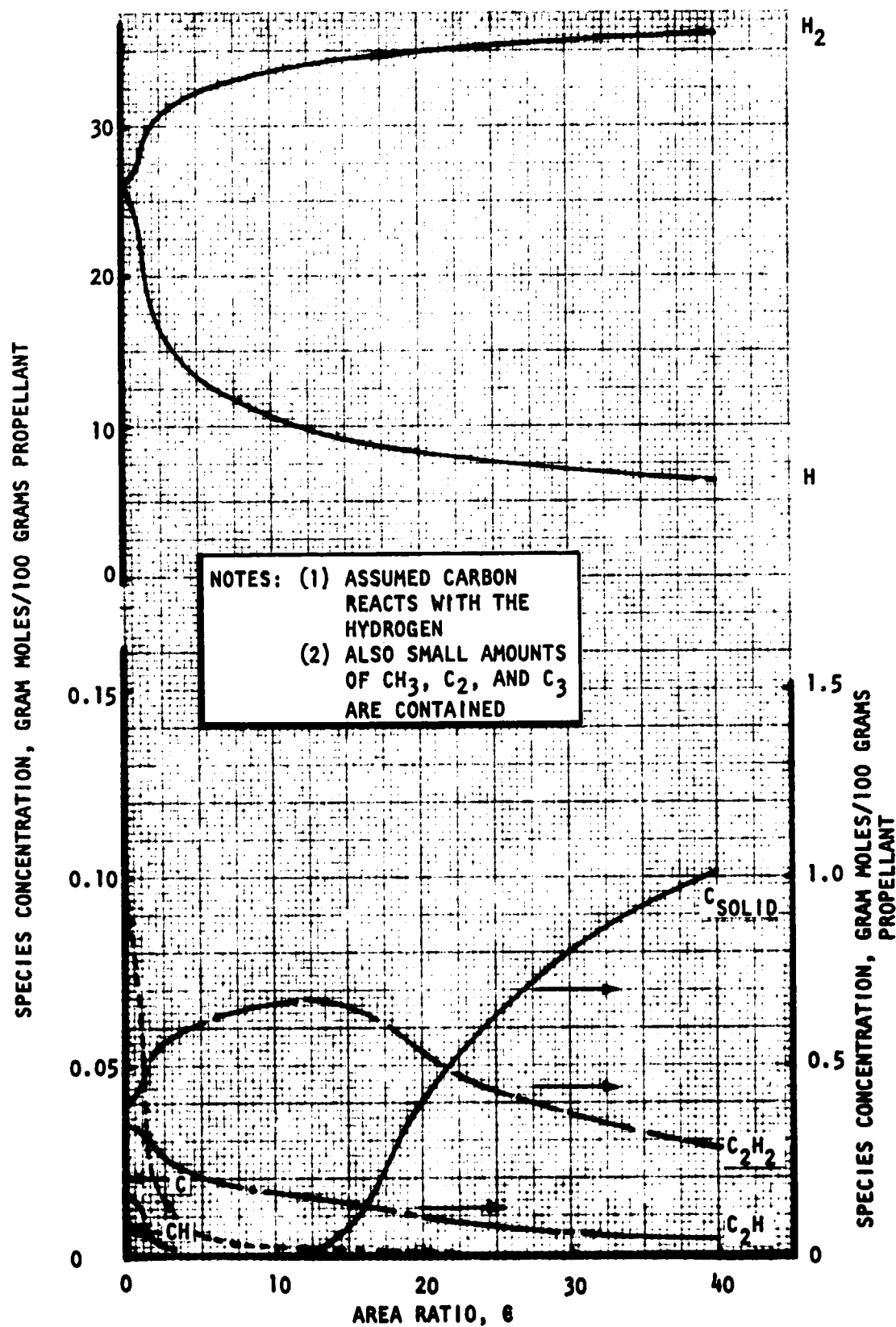


Figure 16. Hydrogen-Carbon Gas Composition ($T_{\text{chamber}} = 3888.9\text{K}$, $C_c = 0.20$)

Delivered Specific Impulse

Performance Loss Mechanism. The performance loss mechanisms associated with the laser-heated rocket are similar in principle to those which occur in a conventional chemical liquid rocket thrust chamber. Therefore, the procedures used in calculating the performance losses can be fashioned after JANNAF methodology.

Propellants (hydrogen, carbon and/or cesium) enter the thrust chamber through an injector. The laser beam sustains the plasma vaporizing the carbon and/or cesium and heating the remaining gas. The performance loss mechanisms of the laser-heated rocket are presented in Fig. 17. Any deviations from complete homogeneous mixing and heating to equilibrium can be referred to as energy release losses (energy release efficiency, η_{er}). The majority of the plasma radiant energy will be absorbed by the carbon-seeded hydrogen; however, some radiation will be lost through the window (plasma radiation loss, η_r). Chemical reactions continue to occur in the subsonic region as well as in the supersonic nozzle. In the expansion process (nozzle), deviations from the local chemical equilibrium condition are losses associated with reaction kinetics (reaction kinetic efficiency, η_k). Also in the physical expansion process, flow velocity components normal to the desired direction of thrust will occur. The loss in momentum and attendant nonuniform expansion is referred as a divergence or geometric loss (geometric efficiency, η_g). A boundary layer is formed in the region adjacent to the chamber wall due to the presence of the wall. Losses in available thrust caused by momentum and heat transfer to the wall are termed boundary layer losses (boundary layer efficiency, η_{bl}). The existence of a nonuniform temperature or carbon and/or cesium concentration distribution at the nozzle exit can result in a performance loss (nonuniform temperature and concentration efficiency, η_{ntc}). This latter influence can be determined using one of two methods. One approach is to use a stream tube analysis and account for the radial distribution of mass flow, gas temperature, carbon concentration, and the different final

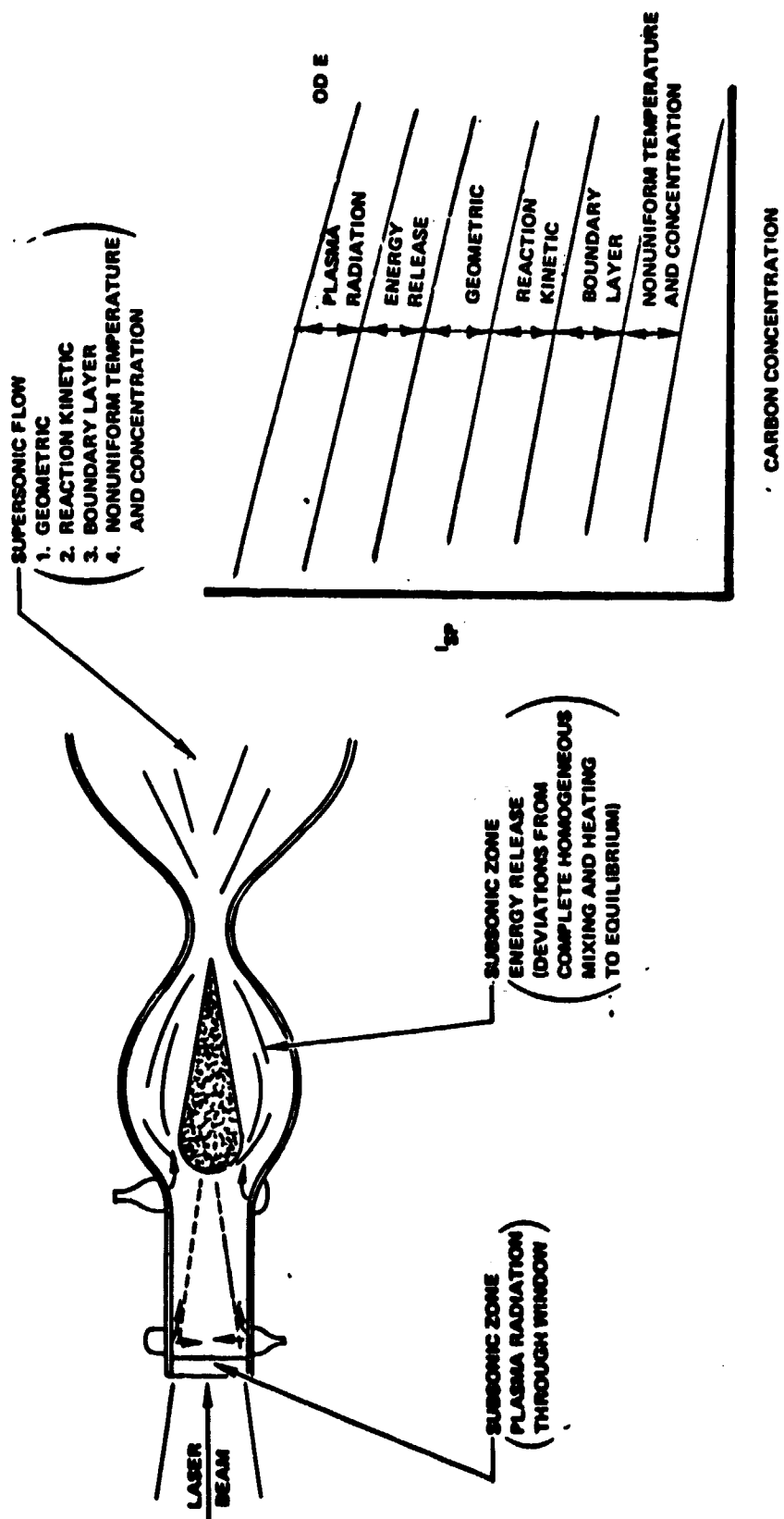


FIGURE 17. PERFORMANCE LOSS MECHANISMS

stream tube area ratios. Another more simplified approach is to utilize an average overall gas temperature and essentially one-dimensional flow.

Nozzle Contour Design.

10-KW Chamber. Since the 10-kw chamber was to be tested essentially at sea level, the nozzle area ratio was sized to have the nozzle flow full without internal flow separation. Based on the chamber pressure of $3.45 \times 10^5 \text{ N/M}^2$ (50 psia) and combustion gas properties, an area ratio of 1.6-to-1 resulted. Also since any performance gained from a contoured bell nozzle would be small for this low area ratio, a simple 15-degree conical nozzle was selected.

5000-KW Chamber To provide an efficient and rapid analysis of the 5000-kw chamber, the nozzle contour in normalized coordinates was designed by analyzing the nozzle contour over a range of conditions. This was accomplished by selecting a parabolic nozzle contour for the 40:1 area ratio, 80-percent length nozzle. This type of contour closely approximates an optimum contour in geometry and performance. For propellant combinations with high temperatures and significant amounts of hydrogen, reaction kinetic loss can be significant. This kinetic loss can be minimized through proper nozzle contouring which can be accomplished simply by increasing the upstream and downstream throat radii of curvature. As shown in Fig. 18, this tends to reduce the flow expansion rate which in turn reduces the kinetic loss.

An 80-percent length, 40-to-1 area ratio nozzle contour designed with a downstream throat radius of curvature of 2, is presented in Fig. 19.

The complexity of radial varying temperatures and carbon concentration precludes the analysis of the supersonic flowfield using full reacting flow. Past analyses conducted with chemical rocket thrust chambers indicated that a constant gamma analysis using the chemical equilibrium throat gamma (γ^*) closely approximated the reacting flowfield analysis. The variation of the

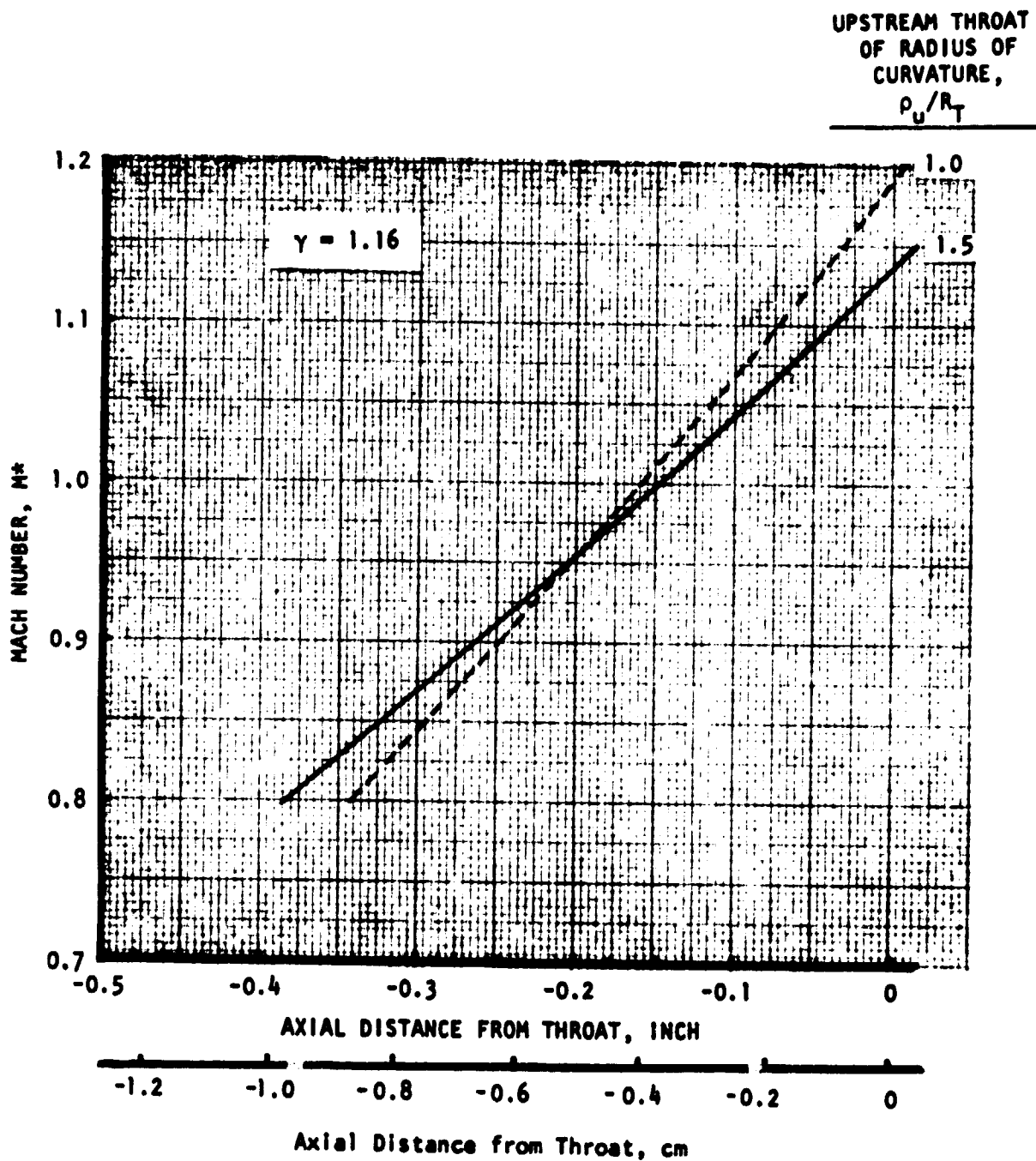


Figure 18. Influence of Upstream Throat Radius of Curvature on Flow Expansion Rate

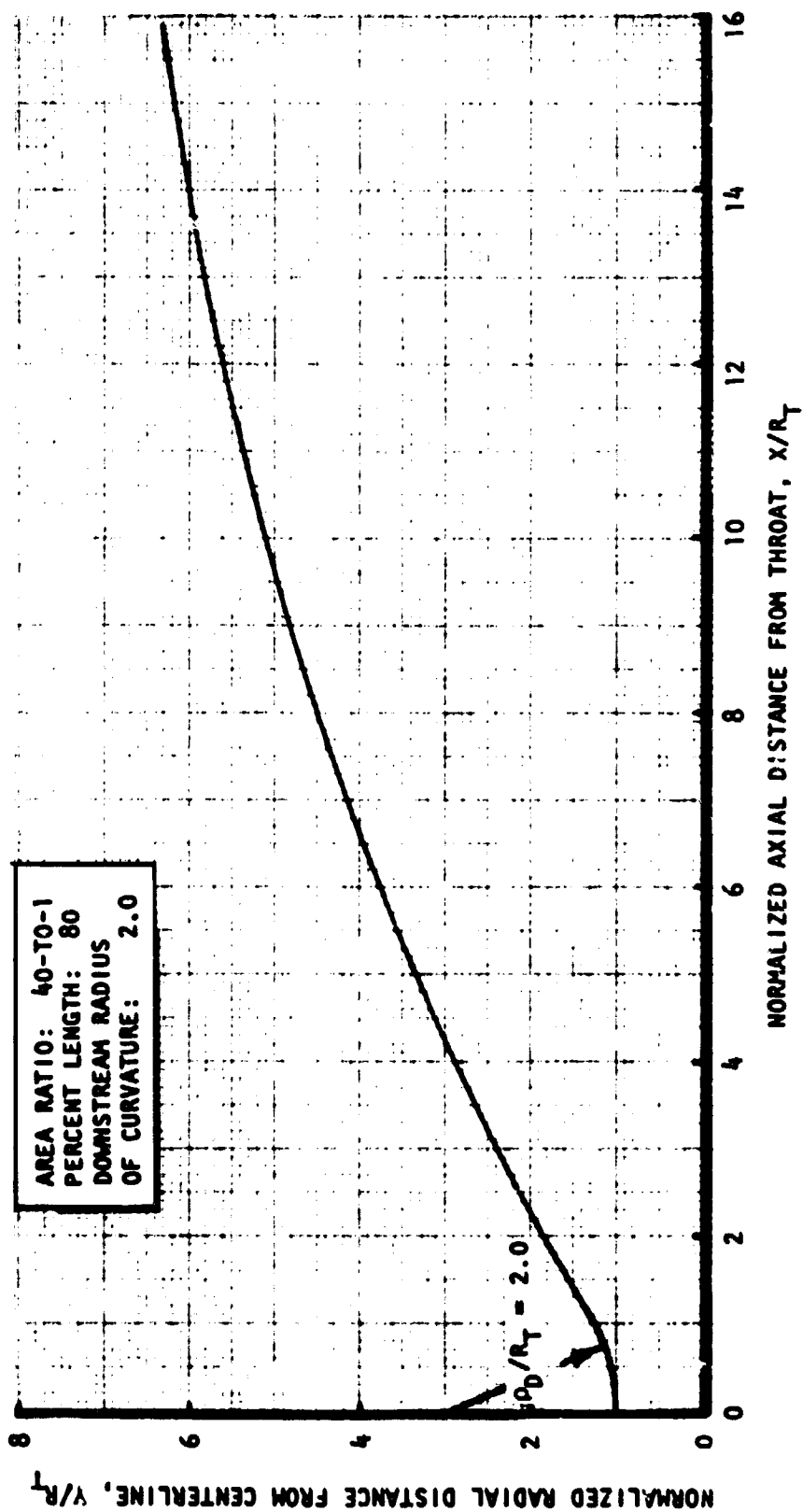


Figure 19. Typical Nozzle Contour

equilibrium throat gamma with an average chamber temperature and carbon concentration is presented in Fig. 20. For a temperature range of 3888.9K (7000 R) to 5555.6 K (10,000 R) the gamma varied from 1.16 to 1.28.

The nozzle contour shown in Fig. 19 was analyzed for these two gammas. First, a transonic solution was performed to describe the flowfield in the 0.8 to 1.2 Mach number region. This was accomplished using a computer which approximates the parabolic partial differential equations using a 33-term power series expansion. The results of this program were fed into the nozzle analysis program which performs the characteristic net solution for the remaining supersonic flowfield. Results of this analysis include the geometric efficiency and the flowfield characteristic net which could be transformed into stream tubes.

Reaction Kinetic Analysis. To perform a reaction kinetic analysis, the pertinent chemical reactions and their reaction rates must be defined. For the hydrogen-carbon propellant combination, two sets were defined. As shown in Table 1, one set is a simple set with only three reactions and the other is a more complete set with ten reactions. The third body efficiencies for the reactions containing a third body (reactions 1, 2, and 3) are presented in Table 2. The difference in reaction kinetic efficiency for these two reaction sets was evaluated for an arbitrarily selected condition of an average chamber temperature of 3888.9K (7000 R) and 20-percent carbon by weight. Using the one-dimensional kinetic (ODK) computer program, the difference in kinetic efficiency was only 0.2 percent. Therefore, the simple reaction set was used.

10-KW Chamber Delivered Specific Impulse. The 10-kw chamber contour, with a 1.6:1 area ratio, 15-degree conical nozzle, was analyzed using the Rocketdyne Boundary Layer Computer Program which utilizes an integral method of solving the momentum and energy equations (Table 3) to determine the boundary layer loss. A laminar boundary layer was assumed. The results of this computer program were also used in determining the convective portion of the chamber heat flux in which the boundary layer recombination influence

HYDROGEN-CARBON
 $P_c = 3.45 \times 10^5$
N/M² (50 PSIA)

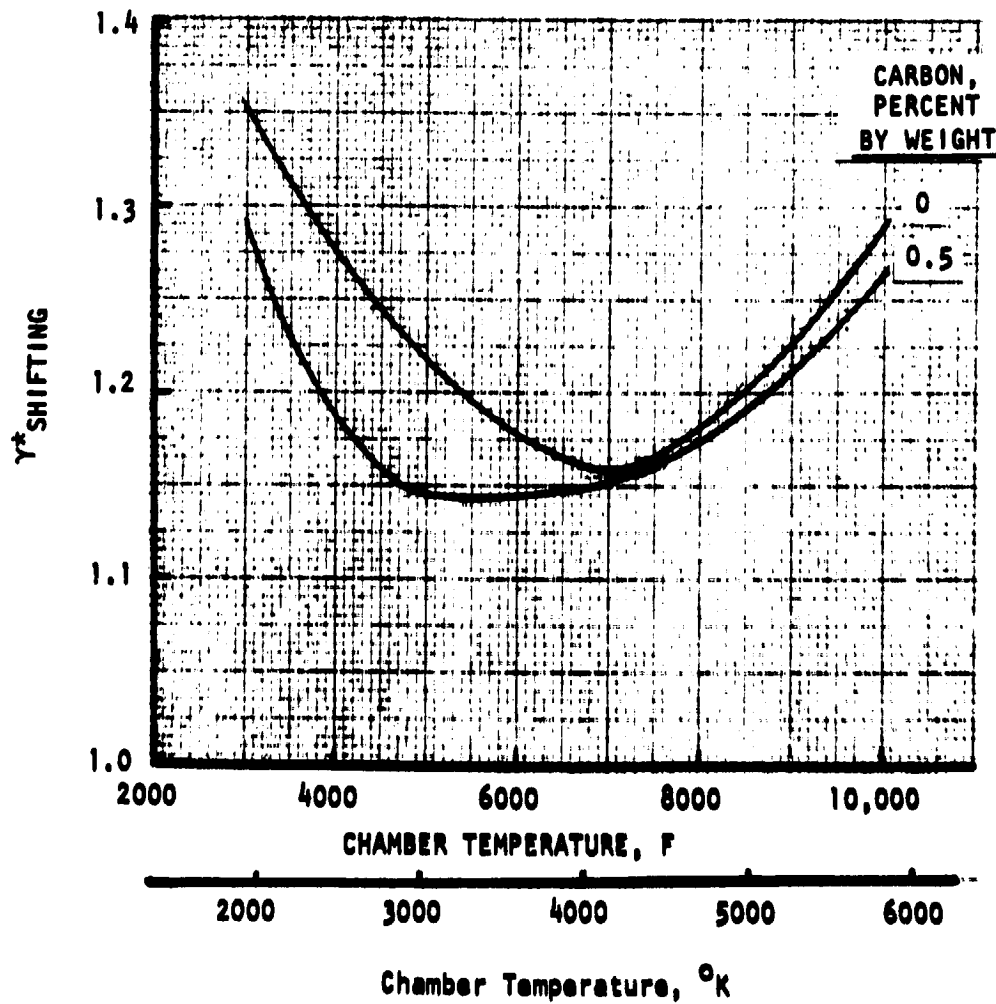


Figure 20. Equilibrium Throat Gamma

ORIGINAL PAGE IS
OF POOR QUALITY

TABLE 1. CARBON-HYDROGEN REACTION SET

$$(k_f = AT^{-n}e^{-B/RT})$$

Reaction No.	Reaction	A	N	B	Ref
1*	$H+H+M = H_2+M$	6.4×10^{17}	1.0	0.0	2
2	$H+C+M = HC+M$	1.0×10^{17}	0.5	0.0	1
3	$H+CH+M = CH_2+M$	3.0×10^{16}	0.5	0.0	3
4	$H+CH_2 = CH+H_2$	4.5×10^{11}	-0.5	25.	1
5*	$H+C_2H = C_2H_2$	4.5×10^{11}	-0.5	0.	1
6*	$H+C_2H_2 = C_2H+H_2$	4.5×10^{11}	-0.5	15.	1
7	$H+C_2 = C_2H$	4.5×10^{11}	-0.5	0.0	1
8	$H+C_2H = C_2+H_2$	4.5×10^{11}	-0.5	35.	1
9	$H+C_2 = CH+C$	4.5×10^{11}	-0.5	10.	1
10	$H+CH = C+H_2$	4.5×10^{11}	-0.5	.5.	1
* Simple Reaction Set					

TABLE 2. THIRD BODY EFFICIENCIES

Reaction No.	Species							
	C	C ₂	CH	CH ₂	C ₂ H	C ₂ H ₂	H	H ₂
1	1.5	1.5	1.5	1.5	1.5	1.5	25.	4.
2	0.2	0.2	0.2	0.2	0.2	0.2	1.	0.2
3	1.	1.	1.	1.	1.	1.	1.	1.

TABLE 3

10-KW CHAMBER PERFORMANCE

CHAMBER CONDITIONS:

$$P_c = 3.45 \times 10^5 \text{ N/m}^2 \text{ (50 psia)}$$

$$C_c = 0.0 \text{ (pure hydrogen)}$$

$$(T_{\text{comb}})_{\text{eff}} = 5556 \text{ K (10,000 R)}$$

$$R_t = 0.0594 \text{ CM (0.0234-inch)}$$

$$\epsilon = 1.6\text{-to-}1$$

EFFICIENCIES:

$$\eta_G = 0.9662$$

$$\eta_K = 0.9765$$

$$\eta_{BL} = 0.8978$$

$$\eta_{c*} = \eta_{HL} = 1.0 \text{ [since the } I_{\text{vac}} \text{ at } (T_{\text{comb}})_{\text{eff}} \text{ was used]}$$

DELIVERED SPECIFIC IMPULSE:

$$I_{s_{\text{del}}} = 1232.5 \text{ lb}_f \text{ sec/lb}_m$$

was neglected. The ODK (One-Dimensional Kinetic) analysis resulted in a reaction kinetic efficiency of 0.9765 for the 10-kw chamber. The geometric efficiency of the 1.6:1 area ratio, 15-degree cone was 0.9662. The simple source flow solution of a 15-degree conical nozzle yields a geometric efficiency of 0.9830, however, due to influences of throat radius of curvature and the low area ratio the geometric efficiency results in a lower actual value. These predicted efficiencies were used in the following simplified JANAF equation.

$$I_{s_{del}} = I_{s_{theor\ vac}} \eta_{c*} \eta_G \eta_K \eta_{HL} - (1 - \eta_{BL}) \quad (1)$$

- where
- $I_{s_{del}}$ = Delivered vacuum specific impulse
 - $I_{s_{theor\ vac}}$ = Theoretical vacuum specific impulse at injected condition
 - η_{c*} = Characteristic velocity efficiency, or η_{er} , Energy release efficiency
 - η_G = Geometric or two-dimensional efficiency
 - η_K = Reaction kinetic efficiency
 - η_{HL} = Heat loss efficiency (includes η_{ntc} and η_r)
 - η_{BL} = Boundary layer efficiency

For this analysis, an effective combustion gas temperature was used rather than the stream tube method; therefore, the non-uniform temperature efficiency (η_{ntc}) is 1.0. A discussion of the method of computing this effective temperature is presented in the Flow Analysis section. Since an effective combustion gas temperature was used which accounted for heat losses, the values of η_{c*} and η_{HL} were 1.0 and the theoretical vacuum specific impulse of 1465 $lb_f \text{ sec}/lb_m$ at the effective temperature of 5556 K (10,000 R) was used. The delivered specific impulse of the 10-kw chamber was computed to be 1232.5 $lb_f \text{ sec}/lb_m$ as shown in Table 3, which is well above the contract specific impulse goal of 1000 $lb_f \text{ sec}/lb_m$. The predicted delivered thrust is 0.387 Newtons (0.087 lb_f).

5000-KW Chamber Delivered Specific Impulse. Using the same procedure outlined for the 10-kw chamber, the boundary layer and reaction kinetic efficiencies were obtained as shown in Table 4. The geometric loss was determined by performing an aerodynamic analysis of the 40-to-1 area ratio bell nozzle. Using the computed effective combustion gas temperature ($T_{\text{eff}} = 5556 \text{ K}$ or $10,000 \text{ R}$) the predicted delivered specific impulse for the 5000-kw chamber was determined to be $1363.3 \text{ lb}_f\text{sec}/\text{lb}_m$. The predicted delivered vacuum thrust is 351.1 Newtons (79.2 lb_f).

TABLE 4

5000-KW CHAMBER PERFORMANCE

CHAMBER CONDITIONS:

$$P_c = 3.45 \times 10^5 \text{ N/M}^2 \text{ (50 PSIA)}$$

$$C_c = 0.5$$

$$(T_{\text{comb}})_{\text{eff}} = 5556 \text{ K (10,000 R)}$$

$$R_t = 1.3358 \text{ CM (0.5259-INCH)}$$

$$\epsilon = 40\text{-to-1}$$

EFFICIENCIES:

$$\eta_G = 0.988$$

$$\eta_K = 0.9737$$

$$\eta_{BL} = 0.9816$$

$$\eta_{c^*} \text{ and } \eta_{HL} = 1.0 \text{ [since the } I_{\text{vac}} \text{ at } (T_{\text{comb}})_{\text{eff}} \text{ was used]}$$

DELIVERED SPECIFIC IMPULSE:

$$I_{s_{\text{del}}} = 1363.3 \text{ lb}_f \text{ sec/lb}_m$$

PLASMA ANALYSIS

The detailed plasma analysis for this program were performed by Physical Sciences, Inc. (PSI) and presented in Ref. 1 . The pertinent results are presented in this section.

Plasma Absorption

Using the hydrogen equilibrium species composition predictions of Patch over the pressure range of 1 to 10^3 atmospheres and temperature range of 6000 K (10,800 R) to 18,000 K (32,400 R), the resulting absorption coefficient for 10.6 μm radiation (normalized by pressure) is shown in Fig. 21 . Since neutral and ionic inverse Bremsstrahlung exhibits different pressure dependence, the individual absorption coefficient, rather than the sum, has been plotted in order to facilitate interpolation between curves. Therefore, the total absorption coefficient is the sum of the two curves. For example, if an absorption coefficient of 1 cm^{-1} (2.54 in.^{-1}) was desired at a pressure of three atmospheres, an operating temperature of approximately 13,000 K (23,400 R) would be required.

Observing Fig. 21, the absorption coefficients are very small at temperatures less than 10,000 K (18,000 R) which represent long plasma lengths. To operate at lower temperatures, one possibility is to seed the hydrogen with a readily ionizable gas such as cesium. Data were obtained for several cesium/hydrogen mixtures; a typical variation with temperature and pressure is illustrated in Fig. 22 which exhibited an interesting trend with temperature. The initial rise in absorption coefficient at 3000-4000 K (5400-7200 R) is due to incomplete cesium ionization. The cesium is typically fully ionized at temperature greater than 4800 K (8640 R). The second increase occurring at temperatures of approximately 8000 K (14,400 R) is due to the onset of significant ionization of the hydrogen. The absorption coefficient may be increased by increasing the cesium concentration; however, this can only be done at the cost of a severe weight penalty since the cesium/hydrogen atomic mass ratio is approximately 133.

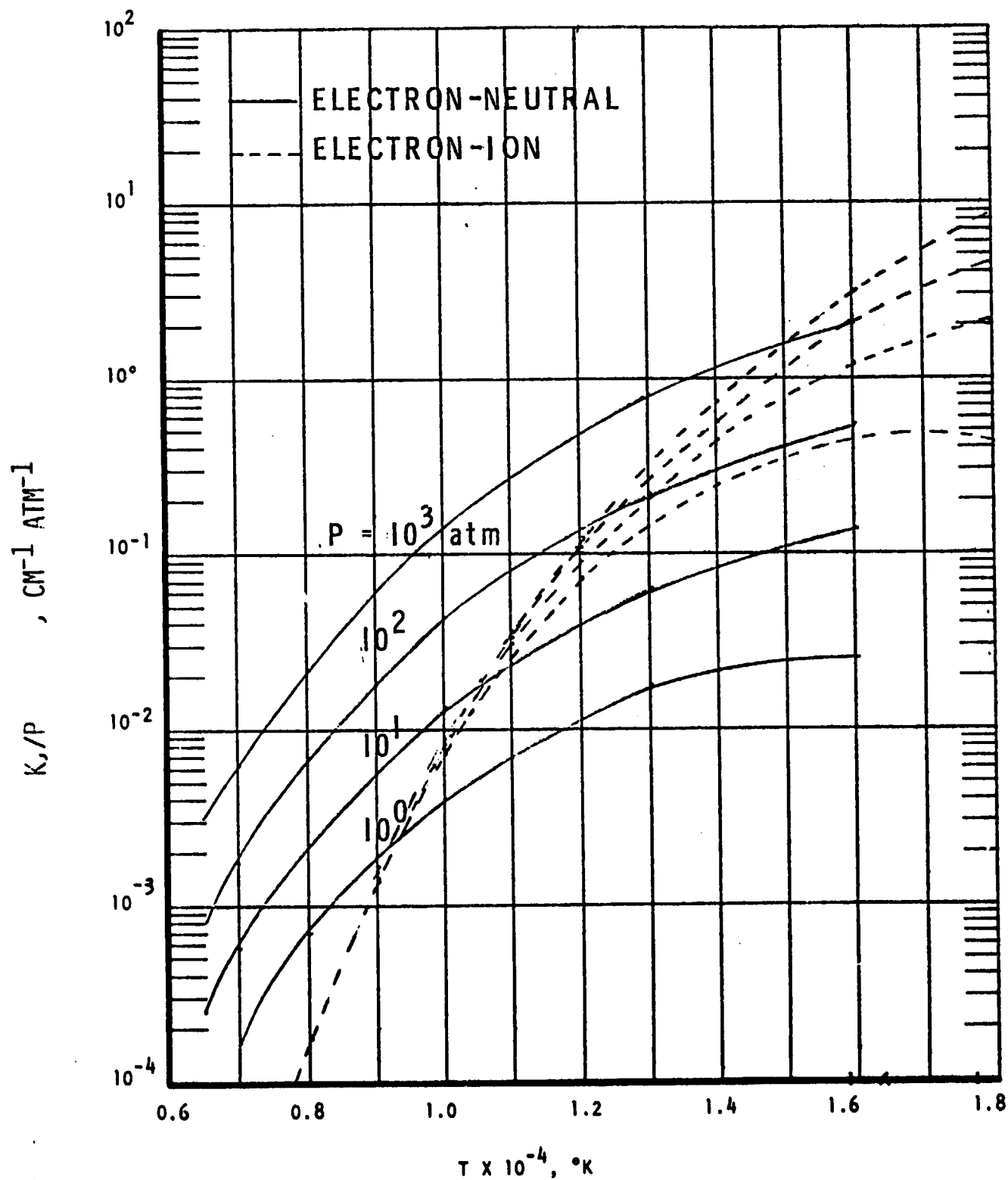


Figure 21. INVERSE BREMSSTRAHLUNG ABSORPTION COEFFICIENT FOR HYDROGEN PLASMA Vs. TEMPERATURE AND PRESSURE, $\lambda = 10.6 \mu\text{M}$

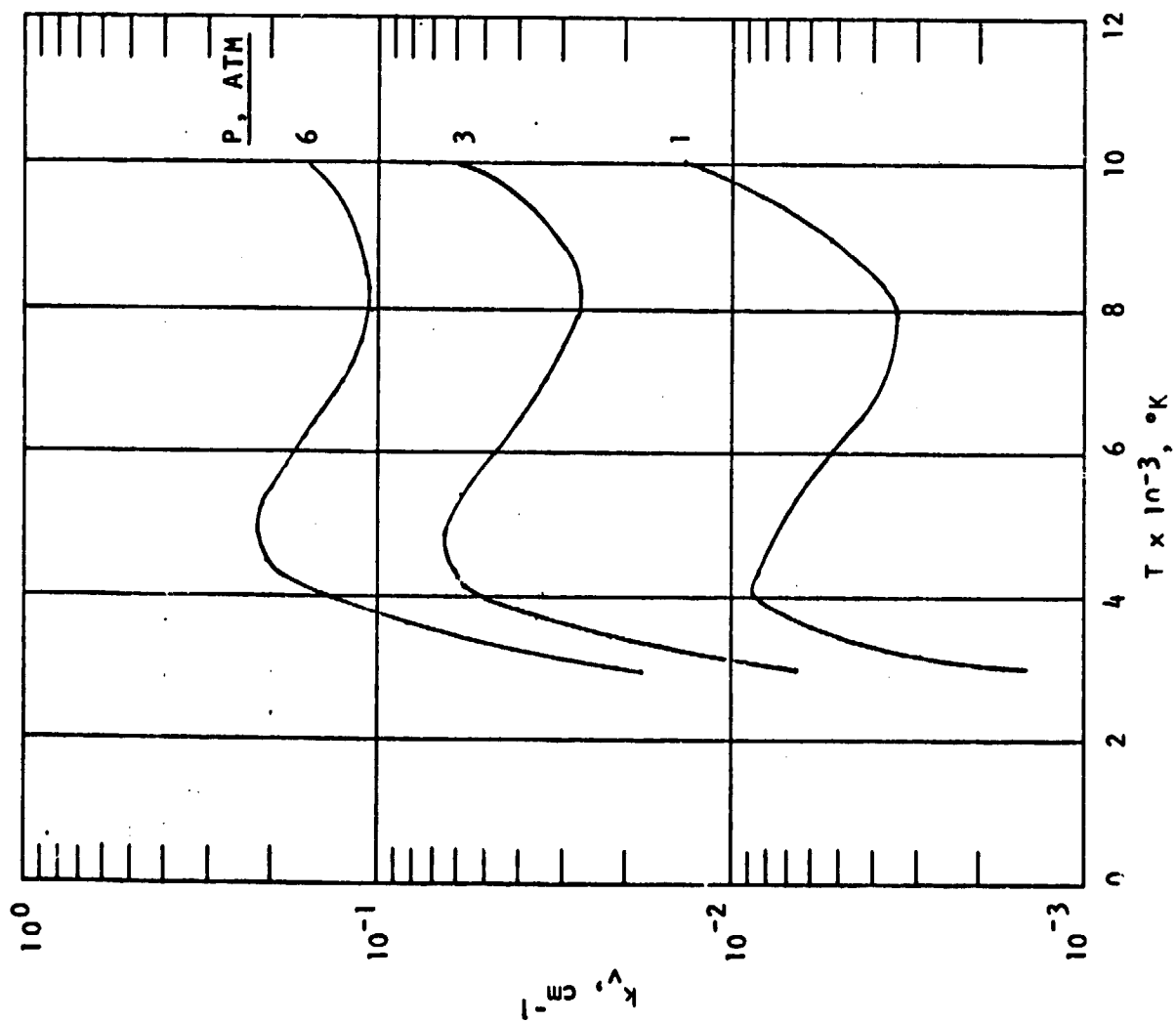


Figure 22.10.6 $10.6 \mu\text{m}$ Absorption Coefficient, $C_s = 0.005$, $H = 0.995$ Mole Fraction

Particulate Absorption

One concept is to provide a layer of seeded gas containing carbon particles as a plasma radiation absorption flow to provide a means of preventing the plasma radiation from reaching the wall. Since the coolant and plasma flows will mix to some degree, carbon particles may be along the laser path and could provide an absorption mechanism for the laser radiation.

The absorption coefficient for small carbon particles with radii within one or two orders of magnitude of the wavelength of the incident radiation was determined through use of Mie theory. The required parameters for evaluation of the Mie equations are the complex index of refraction of the material at the wavelength of interest along with the ratio of particle radius to wavelength. Unfortunately, the complex index of refraction of carbon at 10.6 μ m is not well defined. Mie theory predictions were performed for three representative values of the complex index of refractions: (a) $m = 4.0 - i 0.3$, representative of measurements made of soot both at room temperature and at 2200 K; (b) $m = 4.0 - i 1.0$, representative of room temperature measurements of pyrolytic graphite, where the imaginary part is uncertain to within a factor of two; and (c) $m = 4.4 - i 4.0$, corresponding to a theoretical prediction for graphite particles at 2100 K. While it is not expected that the complex part of the index of refraction of graphite would increase by a factor of 4 between 300 K and 2100 K, this last case (c) has been included to demonstrate the possible temperature variation in the absorption coefficient.

Since the interest of this work is in defining the absorption length for a given particulate mass loading, it is convenient to express particle absorption properties in terms of α , the volume absorption coefficient in cm^{-1} . The absorption cross section for a particle is defined by

$$\sigma_p = \alpha V_p \quad (2)$$

where V_p is particle volume and the total absorption length for a given particle density, N_p , is

$$L = (\sigma_p N_p)^{-1} \quad (3)$$

$$= (\alpha N_p V_p)^{-1}$$

or in terms of particle mass loading/cc, m_p

$$L = (\alpha m_p / \rho_p)^{-1} \quad (4)$$

where ρ_p is the particle specific density. Thus, α may be used to directly relate absorption length to mass loading. Note that the most efficient absorption/unit mass occurs at the largest value of α .

Predicted values of α for the three aforementioned values of the complex index of refraction are shown in Fig. 23, for particle radii between 10^{-1} - 10^{+2} μm . It can be seen in all three cases that the most efficient absorption occurs for particle sizes of 1 - 2 μm . The decrease in α with increasing particle size is due to optical thickness effects.

For purposes of example, if α is taken to be $6 \times 10^3 \text{ cm}^{-1}$, then from Eq. 4 a mass loading of $3.7 \times 10^{-4} \text{ gm/cc}$ would result in an absorption length of 1 cm, where ρ_p has been taken to be 2.25 gm/cc. (For comparison, 3 atm. of H_2 at room temperature would have a density of $2.4 \times 10^{-4} \text{ gm/cc}$.) It should be pointed out that the absorption efficiency of the graphite particles would decrease at higher temperatures because of vaporization effects since the boiling point of graphite is $\approx 4500 \text{ K}$. The magnitude of this effect would, of course, be dependent on flow conditions.

Plasma Core Sizing

Discussions with PSI indicated that the most realistic plasma core concept was the continuous flowing plasma flow pattern (Fig. 24). Therefore, the effort concentrated on this approach.

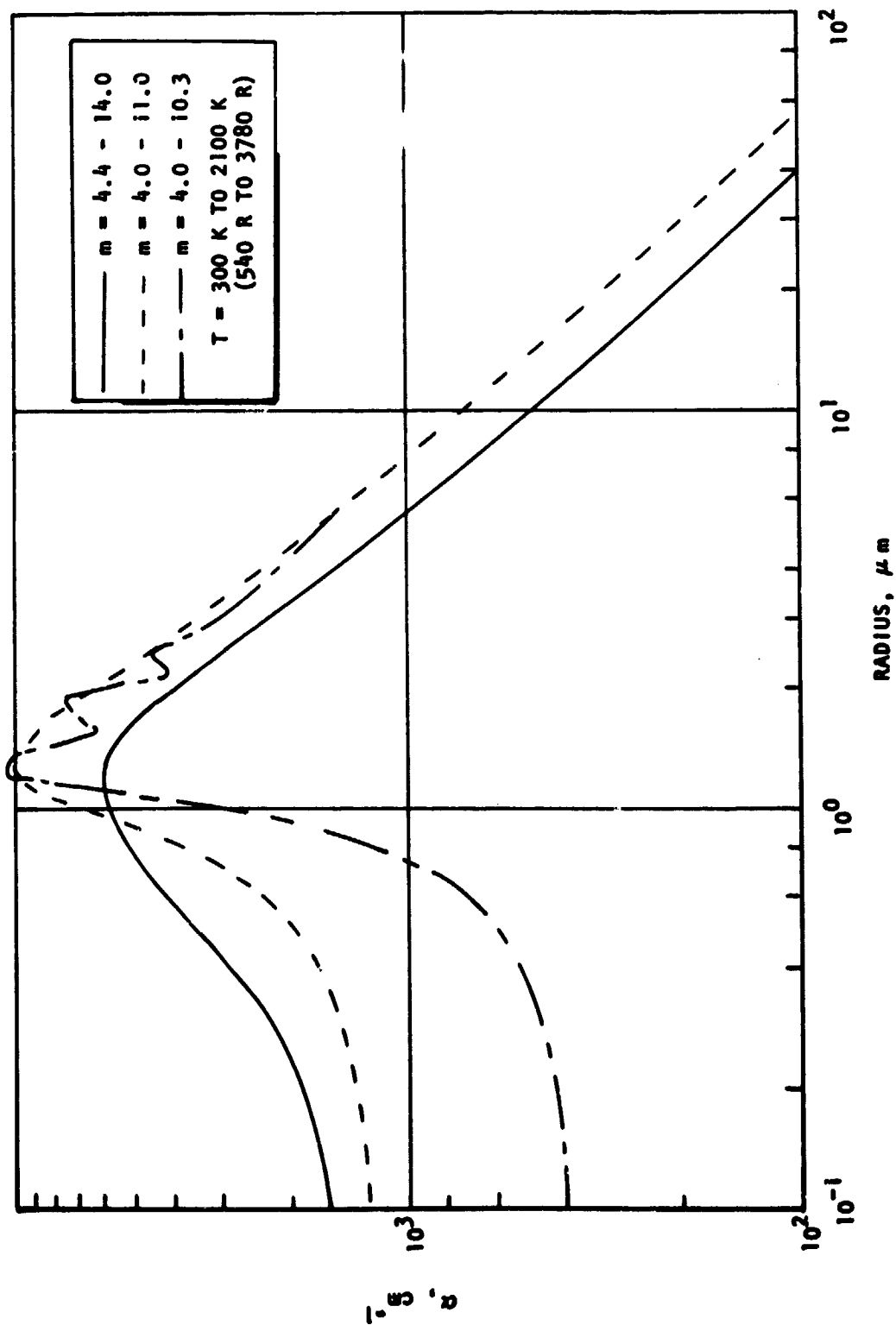


Figure 23. Volume Absorption Coefficient for Carbon

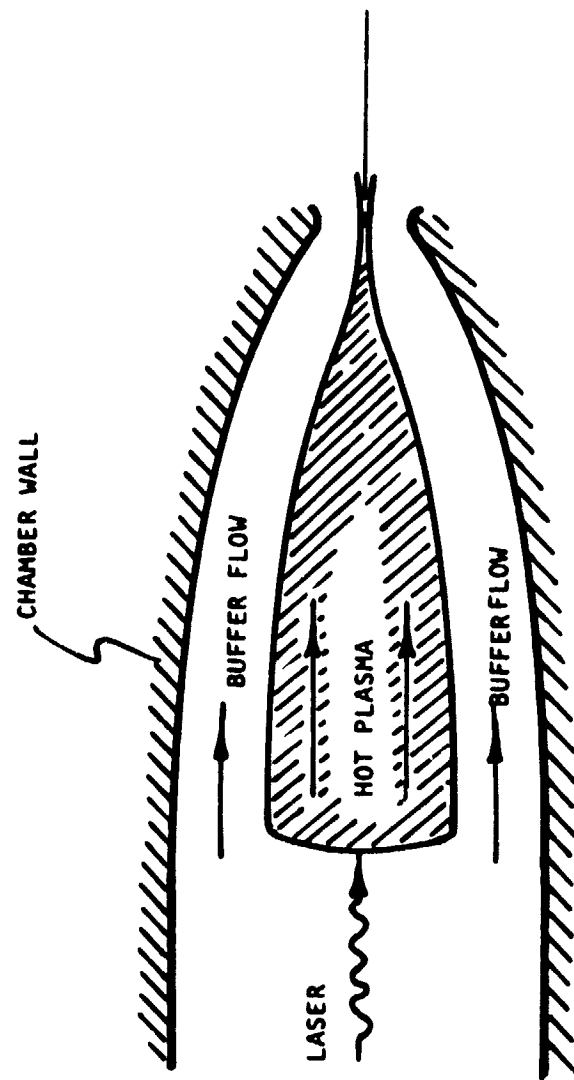


Figure 24. Laser-Heated Rocket Thruster -- Continuous Flow Plasma Concept

The plasma core analysis utilized a one-dimensional laser supported combustion (LSC) wave analysis and an available nozzle computer code to define the plasma core properties.

An LSC wave analysis analogous to that of Jackson and Nielsen (Ref. 2) was performed to estimate the propagation velocity of the plasma as part of Contract NAS3-19695, Laser Heated Rocket Absorption Study. In order for the high temperature plasma to remain stationary within the chamber, the front of the "heated zone" (plasma) must propagate at a velocity equal to but opposite to inlet flow velocity (Fig. 24). The variation of the hydrogen plasma propagation velocity ("cold gas") with laser flux or intensity is presented in Fig. 25. In addition, theoretical results (Ref. 2) and experimental data for air are presented for comparison.

The variation of the initial velocity forward edge of ("hot gas") plasma with laser intensity is shown in Fig. 26 for a chamber pressure of 3 atm (~ 50 psia) and temperatures of 10,000 K (18,000 R) and 12,000 K (21,600 R). From the nozzle code the variation in inlet velocity with throat area-to-inlet area ratio is defined. Therefore, for a given laser intensity the intersection of the LSC wave theory curve and the nozzle code curve (Fig. 27) defines the throat area-to-inlet area ratio. Performing this for laser intensities from 10^5 to 10^6 watts/cm², the ratio of "core" throat area-to-inlet area with laser intensity shown in Fig. 28 was determined. As shown in this figure, the area ratio (inverse of contraction ratio) is not significantly influenced by the plasma temperature. The laser intensity threshold to maintain a sustained H₂ plasma is approximately 10^5 watts/cm². As the laser intensity is increased to greater than 10^7 watts/cm² laser supported detonation wave would form. For the 10-kw configuration the variation of the area ratio with plasma inlet area is obtained from the data presented in Fig. 28, as shown in Fig. 29. The plasma inlet diameter varies from approximately 0.1 cm (0.0394 inch) to 0.4 cm (0.158 inch) depending on the laser intensity. The corresponding plasma throat diameters vary from approximately 0.08 cm (0.0315 inch) to 0.1 cm (0.0394 inch).

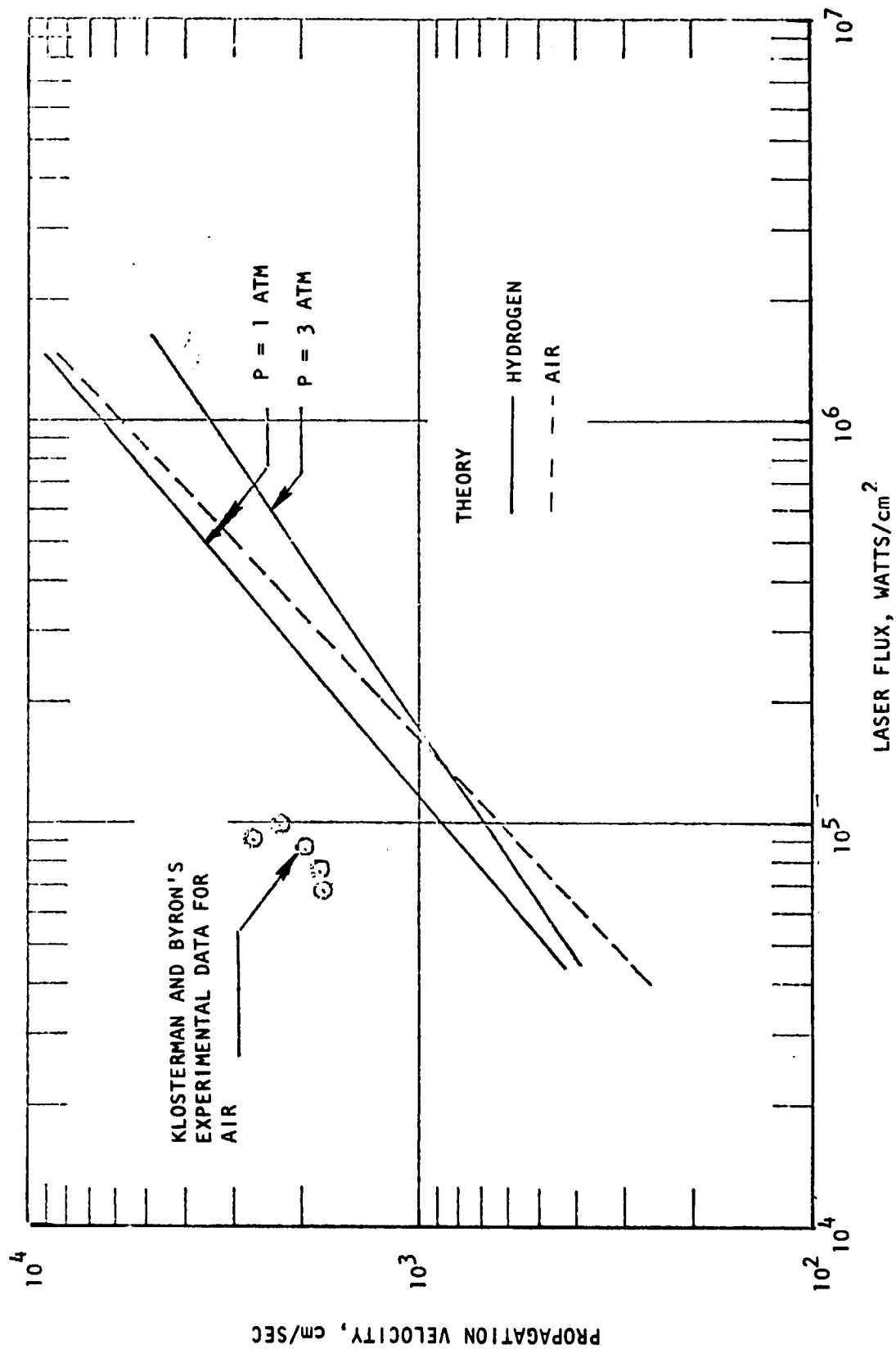


Figure 25. LASER SUPPORTED COMBUSTION (LSC) WAVE VELOCITY VARIATION WITH LASER INTENSITY

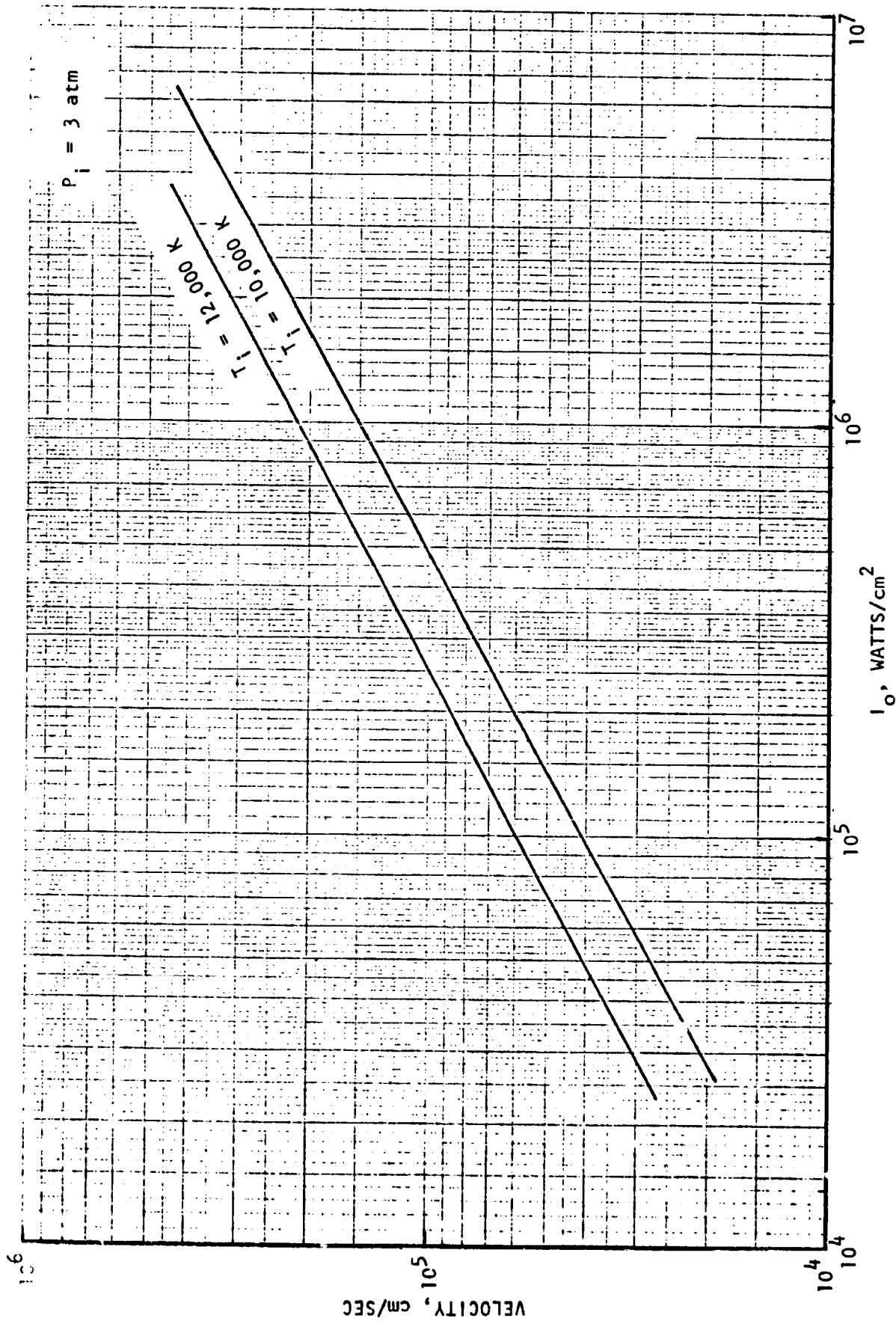


Figure 26. Plasma Inlet Velocity Variation With Laser Intensity and Plasma Temperature

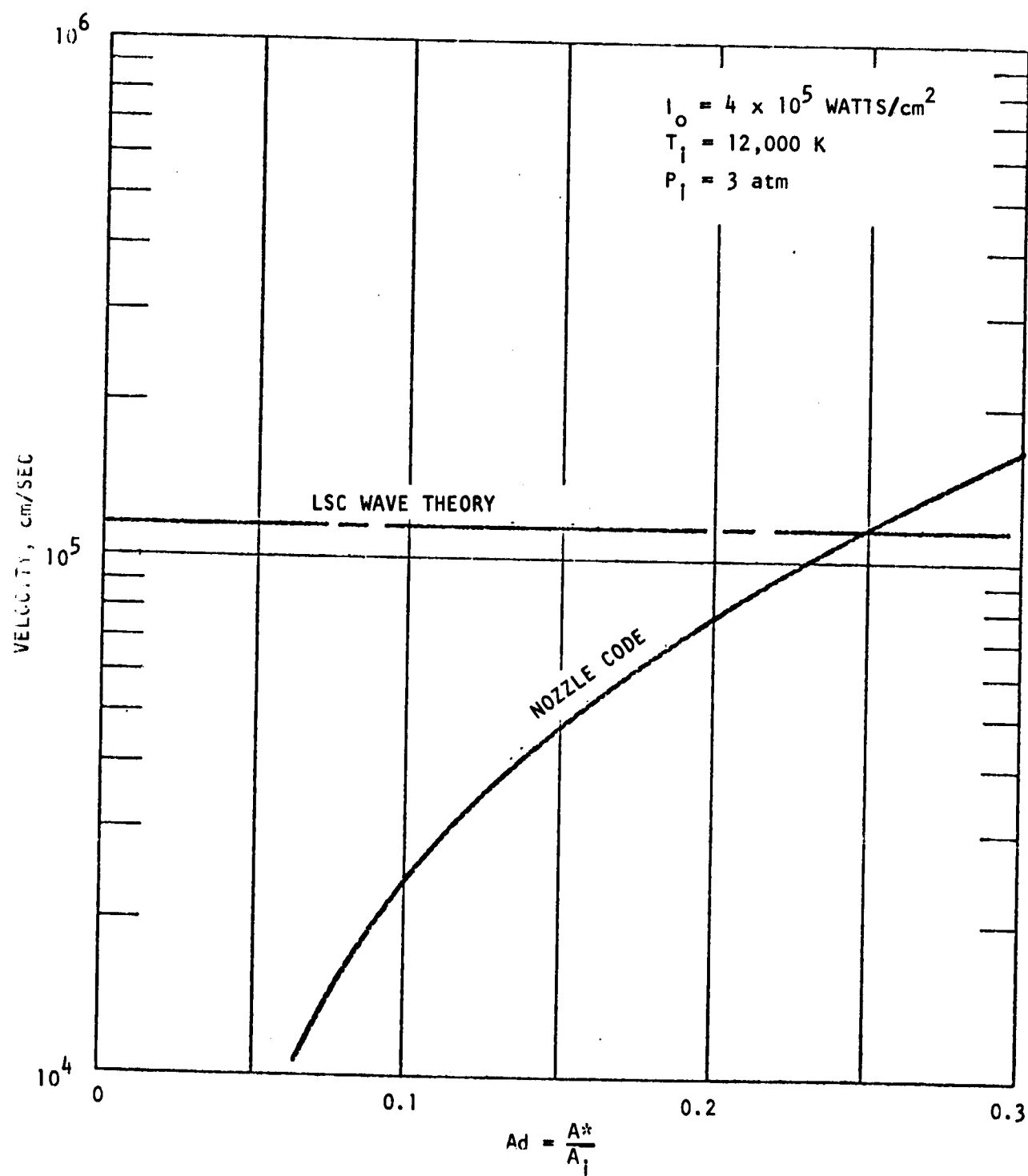


Figure 27. Plasma Inlet Flow Velocity Determination

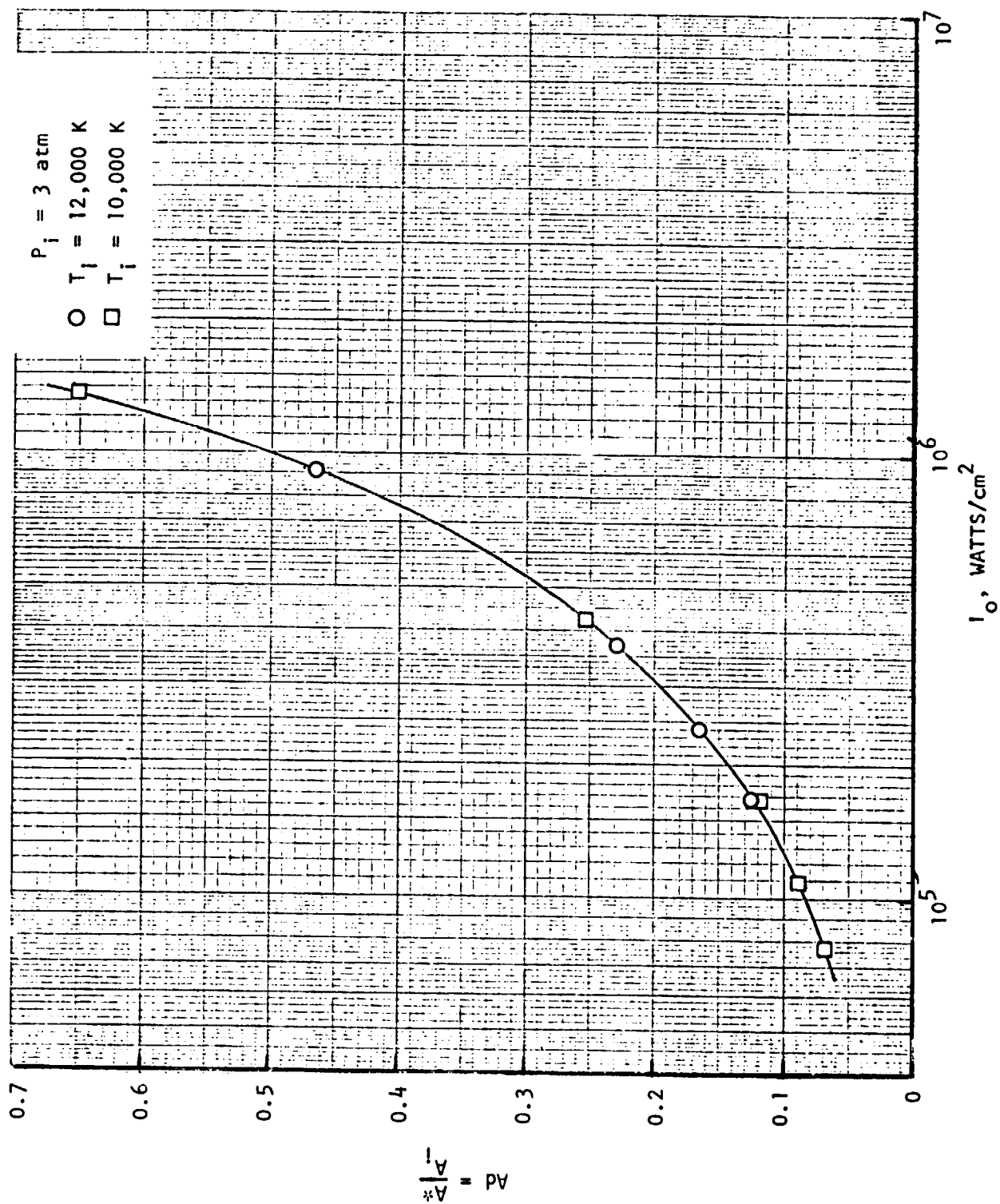


Figure 28 Plasma Throat Area-to-Inlet Area Ratio Variation with Laser Intensity

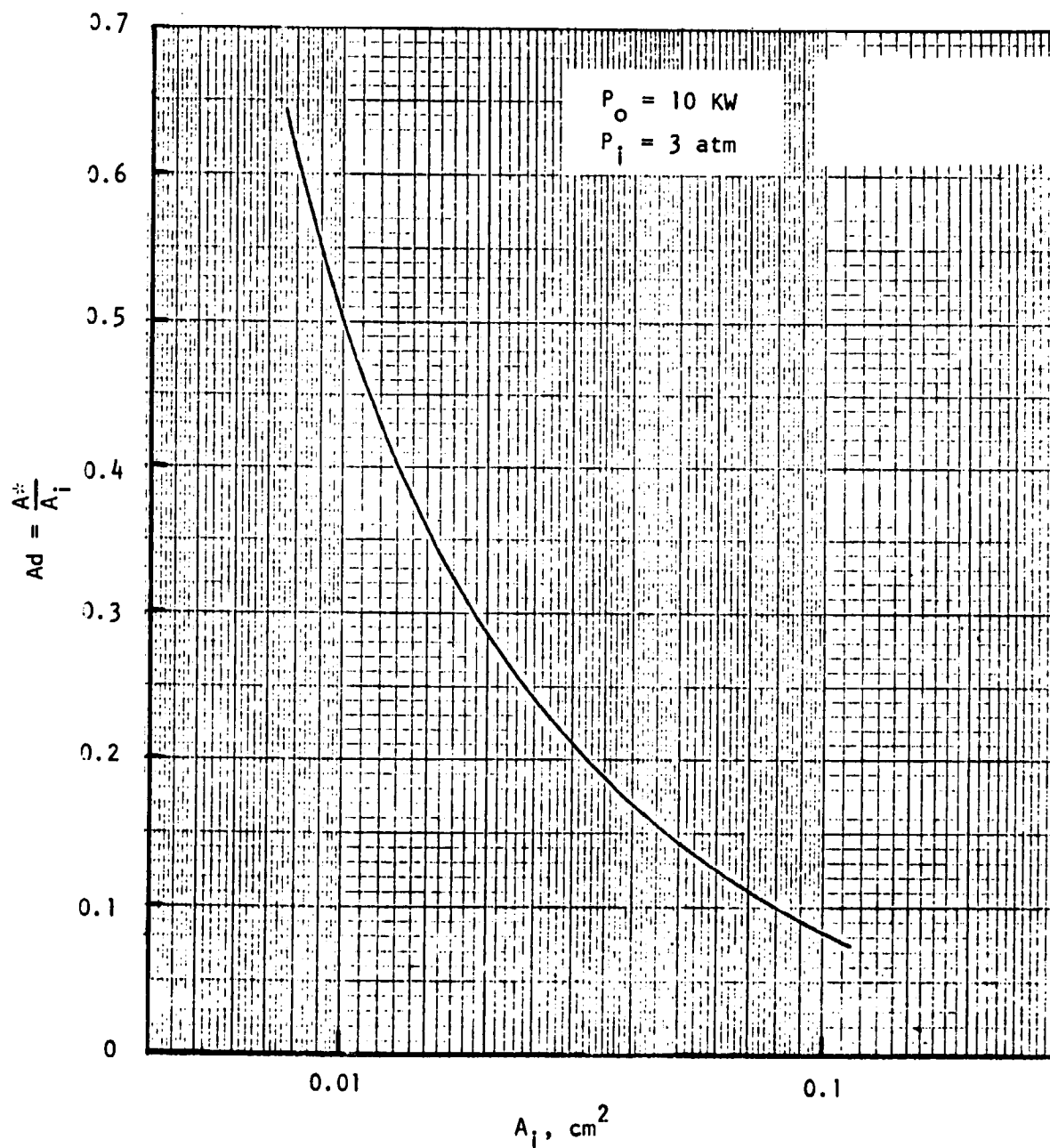


Figure 29. Plasma Throat Area-to-Inlet Area Ratio Variation With Inlet Area

Selecting a laser intensity of 3.7×10^5 watts/cm², the flow analysis for the 10-kw configuration resulted in the pressure and absorption coefficient profiles shown in Fig. 30 in τ space where $\tau = \int_0^x k_v dx$. The plasma static temperature profile in real space is shown in Fig. 31. The actual plasma core dimensions are presented in Fig. 32. Although this does not include the outer buffer gas flow, the relatively small dimensions of the plasma core will necessitate a funnel-type chamber configuration to provide sufficient dimensions in the window and injector region.

In the process of sizing the 10-kw plasma core, PSI determined an approximate scaling law of plasma diameter with laser beam power.

$$\text{Diameter} \propto \sqrt{\text{Power}} \quad (5)$$

Using this law, the plasma core size for the 5000-kw configuration was determined (Fig. 33). The diameter of the plasma varied from 4.13 cm (1.626 in.) at the plasma inlet to 1.98 cm (0.780-in.) at the geometric throat.

Plasma Radiation

The high temperature plasma contained in the chamber loses energy through radiative transfer to the chamber walls. This power loss or wall heat flux contribution was estimated by PSI and was used to determine wall cooling requirements. The plasma radiation loss from the plasma for the 10-kw hardware was computed to be an average of 1200 watts/cm² (7.34 BTU/in.² sec) radiation heat flux and is primarily from the ultraviolet wavelengths. For the 5000-kw configuration, the plasma radiation loss is from both the ultraviolet (UV) and infrared (IR) wavelengths which increased the radiation heat flux to 6400 watts/cm² (39.13 BTU/in.² sec).

Plasma Radiation Absorption by Particles

Small carbon particles, smaller than 1 μ m, are very efficient absorbers of radiation in the visible and infrared wavelength regions, approximately acting as black-body absorbers. A large fraction of the hydrogen plasma radiation

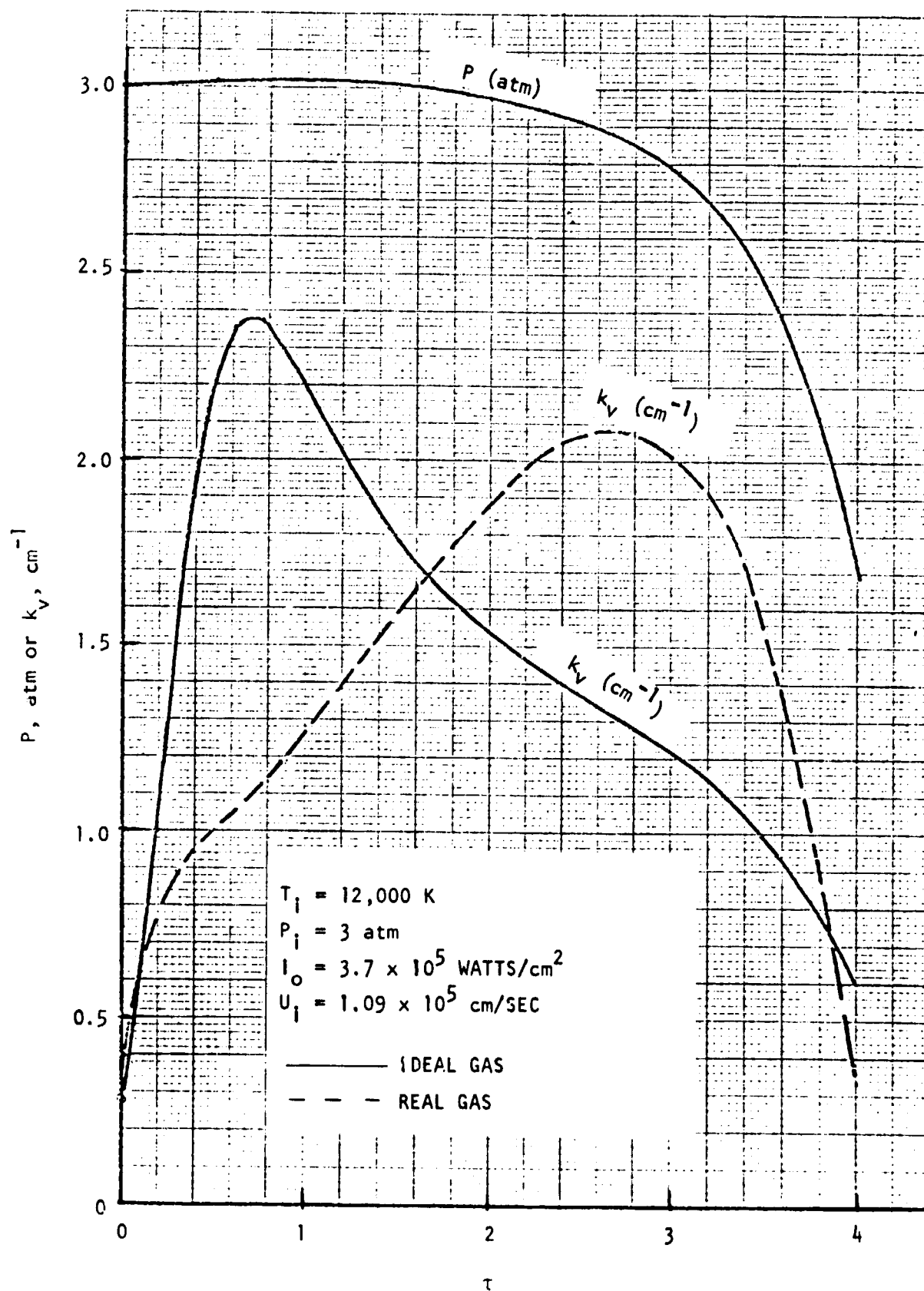


Figure 30. Static Pressure and Absorption Coefficient Distributions for 10-kw Power Input

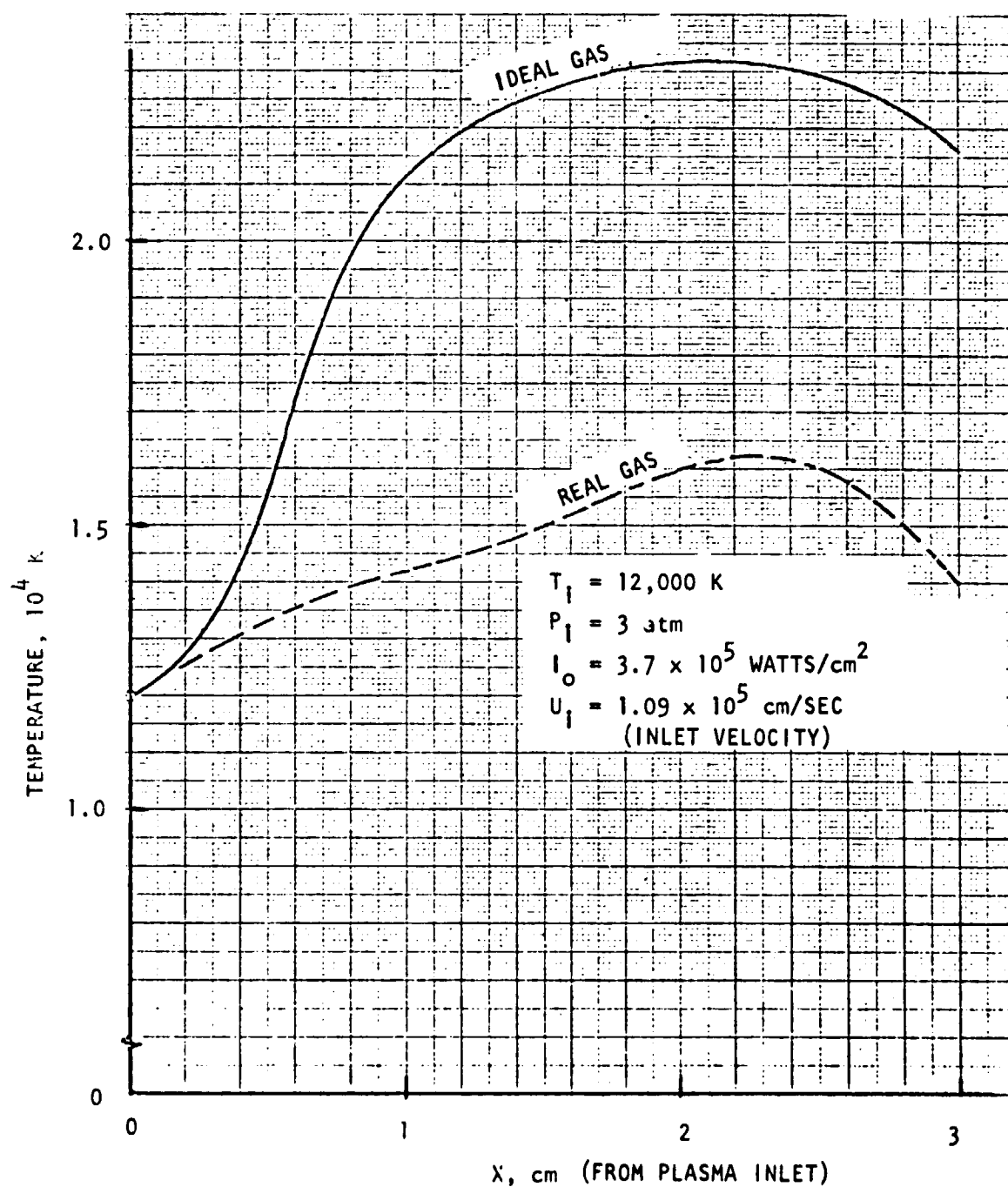


Figure 31. Static Temperature Distribution for 10-kw Power Input

$P = 10 \text{ kw}$
 $P = 3 \text{ atm}$

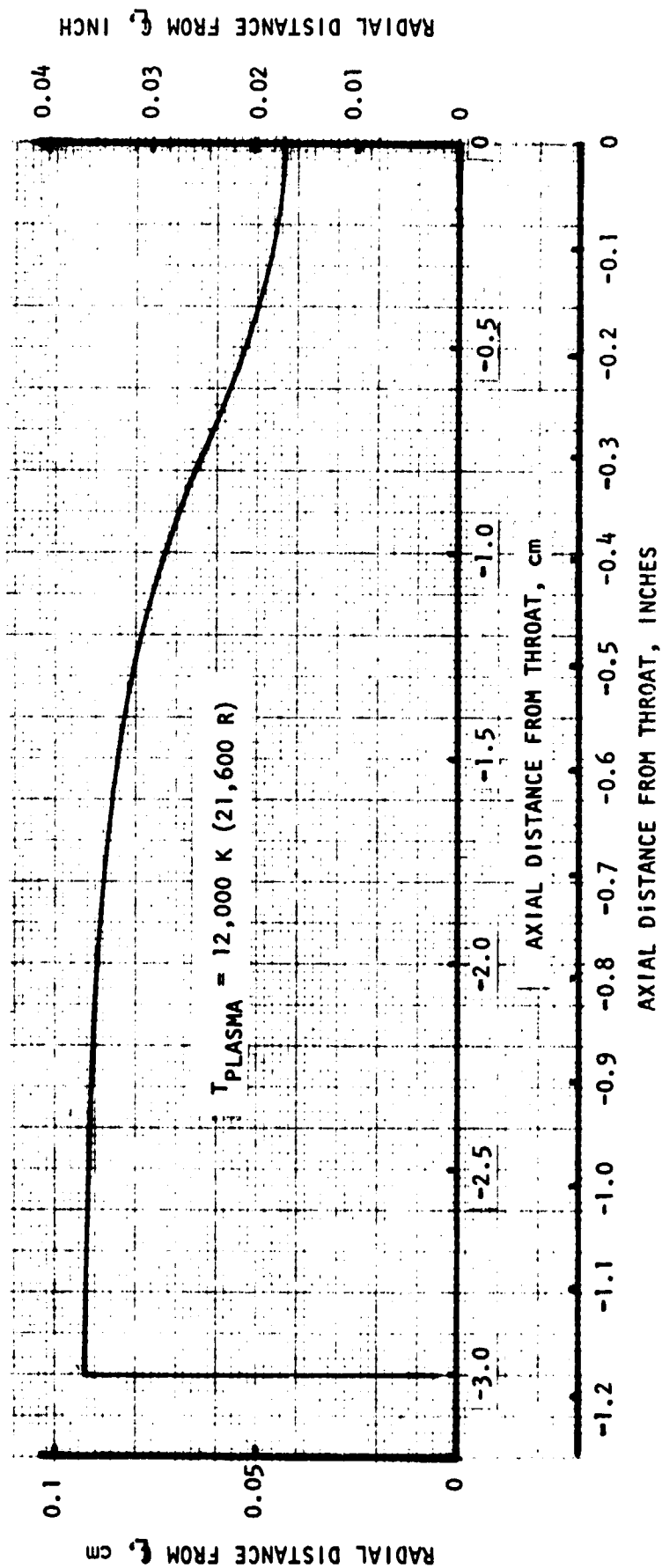


Figure 32. 10-kw Thruster Plasma Core Dimensions

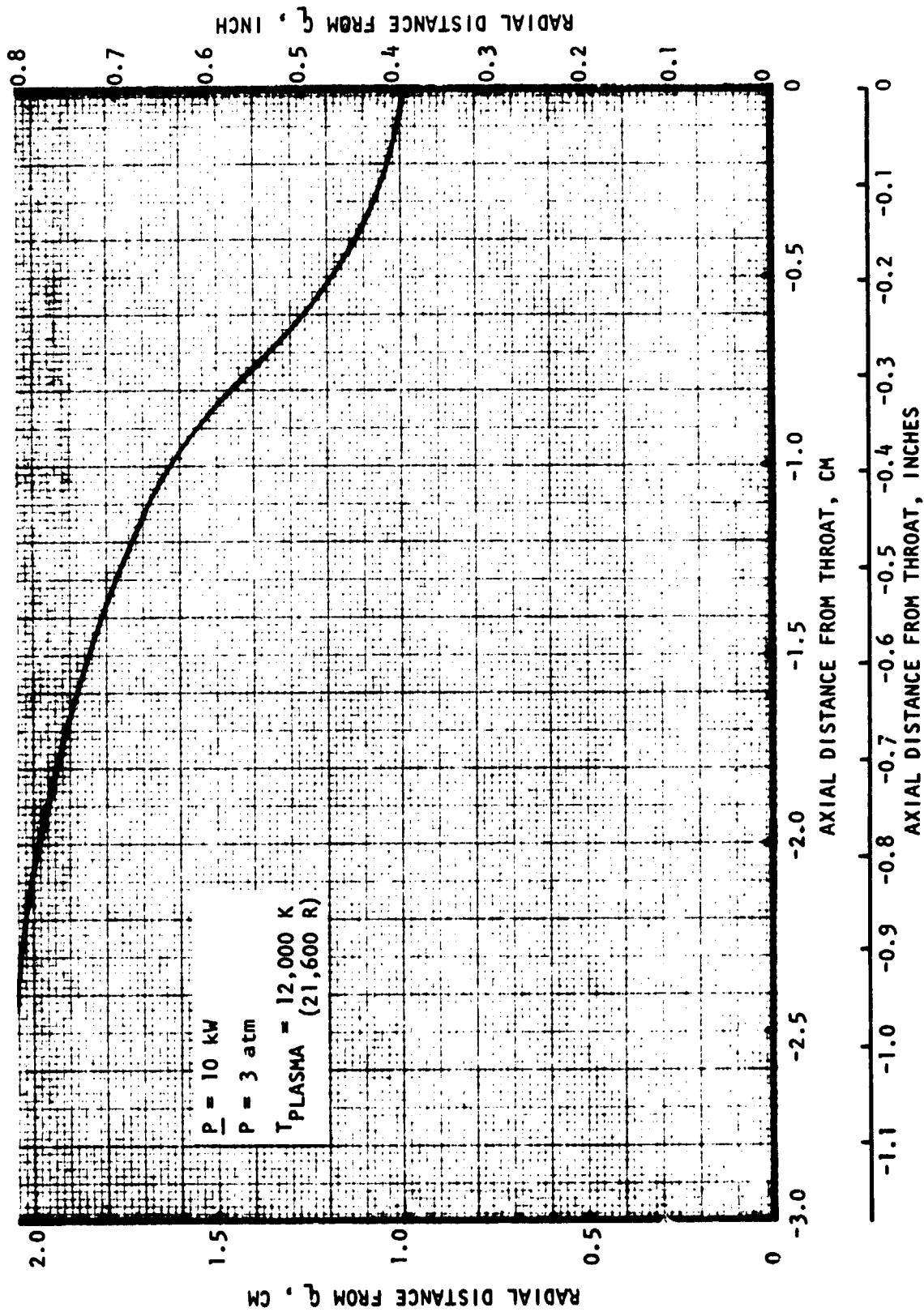


Figure 33. 5000-kW Chamber Plasma Core Dimension

will unfortunately originate in the far UV where little is known about the absorptive properties of carbon. In the following analysis it was assumed that the carbon particles absorb as black bodies at all wavelengths.

The scenario considered is a cylindrical plasma of radius r_1 surrounded by a particle seeded coolant flow of thickness Δr . The particles are taken to be spherical with radius R_p and to have a constant number density N_p in the coolant flow. Each particle has an absorption cross section of πR_p^2 and thus the optical depth, τ , across the coolant layer is defined by

$$\tau = N_p \pi R_p^2 \Delta r \quad (6)$$

An optical depth of 3 is sufficient to absorb 95 percent of the plasma radiation and this condition is met when the particle number density is given by

$$N_p = \frac{3}{\pi R_p^2 \Delta r} \sim \frac{1}{R_p^2 \Delta r} \quad (7)$$

It is perhaps more interesting to examine this quantity in terms of the total mass/cc of particles in the coolant flow, M_p ,

$$M_p = N_p \rho_p (4/3) \pi R_p^3 \quad (8)$$

where ρ_p is the specific density of carbon which is ~ 2 gm/cc. Combining Eq. 7 and 8 results in

$$M_p = 4 \rho_p \frac{R_p}{\Delta r} \sim 8 \frac{R_p}{\Delta r} \quad (9)$$

Equation 9 can readily be extended to deduce the mass flow of particles required to absorb the plasma radiation.

$$\dot{M}_p = M_p U_c A_{\text{coolant}} \quad (10)$$

where

$$A_{\text{coolant}} = \pi(2 r_1 \Delta r + A r_1^2) \quad (11)$$

and U_c is the coolant flow velocity. Since it is desirable to maintain a configuration such that $\Delta r/r_1 \ll 1$, the approximation

$$A_{\text{coolant}} \approx 2 \pi r_1 \Delta r \quad (12)$$

is made. Combining Eq. 9, 10, and 12 results in

$$\dot{M}_p = 8 \pi \rho_p U_c R_p r_1 \approx 48 U_c R_p r_1 \quad (13)$$

Thus it can be seen from Eq. 13 that as long as $\Delta r \ll r_1$, the particle mass flow required to absorb the plasma radiation is independent of the coolant flow thickness and linearly proportional to both the particle and plasma radii. Since in the interest of optimizing thrust one wishes to minimize the coolant flow, it is clear that the smallest particle size, consistent with the assumption of blackbody absorption, should be used.

Another interesting feature is that since the required coolant flow is linearly proportional to plasma radius, the ratio of coolant flow to plasma flow is size dependent, i.e.,

$$\frac{\dot{M}_p}{\dot{M}_{\text{plasma}}} = \frac{8 \rho_p R_p U_c}{\rho_{\text{plasma}} r_1 U_{pl}} \quad (14)$$

where U_{pl} is the plasma flow velocity. For example, for a 14,000 K hydrogen plasma at a pressure of 3 atm

$$\frac{\dot{M}_p}{\dot{M}_{\text{plasma}}} \sim 10^7 \frac{R_p U_c}{r_1 U_{pl}} \quad (15)$$

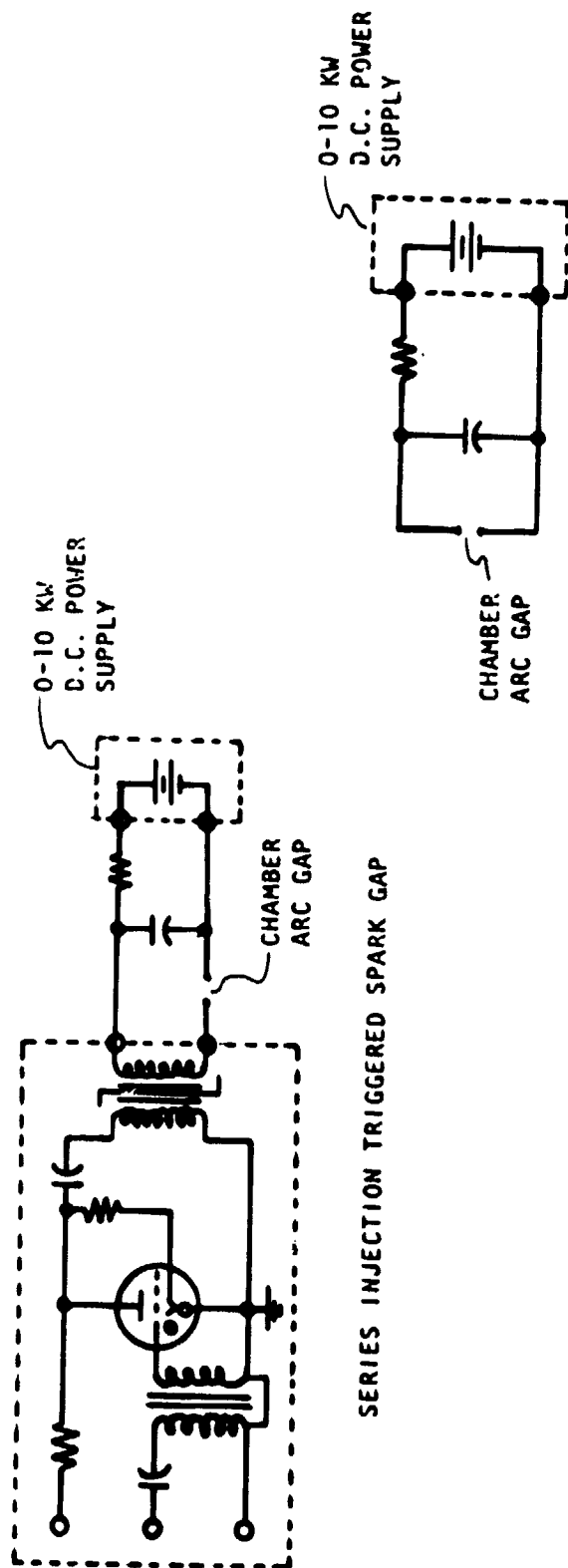
Note that relationship (15) implies that for small devices, i.e., $r_1 \leq 1$ cm, the coolant mass loading would of necessity be orders of magnitude larger than that of the plasma for reasonable particle sizes unless $U_c \ll U_{pl}$.

For the 5000-kw chamber assuming a $1 \mu\text{m}$ carbon particle and a 1.7 cm plasma radius, the required velocity ratio was approximately 1:140. This may or may not represent a realistic situation for a single point seeded carbon injection but could be for a multi-injection scheme.

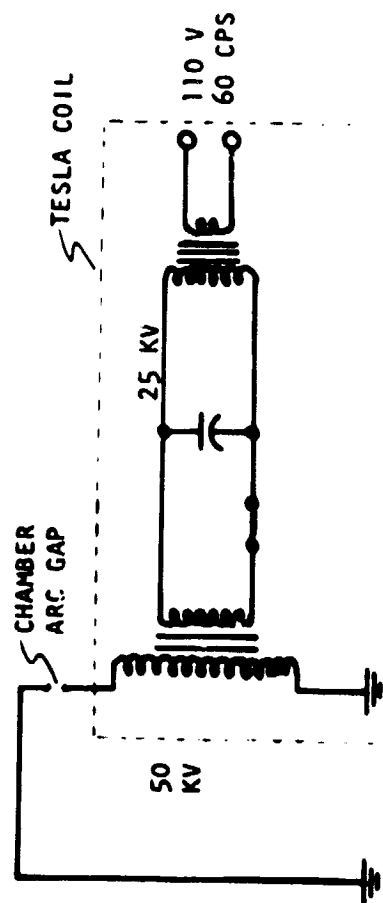
Plasma Arc Initiation

Three power supply systems shown in Fig. 34, were evaluated for potential use with the 10-kw experimental hardware to initiate the gas breakdown. Tesla coil initiation has proven successful in earlier work initiating breakdown in a hydrogen atmosphere when laser power (pulsed) is approximately 10^9 watt/ cm^2 . However, this device may still not produce the high electron densities required of $10^{17}/\text{cc}$. A power supply like the self-firing spark gap shown in Fig. 34, is capable of producing these electron densities and delivering 2000 amps peak current. As shown in Fig. 35, (Ref. 3), a peak current of 2000 amps produced the required $10^{17}/\text{cc}$ electron density in hydrogen. The self-firing spark gap device would arc whenever the capacitor discharged and the exact time may not be predictable.

The most versatile and powerful system would be the series injection triggered spark gap. This system would provide a range of peak current of 1000 to 5000 amps with the 10-kw power supply. The capacitor is charged and the series injection trigger module would cause the capacitor to dump at the exact specified time. This would permit the exact time sequencing of the laser beam, propellant, and initiating arc. Therefore, this system was selected as shown in Fig. 36.



SELF-FIRING SPARK GAP



TESLA COIL INITIATOR

Figure 34. 10 KW Plasma Arc Initiating Candidate Power Systems

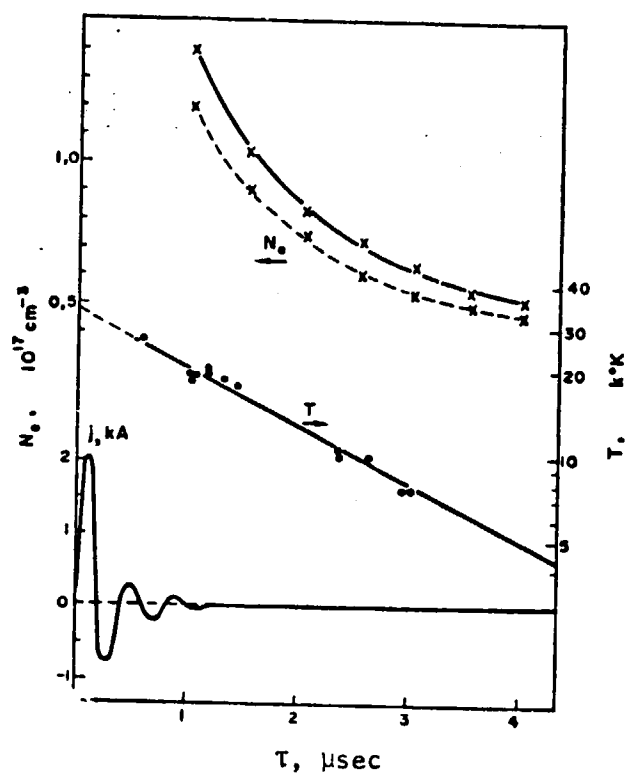
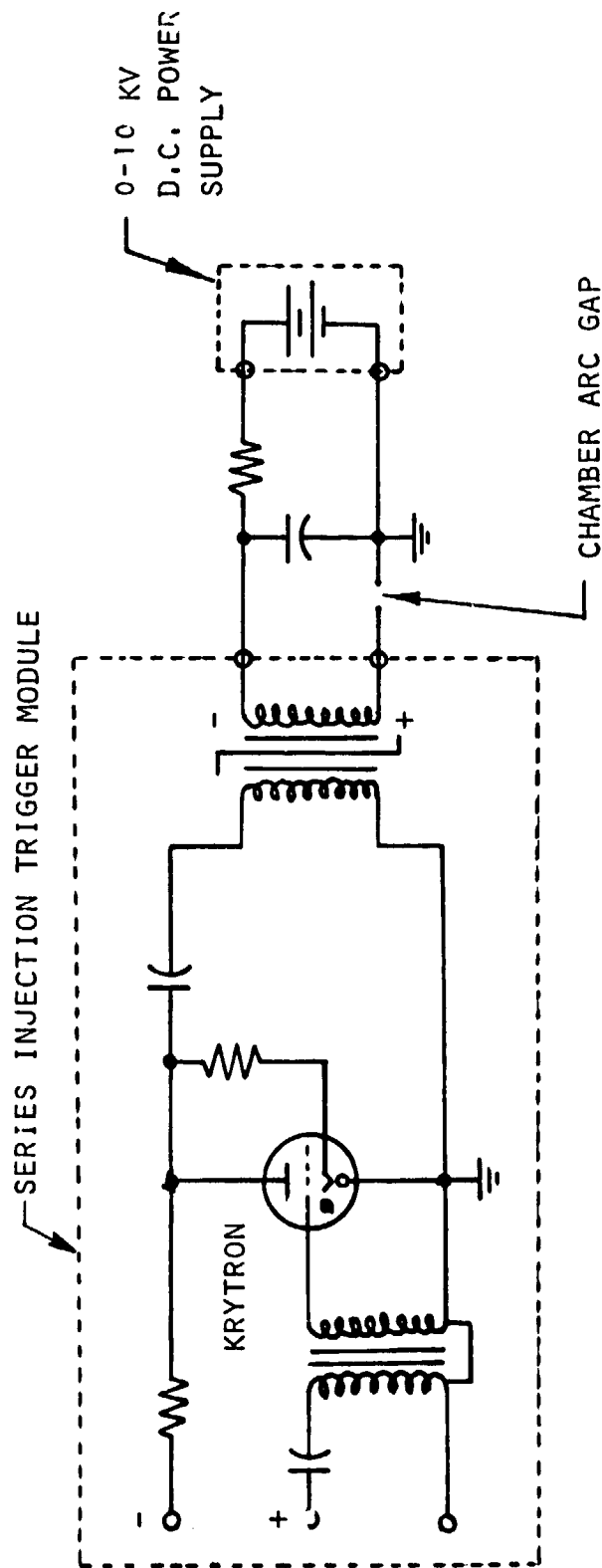


Figure 35 Electron Density, Current and Temperature Variation with Time for an Arc Initiated Hydrogen Breakdown (Ref. 3)

FIGURE 36 SELECTED 10-KW CHAMBER PLASMA ARC INITIATING POWER SYSTEM
(SERIES INJECTION TRIGGERED SPARK GAP)



- MOST VERSATILE SYSTEM
- CAN SELECT EXACT FIRING TIME
- ADJUSTABLE PEAK CURRENT (1000 TO 5000 AMPS)
- MOST POWERFUL

FLOW ANALYSIS

10-kw Chamber Sizing

The procedure used in sizing the 10-kw and 5000-kw chamber is schematically shown in Fig. 37 through 39. The sizing included potential flow (not including boundary layer thickness) sizing of the plasma core and chamber throat (Fig. 37). The latter was sized assuming an average gas temperature and carbon concentration. From laser supported combustion (LSC) wave theory, the flow velocity at the plasma inlet was specified which defined the chamber diameter at this point. Then a heat balance between the plasma, the colder buffer gas, and the chamber wall cooling was performed. The schematic of the heat balance performed is presented in Fig. 38 and 39. The heat balance consists of boundary layer analyses for different freestream conditions and a conduction analysis of the flow between the plasma and the chamber wall. This heat balance results in heat fluxes, freestream conditions, and an average gas temperature. Now accounting for the heat lost to the chamber wall and through the window, the effective average gas temperature is computed. This gas temperature is iterated until the assumed average gas temperature is close to the calculated value.

The total propellant flowrate may be computed by

$$W_{\text{total}} = \frac{(\underline{P}) (0.948)}{\Delta H}, \text{ lb/sec} \quad (16)$$

and the potential or inviscid flow (i.e., not including boundary layer influences) chamber throat radius is given by,

$$R_T = \sqrt{\frac{0.948 \underline{P} c^*_{\text{theor}}}{\pi g \Delta H P_c}}, \text{ inch} \quad (17)$$

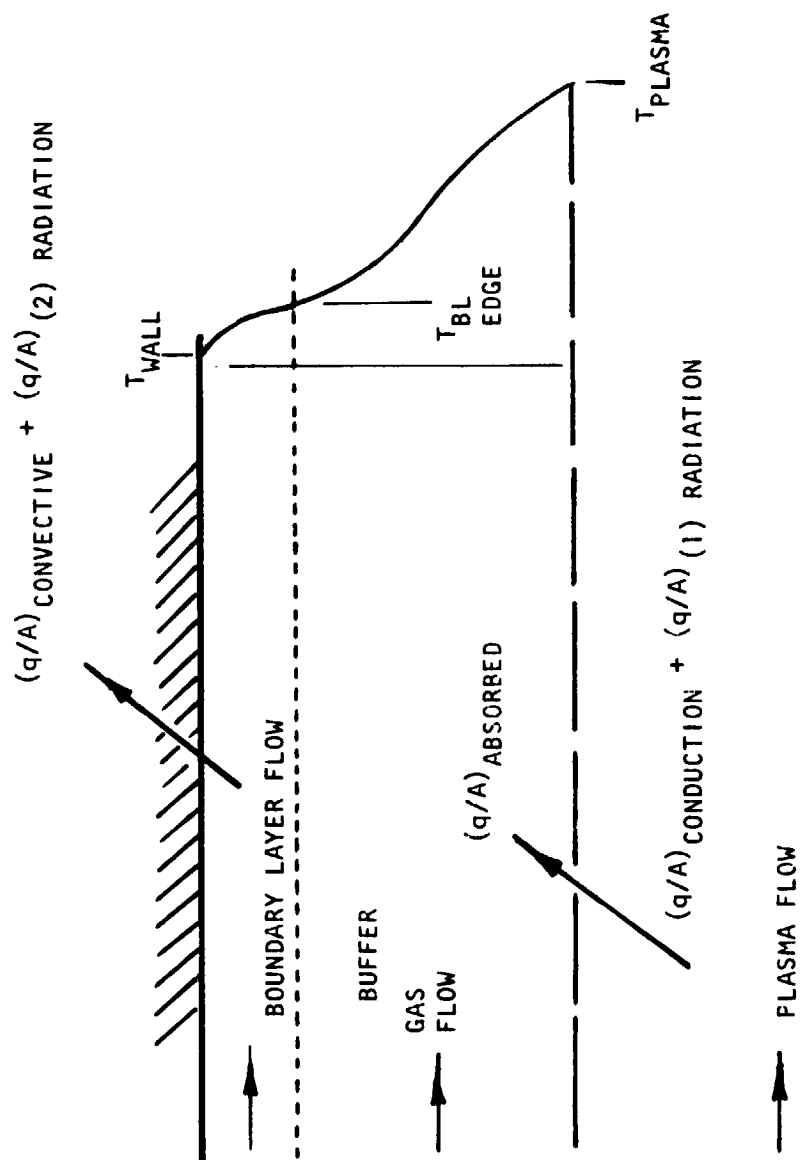


Figure 38. Streamtube Heat Balance Schematic

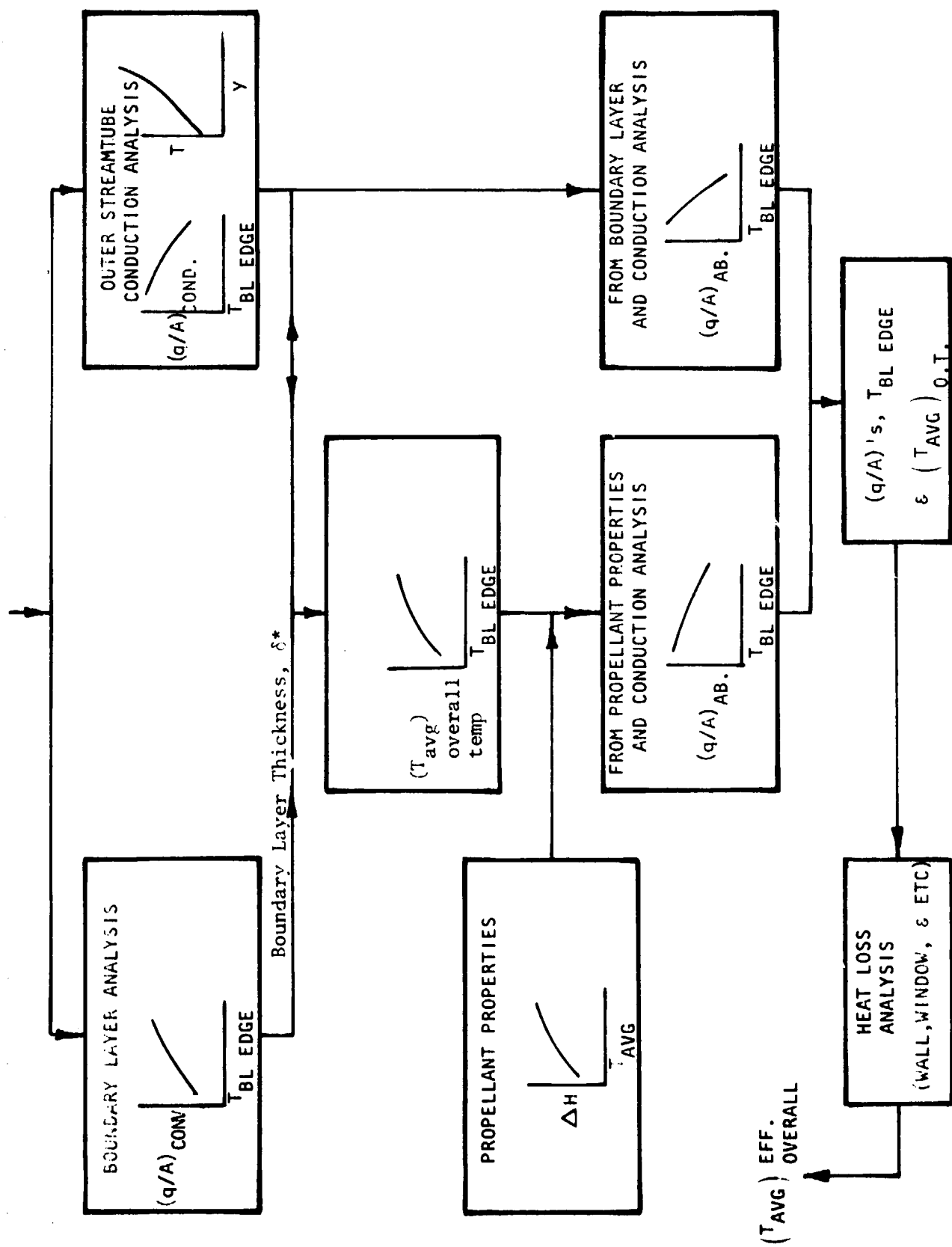


Figure 39. Streamtube Heat Balance

where \underline{P} = Laser beam power input, kilowatts
 ΔH = Propellant enthalpy rise, Btu/lb
 0.948 = Conversion from kilowatts to Btu/sec
 c^* = Theoretical characteristic velocity, ft/sec
 g = Gravitational constant (32.174 ft/sec²)
 P_c = Chamber pressure, psia

The variations of these two parameters with average gas temperature and carbon concentration for the 10-kw configuration are presented in Fig. 40 and 41. Pure hydrogen at an average gas temperature of 5555.6 K (10,000 R) resulted in a 0.0541 cm (0.0213 inch) inviscid flow throat radius and a total propellant flowrate of 0.0000704 lb/sec. For this condition, the plasma core flow would be 31.5 percent of the total flow.

Boundary layer analyses were performed using the Rocketdyne Boundary Layer Analysis Computer program assuming a 10-kw chamber sized for an average gas temperature of 5555.6 K (10,000 R). As shown in Fig. 42, the resulting convective heat flux (maximum and average) on the chamber wall with variation in the boundary layer edge temperature was obtained. An eleven nodal one-dimensional thermal conduction model of the gas was constructed and included the variation in the gas thermal conductivity (Fig. 43). Using an average buffer gas (hydrogen) thickness for the chamber sized for 5555.6 K (10,000 R), the conduction analysis was performed for various boundary layer edge temperatures. The resulting conductive heat flux variation with boundary layer edge temperature is shown in Fig. 44. In addition the resulting temperature profiles through this gas layer are presented in Fig. 45.

The heat flux absorbed by the buffer gas was determined using two methods of computation:

1. From boundary layer and conduction analysis
2. From propellant properties and conduction analysis

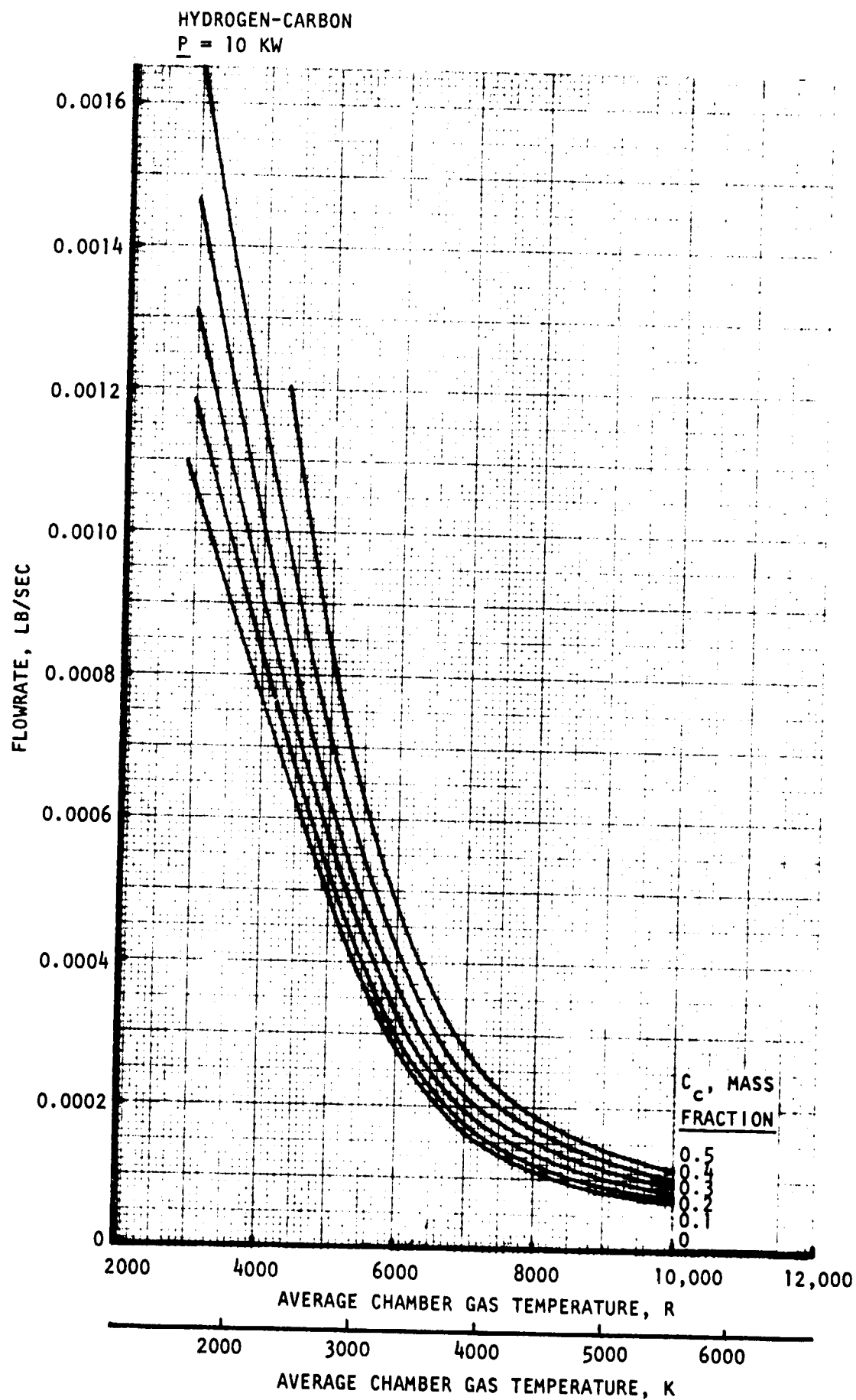


Figure 40. Hot-Gas Flowrate Variation with Gas Temperature and Carbon Concentration (10 KW Configuration)

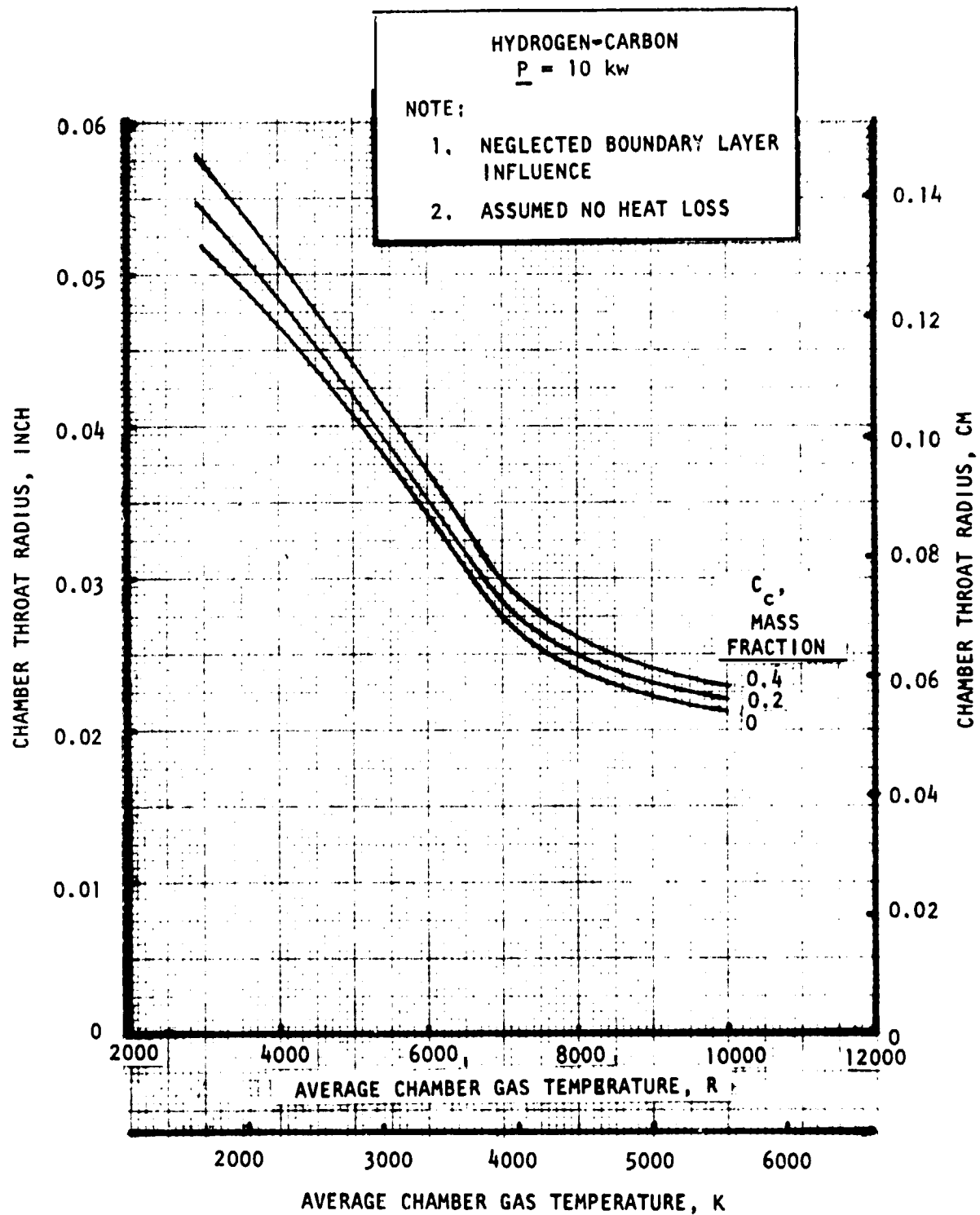


Figure 41. Chamber Throat Radius Variation With Gas Temperature and Carbon Concentration (10 kw Chamber)

$$P_C = 3.45 \times 10^5 \text{ N/M}^2 \text{ (50 PSIA)}$$

PURE HYDROGEN

ASSUMPTION: CHAMBER SIZED FOR

$$T_{AVG} = 5555.6\text{K (10,000 R)}$$

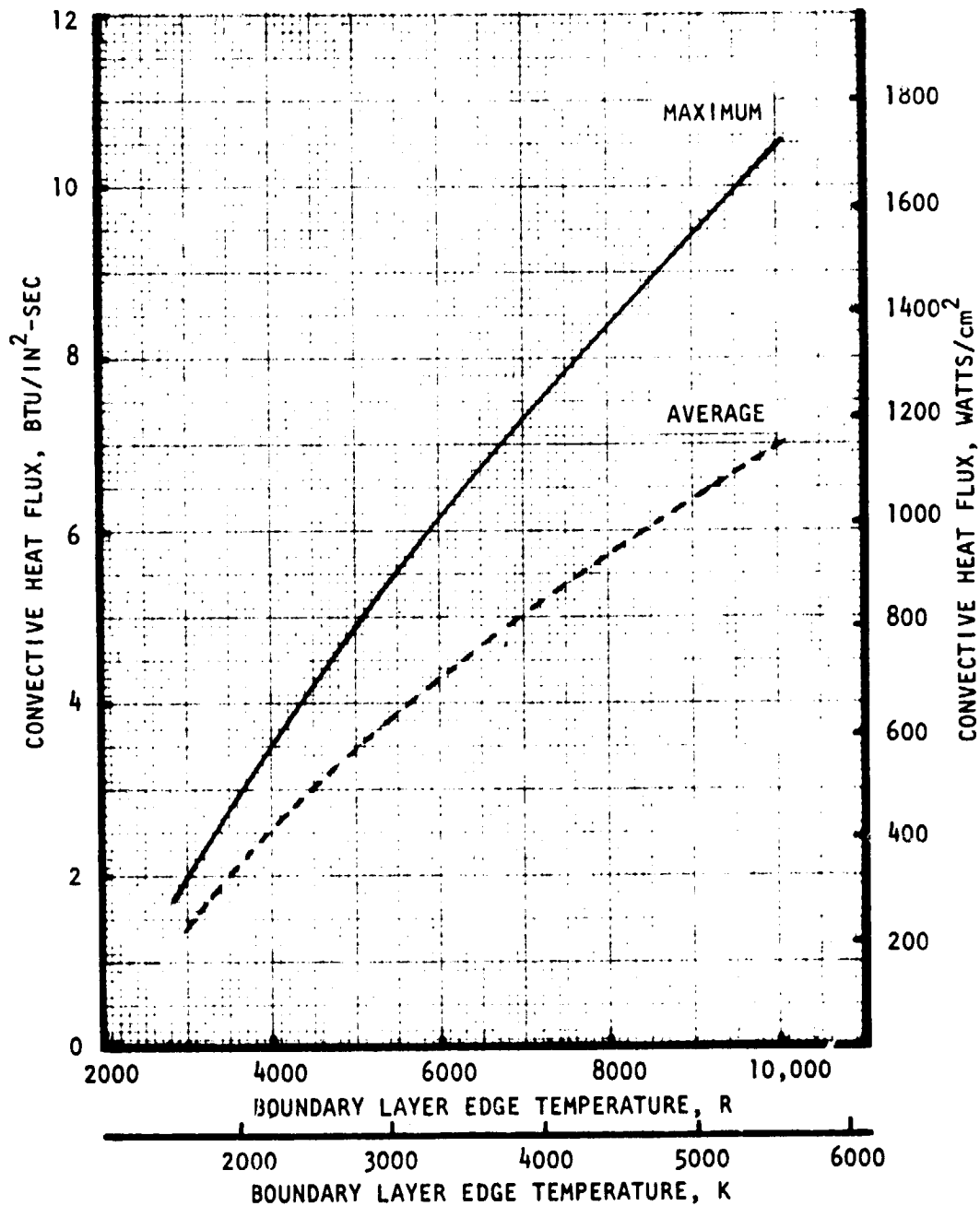


Figure 42. Convective Heat Flux Variation with Boundary Layer Edge Temperature (10 KW Chamber)

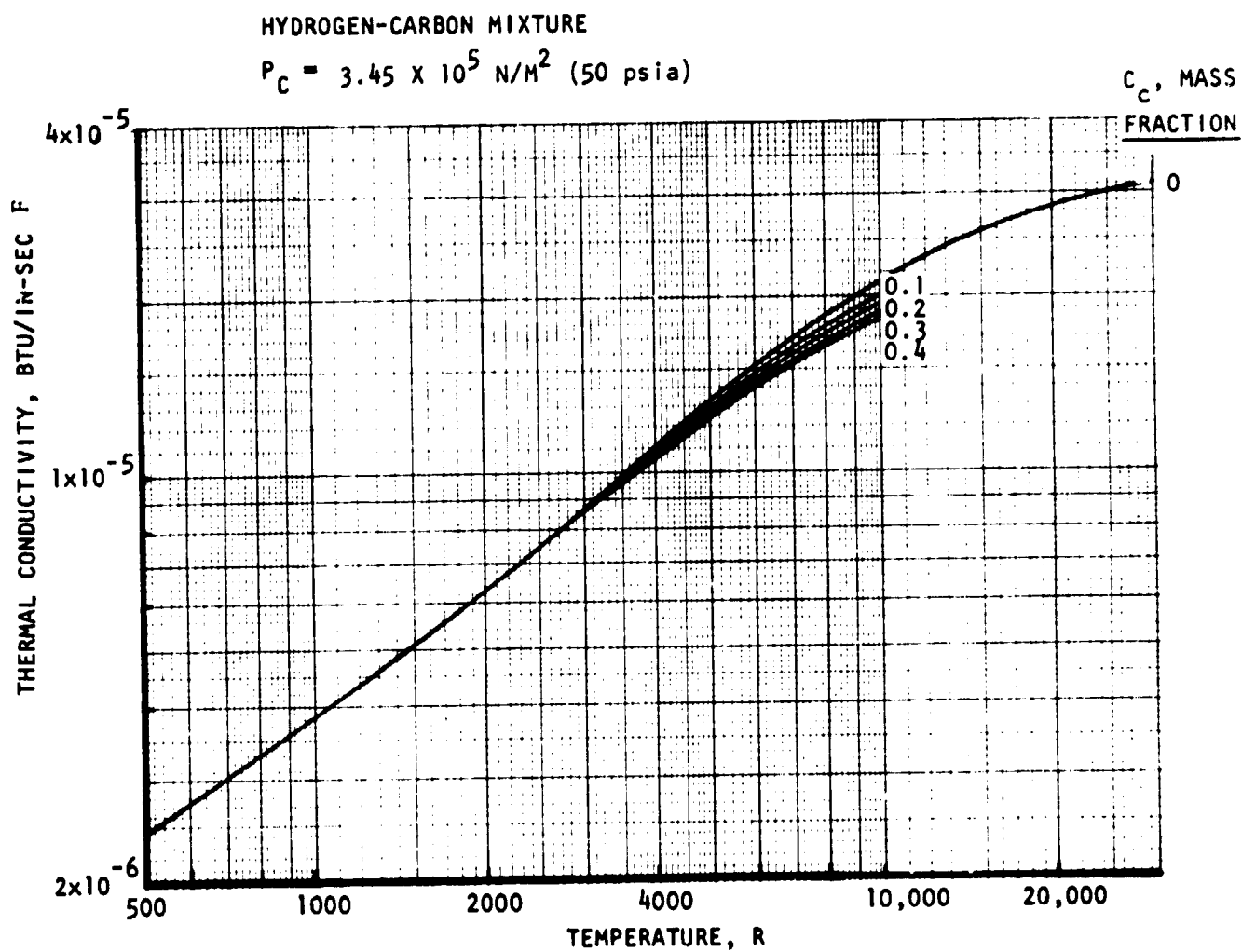


Figure 43. Hydrogen-Carbon Thermal Conductivity Variation with Temperature and Carbon Concentration

H_2 THICKNESS = 0.0254 cm (0.01 inch)

$P_c = 3.45 \times 10^5 \text{ N/M}^2$ (50 PSIA)

$T_{\text{PLASMA}} = 12,000 \text{ K}$ (21600 R)

THERMAL CONDUCTIVITY VARIATION
WITH TEMPERATURE INCLUDED

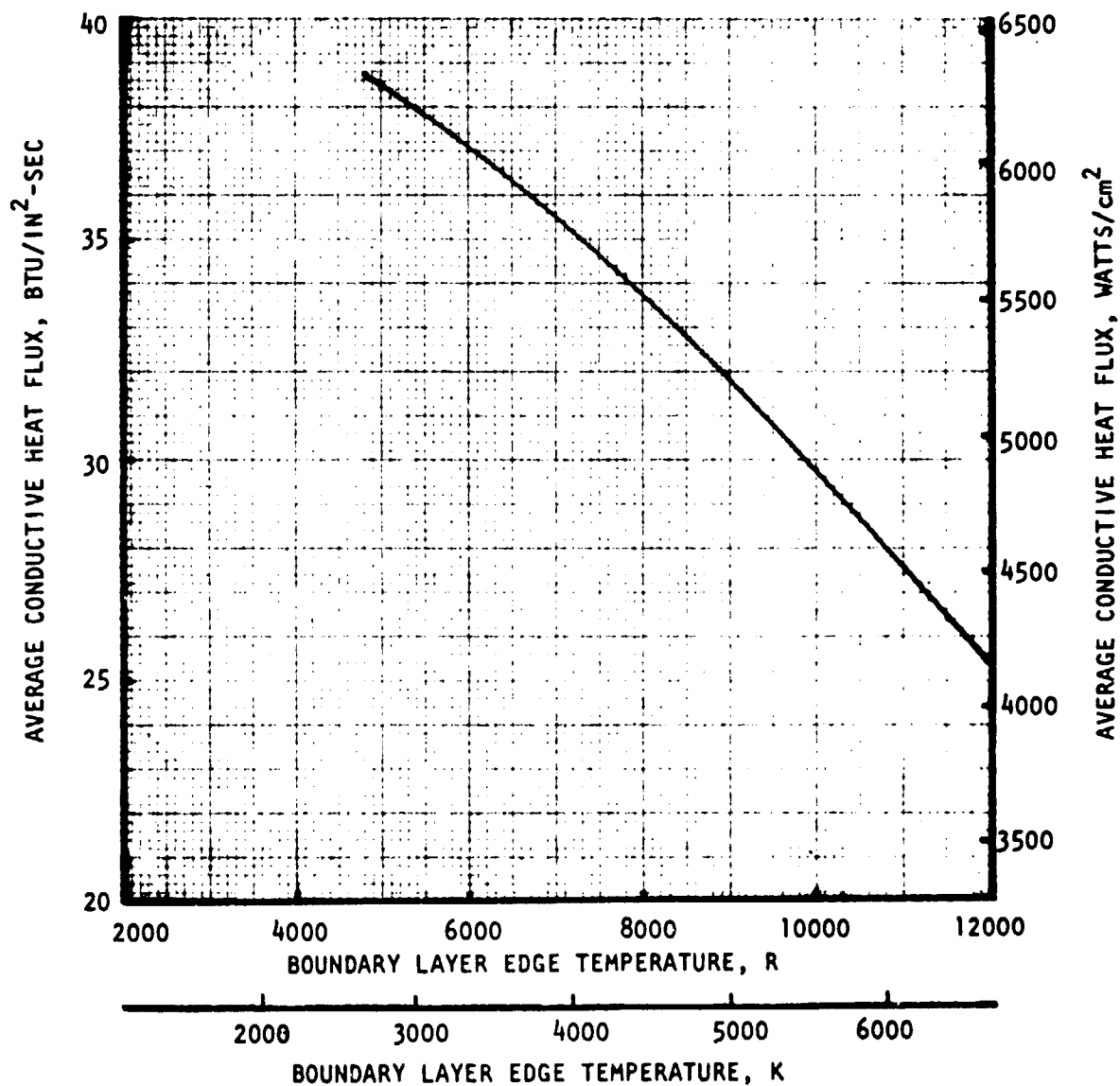


Figure 44. Average Conductive Heat Flux Variation with Boundary Layer Edge Temperature (10 KW Chamber)

HYDROGEN

$$P_c = 3.45 \times 10^5 \text{ N/M}^2 \text{ (50 PSIA)}$$

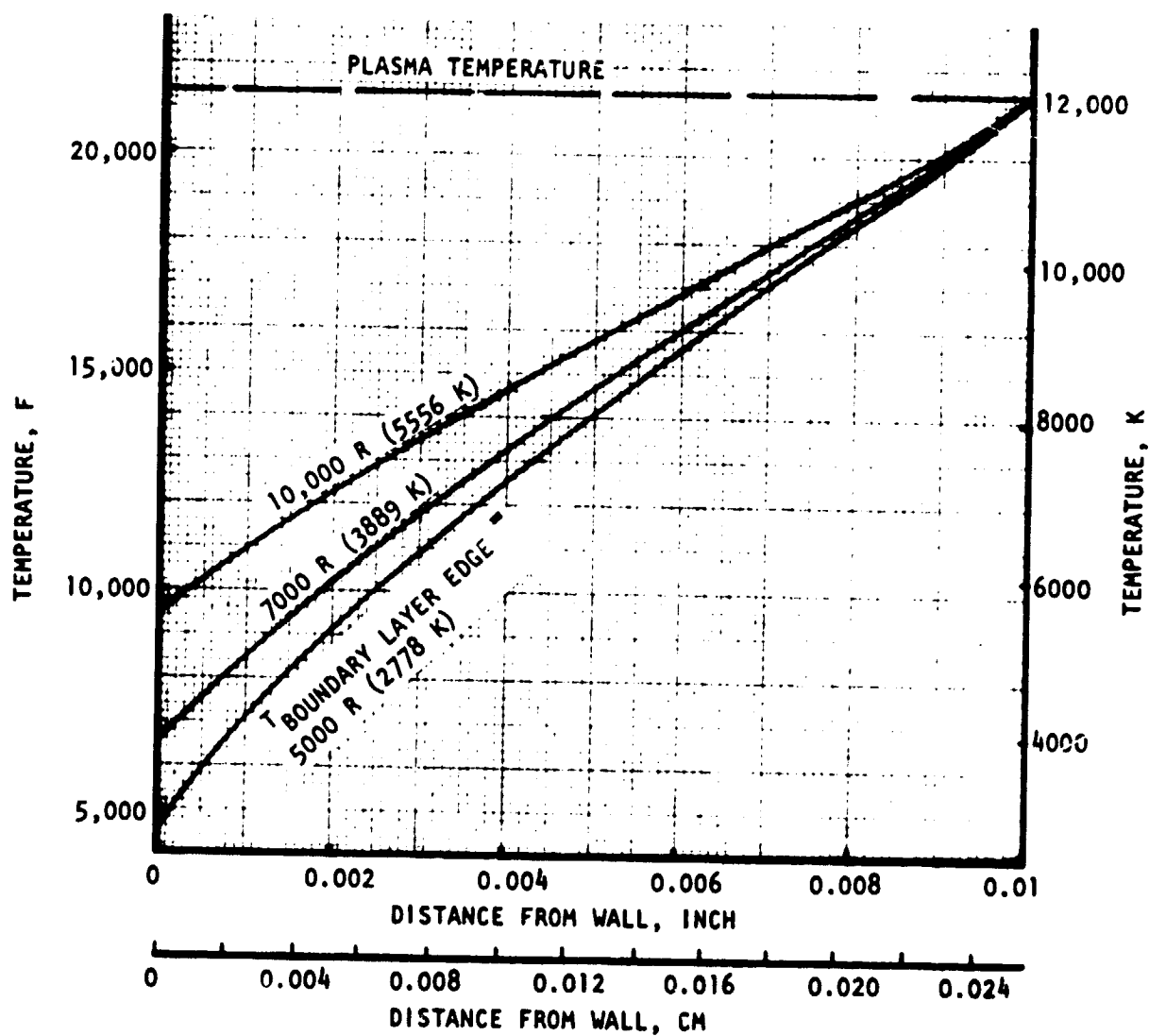


Figure 45. Temperature Profiles from Conduction Analysis (10 kW Chamber)

The conditions were varied until the heat flux absorbed computed from the two calculational methods were equal as illustrated in Fig. 46. The pure hydrogen was assumed to be transparent to the plasma radiation. As shown in Fig. 46, the heat balance resulted in a 4222.2 K (7600 R) boundary layer edge temperature. The average overall temperature of 7972.8 K (14,351 R) was calculated for the no heat loss condition. The average convective heat flux plus the radiation heat flux to the chamber wall ($9.73 \text{ Btu/in}^2\text{-sec}$ or $1591.4 \text{ watts/cm}^2$) represents approximately a 20-percent heat loss. Assuming a 5-percent heat loss through the window, the effective average overall gas temperature was computed to be 5888.9 K (10,600 R) which is amazingly close to the 5555.6 K (10,000 R) assumed.

The dimensions of the resulting 10-kw chamber are shown in Table 5 and Fig. 47. Considering the flow heat balance and the boundary layer influences, a geometric throat diameter of 0.1168 cm (0.046 inch) was determined. This consists of 0.1082 cm (0.0426 inch) for the potential flow and 0.00864 cm (0.0034 inch) for the boundary layer thickness. The geometry of the region near the window and injector illustrated in Fig. 47 was approximated based on window requirements, flow recirculation tendencies, and optical interface difficulties.

10-kw Combustion Chamber (Subsonic) Flow Pattern

The subsonic flow pattern of the 10-kw chamber was estimated by observing past water test results and flow pattern interpretation of actual hot-firing rocket chambers. In subsonic flow with fixed fluid injection locations, the flow recirculation pattern will be independent of the injection velocities. An increase in injection velocities will merely increase the vortex velocities. The predicted subsonic flow pattern for the 10-kw chamber is presented in Fig. 48. Basically two vortices will exist. One will be located near the window flowing counter-clockwise and the other located near the main propellant injection flowing clockwise.

HYDROGEN

$$P_C = 3.45 \times 10^5 \text{ N/M}^2 \text{ (50 PSIA)}$$

$$\underline{P} = 10 \text{ KW}$$

$$T_{\text{PLASMA}} = 12,000 \text{ K (21,600 R)}$$

NOTES:

1. H_2 THERMAL CONDUCTIVITY VARIATION WITH TEMPERATURE INCLUDED
2. CHAMBER SIZED FOR $T_{\text{AVG}} = 5555.6 \text{ K (10,000 R)}$
3. NEGLECT RADIANT HEAT FLUX

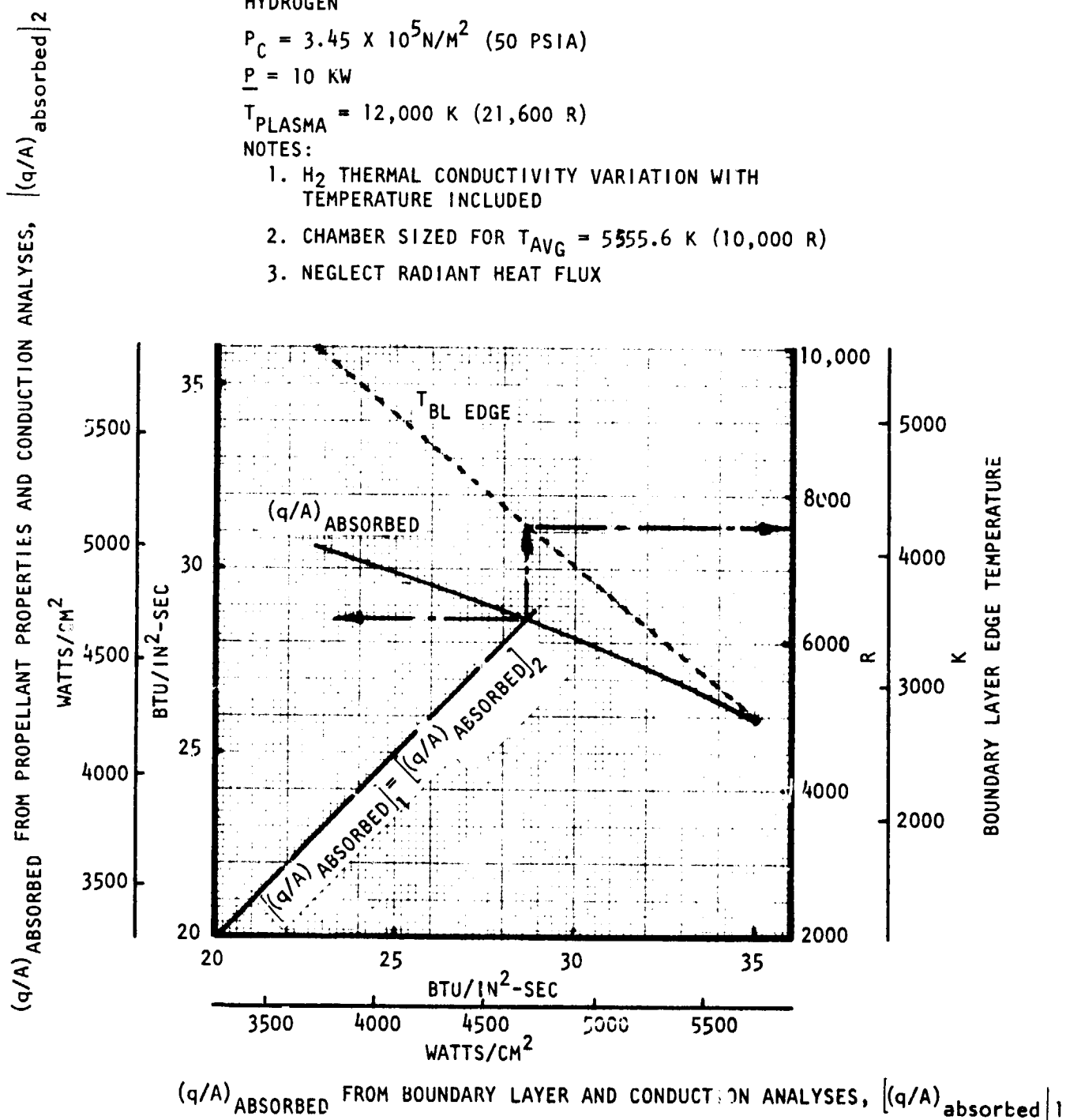


Figure 46. Determination of Absorbed Heat Flux and Boundary Layer Edge Temperature

TABLE 5 10 KW CHAMBER DIMENSIONS

$P = 50 \text{ PSIA}$

$C_c = C \text{ (PURE HYDROGEN)}$

● PLASMA CORE SIZE

- $T_{\text{PLASMA}} = 12,000 \text{ K (21,600 R)}$
 - $D_{\text{INLET}} = 0.1847 \text{ CM (0.07273 INCH)}$
 - $D_{\text{THROAT}} = 0.08859 \text{ CM (0.03488 INCH)}$
 - $\text{LENGTH} = 3 \text{ CM (1.18 INCH) TO THROAT}$
- } FROM PSI

● CHAMBER SIZE

- $(T_{\text{GAS}})_{\text{AVERAGE}} = 5555.6 \text{ K (10,000 R)}$
- $D_{\text{THROAT}} = 0.1168 \text{ CM (0.046 INCH)}$
- $D_{\text{PLASMA INLET}} = 0.2922 \text{ CM (0.11504 INCH)}$
- WINDOW AND INJECTOR REGION WAS APPROXIMATED BASED ON WINDOW REQUIREMENTS, FLOW RECIRCULATION TENDENCIES, AND OPTICAL TRAIN INTERFACE

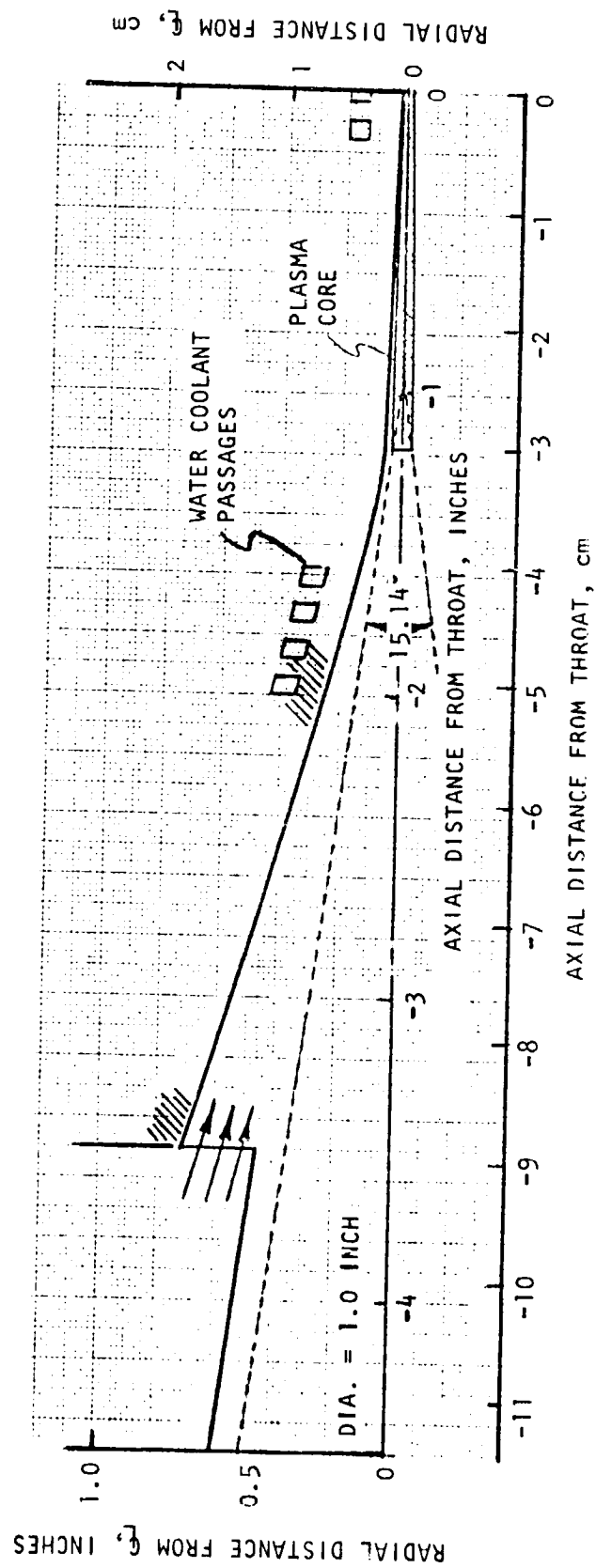


Figure 47. 10-kw Water-Cooled Chamber

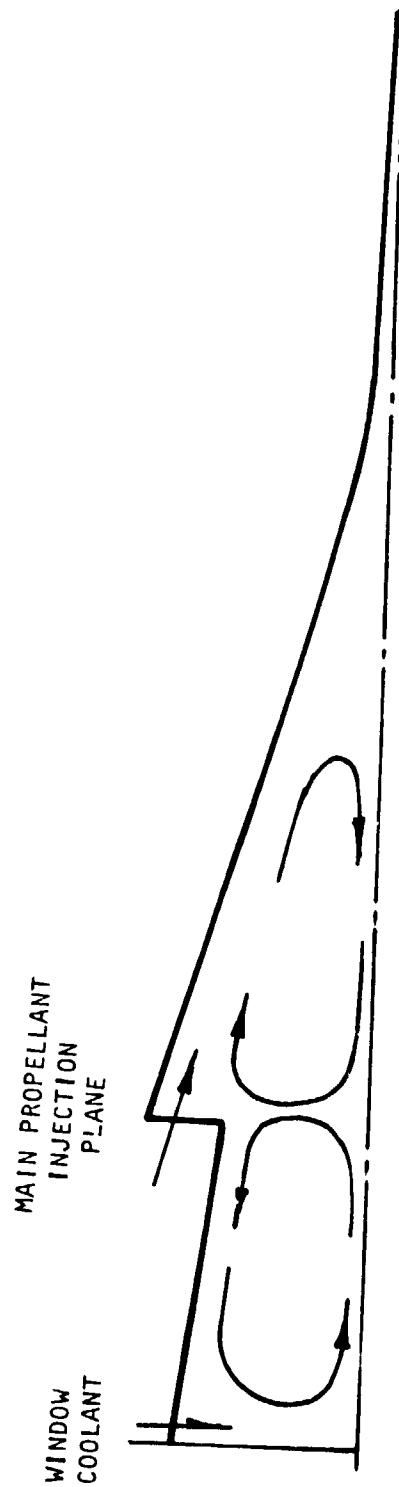


Figure 48.10-kw Chamber Flow Recirculation Patterns

To provide a defined flow of propellant along the wall of the chamber, the flow will be injected parallel to the chamber wall at a velocity the same order of magnitude as the equivalent injector annulus velocity. This injector annulus velocity is the velocity of the injected propellant through the annulus formed by the chamber wall and the inner edge of the injector lip (Fig. 48). A main propellant injection velocity of 152 cm/sec (5 ft/sec) and a window coolant velocity of 40 cm/sec (1.3 ft/sec) were selected.

10-kw Chamber/Facility Flow Stability

A phenomenon which may occur in a test chamber is a coupled chamber-to-test facility flow instability caused by a low chamber injector pressure drop. A flow disturbance occurring within the chamber propagates into the facility line which decreases the flowrate into the chamber. The chamber pressure then decays and the flowrate increases resulting in an unstable flow condition. Past experience has indicated that an injector pressure drop of approximately 10 percent of chamber pressure eliminates the unstable condition. Due to the small flowrate of the 10-kw chamber, the only feasible method of creating this magnitude of hydraulic resistance was the use of an orifice consisting of a plate of rigimesh.

5000-kw Chamber Sizing

The sizing of the 5000-kw chamber was accomplished using the same procedure used for the 10-kw chamber. The variation of the 5000-kw chamber flowrate and the potential flow (i.e., not including boundary influences) throat radius with average gas temperature and carbon concentration are presented in Fig. 49 and 50. Due to the high plasma radiation heat flux (Plasma Analysis Section) for this configuration of 6400 watts/cm^2 ($59.13 \text{ Btu/in}^2\text{-sec}$), a high concentration of carbon was assumed of 0.5. It was felt that 50 percent carbon represented perhaps an upper limit in efficient mixing with injected hydrogen. The heat flux results of the boundary layer and conduction analyses are presented in Fig. 51 and 52.

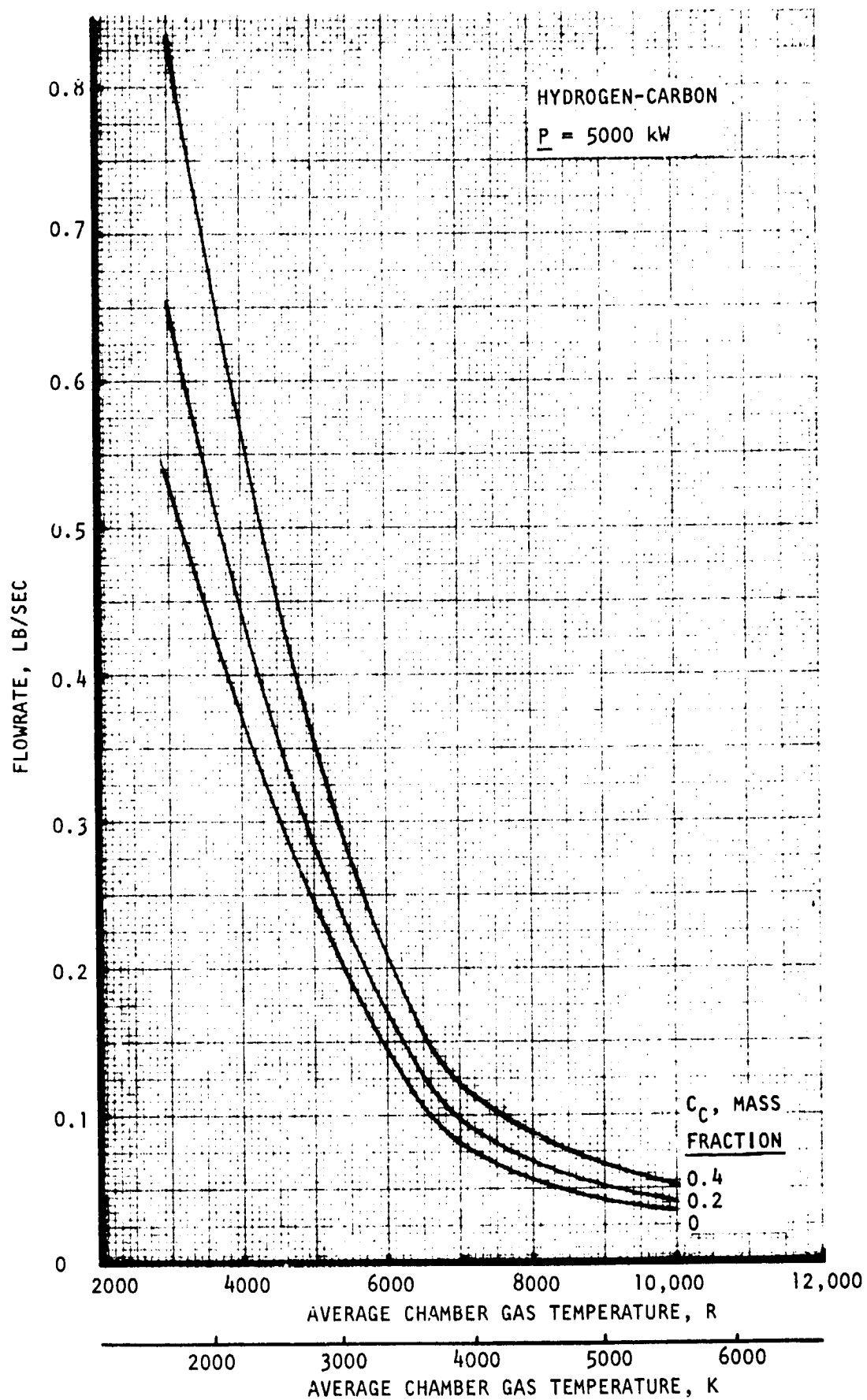


Figure 49. Hot-Gas Flowrate Variation with Gas Temperature and Carbon Concentration (5000 kW Configuration)

HYDROGEN-CARBON

$\underline{P} = 5000 \text{ kw}$

- NOTE: 1. NEGLECTED BOUNDARY LAYER INFLUENCE
2. ASSUMED NO HEAT LOSS

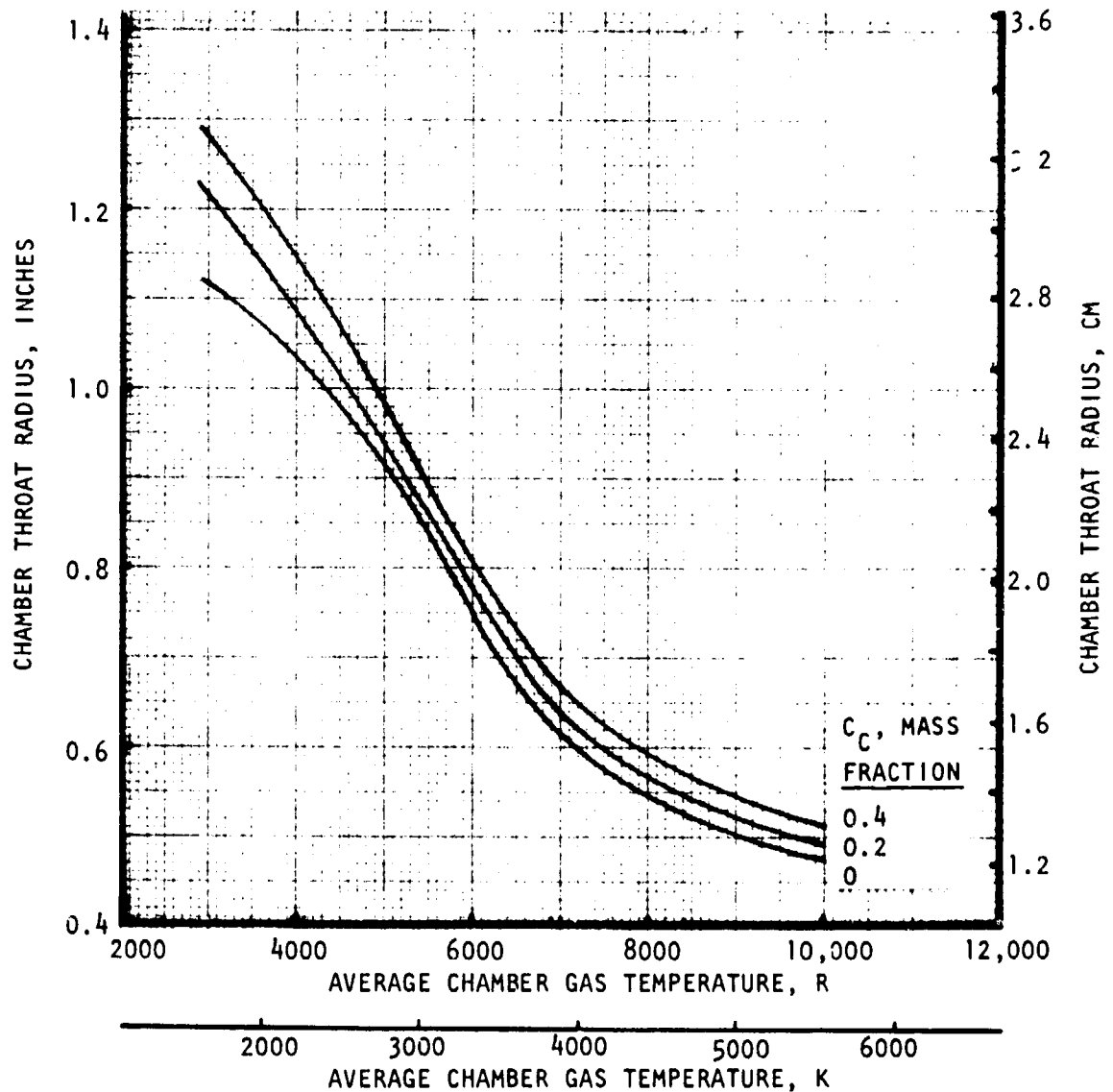


Figure 50. Chamber Throat Radius Variation with Gas Temperature and Carbon Concentration (5000 kW Chamber)

$$P_C = 3.45 \times 10^5 \text{ N/M}^2 \text{ (50 PSIA)}$$

$$C_C = 0.50$$

ASSUMPTION: CHAMBER SIZED FOR
 $T_{\text{AVG}} = 5555.6 \text{ K (10,000 R)}$

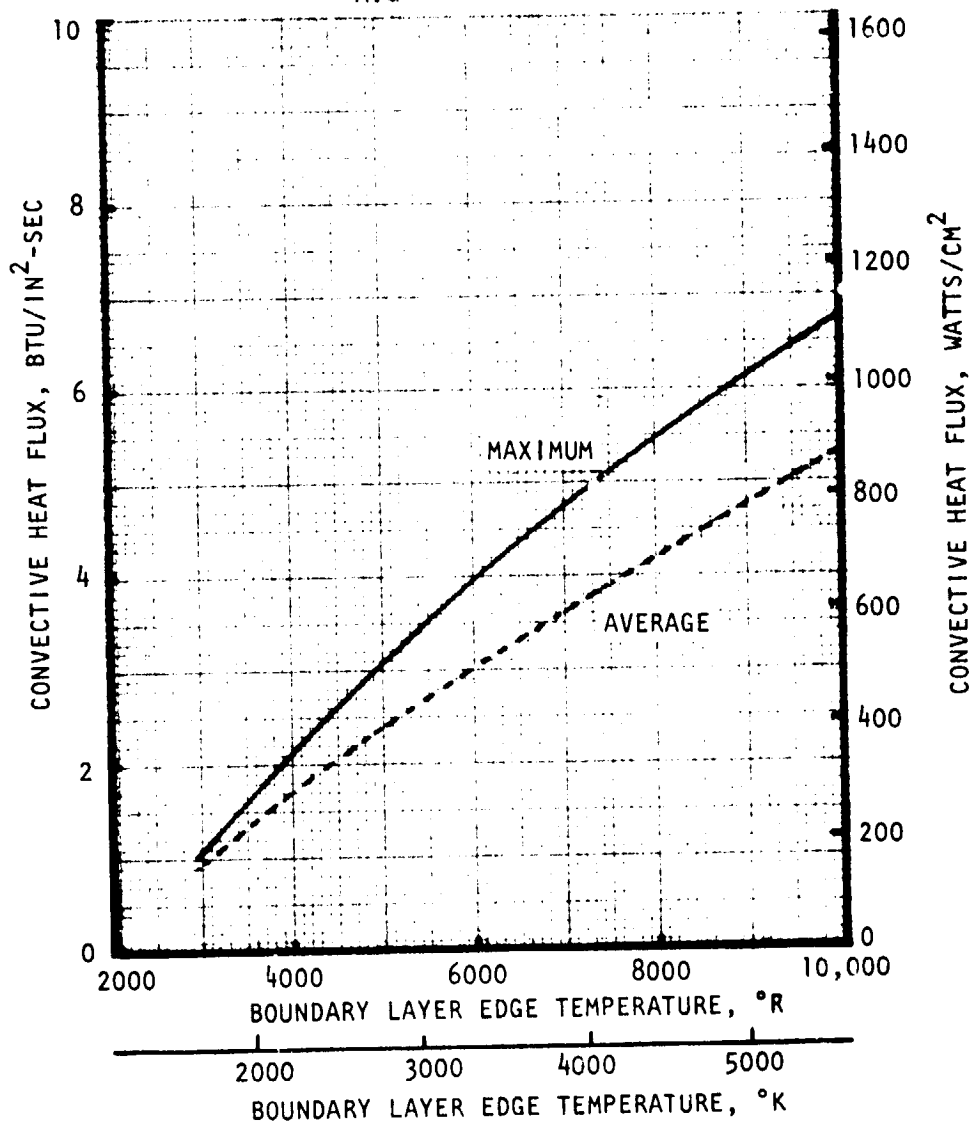


Figure 51. Convective Heat Flux Variation with Boundary Layer Edge Temperature (5000 KW Chamber)

C-H₂ THICKNESS = 0.508 cm (0.2 INCH)

$P_c = 50$ PSIA; $C_c = 0.5$

$T_{\text{PLASMA}} = 12,000$ K (21,600 R)

THERMAL CONDUCTIVITY VARIATION WITH TEMPERATURE INCLUDED

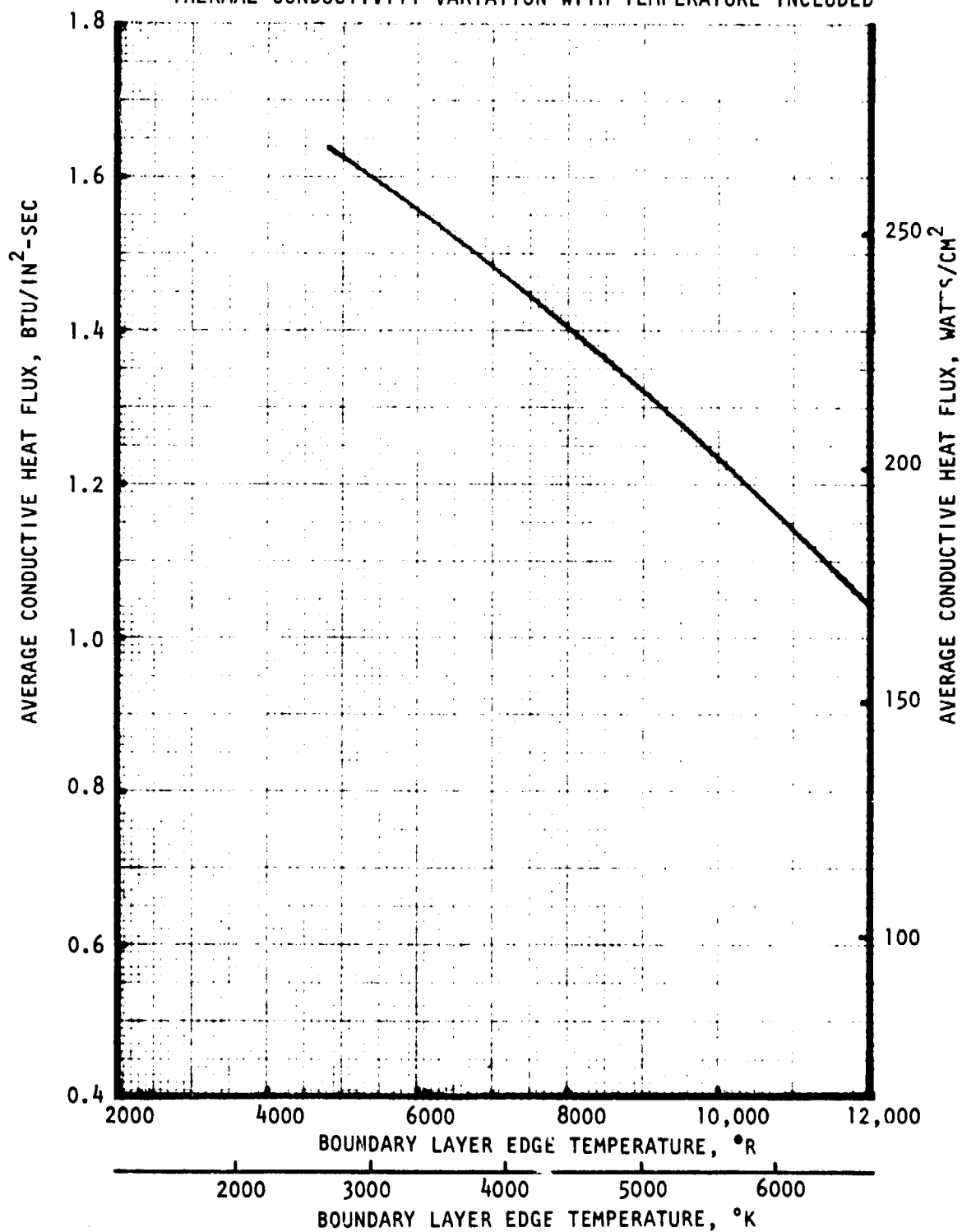


Figure 52. Average Conductive Heat Flux Variation with Boundary Layer Edge Temperature (5000 KW Chamber)

An attempt was made at cooling the convective heat flux (approximately 491 watts/cm² or 3 Btu/in²-sec and 20 percent of the radiation heat flux approximately 1309 watts/cm² or 8 Btu/in²-sec). This assumed that 80 percent of the radiation was absorbed by the seeded carbon layer. However, as will be discussed in the Cooling Analysis section the available hydrogen flow was not sufficient to cool the chamber. Increasing the amount of radiation absorbed by the carbon layer to 90-percent, the chamber could be satisfactorily cooled.

Performing the heat balance to size the chamber, a 2778 K (5000 R) boundary layer edge temperature resulted. With the 10-percent radiation heat flux value of 654 watts/cm² (4 Btu/in²-sec) and an average convective value of 393 watts/cm² (2.4 Btu/in²-sec), the effective average overall gas temperature was computed to be 5555.6 K (10,000 R).

The dimensions of the resulting 5000-kw chamber are shown in Table 6 and Fig. 53. Considering the flow heat balance and the boundary layer influences, a geometric throat diameter of 2.672 cm (1.052 in) was determined. The geometry of the region of the window and injector illustrated in Fig. 53, was approximated based on laser beam clearance. To provide a stable plasma the LSC theory required that a laser intensity of 3.7×10^5 watts/cm² (specifies beam diameter at $\lambda = -3$ cm or -1.18 in.) that the chamber diameter at this location be 6.528 cm (2.57 in.). Therefore to provide that the incoming laser beam clear the thrust chamber wall, the 45.76 degree included angle was necessary.

Carbon Seeder

During the initial portion of the program, the carbon was thought to be required for the 10-kw experimental hardware to result in a reasonable size plasma and to provide cooling of the chamber, therefore an analysis toward the definition of a carbon seeder was performed. The carbon was to consist of submicron solid particles and was to be mixed with the hydrogen and intro-

Table 6. 5000-kw Chamber Dimensions

$$P = 3.45 \times 10^5 \text{ N/M}^2 \text{ (50 PSIA)}$$

$$C_c = 0.5$$

● PLASMA CORE

● $T_{\text{PLASMA}} = 12000\text{K (21,600R)}$

● $D_{\text{INLET}} = 4.13 \text{ CM (1.626 IN)}$

● $D_{\text{THROAT}} = 1.981 \text{ CM (0.780 IN)}$

● $\text{LENGTH} = 3 \text{ CM (1.18 IN) TO THROAT}$

● CHAMBER

● $(T_{\text{GAS}})_{\text{AVERAGE}} = 5555.6\text{K (10,000R)}$

● $D_{\text{THROAT}} = 2.672 \text{ CM (1.052 IN)}$

● $D_{\text{PLASMA INLET}} = 6.528 \text{ CM (2.57 IN)}$

$$P_c = 3.45 \times 10^5 \text{ N/M}^2 \text{ (50 PSIA)}$$

$$C_c = 0.5$$

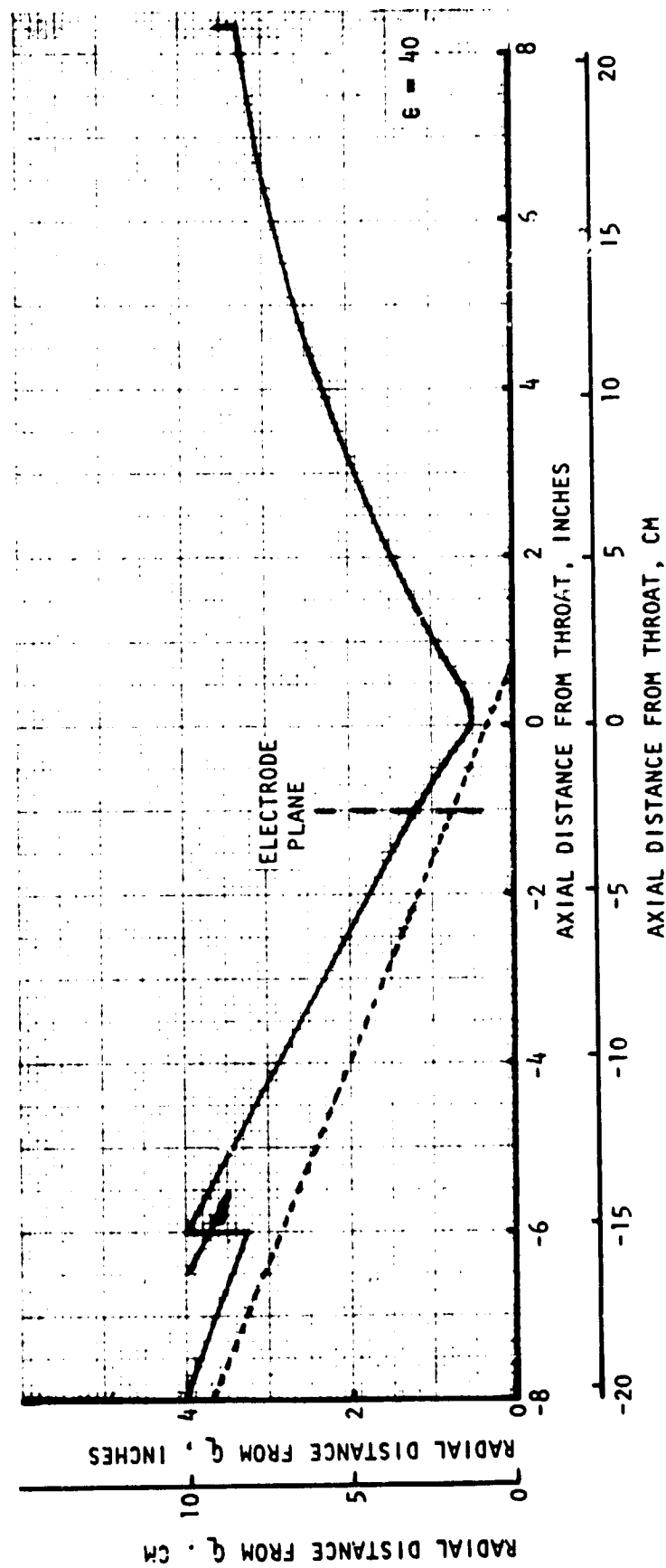


Figure 53. 5000 KW Chamber Contour

duced at a uniform rate into the chamber at one or more axial locations. However, from the plasma analysis, the carbon was found not to significantly influence the plasma size and the chamber could more than adequately be cooled with water. Therefore a pure hydrogen system was selected for the 10-kw chamber; this system would also eliminate the possibility of plugging the chamber throat with the carbon particles.

The investigation of the carbon seeder consisted of an evaluation of off-the-shelf gas-solid mixers to select a mixer to be incorporated in the carbon seeder system. As shown in Fig. 54 and Table 7, three basic types of mixers exist which include: (1) screw-feed, (2) paddle-wheel, and (3) slotted-wheel. All these concepts are normally used in conjunction with a fuel-fired torch or a plasma arc unit. The screw-feed type made by Sylvester and Company would provide a continuous flow of carbon and also contains a vibrating unit which constantly agitates the powder container. The paddle-wheel type manufactured by MEICO and the slotted-wheel type made by Plasmadyne are currently used at Rocketdyne in plasma spraying. In talking to personnel using the equipment several pertinent comments were made. The discrete paddles of the paddle-wheel concept can result in discontinuous powder flow, particularly at low powder feed rates. In the slotted-wheel concept the powder container is inclined on an angle and the slotted-wheel is located eccentric to the powder container. A separate impeller feeds the slot and as the wheel turns the powder is fed into the gas stream. Of the two types used at Rocketdyne, personnel using the equipment preferred the slotted-wheel configuration.

As shown in Table 7, these mixers utilize an electric motor for the powder feed and contact of these motors with the hydrogen propellant may present a fire and/or explosion problem which would require isolation and/or inertion of the motor. Also, most of these mixers are designed for low pressure ($6.9 \times 10^4 - 1.379 \times 10^5 \text{ N/m}^2$ or 10-20 PSIA) and the high pressure systems proposed will require containment of the entire mixer or a low pressure system which is boosted to high pressure through an aspiration system.

TABLE 7. POWDER FEED UNITS

MANUFACTURER	OVERALL DIMENSIONS	METERING DEVICE	MOTOR DRIVE	POWDER AGITATING DEVICE	CANISTER CAPACITY
METCO	8" x 11" x 19-1/2" HIGH (30 LB)	ROTATING GEAR WHEEL	DC MOTOR (OPEN)	VIBRATOR	2294.6 CU. CM (140 CU. IN.)
PLASMADYNE	---	ROTATING SLOTTED DISC	DC MOTOR (OPEN)	TAMPING DEVICE	2622.4 CU. CM (160 CU. IN.)
SYLVESTER	22" x 14" x 21" HIGH (APPROXIMATELY 55 LB)	ROTATING METER- ING SCREW	DC MOTOR (ENCLOSED)	VIBRATOR	2212.7 CU. CM (135 CU. IN.)

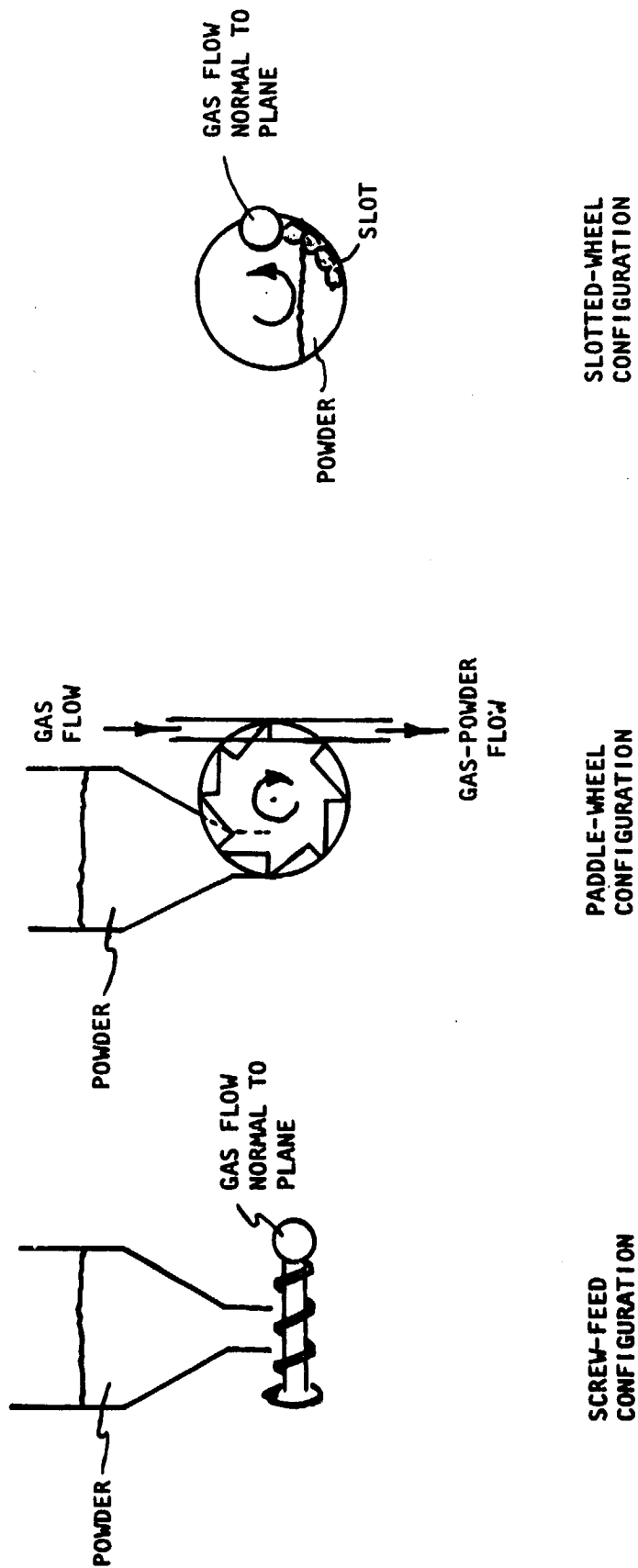


Figure 54. Schematic of Candidate Gas-Solid Mixers

The conceptual carbon seeder system analysis considered the carbon power feeder in a high pressure (approximately $3.45 \times 10^6 \text{ N/M}^2$ or 500 psia) enclosure and a low pressure (approximately $3.45 \times 10^5 \text{ N/M}^2$ or 50 psia) enclosure. The difficulty and cost in design and fabrication of a high pressure enclosure led to the selection of the low pressure carbon powder feeder enclosure. As shown in Fig. 55, the selected seeder system has the feeder enclosed and purged with gaseous nitrogen to eliminate the hydrogen fire and/or explosion hazard. The low pressure mixture of hydrogen and carbon is aspirated by a high pressure ejector which will tend to further deagglomerate the carbon. This mixture represents the carbon seeded hydrogen flow.

Since submicron carbon particles tend to cake, the carbon powder must be thoroughly dried under high temperature and vacuum before being sealed inside the gas-solid mixers.

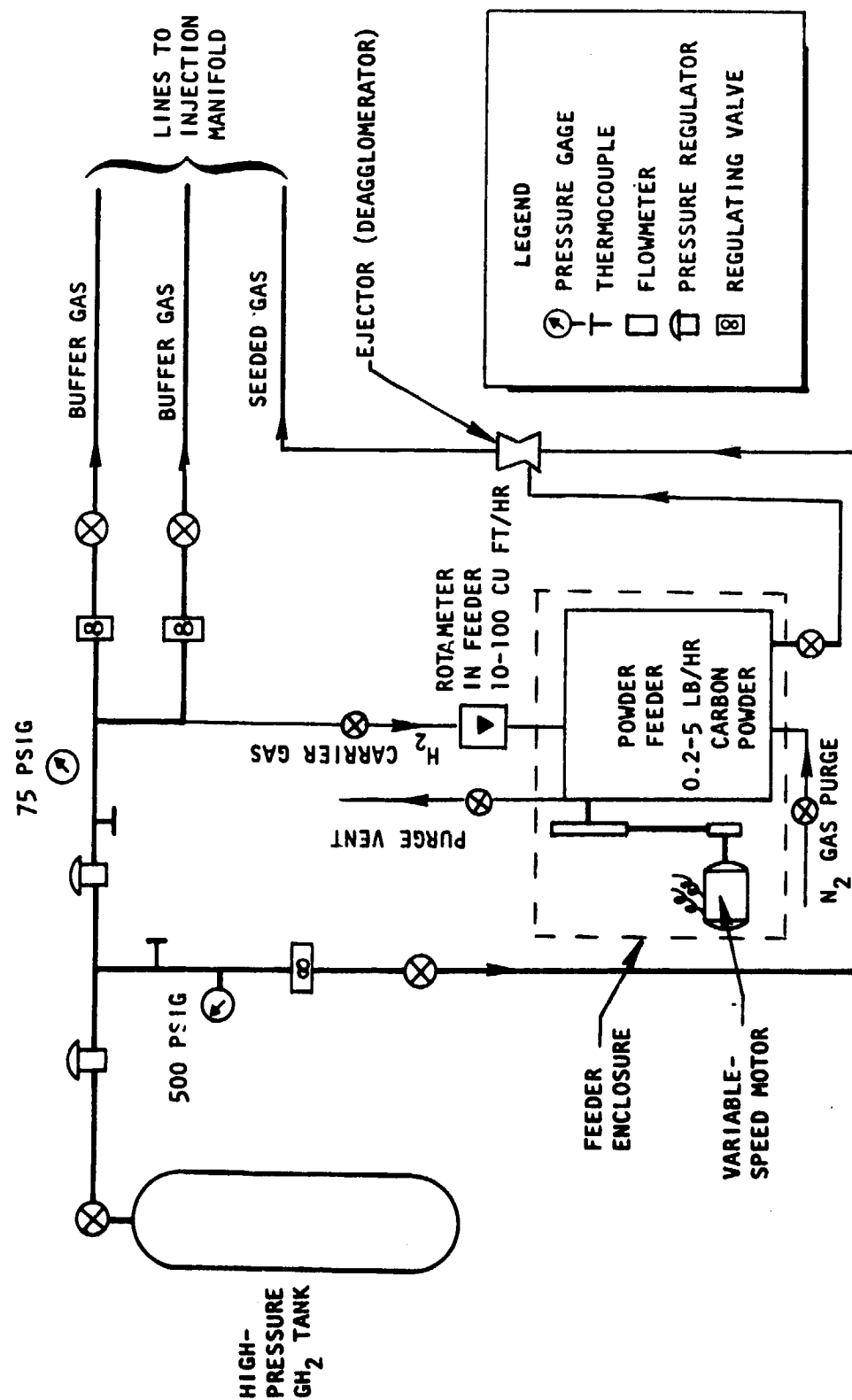


Figure 55. Typical Test Setup of Feed System

COOLING ANALYSIS

10-KW Cooled Chamber

Forced convection water-cooling of a hot-firing thrust chamber provides a reliable, durable, and continuously operable experimental device. This cooling method has been successfully demonstrated on rocket thrust chambers having heat fluxes as high as $16,357 \text{ watts/cm}^2$ or $100 \text{ Btu/in.}^2\text{-sec}$ which is a factor of 6 higher than the predicted peak value of the 10-KW chamber. In addition, this concept allows the determination of an axial heat flux distribution. Therefore, this method of cooling was selected for the 10-KW chamber.

As shown in Fig. 47, the region adjacent to the plasma core will be water cooled using circumferentially machined coolant channels. For the 10-KW chamber the predicted maximum heat flux is 2500 watts/cm^2 ($15.29 \text{ Btu/in}^2\text{-sec}$). The predicted plasma radiation heat flux is 1200 watts/cm^2 ($7.34 \text{ Btu/in}^2\text{-sec}$) and 1300 watts/cm^2 ($7.95 \text{ Btu/in}^2\text{-sec}$) is the convective portion.

The approximate burn-out heat flux using water as a coolant is presented in Fig. 56 along with the predicted maximum heat flux for the 10-KW chamber. As shown in Fig. 56, a water velocity of 15.24 M/sec (50 ft/sec) provides a 1.7 safety factor on burn-out heat flux and increasing the velocity to 30.48 M/sec (100 ft/sec) resulted in a 2.3 safety factor.

The following water coolant passages were selected:

Channel width	=	0.1524 cm (0.060 inch)
Land width	=	0.3175 cm (0.125 inch)
Channel depth	=	0.1524 cm (0.060 inch)
Wall thickness	=	0.254 cm (0.10 inch)

The wide land width which is satisfactory from heat transfer standpoint will allow individual coolant flow exit lines of reasonable diameters. The individual water exit lines permit the measurement of the individual flowrates and

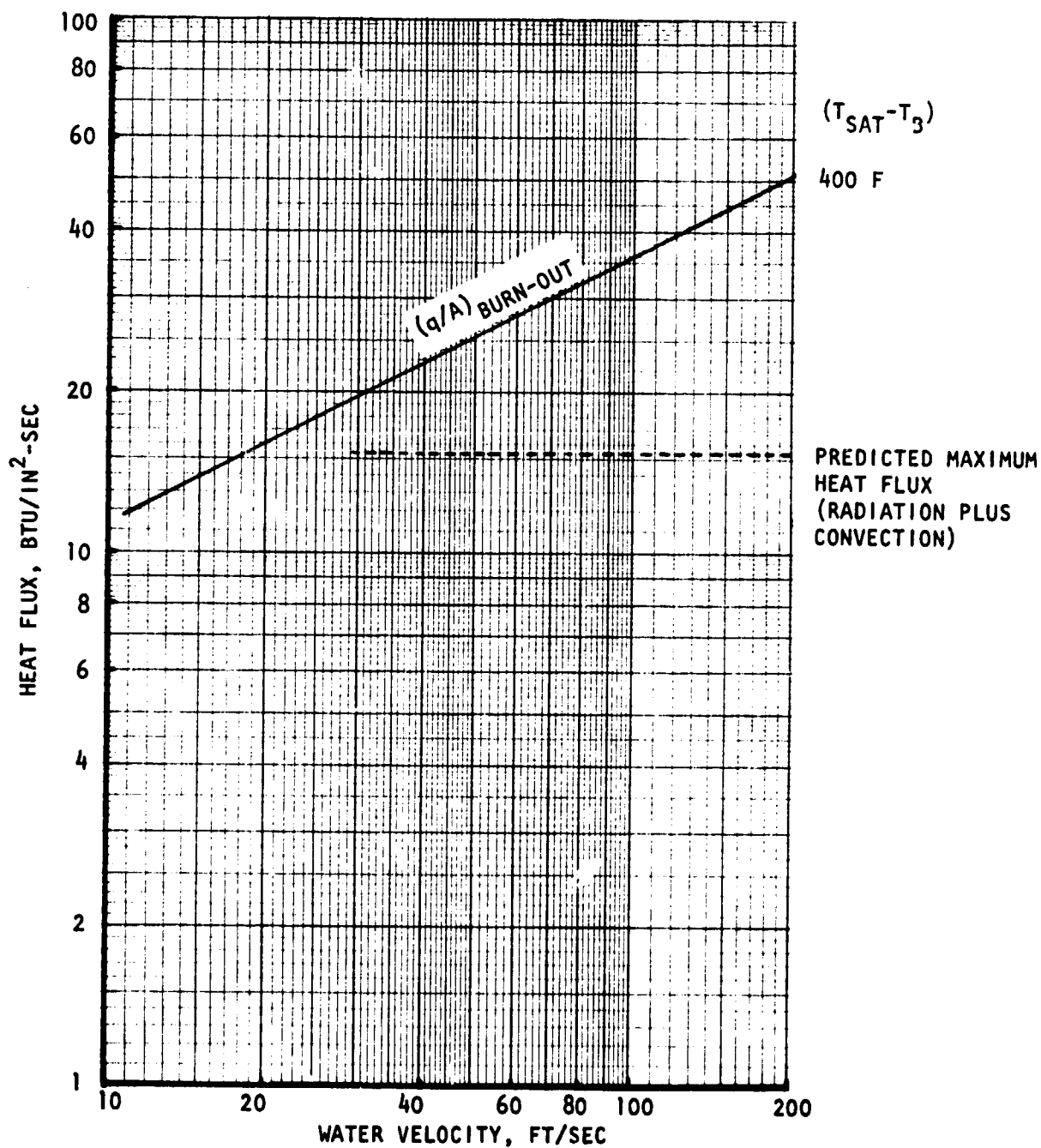


Figure 56. 10-kW Water-Cooled Chamber Cooling Capability

outlet temperatures which allows the determination of the chamber heat flux profile.

With the selected coolant channel configuration, the resulting two-dimensionally calculated wall temperature distributions for a water velocity of 15.24 and 30.48 M/sec (50 and 100 ft/sec.) respectively, are presented in Fig. 57 and 58. The computed two-dimensional temperatures outline the cross-sectional of a half channel. The maximum wall temperatures of 587 C (1089 F) and 462 C (862 F) are satisfactory for operation of the copper chamber.

A brief analysis of the water coolant pressure drop and flow requirements resulted in a $2.965 \times 10^5 \text{ N/M}^2$ (43-psi) pressure drop and 0.907 Kg/sec (2 lb/sec) for 15.24 M/sec (50 ft/sec) and $1.136 \times 10^6 \text{ N/M}^2$ (172 psi) pressure drop and 1.814 Kg/sec (4 lb/sec) for 30.49 M/sec (100 ft/sec).

As shown in Fig. 59, the heat going into the electrode insulator (alumina) can only be cooled by the adjacent water passages and any leakage of pressurizing gas (hydrogen) along the electrode. A two-dimensional model of the insulator and the adjacent water passage was constructed. As shown in Fig. 59, without gas leakage past the electrode, the insulator would melt ($> 2172 \text{ K}$ or 3450 F) based on the predicted heat flux value. However, a minute leakage of $3.17 \times 10^{-6} \text{ Kg/sec}$ or 0.000007 lb/sec (1-percent of the main propellant flow) cools the insulator to a maximum temperature (Fig. 60) well below the melting temperature of the alumina insulator. The alumina was replaced later with lavite, a lower cost and more easily machined material.

Observing Fig. 47, the risks in hot-firing such a chamber contour (required from LSC theory and throat area calculations) without previous experimental data are apparent. If the resulting plasma is larger than predicted, the chamber wall would be exposed to the 12,000 K (21,600 R) temperature plasma. Also, if the laser beam moves significantly relative to the chamber, the laser beam would hit the chamber wall. These two occurrences could result in hardware damage. Therefore, an alternate 10-KW chamber concept was conceived.

NUMBER OF ITERATIONS = 97
 DIFFERENCE BETWEEN HEAT IN AND HEAT OUT = 0.22269%
 HEAT INFLUX = 15.084

1085° F	1085	1086	1086	1088	1089
977	977	977	978	981	983
867	867	867	868	876	881
755	754	753	750	777	788
			717	757	770
			690	739	754
			667	723	740
			649	709	728
			632	698	718
			618	689	711
			605	683	706
238	264	361	591	680	703
486	493	511	538	597	617
525	528	534	544	580	594

- 1: LAND WIDTH = 0.12500
- 2: CHANNEL WIDTH = 0.06000
- 3: WALL THICKNESS = 0.10000
- 4: CHANNEL DEPTH = 0.06000
- 5: CLOSEOUT THICKNESS = 0.08000
- 6: TAW = 7600. DEG. F
- 7: HG = 0.0023160
- 8: TC = 90. DEG. F
- 9: REFERENCE HC = 0.0226200
- 10: HC FACTOR FOR UPPER WALL = 1.0000
- 11: HC FACTOR FOR LOWER WALL = 1.0000
- 12: EXPONENT = 0.00
- 13&14: K OF REGION 1 = 0.004875 + (-.1870E-06) * T
- 15&16: K OF REGION 2 = 0.004875 + (-.1870E-06) * T
- 17&18: K OF REGION 3 = 0.000200 + (0.0000E+00) * T
- 19: CONVERGENCE CRITERION = 0.1000 DEG. F

Figure 57 Predicted 10-kw Water-Cooled Chamber Wall Temperature
 Distribution at Peak Heat Flux Location ($V_{H2O} = 15.24$ M/sec or
 50 ft/sec.) 93

NUMBER OF ITERATIONS = 68
 DIFFERENCE BETWEEN HEAT IN AND HEAT OUT = 0.14512X
 HEAT INFLUX = 15.611

857 F	857	858	853	860	862
746	746	747	747	751	753
632	632	633	634	644	649
513	513	513	512	544	555
			480	524	538
			454	506	522
			433	491	509
			417	478	497
			402	467	487
			390	459	480
			379	453	475
135	149	206	369	450	473
305	310	323	341	388	403
333	335	340	347	374	385

- 1: LAND WIDTH = 0.12500
- 2: CHANNEL WIDTH = 0.06000
- 3: WALL THICKNESS = 0.10000
- 4: CHANNEL DEPTH = 0.06000
- 5: CLOSEOUT THICKNESS = 0.08000
- 6: TAW = 7600. DEG. F
- 7: HC = 0.0023160
- 8: TC = 85. DEG. F
- 9: REFERENCE HC = 0.0393800
- 10: HC FACTOR FOR UPPER WALL = 1.0000
- 11: HC FACTOR FOR LOWER WALL = 1.0000
- 12: EXPONENT = 0.00
- 13&14: K OF REGION 1 = $0.004875 + (-.1870E-06) * T$
- 15&16: K OF REGION 2 = $0.004875 + (-.1870E-06) * T$
- 17&18: K OF REGION 3 = $0.000200 + (0.0000E+00) * T$
- 19: CONVERGENCE CRITERION = 0.1000 DEG. F

Figure 58. Predicted 10-kw Water-Cooled Chamber Wall Temperature Distribution at Peak Heat Flux Location ($V_{H2O} = 30.48$ M/sec or 100 ft/sec)

V=50FT/SEC D(RL)=0.185 X(CU)=0.138 NO H2 ON ELECTRODE

055528799
020276 0002

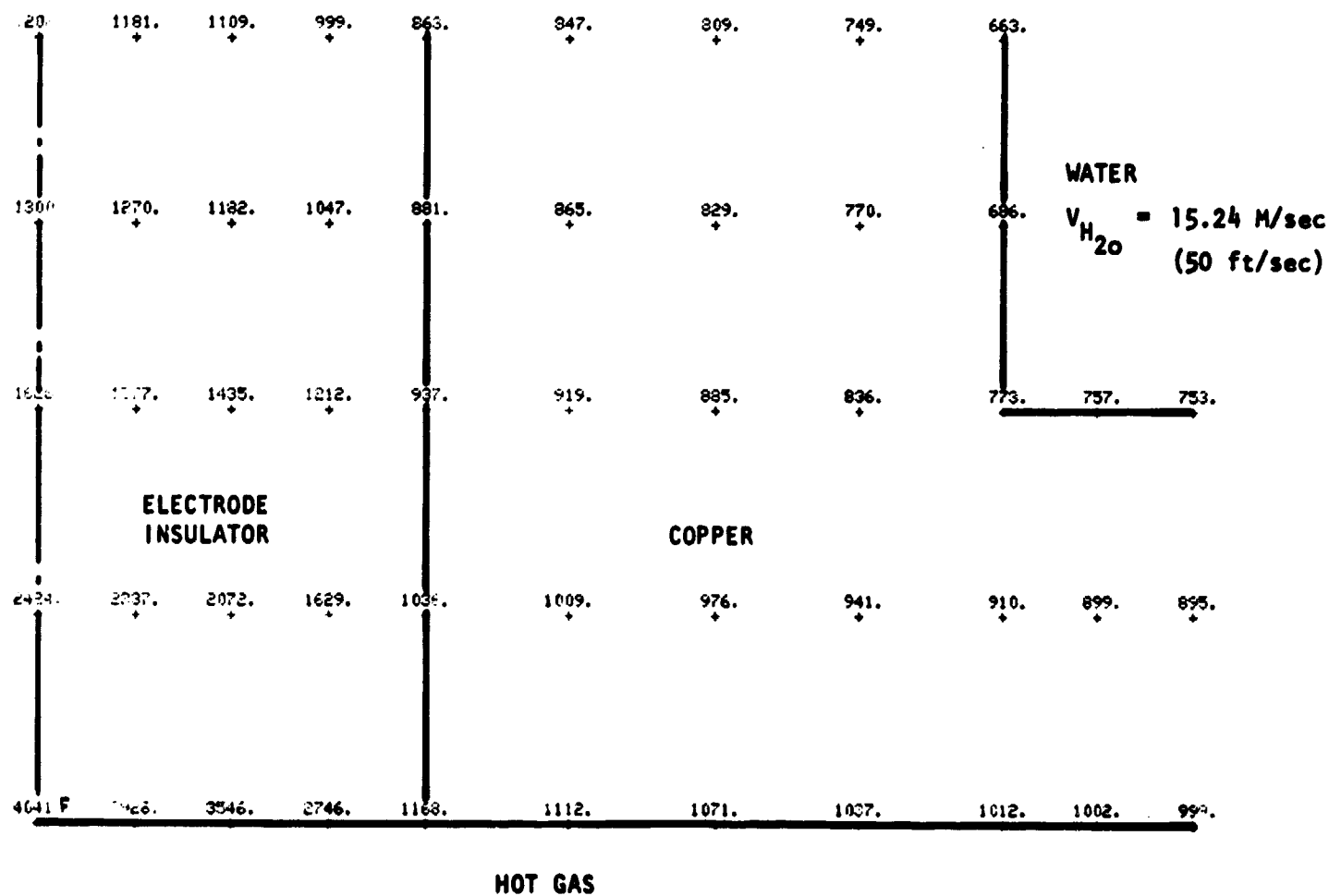


Figure 59. 10-kw Chamber Arc Initiating Electrode Insulator Wall Temperature Distribution (Water Cooling Only)

$V=50\text{ FT/SEC}$ $D(\text{AL})=0.185$ $D(\text{CU})=0.138$ H_2 ON ELECTRODE (1-P)

#055528798
013076 0002

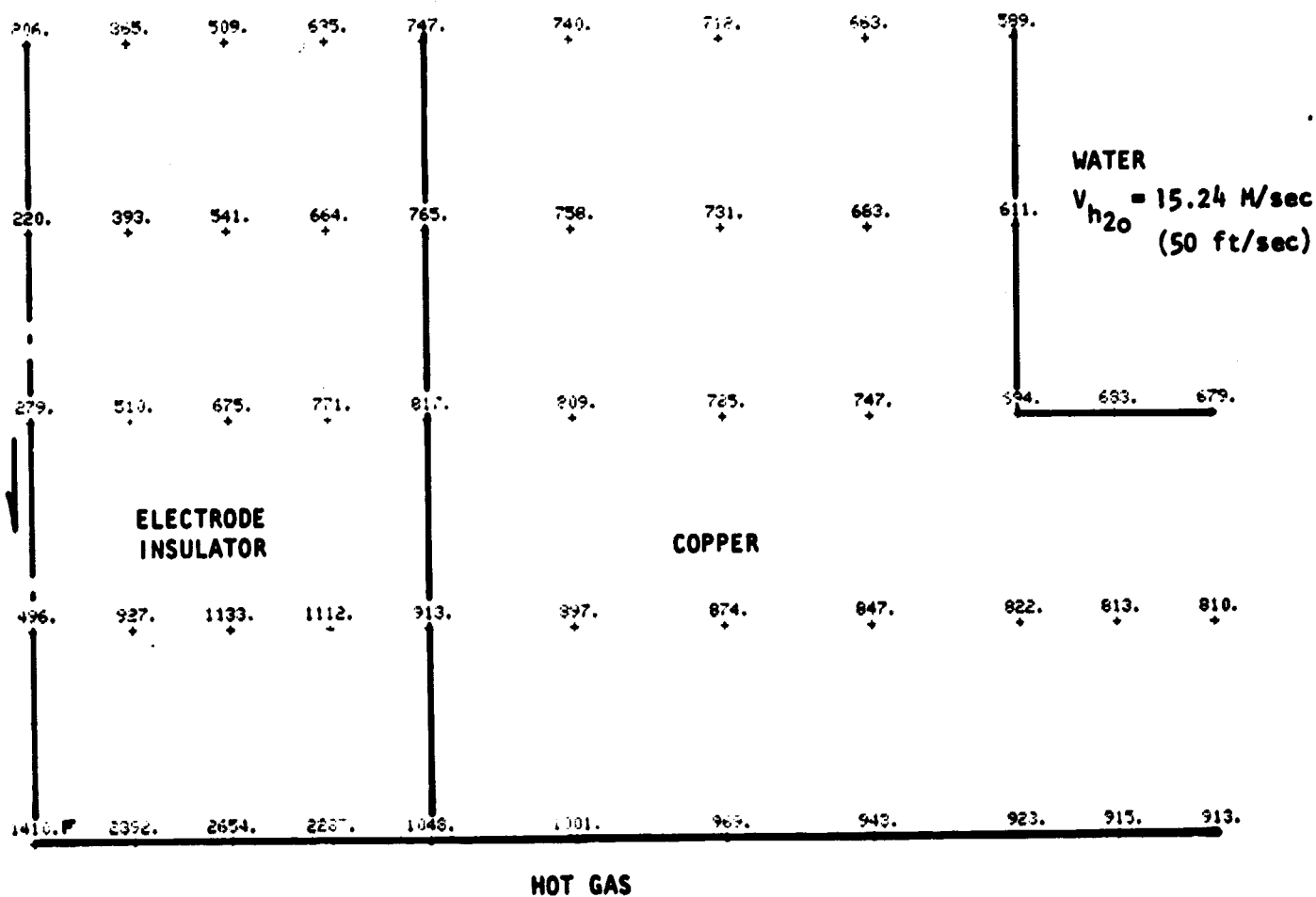


Figure 60. 10-kw Chamber Arc Initiating Insulator Wall Temperature Distribution (Water and H_2 Cooling)

10-kw Uncooled Chamber

To provide the test program with a higher assurance of success with the 10-kw experimental hardware, an additional chamber (a heat sink chamber) was designed and fabricated. The additional chamber is a copper heat sink chamber with graphite inserts (Fig. 61) which provides a highly flexible, short duration test device. This chamber allows for a larger-than-predicted plasma size and is significantly less critical with regard to the relative movement of the laser beam with respect to the chamber. Also with the incorporation of the graphite inserts, the internal gas diameter may be varied to evaluate the plasma-buffer gas flow interaction. Also, the water-cooled chamber has the flexible capability of being machined to increase the hot-gas diameter by a factor of two. The water-cooled chamber provides a test device capable of continuous operation and allows measuring of chamber heat flux.

Analyses of the uncooled chamber included the chamber configurations with and without a graphite insert. Also, the feasibility of a plasma viewing window was evaluated.

Without Graphite Insert. A thermal model of a thick wall cylinder was constructed to simulate the uncooled chamber cross section. An effective convective heat transfer coefficient was obtained to represent the combined radiation and convective heat flux. The copper heat sink chamber was evaluated near the plasma inlet ($X = 2.5$ cm or -1.0 inch) and at the geometric throat ($X = 0.0$ cm). Using a conservative maximum wall temperature limit of 649 C (1200 F) for the copper, the location at $X = -2.54$ cm (-1.0 inch) resulted in maximum test duration of approximately 8 seconds as shown in Fig. 62.

The thermal analysis of the geometric throat was more difficult in that excessive computer time would have been required to obtain the time to a temperature of 649 C (1200 F). This was due to the small value of the inner radius (0.0594 cm or 0.0234 inch). Therefore, data for larger radii were run (Fig. 63) and cross-plotted to obtain the 42.5 seconds required to reach the

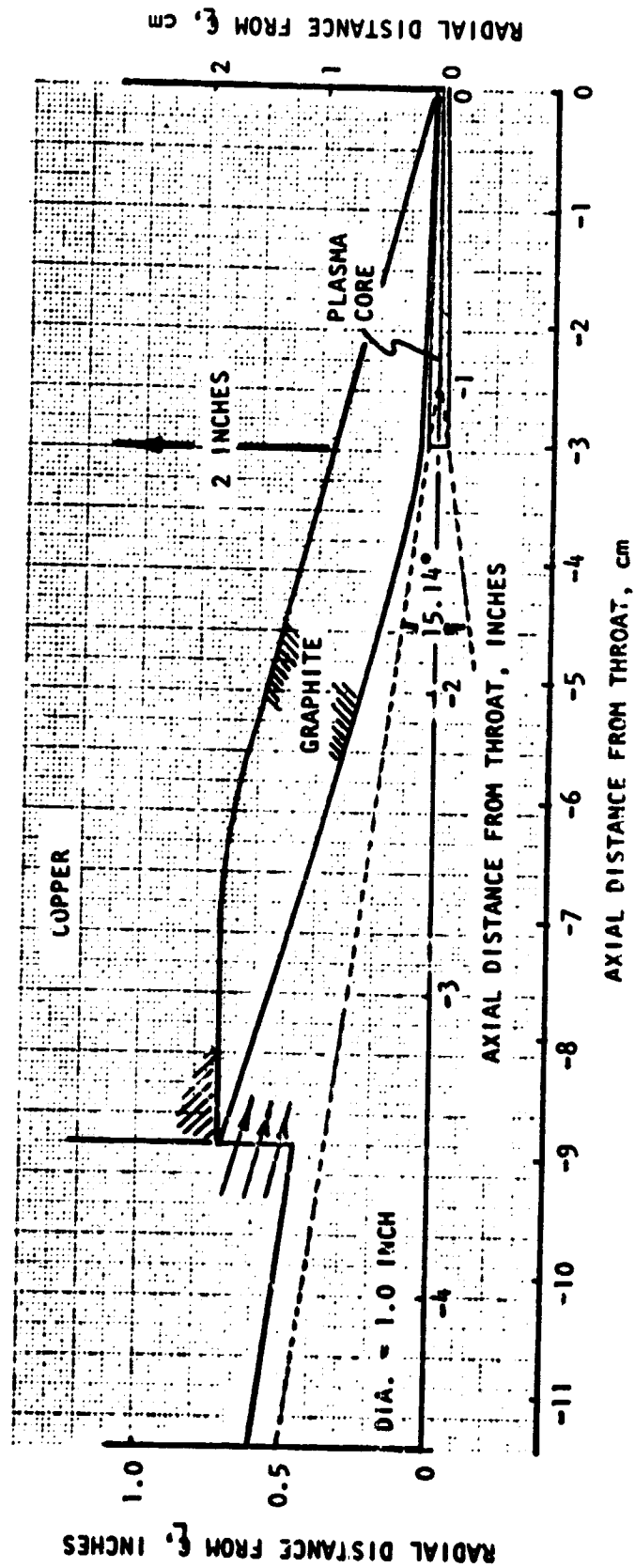


Figure 61. 10-kw Heat Sink Chamber With Graphite Inserts

$x = -2.54 \text{ CM } (-1.0 \text{ IN.})$

GAS CONDITIONS:

$T_{AW} = 4222 \text{ K } (7140 \text{ F})$

$h_g = .6156 \text{ CAL/CM}^2\text{-SEC-C}$
 $(.001357 \text{ BTU/IN.}^2\text{-SEC F})$

COPPER THICKNESS - (5.08CM) 2 IN.

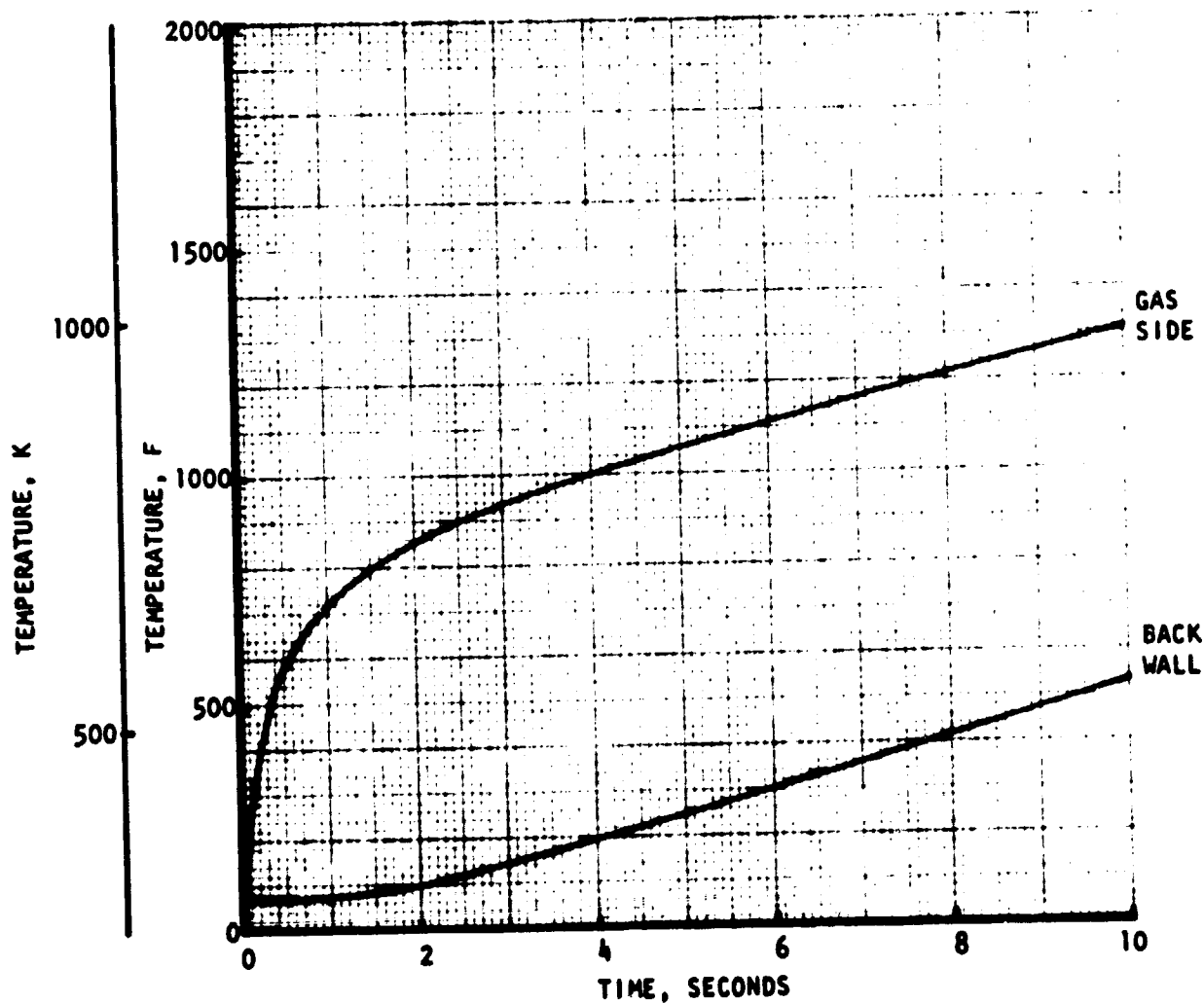
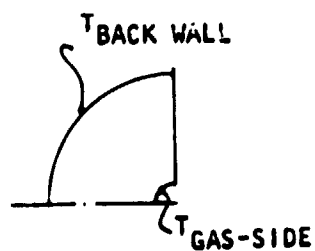
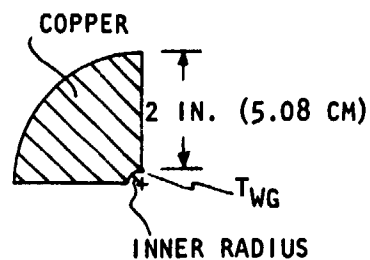


Figure 62. 10 KW Uncooled Chamber - Temperature History at $x = -2.54 \text{ cm } (-1.0 \text{ in.})$



$X = 0.0 \text{ CM} \quad (0.0 \text{ IN.})$

GAS CONDITIONS:

$$P_C = 3.45 \times 10^5 \text{ N/M}^2 \quad (50 \text{ PSIA})$$

$$T_{AW} = 4222 \text{ K} \quad (7140 \text{ F})$$

$$h_g = 1.1295 \text{ CAL/CM}^2\text{-SEC-C} \quad (0.00249 \text{ BTU/IN.}^2\text{-SEC-F})$$

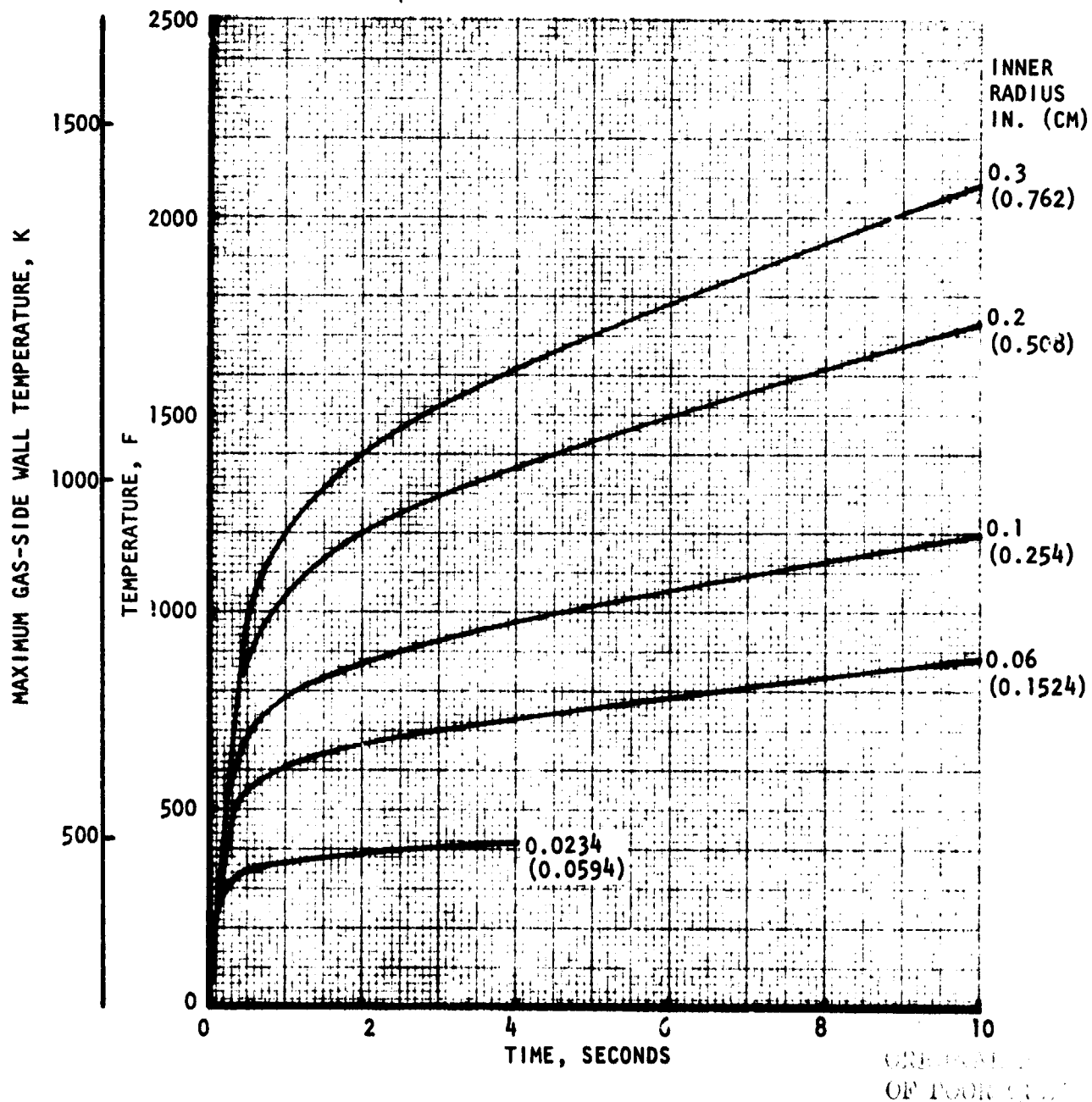


Figure 63. 10 KW Uncooled Chamber - Temperature History at $X = 0.0 \text{ CM}$ with Variation in Inner Radius

649 C (1200 F). The data for the various radii clearly indicated that as the inner radii were decreased (surface area exposed to the hot gas is decreased), the time to reach a fixed temperature increased.

Therefore, without the plasma viewing window, the hot-fire test duration limit of the 10-kw uncooled chamber without the graphite insert is approximately 8 seconds (Fig. 64). The limiting location was the plasma inlet region.

Plasma Viewing Window. To enable plasma viewing, photography, and any other diagnostics, a transparent viewing window near the plasma inlet could be provided as shown in Fig. 65. Two candidate materials (calcium fluoride and fused quartz) were thermally evaluated. The primary requirement for the window was a high transmittance in the visual wave length. Other pertinent property data are presented in Table 8. As shown in Table 8, calcium fluoride has five times higher thermal conductivity than fused quartz. However, the fused quartz is capable of extreme thermal shock and the calcium fluoride has poor thermal shock characteristics.

The results of the thermal analysis of the calcium fluoride plasma viewing window are presented in Fig. 66. The analysis indicated that an uncooled calcium fluoride window could last approximately 2 seconds and cooled to steady-state maximum wall temperatures of approximately 649 C (1200 F). However, in both uncooled and cooled configurations a thermal gradient exceeding 204 C (400 F) existed; therefore, due to the poor thermal shock characteristics of calcium fluoride and the relatively high thermal gradients which would exist, this material was eliminated.

Similar analyses for fused quartz were performed and, as shown in Fig. 67, the maximum test duration was limited to 1 second with or without cooling. The extremely low thermal conductivity of fused quartz did not permit appreciable heat conduction to provide a cooler wall. However, the excellent thermal shock characteristics of fused quartz would most likely allow the 871 C (1600 F) thermal gradient predicted.

FIGURE 64.

10-KW UNCOOLED CHAMBER THERMAL ANALYSIS

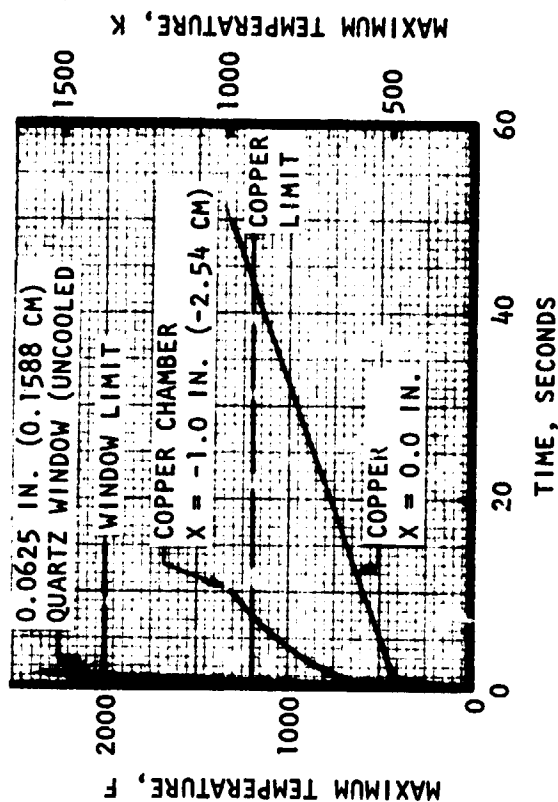
(COPPER ONLY)

• WITHOUT PLASMA VIEWING WINDOW

- TEST DURATION
 - ~8 SECONDS
- LIMITING LOCATION ON CHAMBER
 - $X = -2.54 \text{ CM}$ (-1.0 IN.)

• WITH PLASMA VIEWING WINDOW

- UNCOOLED WINDOW
 - TEST DURATION ~ 1 SECOND
 - WINDOW LIMITS TEST DURATION
- COOLED WINDOW
 - TEST DURATION ~ 1 SECOND (LOW THERMAL CONDUCTIVITY WINDOW)
 - WINDOW LIMITS TEST DURATION



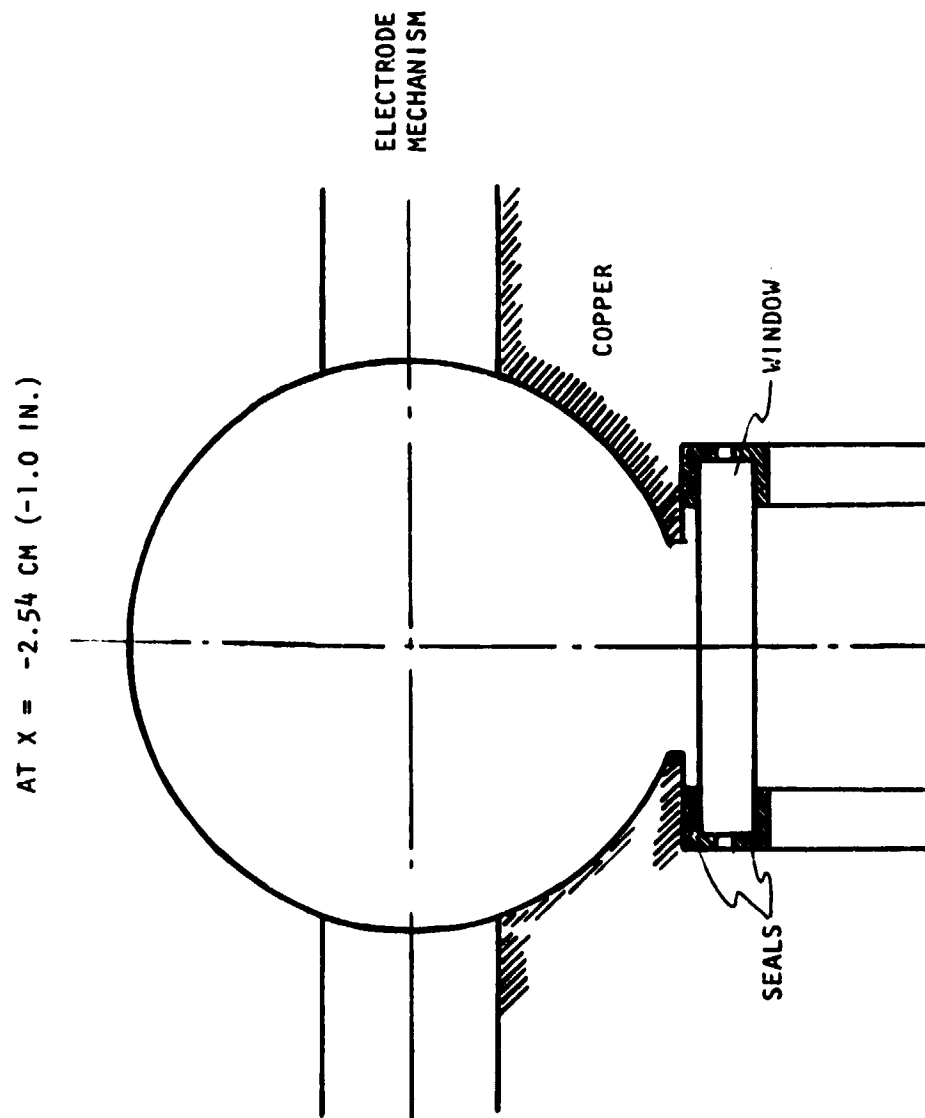


Figure 65. 10 KV Uncooled Chamber - Plasma Viewing Window

TABLE 8

PLASMA VIEWING WINDOW MATERIALS

OPTICAL QUALITY: HIGH TRANSMITTANCE IN VISUAL WAVE LENGTH RANGE

	CALCIUM FLUORIDE (CaF ₂)	FUSED QUARTZ
THERMAL CONDUCTIVITY, BTU/IN-SEC-F (CAL/CM-SEC-K)	0.0000896 (0.016)	0.00001848 (0.0033)
DENSITY, LB/IN ³ (G/CC)	0.0955 (2.64)	0.0795 (2.2)
SPECIFIC HEAT, BTU/LB-F OR CAL/GM	0.27	0.18
THERMAL SHOCK CHARACTERISTICS	SMALL CRACKS & SURFACE CRAZING OCCURRED WHEN SHOCKED FROM ABOVE 55 C (131 F) TO WATER AT AMBIENT TEMPERATURE	HEATED RAPIDLY TO 1500 C (2732 F) AND PLUNGED INTO AMBIENT WATER WITHOUT CRACKING
REASONABLE TEMPERATURE LIMIT, F (C)	1650 (900)	2032 (1100)

MATERIAL: CALCIUM FLUORIDE

$$h_g = 0.0001617 \text{ BTU/IN}^2\text{-SEC-F}$$
$$(0.07335 \text{ CAL/CM}^2\text{-SEC-C})$$

EXCEPT AS NOTED

$$h_c = \text{BTU/IN}^2\text{-SEC-F}$$
$$(\text{CAL/CM}^2\text{-SEC-C})$$

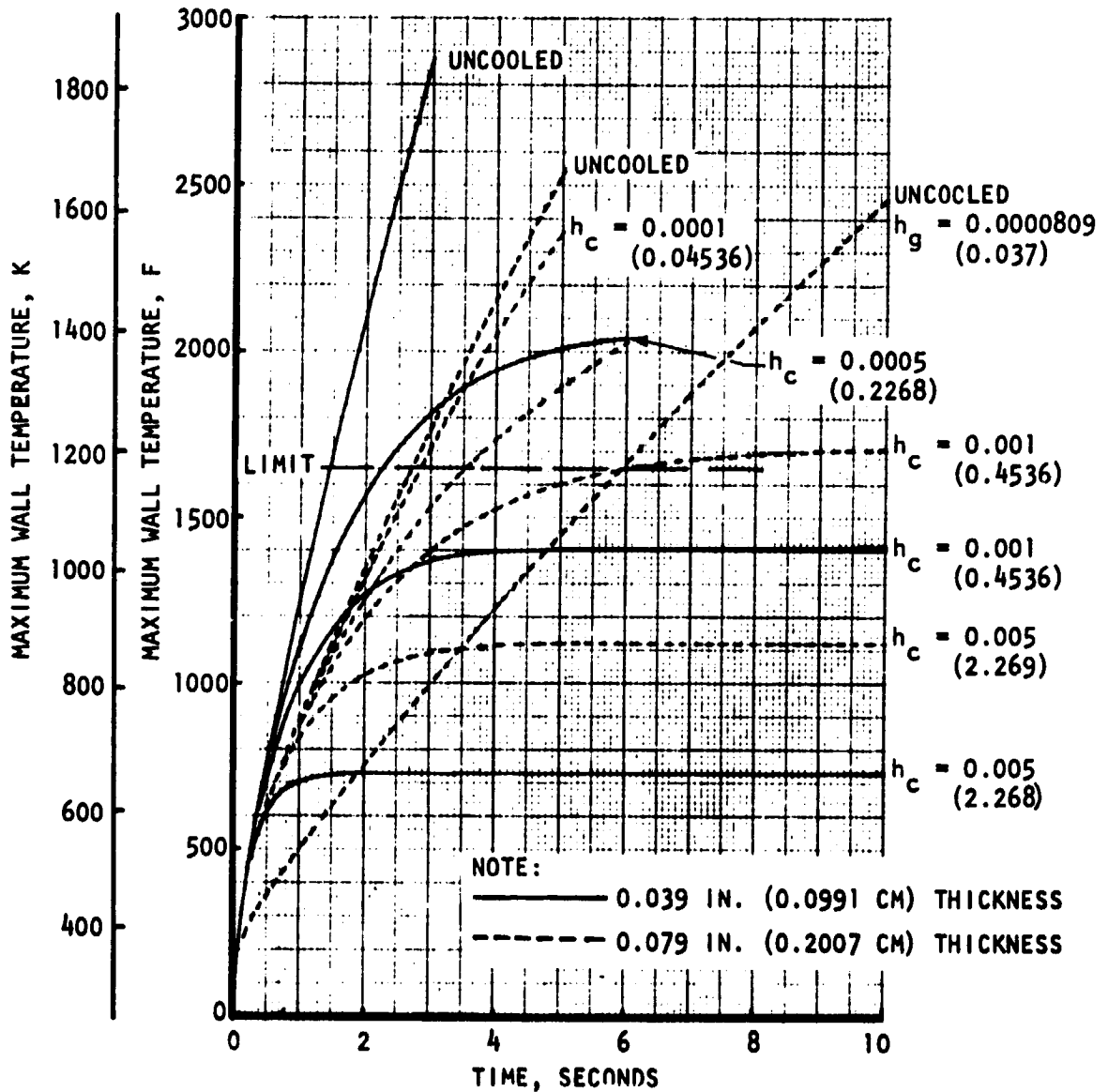


Figure 66. 10 KW Chamber Plasma Viewing Window Temperature History - Calcium Fluoride

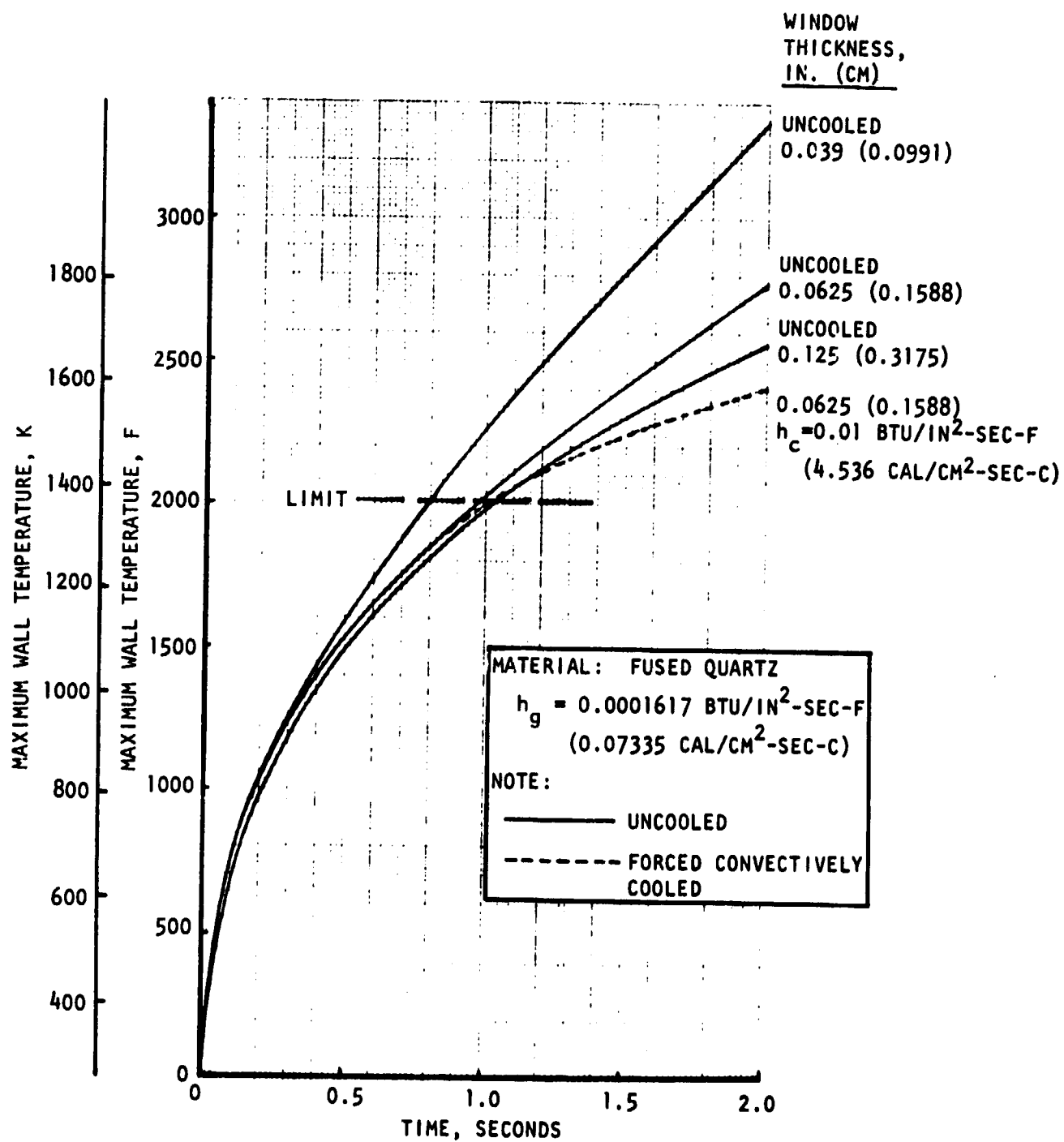


Figure 67. 10 KW Chamber Plasma Viewing Window Temperature History - Fused Quartz

Therefore, combining the heat sink and plasma viewing window temperature limits (Fig. 64), the viewing window would limit the test duration to approximately 1 second. Therefore, the thermal analysis indicated that a fused quartz viewing window (uncooled) is feasible but severely limits the test duration of the uncooled chamber. The value of the information that can be obtained through this window in the 1-second duration must be weighed against the increased complexity incorporating the window and the difficulty in sealing the hot gas using the high temperature seals required.

With Graphite Insert. When the graphite insert is to be used, the plasma viewing window could be replaced with a solid copper plug. Since the graphite ends slightly upstream of the geometric throat, the previous analysis of the geometric throat location applies with or without the graphite insert. At the plasma inlet, the thermal results (Fig. 68) show that the copper portion would reach the 649 C (1200 F) limit before the graphite would reach a limit of 1649C (3000 F) . A composite of the locations analyzed (Fig. 69) indicated that geometric throat location would limit the test duration to approximately 42.5 seconds.

Thermocouples were placed on the uncooled chamber within 1 inch of the copper hot gas wall (see design drawings). These will allow the indirect monitoring of the gas-side wall temperature and will enable the detection of an over-temperature condition.

5000-KW Chamber

A single uppass and a split-flow cooling circuit (Fig. 70) were evaluated for the 40-to-1 area ratio 5000-kw chamber. The first circuit is a single uppass circuit with the coolant inlet at the nozzle exit (40-to-1 area ratio). This circuit is perhaps the simplest circuit. The entire thrust chamber could be fabricated using channels or using the combined construction technique of channels and tubes. The second coolant circuit which is slightly more complicated would tend to minimize the coolant pressure drop. The same fabrication techniques could be applied for this circuit.

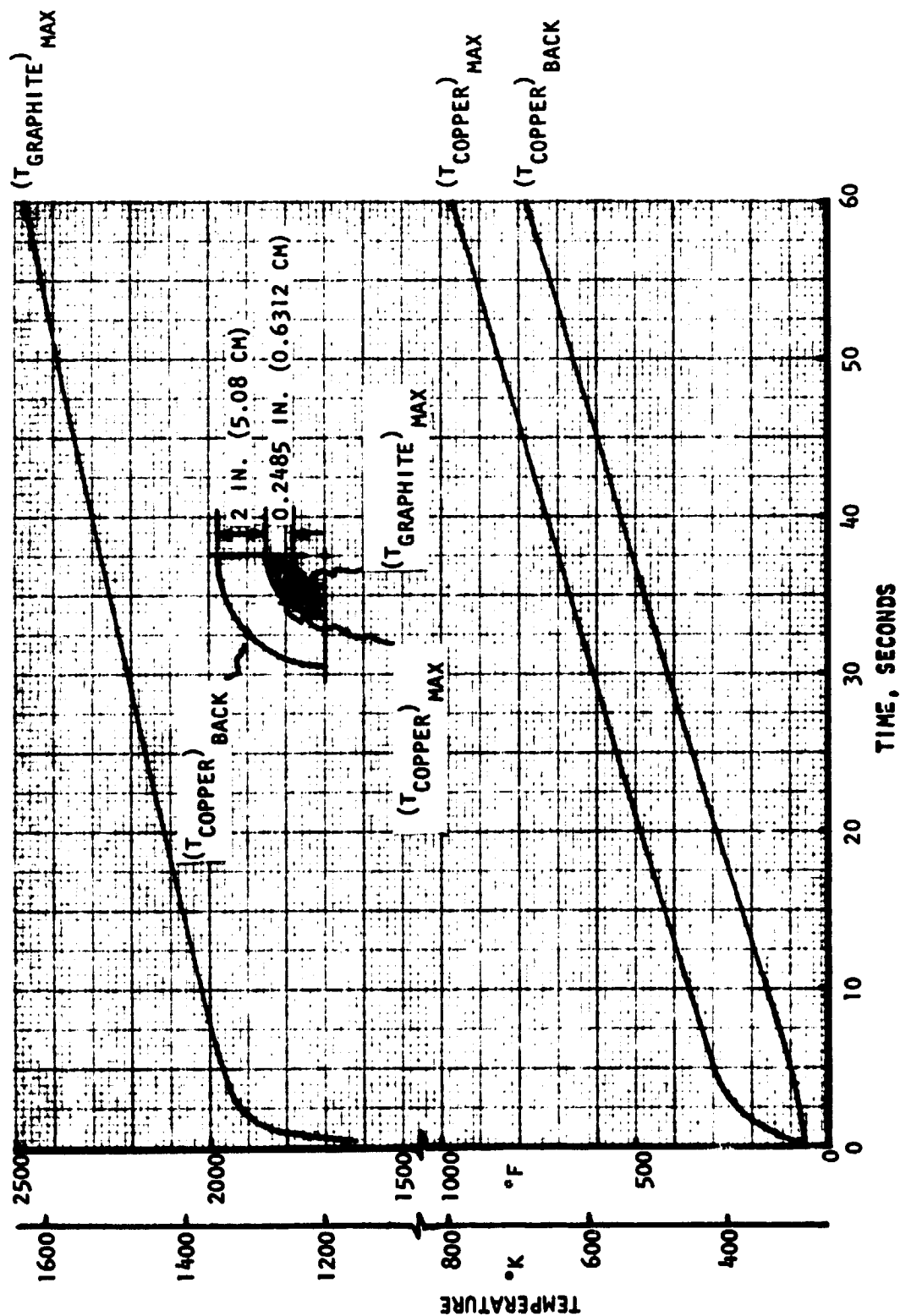


Figure 68. 10 KW Uncooled Chamber - Chamber Temperature History with Graphite Insert at $X = -2.54 \text{ CM}$ (-1.0 IN.)

FIGURE 69. 10-KW UNCOOLED CHAMBER THERMAL ANALYSIS
(COPPER CHAMBER WITH GRAPHITE INSERT)

• CONFIGURATION

- VIEWING WINDOW IS REPLACED WITH SOLID COPPER PLUG

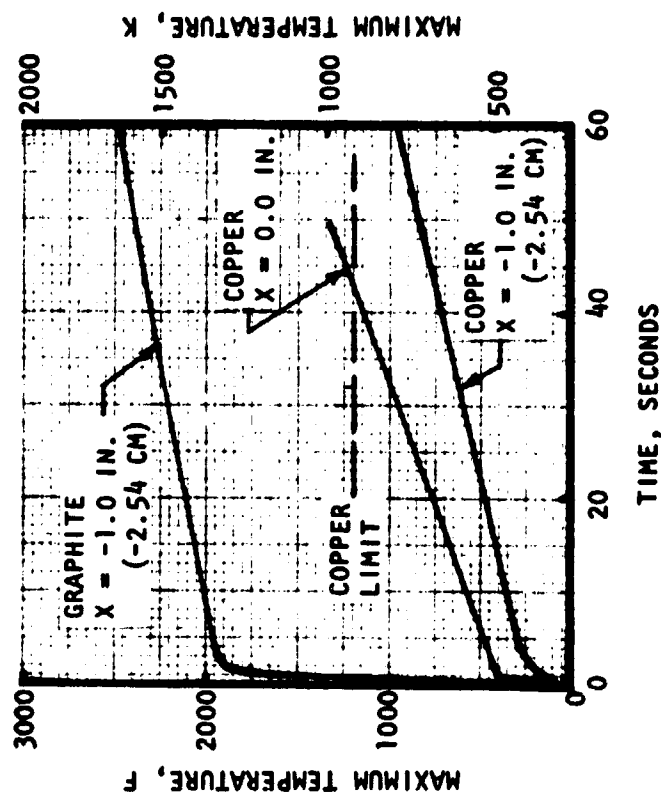
• RESULTS

- TEST DURATION

- ~42 SECONDS

- DURATION LIMITED BY COPPER AT

- $X = 0.0$ IN. (THROAT)



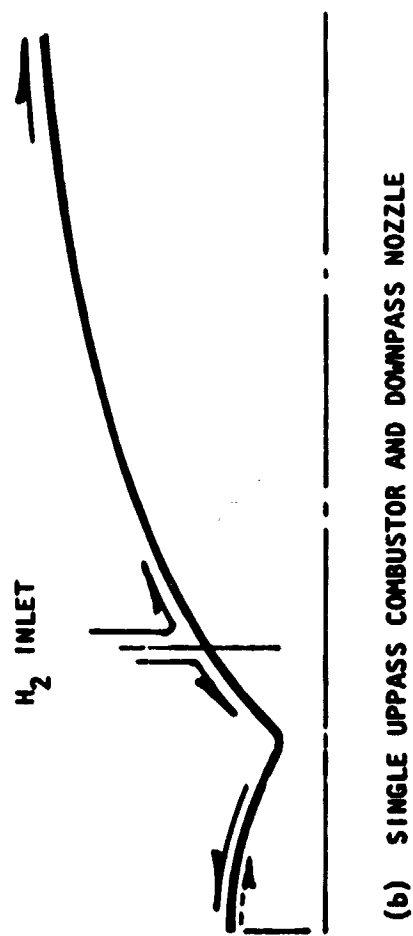
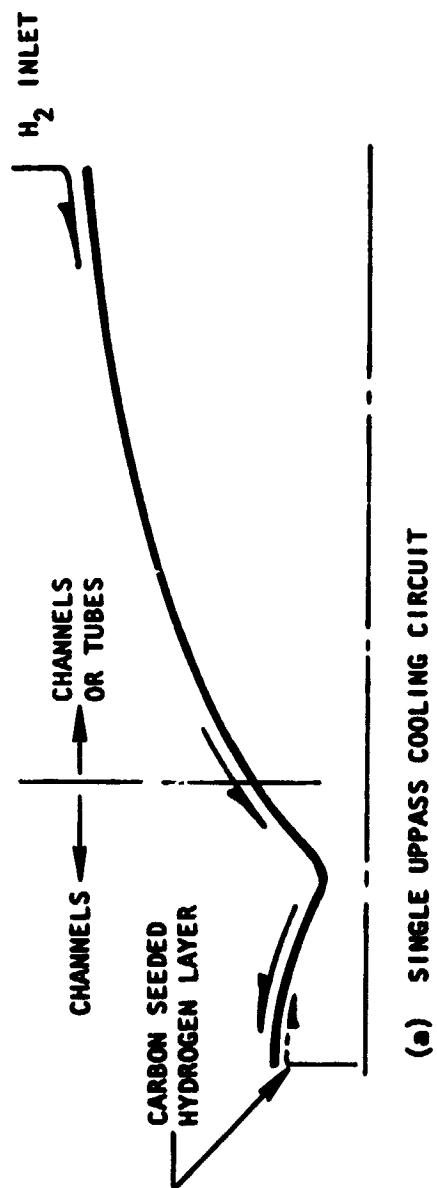


Figure 70. Chamber/Nozzle Cooling Circuits

Preliminary analysis of tube versus channels for the supersonic portion of the thruster (nozzle) from an area ratio of 10 to that of 40 revealed that for comparable wall temperatures the tubular design resulted in a factor of 15 to 20 in weight savings. Therefore, due to this obvious weight advantage, a tubular nozzle configuration was selected.

In the evaluation of the coolant circuit, the high coolant bulk temperature rise which primarily occurs in the plasma containing region of the chamber ($X=0$ to $X=-3$ cm or $X=0$ to $X=-1.18$ in.), reduced combustor coolant flow of the split-flow coolant circuit resulted in higher wall temperatures than the single uppass coolant circuit. Therefore, the single uppass circuit was selected.

An evaluation of how much of the plasma radiation heat flux the regenerative cooling could satisfactorily handle was performed. The results indicated that 20 percent of radiation heat flux could not be handled by the available coolant flow but 10 percent was allowable which was approximately 654 watts/cm^2 ($4 \text{ Btu/in.}^2 \text{ sec}$). Therefore, the combined (convective plus radiation) maximum heat flux was 1153 watts/cm^2 ($7.05 \text{ Btu/in.}^2 \text{ sec}$). As previously discussed, the carbon seeded hydrogen is capable of absorbing 95 percent of the plasma radiation provided certain conditions are satisfied.

The parametric results of the 5000-kw chamber nozzle cooling analysis are shown in Fig. 71. As the number of tubes (round configuration) was increased, the maximum tube gas-side wall temperature and the minimum tube inside diameter decreased. Since a large number of tubes increases fabrication cost, a design with 80 tubes was selected which resulted in a satisfactory 540 K (890 F) maximum wall temperature. The tube dimensions of the selected design are presented in Fig. 72 and resulting tube wall temperature distribution is shown in Fig. 73.

In the design of the Zr-Cu channel wall combustor capable of cooling the convective heat flux plus 10 percent of the radiation heat flux, the following guidelines were used:

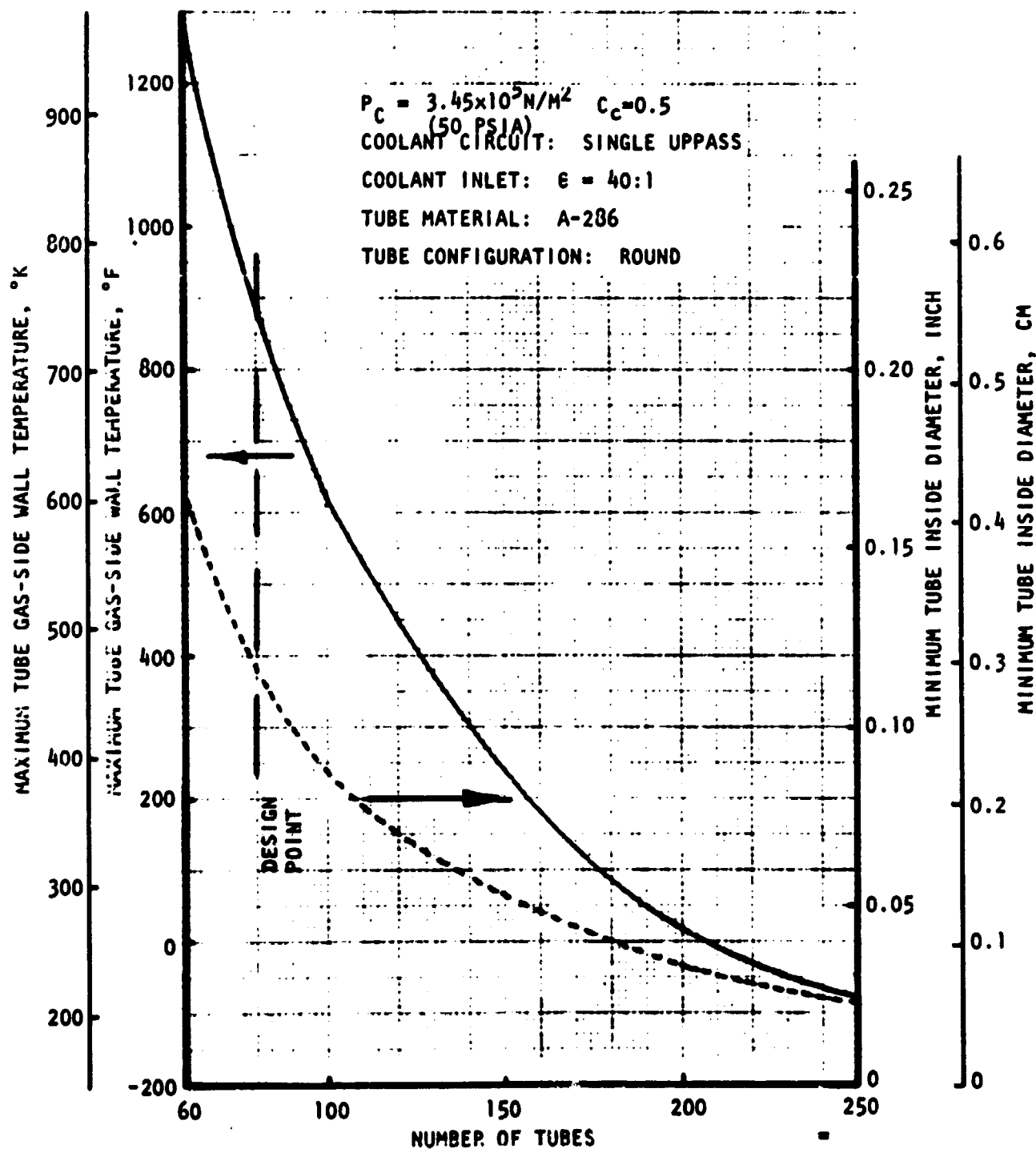


Figure 71. 5000 KW Chamber Nozzle Maximum Tube Gas-Side Wall Temperature and Minimum Tube Diameter Parametric Data

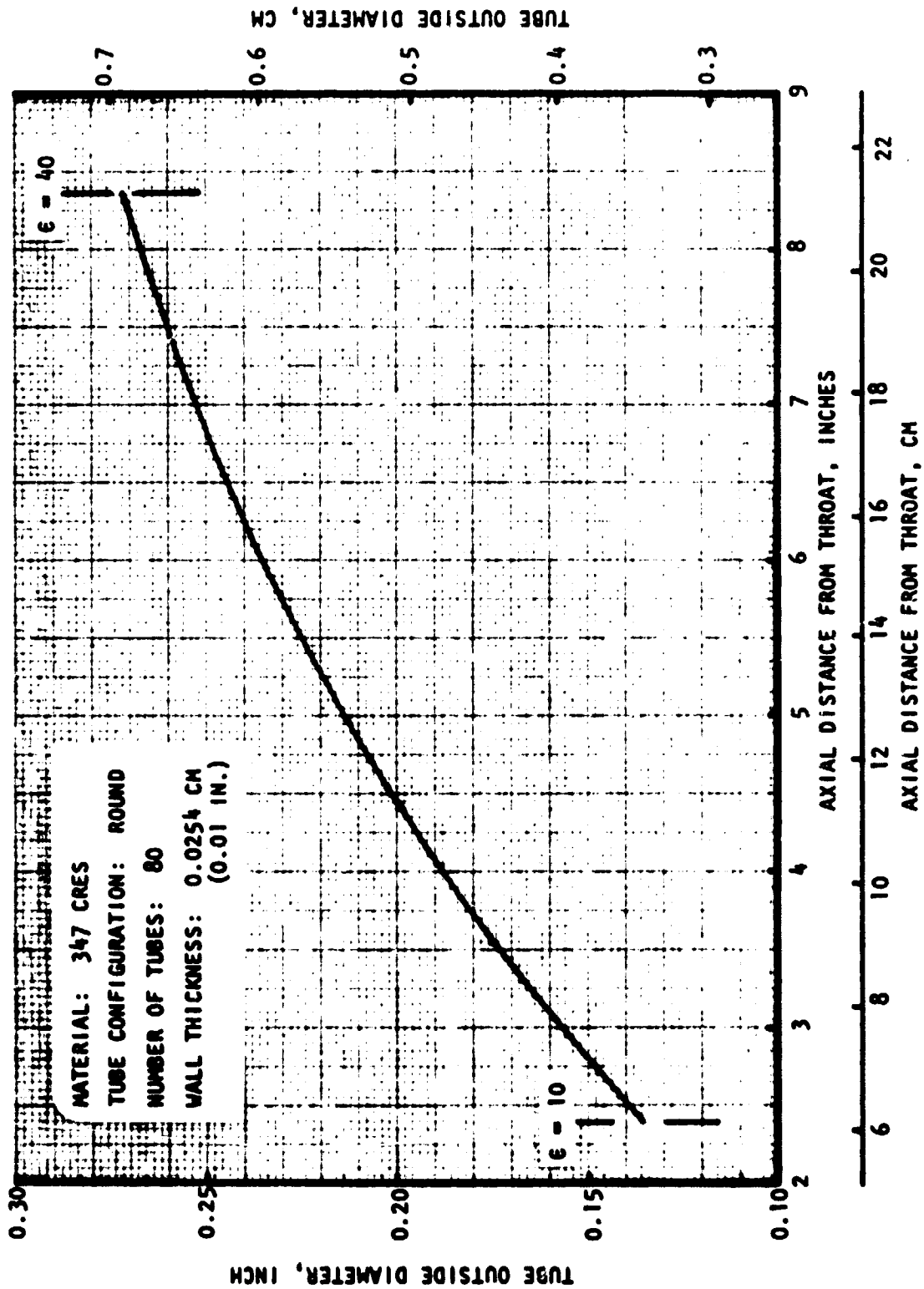


Figure 72. 5000 KV Chamber Nozzle Tube Dimensions

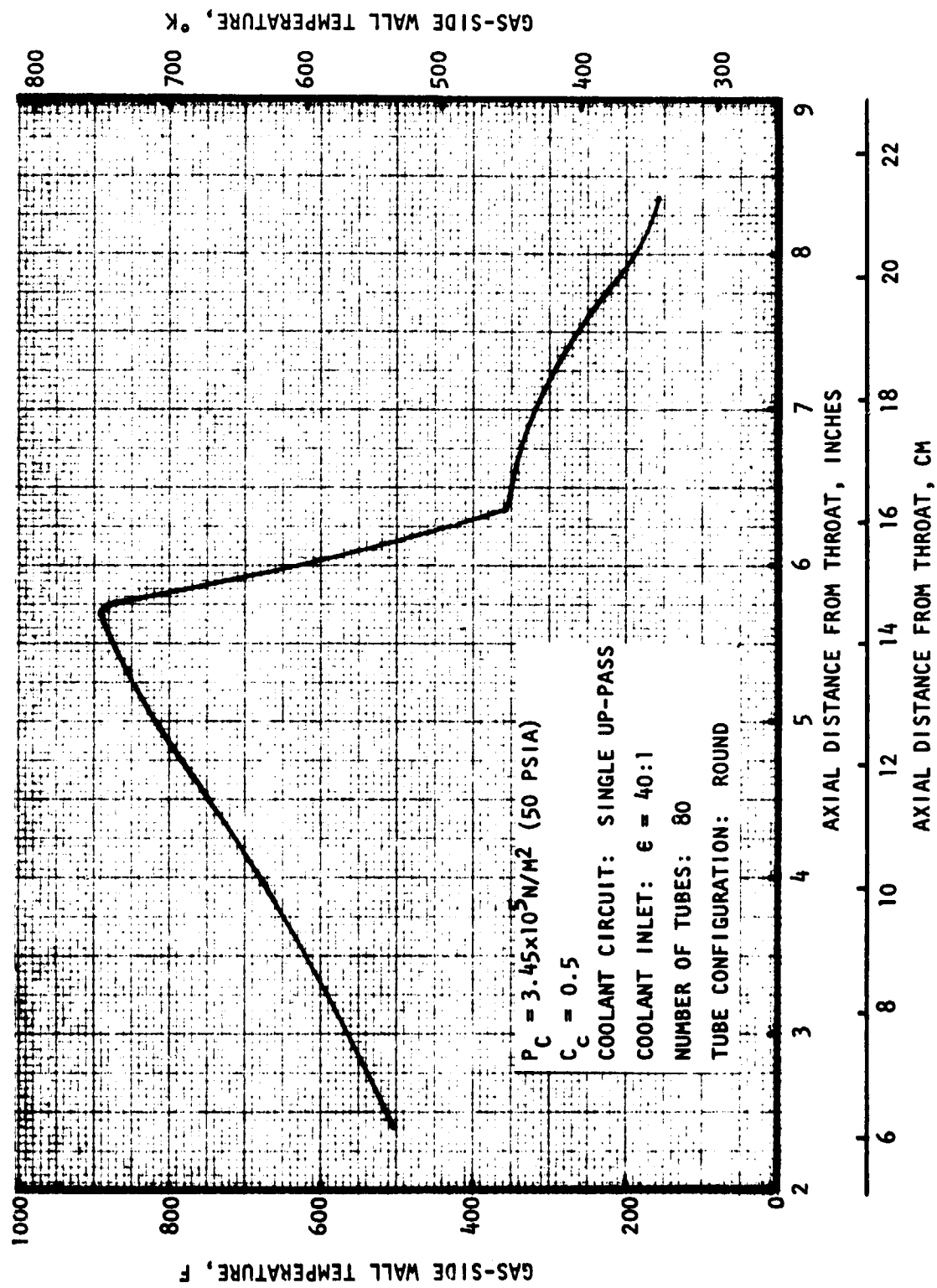


Figure 73 5000 KW Chamber Tube Gas-Side Wall Temperatures

1. Minimum Wall Thickness = 0.076 cm (0.03 in.)
2. Minimum Channel Width = 0.076 cm (0.03 in.)
3. Maximum Channel Depth-to-Width Ratio

The coolant channel design for the 5000-kw chamber is presented in Fig. 74. A bi-width channel design (0.154 cm and 0.076 cm, or 0.06 in. and 0.03 in.) was utilized to minimize coolant pressure drop. This coolant circuit resulted in a $1.86 \times 10^5 \text{ N/M}^2$ (27 psi) coolant pressure drop and a maximum gas-side wall temperature of 874 K (1114 F). The axial distribution of wall temperature, backwall temperature, and the coolant bulk temperature is shown in Fig. 75. A coolant inlet pressure of $1.241 \times 10^6 \text{ N/M}^2$ (180 psi) was necessary to provide cooling without choked flow. A maximum coolant Mach number of 0.542 was obtained as illustrated in Fig. 76.

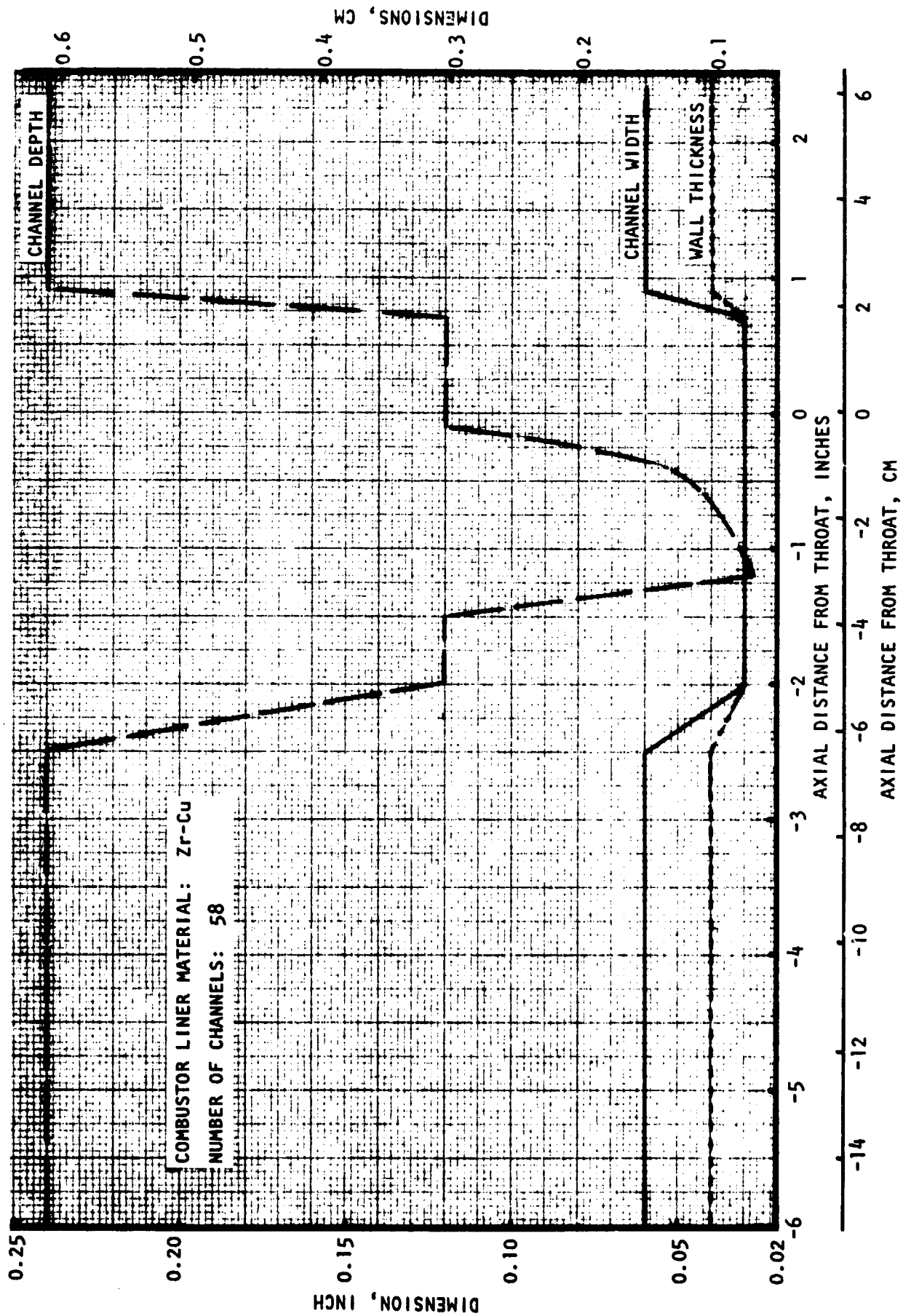


Figure 74. 5000 KW Chamber Combustor Channel Dimensions

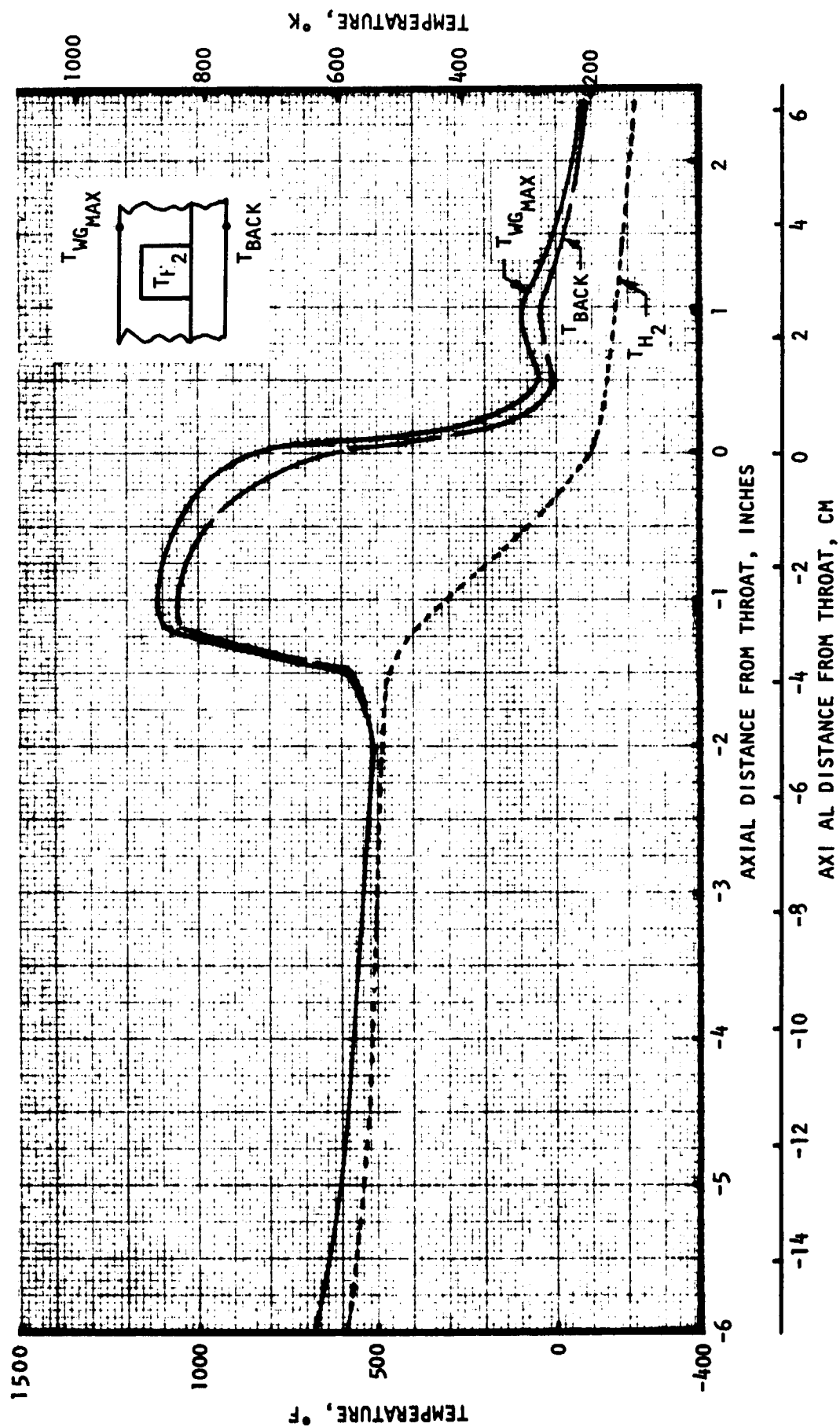


Figure 75. 5000 KW Chamber Combustor Wall Temperature Distribution

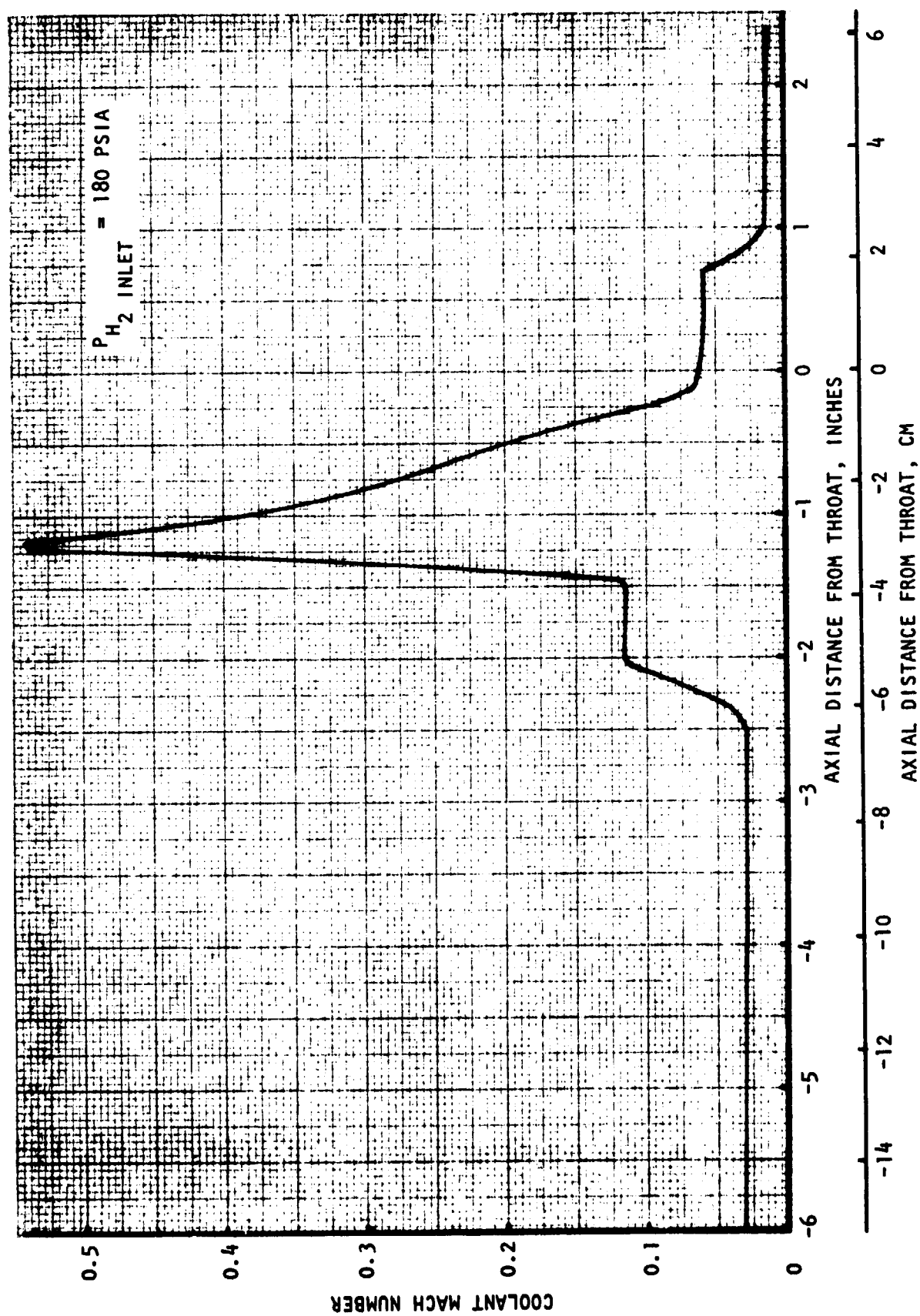


Figure 76. 5000 KW Chamber Combustor Coolant Mach Number Distribution

CONCEPTUAL DESIGN AND SCALING

Plasma

From the plasma core flow analysis performed by Physical Sciences Inc. (Ref. 1), the plasma core dimensions for a given laser intensity can be approximately scaled with laser power using the relationship:

$$\begin{aligned} \text{Plasma Cross-sectional Area, } A &\propto \text{Power, } \underline{P} \\ &\text{or that} \\ \text{Plasma Diameter, } D &\propto \sqrt{\underline{P}} \end{aligned}$$

This relationship was used in scaling the plasma core dimensions of the 10-kw configuration to obtain those for the 5000-kw configuration.

The radiation loss from the plasma is an important parameter that is not scalable. For the 10-kw thruster, the loss is primarily at the ultra-violet wavelength. However, the plasma radiation loss for the 5000-kw thruster would be at the ultra-violet and infrared wavelengths. Therefore, although the plasma formation mechanisms may be scaled with input laser power, the plasma radiation loss can not be scaled.

Flow Analysis

The relationships developed for the propellant flowrate and chamber throat radius (not including the boundary layer influence) result in the following scaling relationships with laser power level,

$$\begin{aligned} \dot{w}_{\text{total}} &\propto \underline{P} \quad (\text{for constant specific impulse}) \\ \text{and} \quad R_T &\propto \sqrt{\underline{P}} \end{aligned}$$

However, the chamber pressure, the amount of carbon seed, and the combustion gas temperature will also influence these parameters and must be considered in determining the flowrate and throat radius.

Performance

A comparison of the performance losses of the 10-kw and 5000-kw configurations (Table 3 and 4) reveal some scaling trends. The major influence of the large size difference between these two chambers is the decrease in boundary layer efficiency for the 10-kw thruster. The reaction kinetic efficiency would decrease with decrease in chamber size (thrust) for a fixed area ratio. However, the kinetic efficiency for the 10-kw thruster is higher than that of the 5000-kw thruster due to the lower area ratio.

Optical Train

Company-funded studies of beam propagation relating to the laser-heated rocket indicated that an initially annular beam will not remain annular in the "far field." Therefore, for space applications such as the 5000-kw configuration, the optical train configuration of the 10-kw configuration (an on-axis cassegrain used as a pointer) cannot be directly used since the beam is no longer annular. As described in the Optical Train Section, the concepts evaluated the solid beam as well as means of forming an annular beam after it was received.

OPTICAL TRAIN ANALYSIS

The laser-heated rocket thruster as configured requires a focused laser beam. The optical train is to receive the incoming laser beam and propagate the beam through a series of mirrors and/or lenses with minimum power loss and beam distortion to the thruster at the required focus angle. The laser beam enters the thruster through a solid, transparent window and focused to a spot size sufficient to generate the intensity required to sustain a plasma within the hydrogen propellant gas.

The basic analysis for the optical train configurations (i.e., specifying required components; mirror design, type, cooling, mount, window/lens configuration) was made available from a company-funded optical systems study task.

10-kw Experimental Optical Train

10-kw Laser Beam Characteristics. The following CO₂ laser mirror arrangement was assumed to determine the laser output beam characteristics.

Cavity length: 209 cm (82.28 in.)

Mirror radius of curvature:

Concave mirror: 12 m (39.372 ft.)

Convex mirror: 8 m (26.248 ft.)

Scraper distance from convex mirror: 13 cm (5.118 in.)

Laser beam diameter: 5 cm (1.969 in.)

Hole diameter: 3.3 cm (1.299 in.)

Magnification: 1.523

Equivalent Fresnel Number: 3.18

Tube Fresnel Number: 28.2

The above configuration (Fig.77) essentially represents one of the NASA-LeRC configurations. Also the laser beam output was assumed to be 7.62 meters (25 feet) from the thruster.

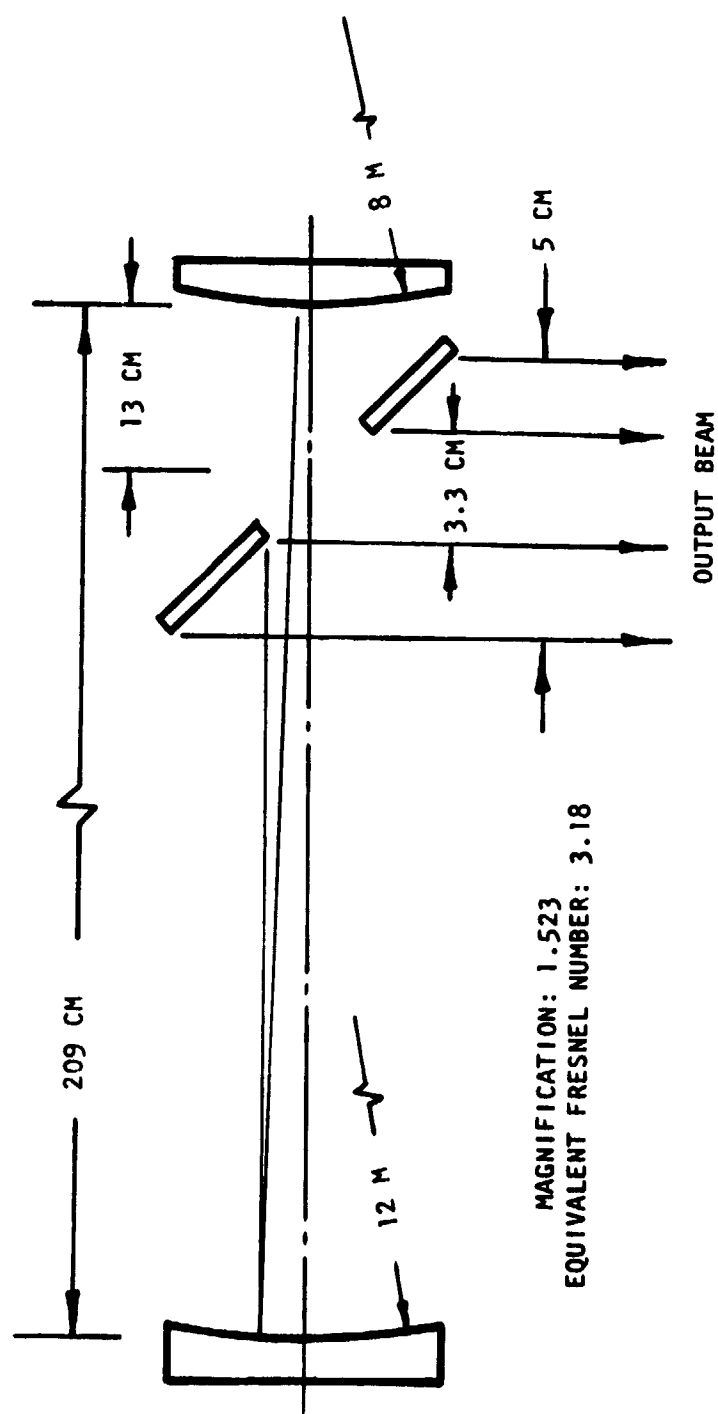


Figure 77. 10 KW CO₂ Laser Configuration

The laser beam characteristics were determined using the wave XX computer program. This program computes modes of an unstable confocal resonator by a wave launching technique. The integrals required are determined using an average kernel technique. Using the above unstable resonator mirror configuration, a 40 X 40 grid analysis of the "far-field" was performed and then a finer 80 X 80 grid analysis was attempted. The analysis indicated a mode control problem at this low magnification of 1.523. Available computer codes could not propagate a laser beam with multiple modes. A minimum magnification of 2.0 is desirable to obtain a single transverse mode. High beam quality is difficult, if not impossible, to achieve with a multi-mode output beam. Two approaches to analyze the optical train were taken:

1. Design an optical train for the 1.523 magnification.
2. Design an optical train for a magnification of 2 and define a set of mirrors for the unstable resonator to give this magnification.

This latter optical train design would accommodate both magnification configurations. Since the beam output characteristics of the 1.523 magnification configuration cannot be defined analytically, the magnification 2 output beam was analyzed to establish the beam quality. It was recommended that the laser output beam have a magnification of 2 to ensure mode control and minimum blur circle size, and although the 1.523 magnification configuration can be used in the same optical train the beam quality, using the lower magnification particularly at focus, cannot be guaranteed. In part, the intensity may be lower than that required to sustain the plasma.

The unstable resonator mirror configuration with a magnification of 2.0 shown in Fig. 78, was assumed. The cavity length and the scraper distance from the convex mirror were the same as those for the configuration having the lower magnification. The CO₂ laser beam output intensity and phase angle distribution for the configuration having a magnification of 2.0 are shown in Fig. 79 and 80.

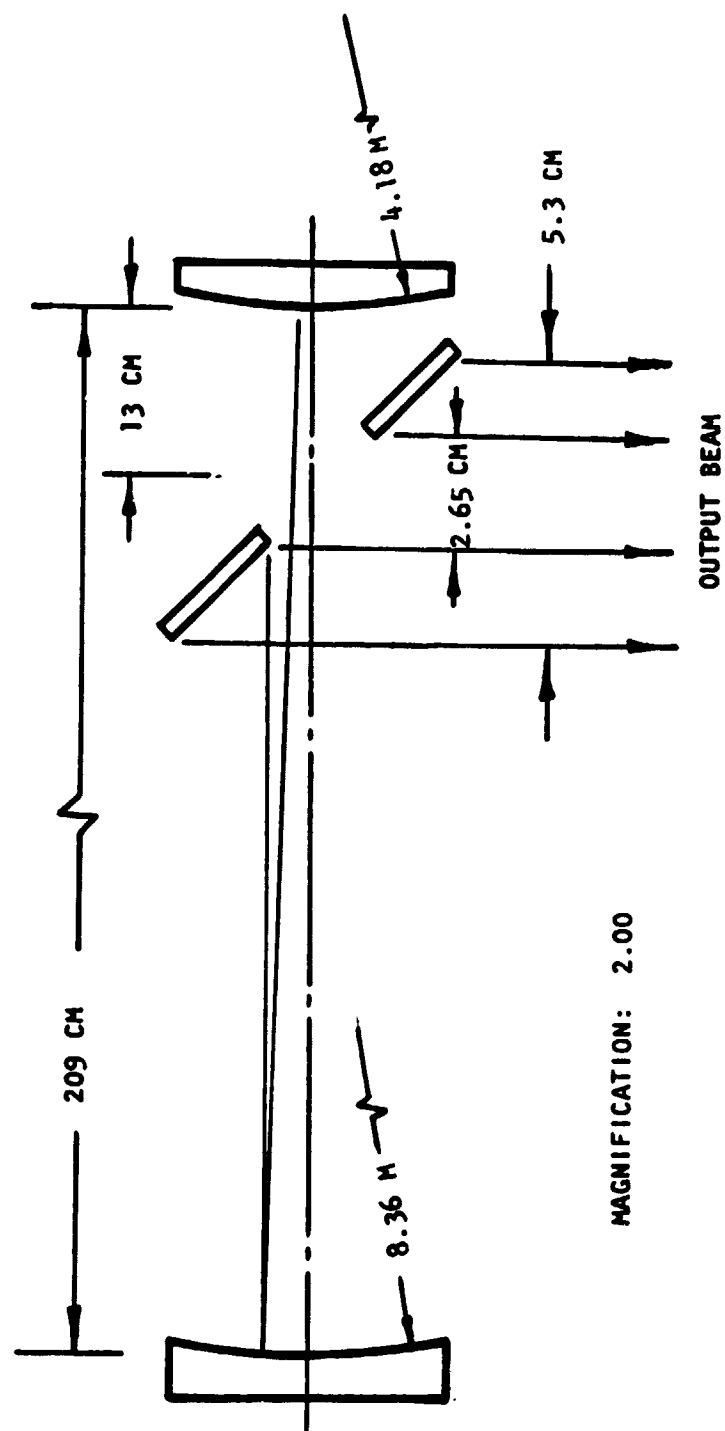


Figure 78. 10 KW CO₂ Laser Configuration (Magnification = 2.0)

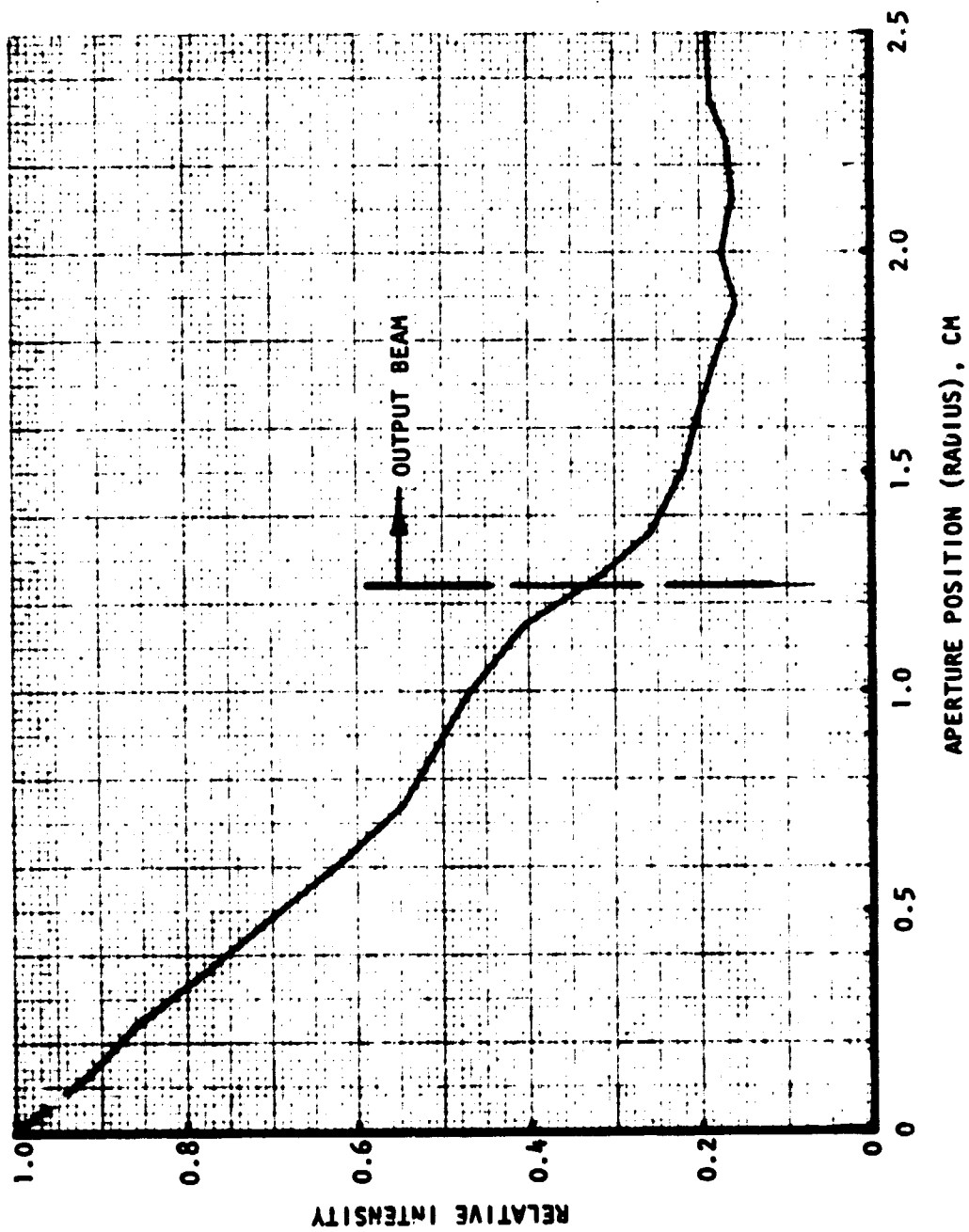


Figure 79. 10 KW CO₂ Laser Relative Intensity Distribution (Output Beam
Magnification = 2.0)

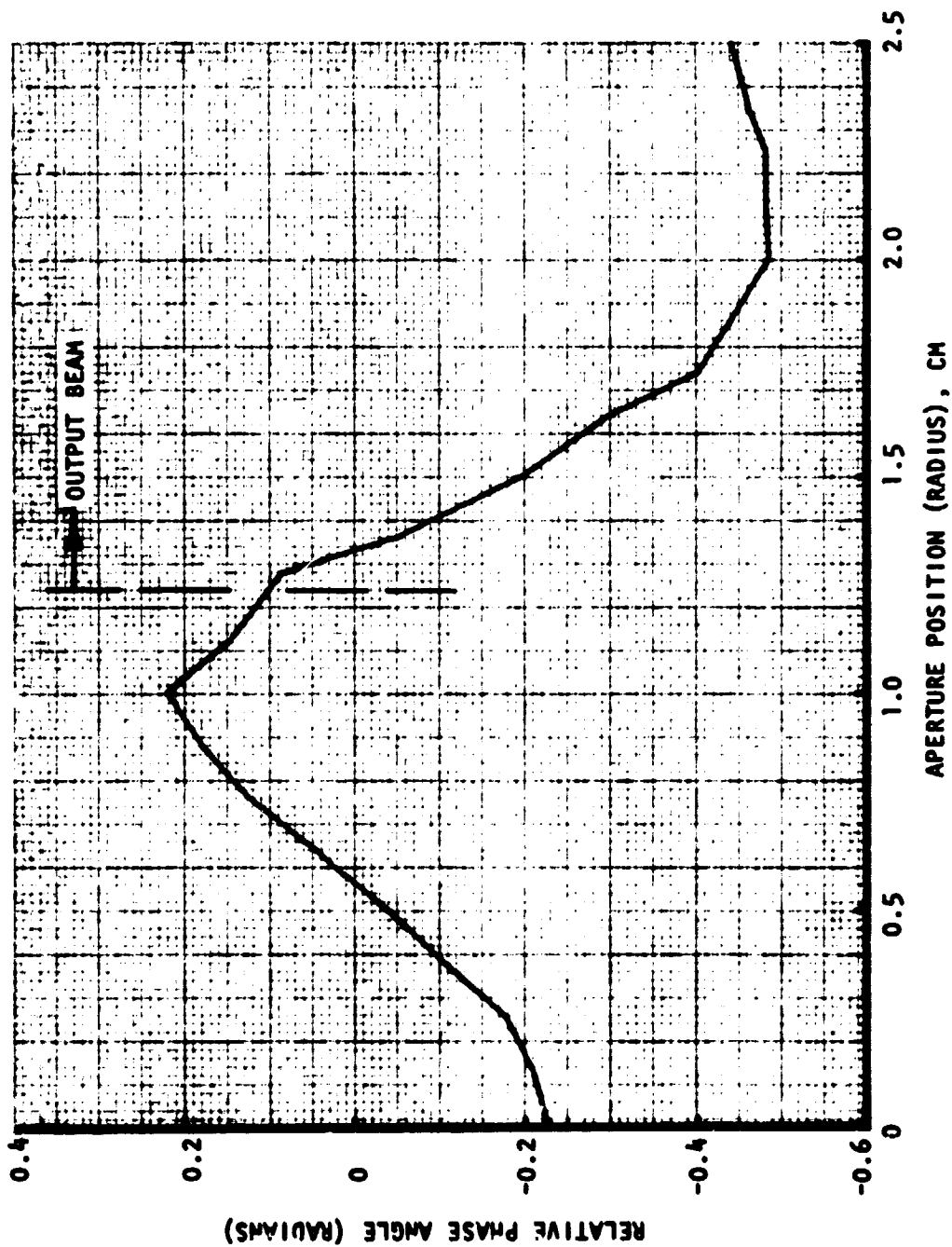


Figure 80. 10 KW CO₂ Laser Relative Phase Angle Distribution (Output Beam Magnification = 2.0)

10-kw Optical Train Configuration. As shown in Fig. 81, several optical train concepts were evaluated which included:

1. Off-axis parabola
2. On-axis cassegrain used as a telescope
3. On-axis cassegrain used as a pointer
4. Scraper/spherical concept

Due to the problem of clearance of the flat mirror and the thruster, the off-axis parabola concept required a 45-degree off-axis parabola which is not readily available especially for high power applications. The telescope cassegrain and the Scraper/spherical concept required that the thrust chamber be located within the optical train. Therefore, the optical train concept selected for the 10-kw chamber was the pointer cassegrain. This concept, as shown in Fig. 81, utilizes a flat mirror and two spherical mirrors and tends to dampen any output beam tilt.

The configuration for the 1.523 magnification output beam is presented in Fig. 82. Since both mirrors are spheres and since the optical system is to be used for on-axis object points at infinity (collimated input, parallel to the optical axis) the only aberration that need be considered is spherical aberration assuming single transverse mode operation. Therefore, a number of runs were made with a geometrical optics computer code that predicts the spherical aberration blur circle size at focus of a cassegrain system that has spherical mirrors. The code predicts spherical aberration blur circle sizes as a function of initial ray height, initial ray slope, mirror separation, $f/\#$ of the secondary, and the radii of curvature of the mirrors. It was initially hoped that a very fast secondary mirror would give a small blur circle. This would allow for a very compact system. It turned out, however, that the system had a blur circle size that was very sensitive to the $f/\#$ of the secondary (i.e., an $f/1$ secondary yielded blur circle diameter of 200μ

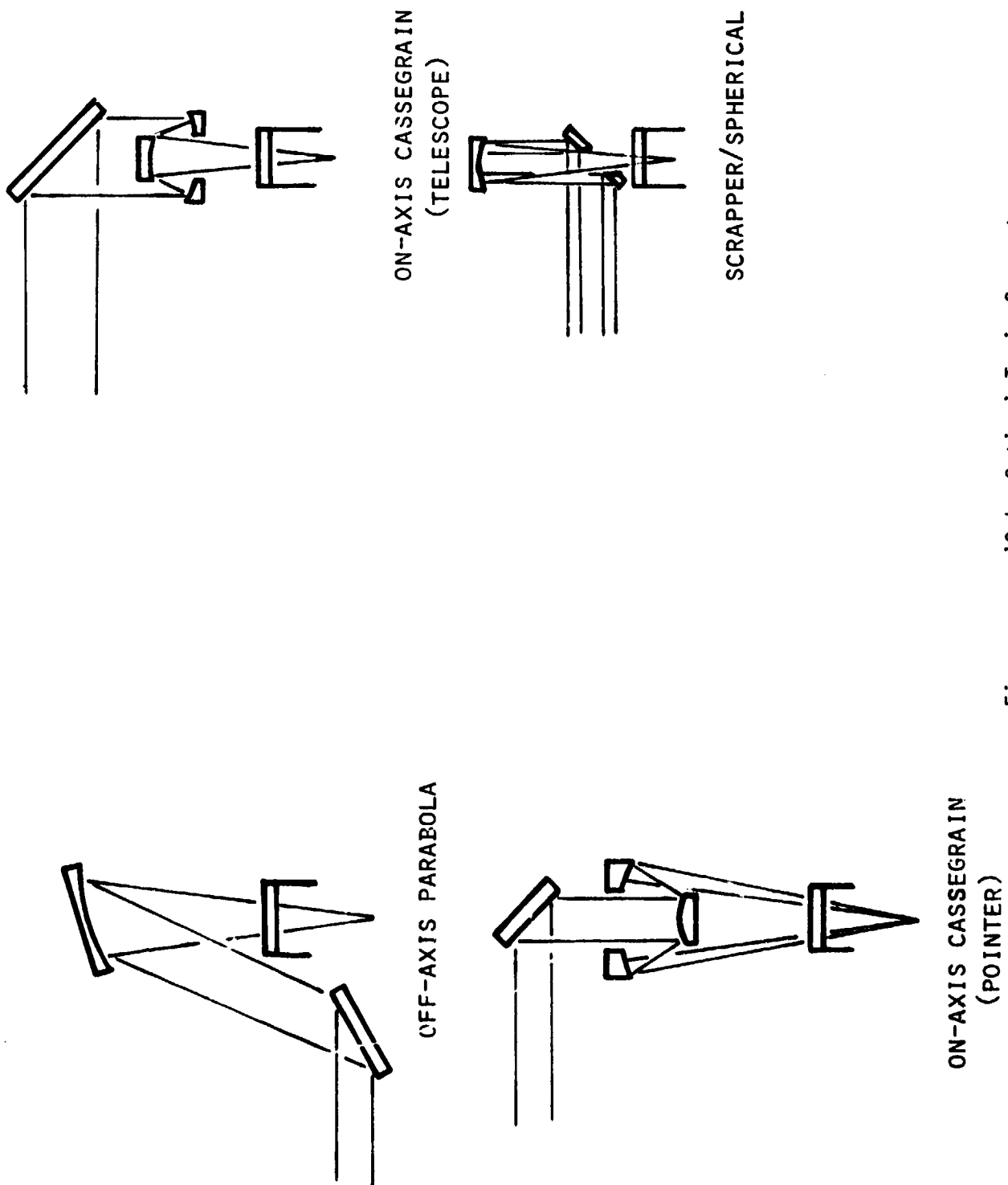
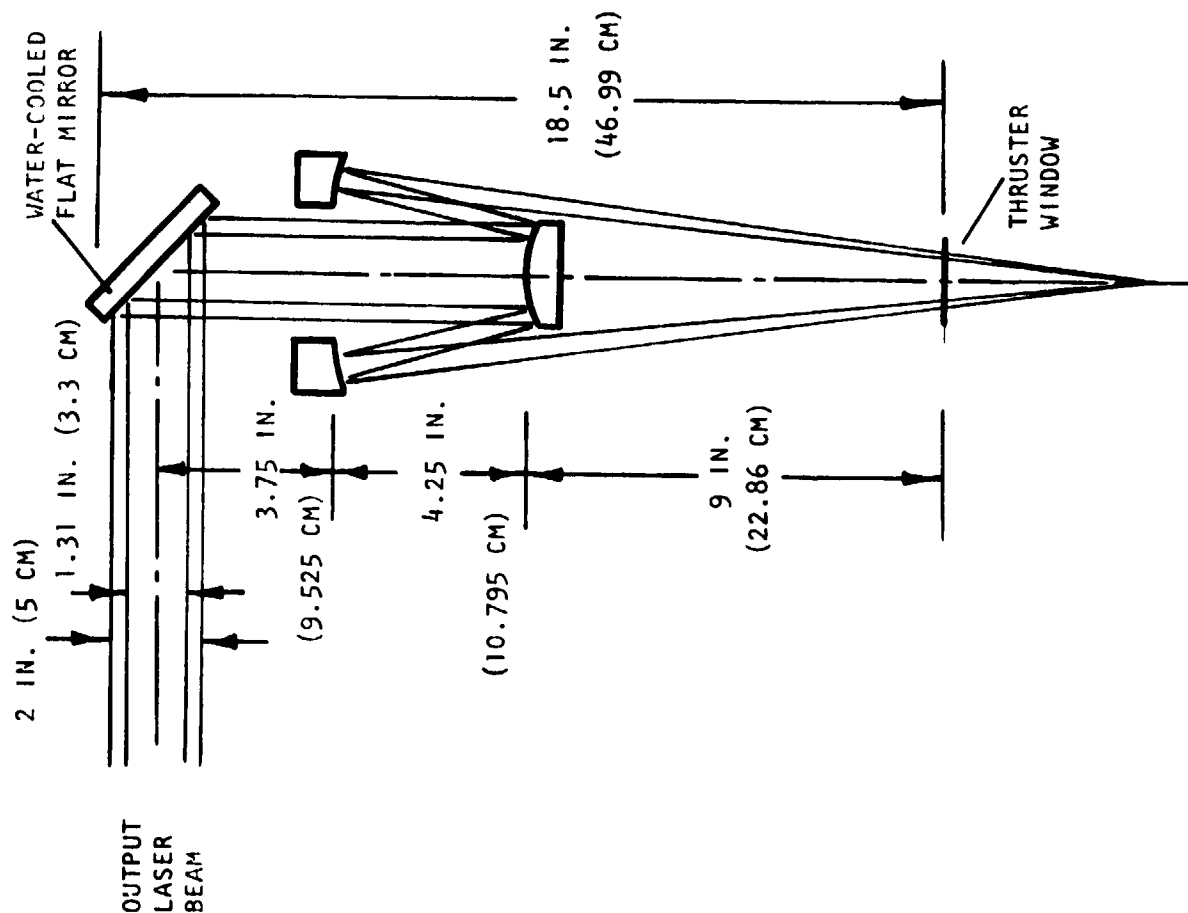


Figure 8]. 10-kw Optical Train Concepts



PRIMARY:

DIAMETER: 5 IN. (12.7 CM)
 RADIUS OF CURVATURE: 10.21 IN. ± 0.001 IN.
 (25.93 CM ± 0.0025 CM)

SECONDARY:

DIAMETER: 2 IN. (5 CM)
 RADIUS OF CURVATURE: 6.0 IN. ± 0.001 IN.
 (15.24 CM ± 0.0025 CM)

f NUMBER: 1.5

SPHERICITY: $\lambda/20$ PEAK-TO-PEAK AT 0.6μ

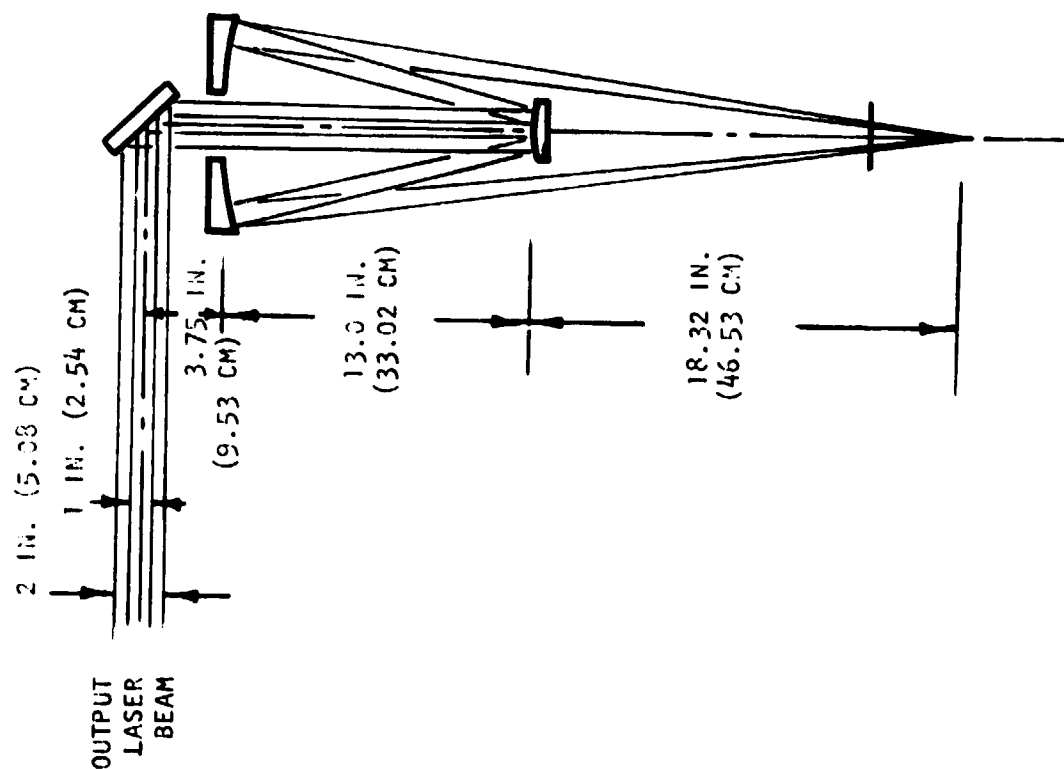
SPHERICAL ABERRATION
 BLUR CIRCLE SIZE: 51.5μ

Figure 82. 10-kw Experimental Hardware Optical Train (Laser Beam Output Magnification=1.523)

when an $f/2$ secondary yielded one of diameter of 40μ). Therefore, an $f/1.5$ secondary was used (blur circle of $51-55\mu$) and the system is shown in Fig. 83. The blur circle will be somewhat smaller than predicted, for the following reason: Blur circles due to spherical aberration compare the focusing properties of a meridional ray near the edge of the system aperture to a para-axial ray, which is close to the system's optical axis. In this case, however, the input beam has a rather large hole in it and, therefore, there are no rays near the optical axis. Therefore, the spherical aberration will be reduced because there essentially are no para-axial rays.

Using the on-axis cassegrain concept used for the output beam with 1.523 magnification, an optical train was also designed for the magnification of 2.0. As shown in Fig. 83, the on-axis spherical mirrors are larger and the distance between them is larger than for the configuration for the lower magnification. However, the configuration still lends itself to efficient and compact packaging. A schematic of the optical train and thrust stand is illustrated in Fig. 84 and 85 for both magnification values. The included laser beam focus angle for both configurations is 15.14 degrees.

10-KW Chamber Laser Beam Receiving Window. A comprehensive thermal model of the 10-kw chamber window was constructed for the use on the Differential Equation Analyzer Program (DEAP). The two-dimensional thermal model was a lumped parameter representation of the physical window consisting of 60 nodes, and capable of both transient and steady-state analyses. Each lump or node is connected to its adjacent nodes by the appropriate conduction, convection or radiation type of connector which is representative of the heat transfer nodes between the two locations on the physical model. Heat absorption arising from the penetration of a laser beam through the window is represented by heat sources at appropriate nodes. Window back face surface nodes are connected to a single sink node representing the flowing hydrogen coolant.



PRIMARY:

DIAMETER: 9 IN. (22.86 CM)

RADIUS OF CURVATURE: 22.04 IN. ± 0.001 IN. (55.98 CM ± 0.0025 CM)

SECONDARY:

DIAMETER: 2.5 IN. (6.35 CM)

RADIUS OF CURVATURE: 8.0 IN. ± 0.001 IN. (20.32 CM ± 0.0025 CM)

f NUMBER: 2

SPHERICITY: $\lambda/20$ PEAK-TO-PEAK AT 0.6 μ

SPHERICAL ABERRATION BLUR CIRCLE SIZE: 54 μ

Figure 83. 10 kW Experimental Hardware Optical Train (Laser Output Beam Magnification = 2.0)

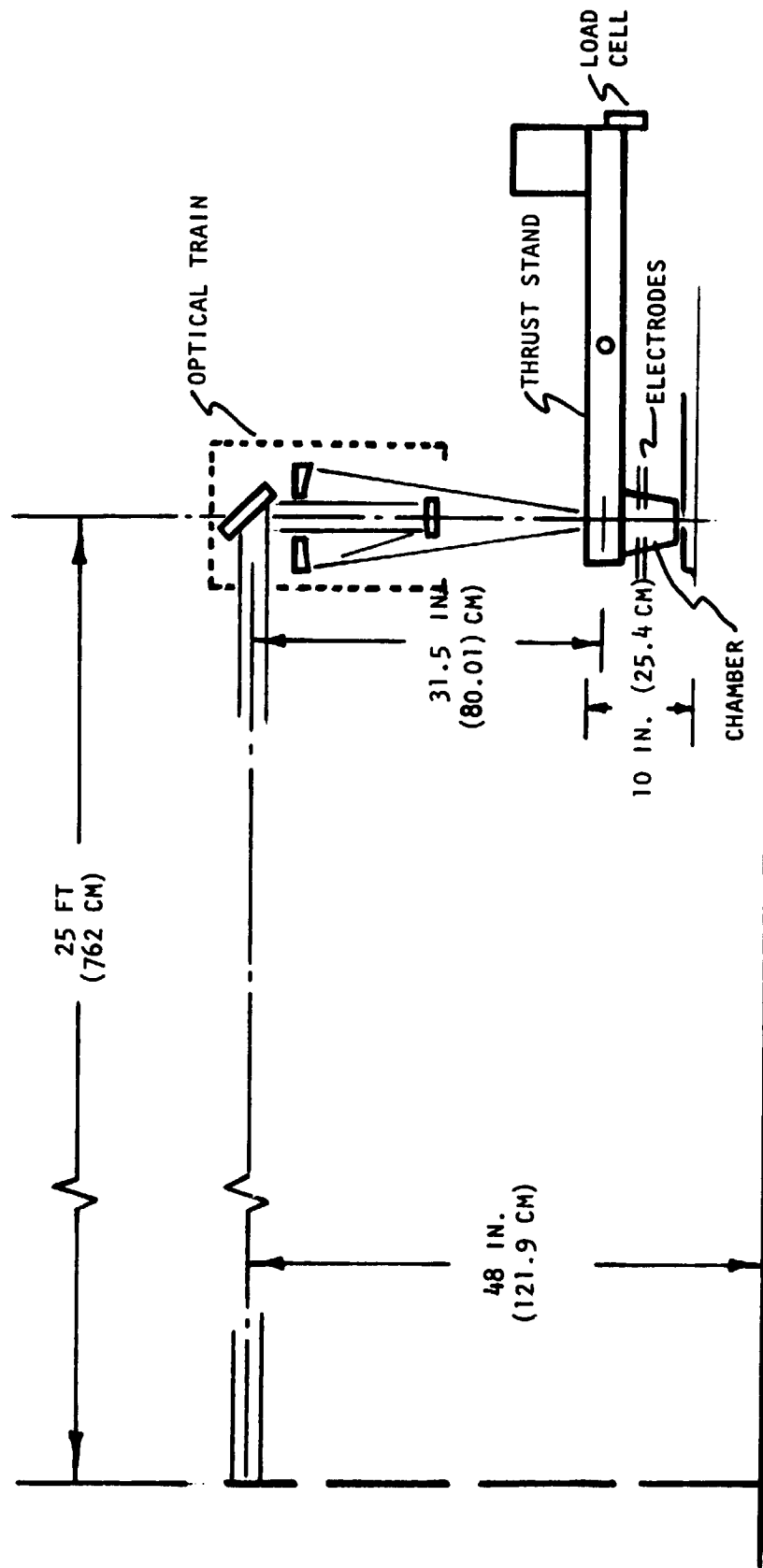


Figure 84. 10 kW Laser-Heated Rocket Thruster Test Apparatus (Laser Output Beam Magnification = 2.0)

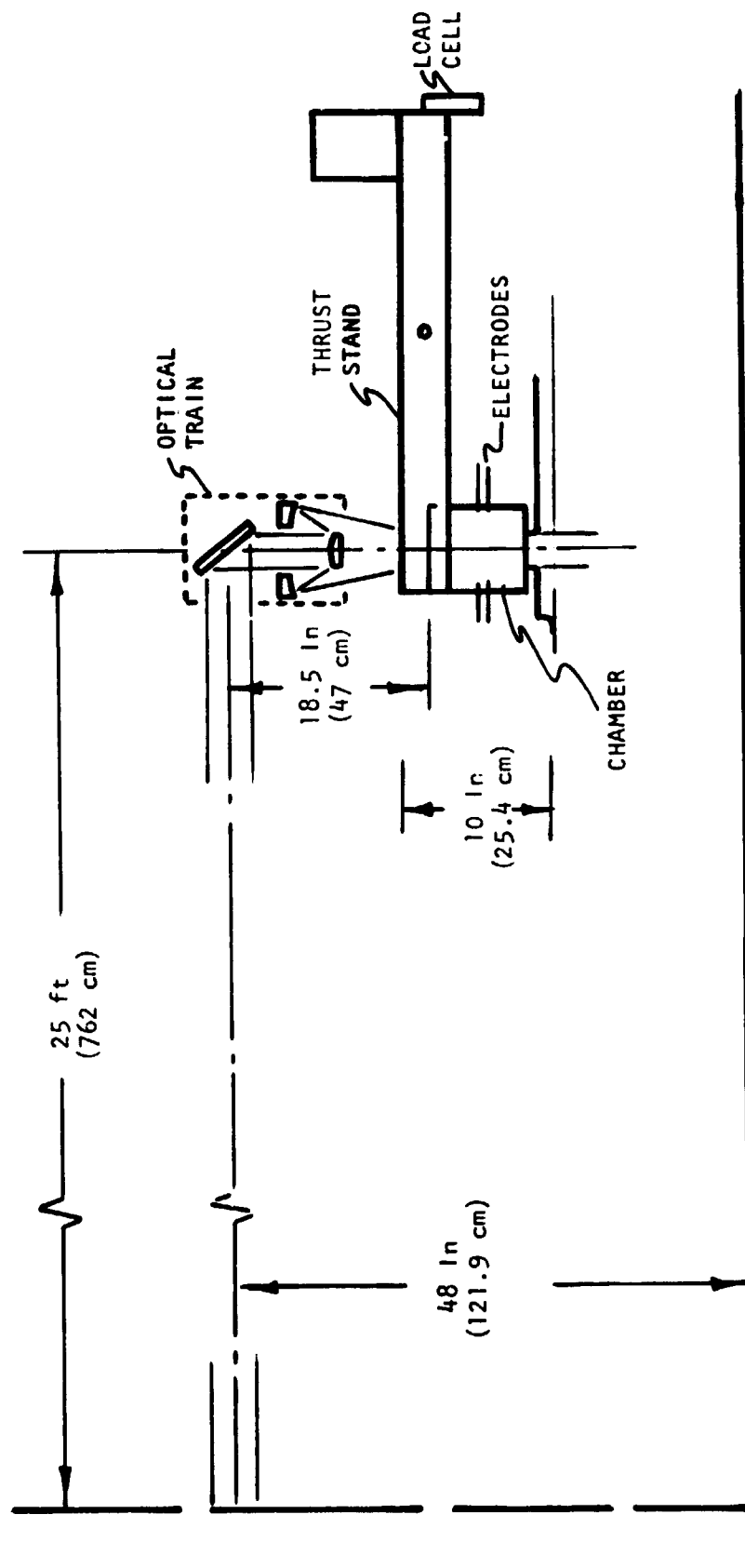


Figure 85 . 10-KW LASER - HEATED ROCKET TEST APPARATUS
(LASER OUTPUT BEAM MAGNIFICATION = 1.523)

The output laser beam (magnification of 2.0) was propagated through the optical train and the laser beam intensity distribution on the window is presented in Fig. 86.

Both zinc sulfide and zinc selenide windows were considered. Zinc selenide has a flatter transmittance versus wave length curve at $10.6\text{ }\mu\text{m}$. Although the transmittance at exactly this wave length are similar, the cost of zinc sulfide is significantly lower than for zinc selenide; however the experience with zinc selenide led to its selection for the 10-kw chamber window material. Physical dimensions of the window were 3.048cm (1.200-inch) diameter and a thickness of 0.6 cm (0.236-inch). An absorption coefficient of 0.0005cm^{-1} (0.00127-inch^{-1}) was used for the zinc selenide (ZnSe).

Using the sixty nodal thermal model described, the temperature distribution of the zinc sulfide or zinc selenide window was determined using window intensity shown in Fig. 86. Cooling of the window by the hydrogen coolant flow on the chamber side and air free convection was included. The resulting axial and radial temperature distributions at 60-seconds and steady-state are shown in Fig. 87 and 88, respectively. A maximum temperature of 159C (319 F) and a maximum axial gradient of 3C (5 F) occurred on-axis.

Beam Propagation. Laser beam propagation through the thruster ZnSe window resulted in the prediction that the focal point in the thruster would move 0.18cm (0.07-inch) toward the window due to the thermal variations in the index of refraction of the ZnSe. The beam was propagated from the thruster window to focus. For the aberrated wave even in the presence of thermal phase distortions resulting from the window, the focal point intensity distribution was not appreciably different from an unaberrated wave. The on-axis intensity was computed to be $2.4 \times 10^8\text{ W/cm}^2$. This intensity is three orders of magnitude greater than the intensity required to sustain the plasma ($3.7 \times 10^5\text{ W/cm}^2$) for this configuration.

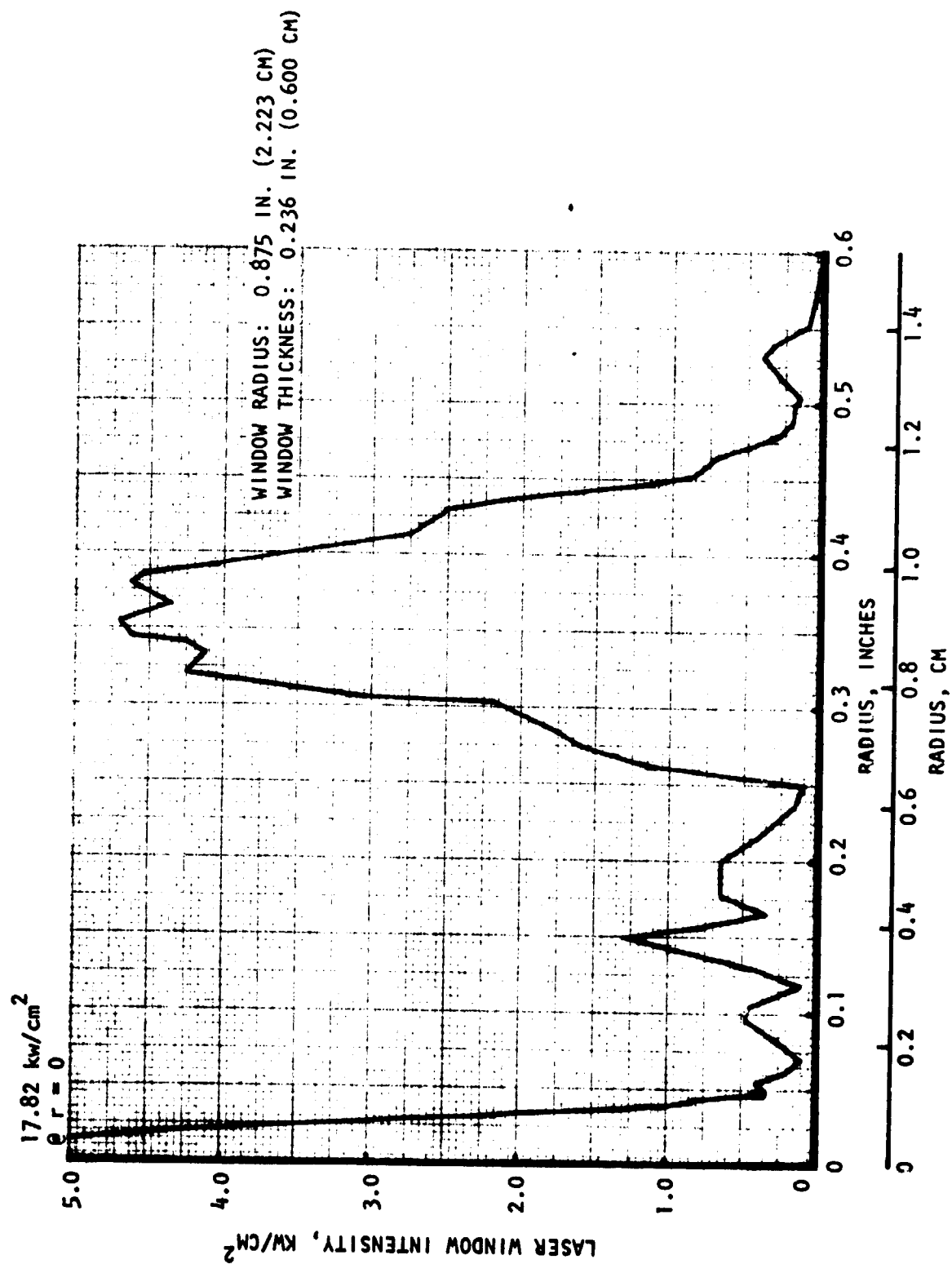


Figure 86. 10 KW Chamber - Laser Window Intensity Distribution

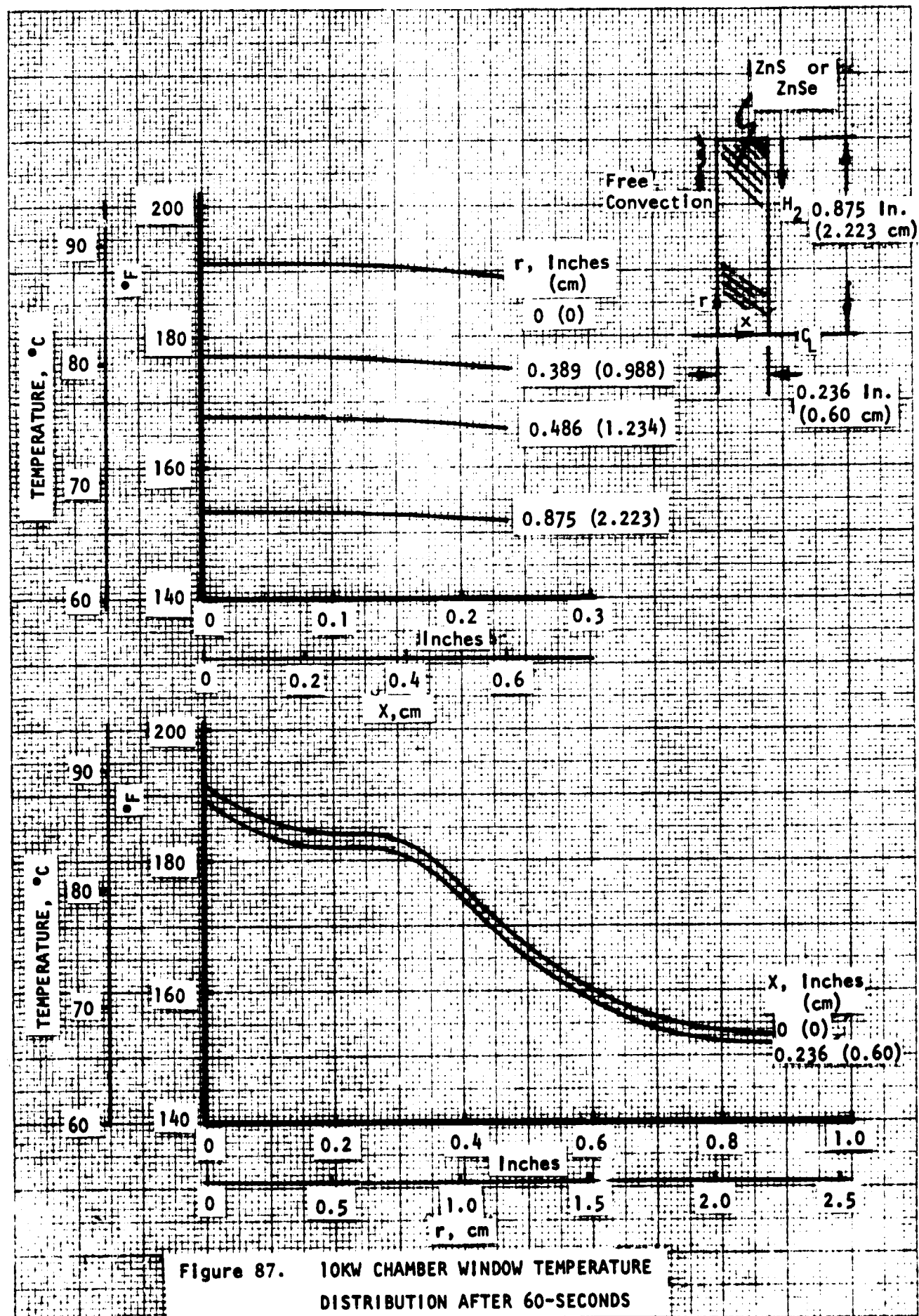


Figure 87. 10KW CHAMBER WINDOW TEMPERATURE DISTRIBUTION AFTER 60-SECONDS

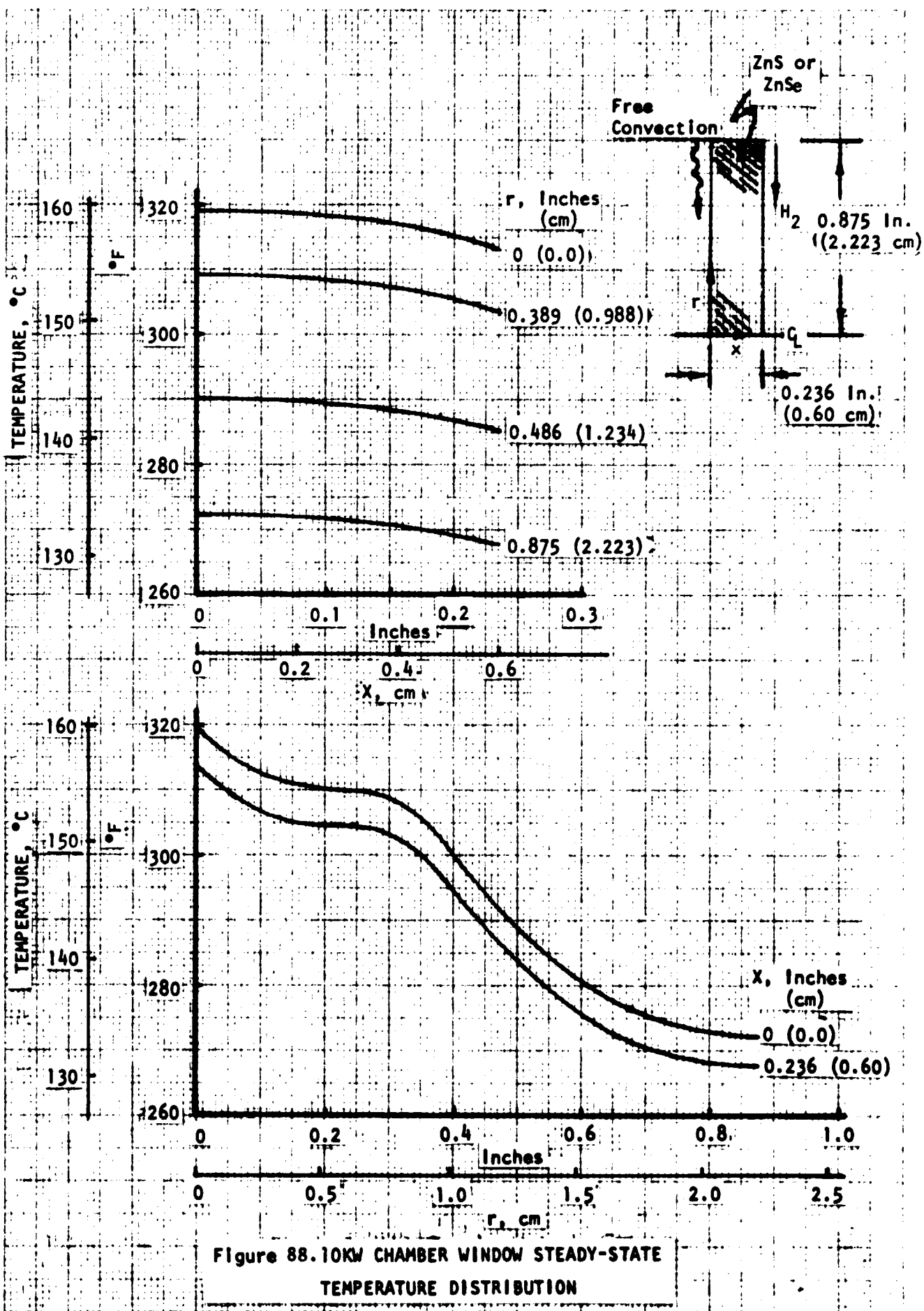


Figure 88.10KW CHAMBER WINDOW STEADY-STATE TEMPERATURE DISTRIBUTION

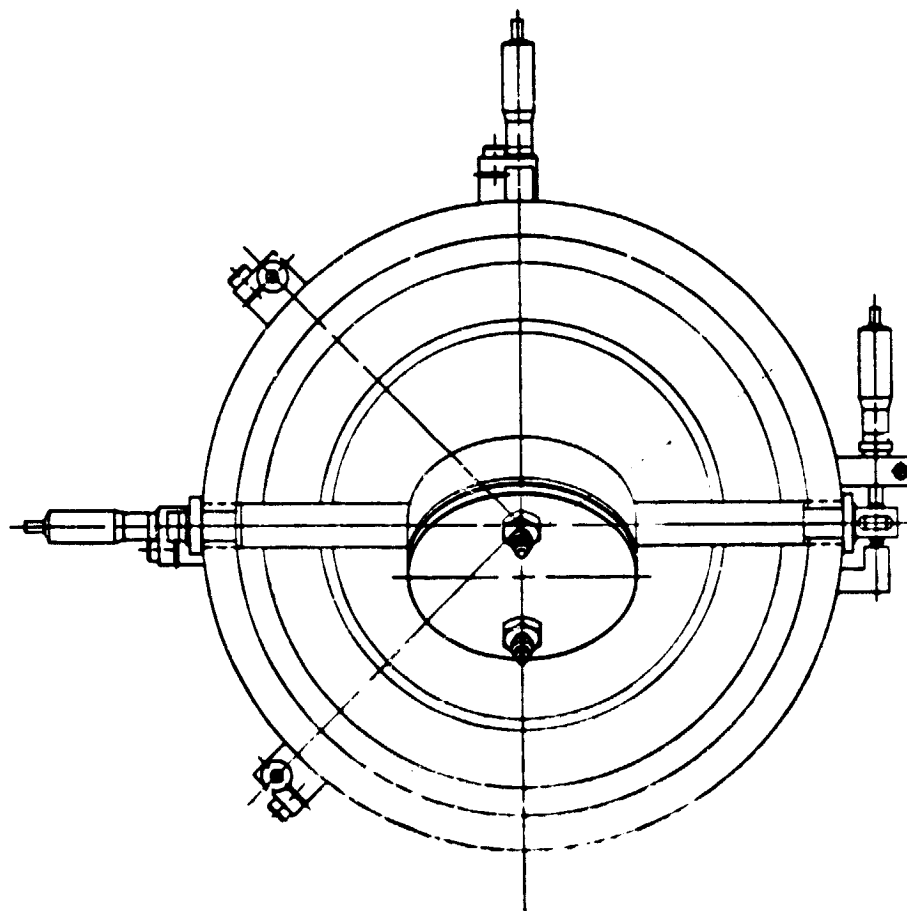
Geometric optic thermal blooming analysis was performed assuming no convective cooling. The analysis indicated that thermal blooming was not a problem.

Optical Train Design. The assembly drawings of the optical trains which are recommended for use with the 10-kw chamber are presented in Fig. 89 and 90. Both configurations are identical in concept and differ only in size. The flat mirror and the secondary mirror are water-cooled and the primary mirror is un-cooled. The three mirrors are essentially contained in the same housing. The micrometer adjustments on the three mirrors allow tilt and the primary and secondary mirror tilt on two axes and a horizontal translation adjustment is provided on the secondary mirror. The optical train for the laser output beam magnification of 2.0 is shown in Fig. 89. The one for a 1.523 magnification is shown in Fig. 90. The detail design drawing package composing of twenty drawings was prepared and was sent to the NASA-LeRC Project Manager.

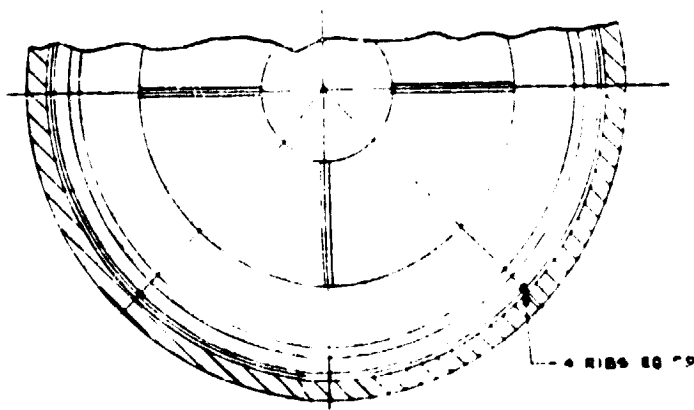
5000KW Optical Train

Beam propagation analyses indicated that an initially annular beam will not remain annular in the "far field." Therefore, for space applications such as the 5000-kw configuration, the optical train configuration of the 10-kw configuration (an on-axis cassegrain used as a pointer) cannot be directly used since a hole no longer exists in the beam.

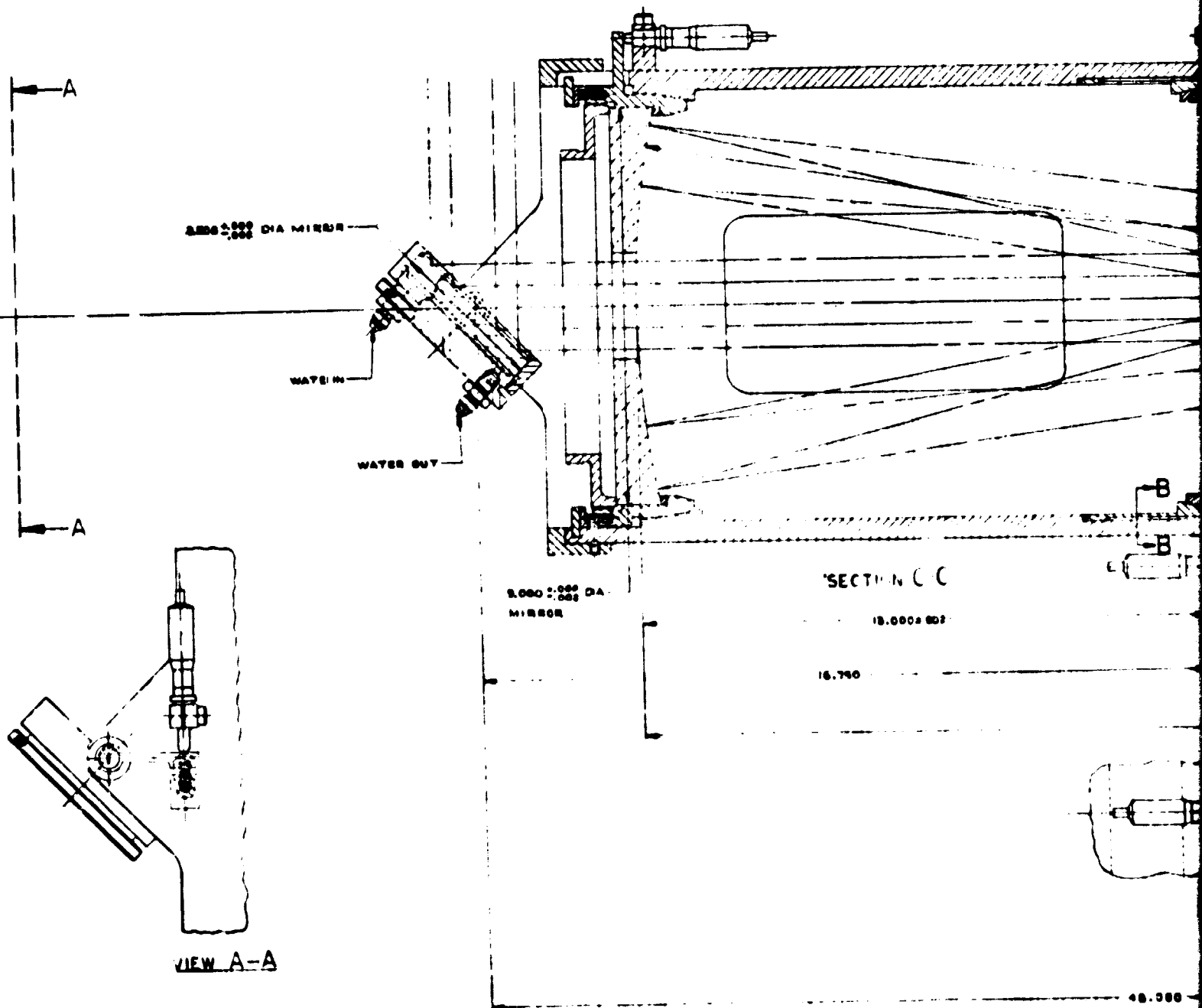
A conceptual design evaluation of the orientation of the incoming laser beam relative to the line of thrust indicated that a 90-degree orientation provides the optimum orientation based on beam reception from a fixed point (Fig. 91). Four candidate concepts employing the 90-degree orientation for the 5000-kw optical train are presented in Fig. 92. Two of the design concepts employ flat, conical and spherical mirrors, whereas the other two use aspherics (elliptical and parabolic mirrors). In all these concepts, the flat mirror could be rotated and tilted to increase the envelope of the laser beam receiver system. This envelope is illustrated in Fig. 93 for an attitude engine and for drag make-up, orbital changing, or planetary injection engines.



FOLDOUT FRAME



SECTION B-B



VIEW A-A

FOLDOUT FRAME 2

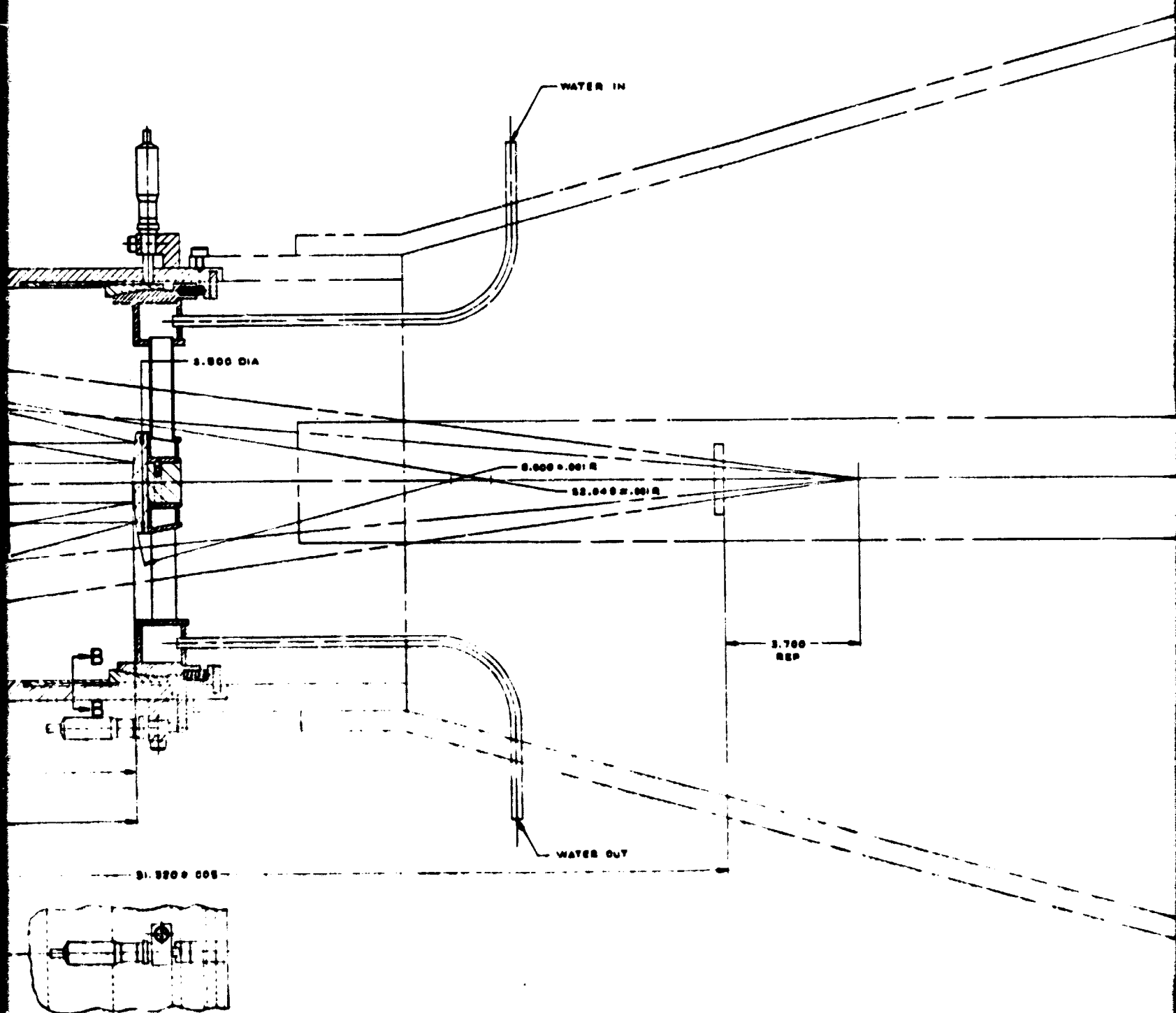
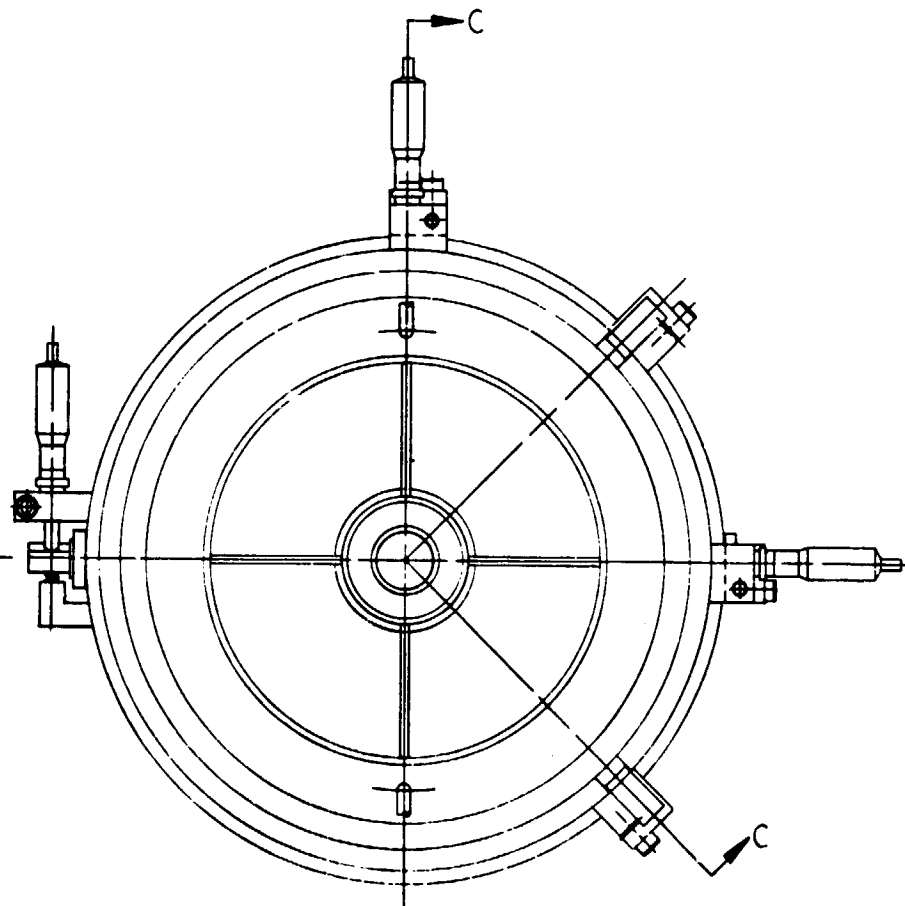


Figure 89. 10-kw Optical Train Assembly
(M = 2.0)


LOLDOOT FRAME 3

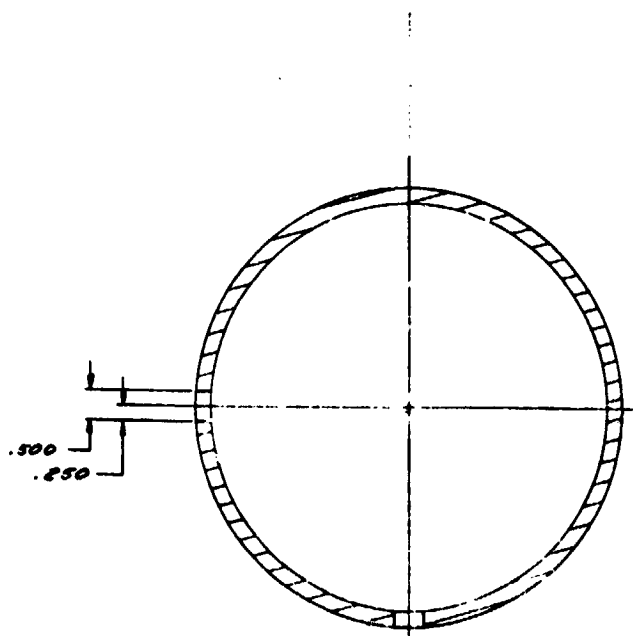


FOLDOUT FRAME 4

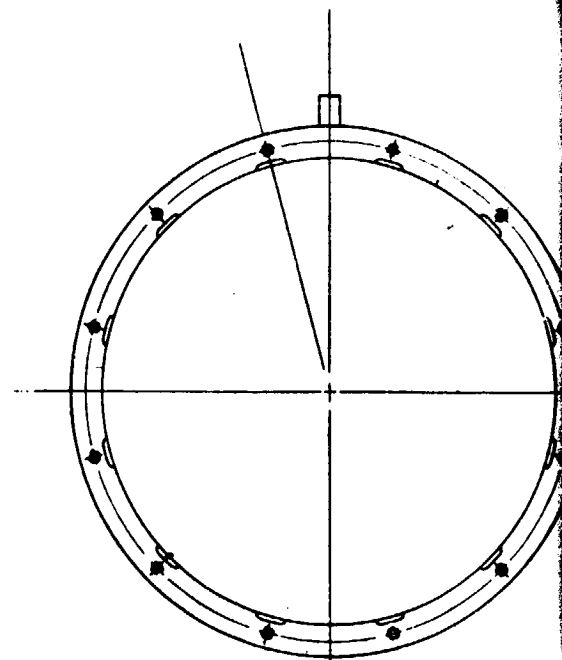
139/140

ADVANCED DESIGN

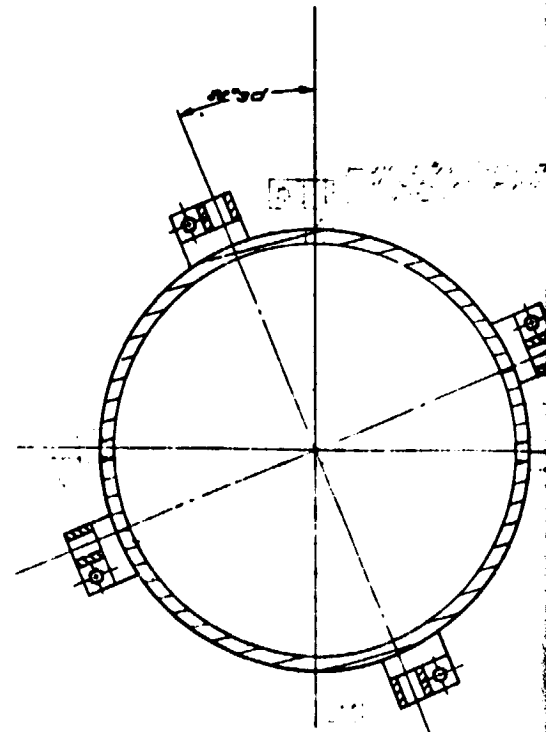
 Rockwell International Rockwell Division 2500 Canyon Boulevard Torrance, CA 90501-5001	
LASER INTERFEROMETER MOUNTING MOUNT (M=)	
DESIGNED BY: J.A.	DATE: 1/1
DRAWN BY: J.A.	DATE: 1/1
CHECKED BY: J.A.	DATE: 1/1
APPROVED BY: J.A.	DATE: 1/1
02603	
AP-	



SECTION G G

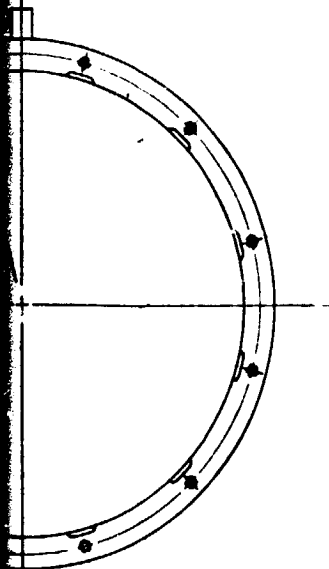


SECTION F-F

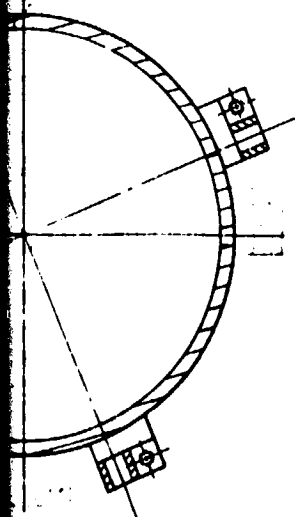


SECTION D-D

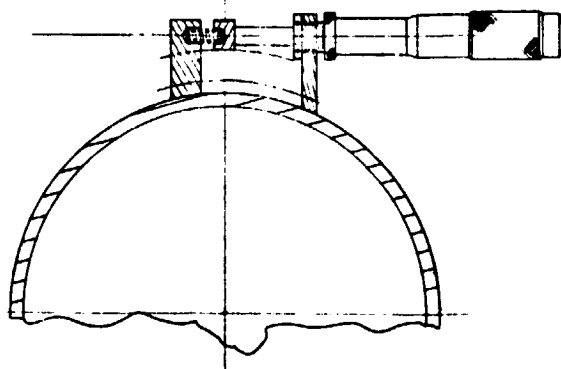
FOLDOUT FRAME 1



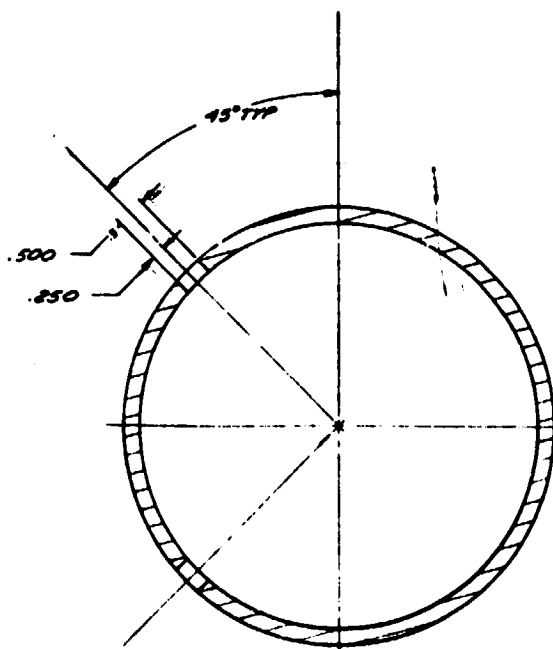
F-F



ON D-D

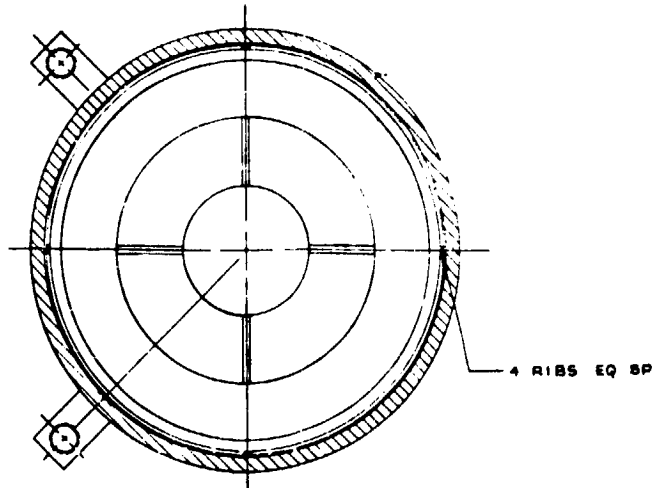


SECTION E-E

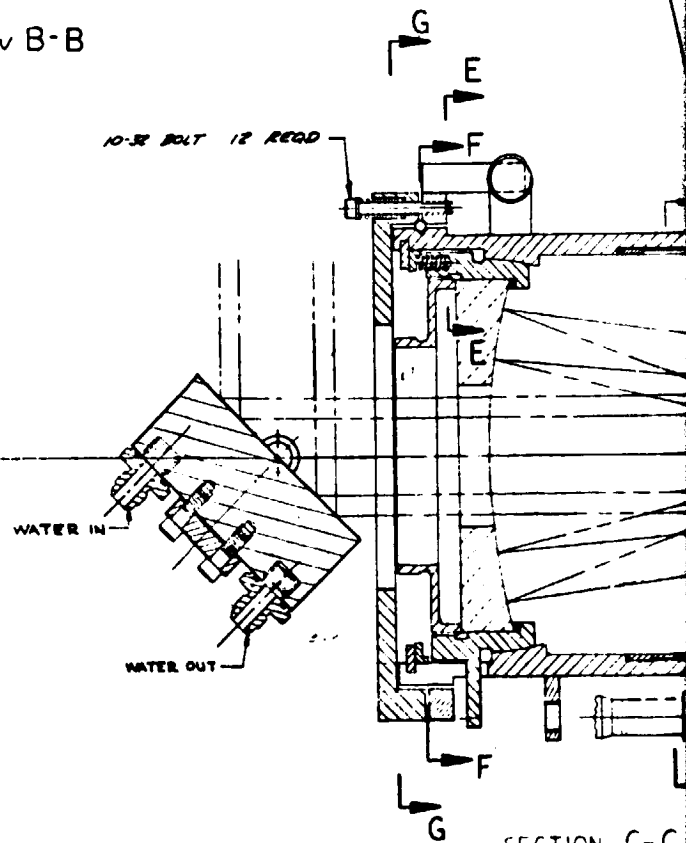
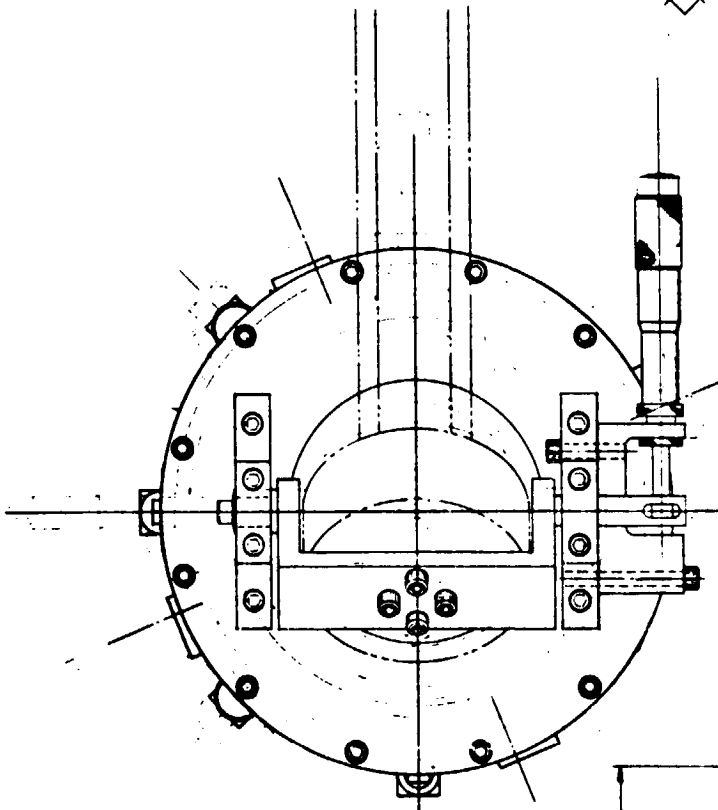


SECTION H-H

FOLDOUT FRAME 2



SECTION B-B



MIKE HEAD FULLEY
EXTENDED 4.12

LAUSING DIFFERENTIAL
SCREW TRANSLATOR 6 REQD
TRAVEL .05 PER INCH
DIVISION .000005 (NOM)

MIKE MAGNATION
 $\pm 1.27^\circ$

VIEW A A

4 282D

STARRETT MICRONETER HEAD 2 282D
 SET NO 263L WITH 30 DIA
 MOUNTING SURFACE

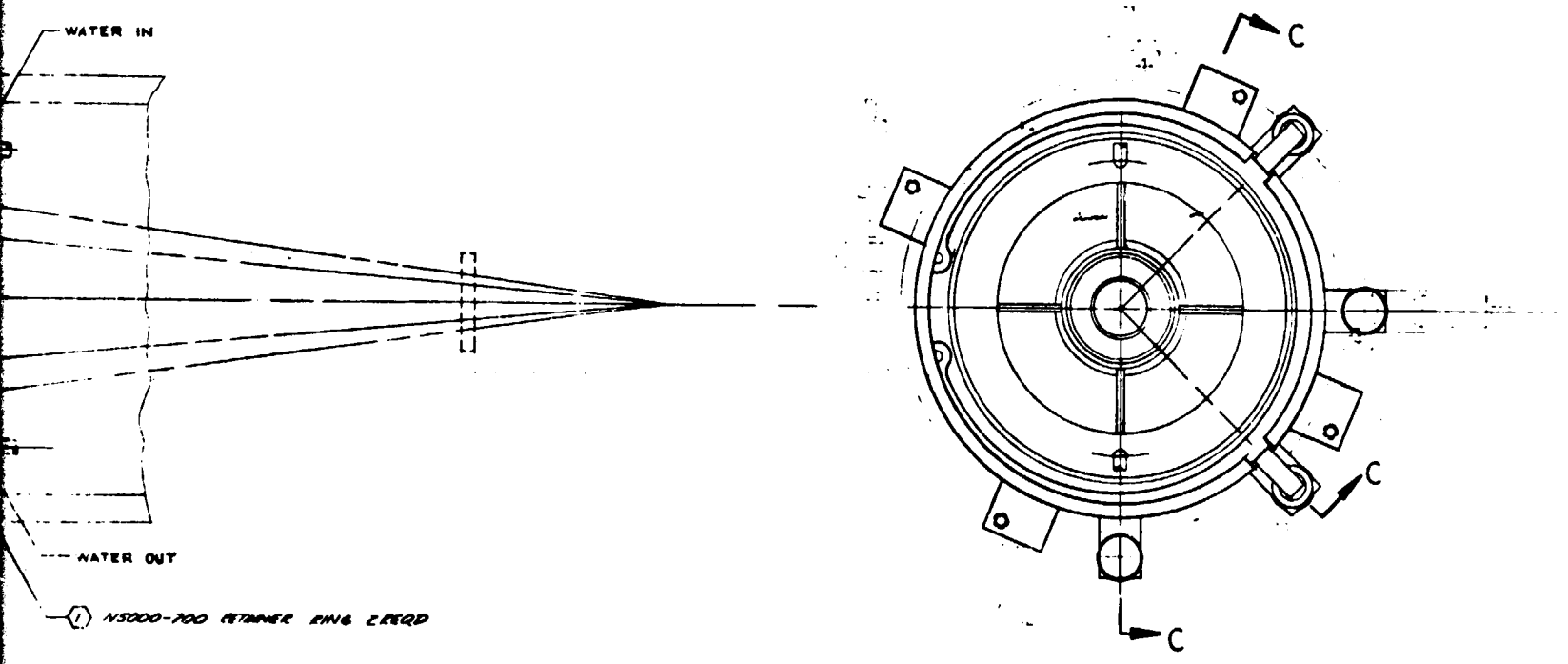


Figure 90. 10-KW Optical Train Assembly (M=1.523)

OLDOUT FRAL 4

- ① SAMPSON OPTICAL RESEARCH, INC. WILMINGTON, CALIF. 91790
- ② LAWRENCE RESEARCH CORP. ITHACA, NEW YORK, 14850
- ③ STARRETT CORP. MILFORD, MASSACHUSETTS, 01931
- ④ TRIMBLE OPTICAL RINGS, LONG ISLAND CITY, N.Y. 11101

ADVANCED DESIGN

Rockwell International <small>10000 Wilshire Blvd. Suite 1000 Los Angeles, CA 90024</small>	
DESIGNED BY DATE / /	DRAWN BY DATE / /
CHECKED BY DATE / /	APPROVED BY DATE / /

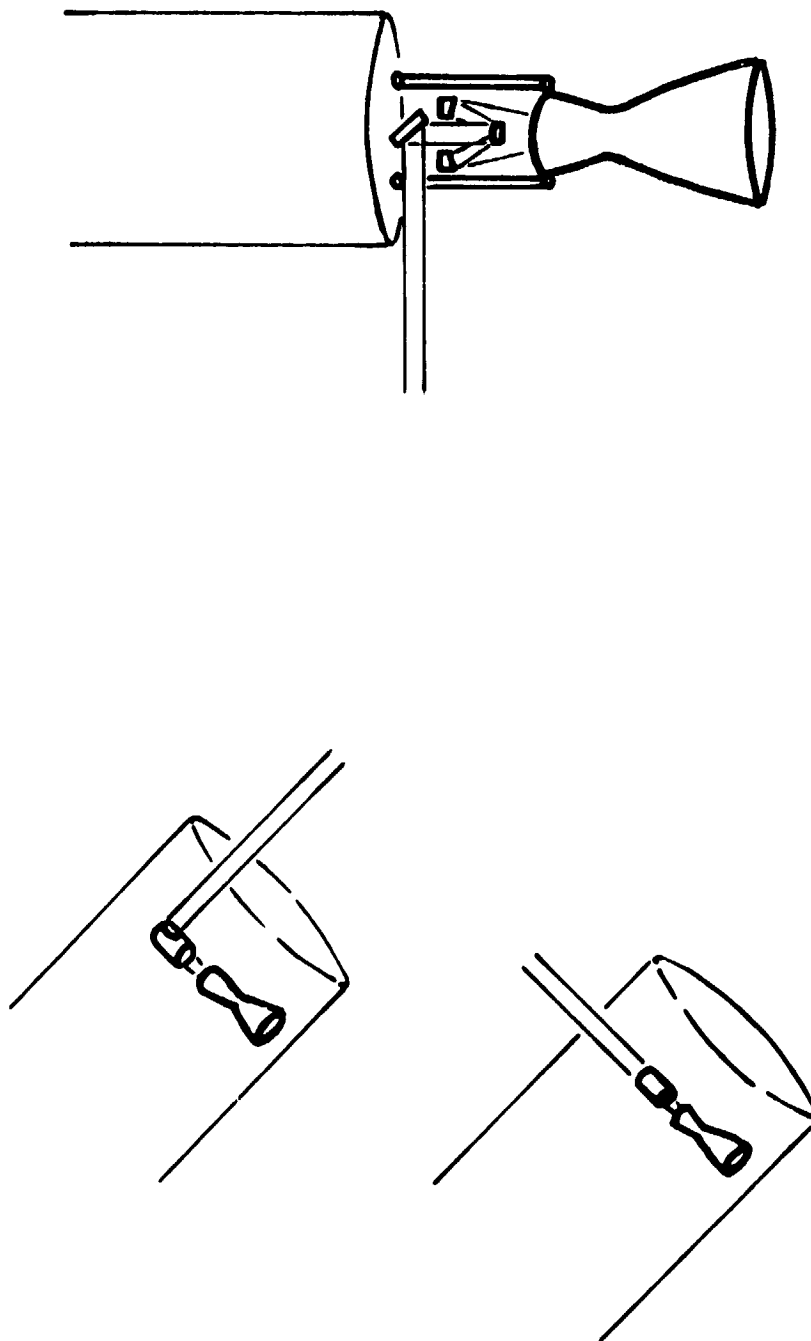
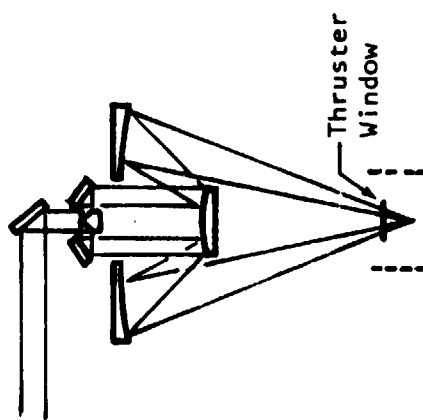
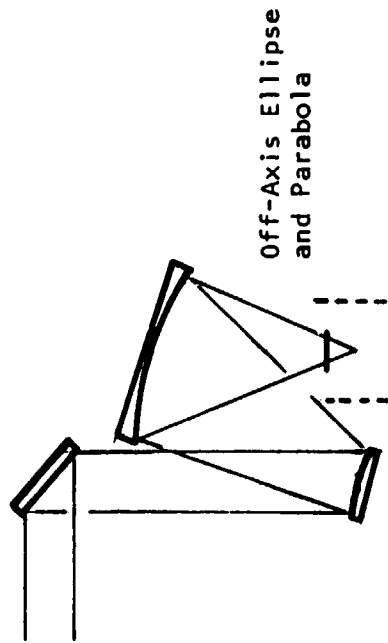


Figure 91. Typical Space Vehicle Installations

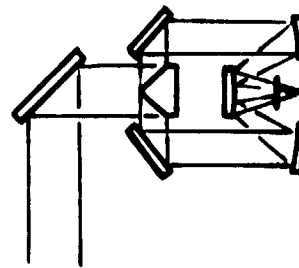
Fig. 92. 5000-KW OPTICAL TRAIN CONCEPTS



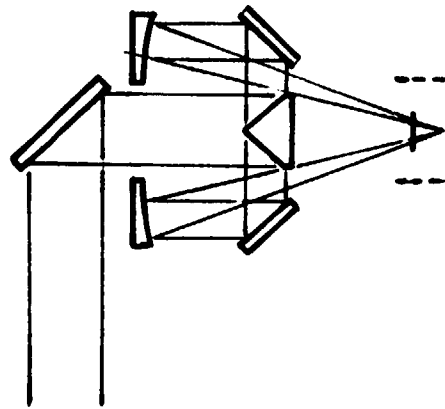
On-Axis Cassegrain (Pointer)
with Axicon (flat, conical,
and spherical mirrors)



Off-Axis Ellipse
and Parabola

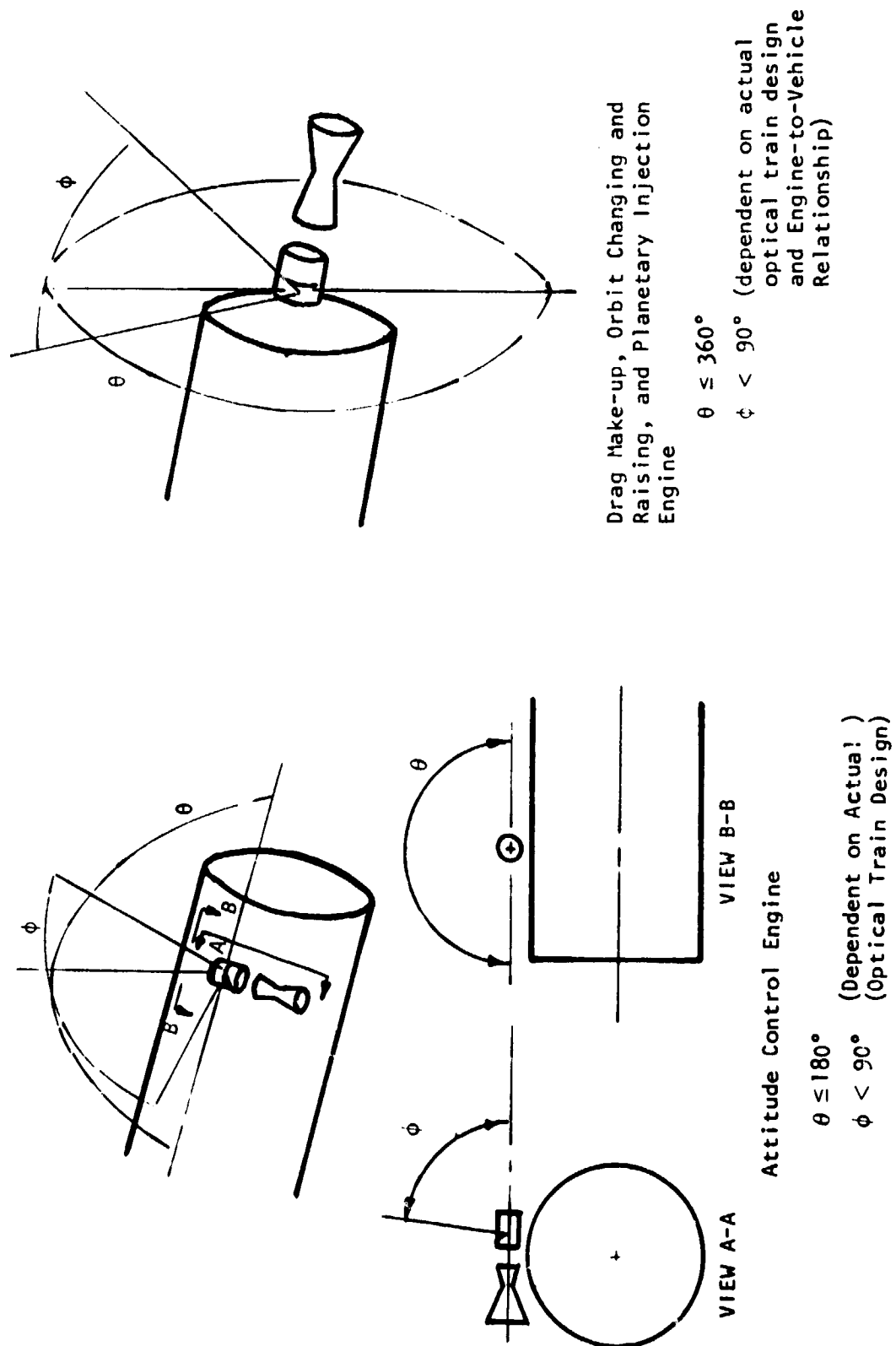


On-Axis Cassegrain (telescope)
with Axicon (flat, conical,
and Spherical Mirrors)



On-Axis Cassegrain (pointer)
with Axicon (flat, conical, and
Elliptical Mirrors)

Fig. 93. LASER BEAM-TO-OPTICAL TRAIN ENVELOPE LIMITATIONS



10-KW EXPERIMENTAL HARDWARE DESIGN

Water-Cooled Chamber

Initially an evaluation of the overall fabrication technique for the 10-kw water-cooled chamber was conducted to develop a design incorporating forced convection cooling with water. The coolant passage sizes defined in the Cooling Analysis section were to be incorporated with a common coolant inlet and individual coolant outlet lines.

In designing the water-cooled chamber several fabrication techniques currently used in rocket thrust chambers were evaluated and these included:

1. OFHC copper liner with an electrode-formed nickel closeout
2. OFHC copper liner with "O" rings within a stainless steel shell
3. OFHC copper liner brazed to a stainless steel structural shell

In the first fabrication technique, the electrode-formed nickel closeout would have provided a more than adequate structural closeout; however, for this particular chamber this technique would have resulted in an expensive solution. The second fabrication technique using "O" rings to seal the water resulted in a low cost technique and the capability of replaceable liners; however, the difficulty in sealing the electrode (igniter) region resulted in the elimination of this technique. A water leak into this area could result in a failure of the electrode mechanism to arc. The third technique of brazing of the copper liner and the structural steel shell eliminated the sealing problem with only slight increase in cost. The inner liner could still be replaced by machining out the "old" liner and brazing in a "new" liner. Therefore, this fabrication technique was selected.

The ignitors or plasma arc electrodes must pass through the cooled chamber wall; and the design of the water coolant passage arrangement in the vicinity of the electrodes must be such that adequate cooling be provided as well as sufficient space for the electrode. Therefore a small diameter electrode was desirable. This was also desired from a fluid dynamic aspect since an electrode larger in diameter than the hot-gas diameter would literally stop the gas flow.

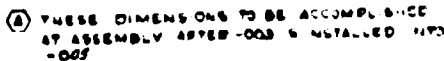
Since the plasma was predicted to exist 3 cm (1.13-inch) upstream of the geometric throat, water cooling was provided 5.08 cm (2-inches) upstream of the throat. The arc-initiating electrode mechanism mounting flanges are located 90 degrees from the water coolant lines.

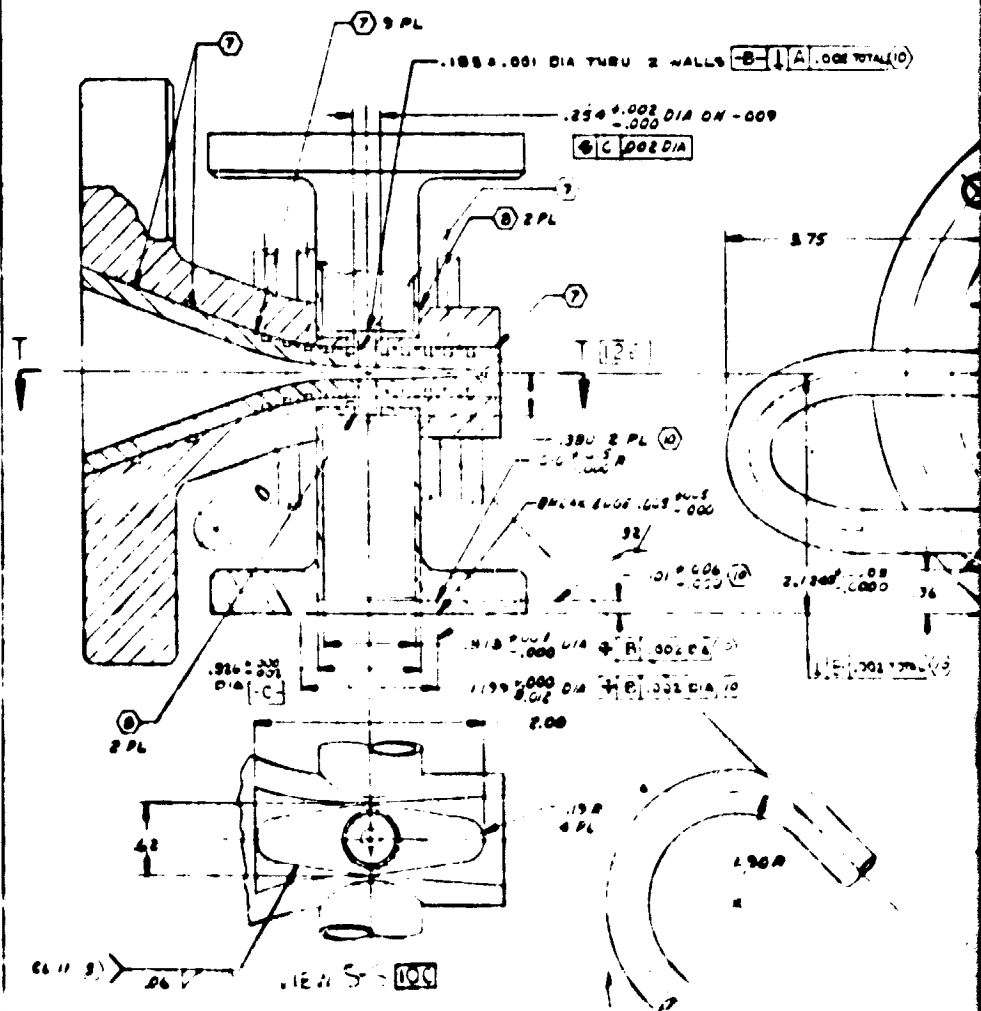
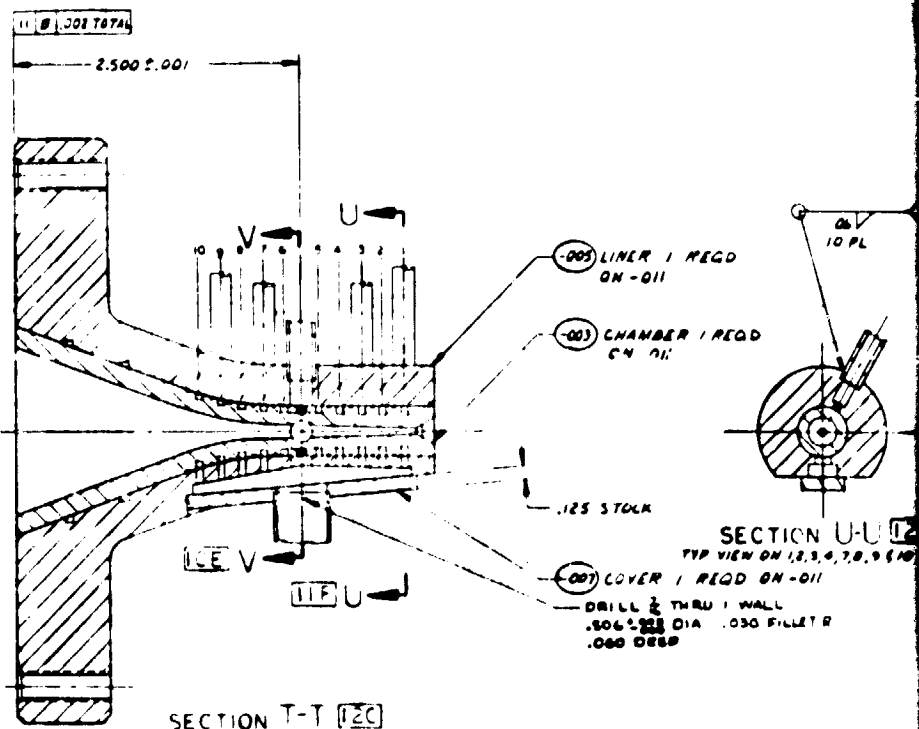
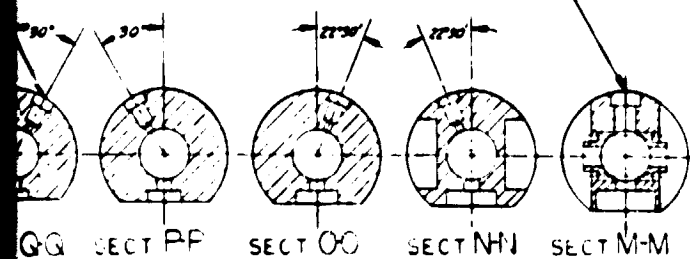
For testing at sea level, the 1.6:1 area ratio will result in a full flowing nozzle at a chamber pressure of $3.45 \times 10^5 \text{ N/M}^2$ (50 psia).

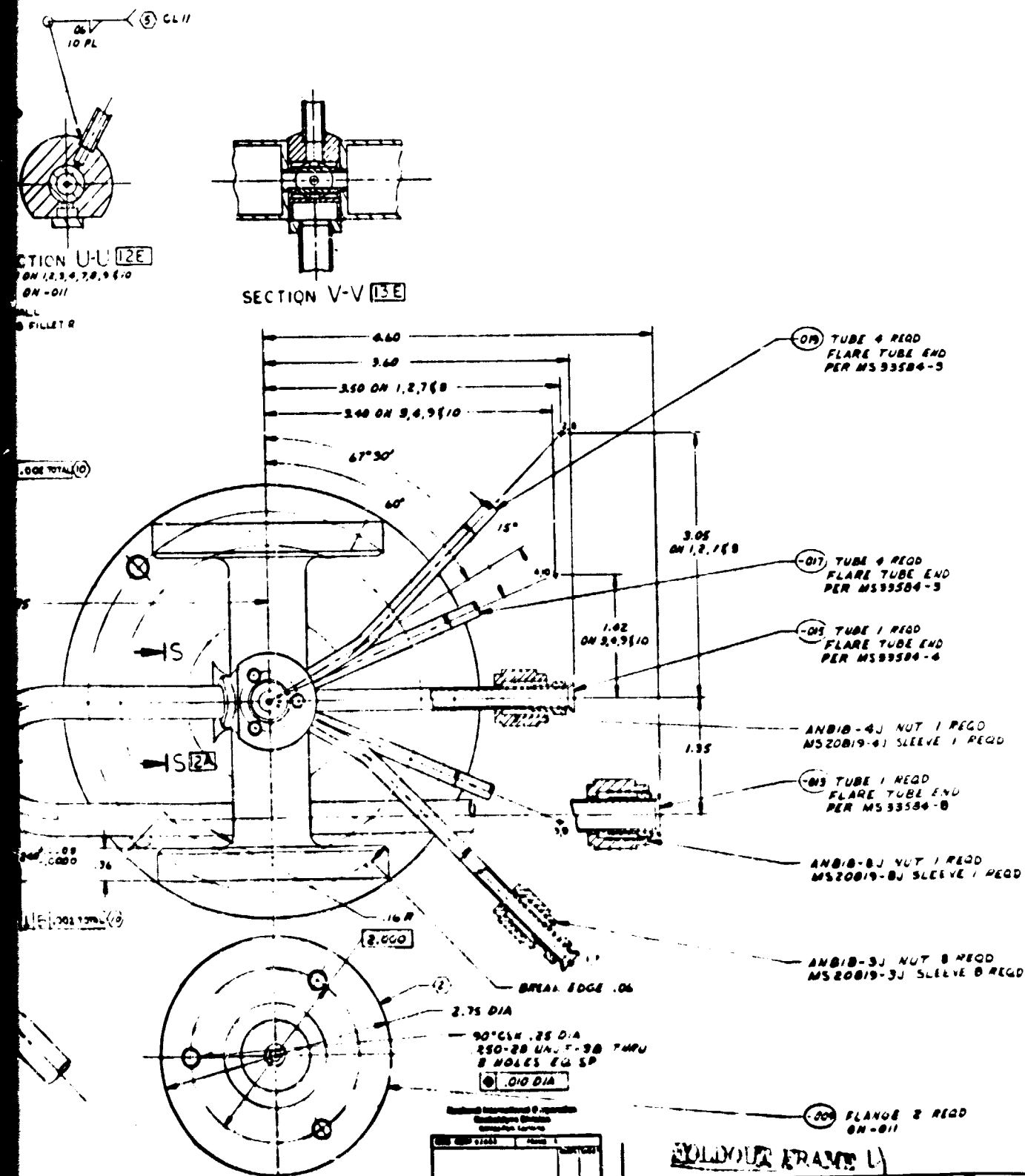
The chamber with the gas side wall thickness (wall thickness between the hot gas and the water coolant) of 0.254 cm (0.1-inch) allows the capability of increasing the hot gas diameter by a factor of 2. This hardware flexibility will allow hardware growth if the plasma size is larger than predicted. The assembly drawing of the 10-kw water-cooled chamber is presented in Fig. 94.

Ignitors (Plasma arc Initiating Electrode Mechanism)

The electrode design uniquely incorporated two modified TIG welding tips with 0.1016 cm (0.04-inch) diameter tungsten electrodes with a micrometer adjustment to set the arc gap. The basic concept is a pneumatic cylinder which when pressurized (gaseous nitrogen at $3.45 \times 10^6 \text{ N/M}^2$ or 500 psig) moves the two electrodes into the chamber to a preset arc distance. The instant the arc occurs, the nitrogen pressure is released and the spring withdraws the electrodes flush with the chamber wall. Hydrogen pressure placed in the electrode mechanism will provide positive pressure against incoming hot gas from the







Assembly

REVISIONS			
REV	DATE	DESCRIPTION	APPROVED
1		1. REV BE REWORKED	
2		2. RECORD CHANGE	
3		3. CHECK BE REWORKED	
4		4. NEW SHOP PRACTICE	
5		5. PARTS NAME CH	

149/150

- ⑩ DRILL THRU & MACHINE AFTER BRAZING.
- 9 CONSULT WITH ENGINEERING AS TO BRAZING PROCEDURE.
- ⑧ BRAZE PER RBO170-064 (NIORO) AT 1810°-1825°F IN DRY HYDROGEN.
- ⑦ BRAZE WITH 50-50 Au-Cu AT 1810°-1825°F IN DRY HYDROGEN.
- ⑥ LEAK CHECK WELDS PER ENGRG INSTRUCTIONS.
- ⑤ WELD PER RAO107-027.
- ④ FURNISH ONLY AS A MATCHED SET.
3. FILLET RADIUS .030.
- ② DEEP ELECTROCHEMICAL ETCH IDENTIFY ASSY PER RAO104-008.
1. MACHINE PER RAO103-016.

-011	SUB ASSY
-001	ASSY
NO	

-019	321 CRES TUBE	3/16 CD X .025	WIL-T-8808	80
-017	321 CRES TUBE	3/16 CD X .025		80
-015	321 CRES TUBE	3/16 CD X .025		80
-013	321 CRES TUBE	3/16 CD X .025	WIL-T-8808	80
-009	304L CRES BAR		QQ-S-769 CL304L G-10A	84
-007	304L CRES SH		QQ-S-769 CL304L G-10A	12
-005	304L CRES BAR		QQ-S-769 CL304L G-10A	12
-003	COPPER BAR CK ROD		RBO170-047 GFNC LENS	23
NO	MATERIAL	SIZE	SPECIFICATION	20

LDOUT FRAME 5

NON- NONE NOTED		UNLESS OTHERWISE SPECIFIED DIMENSIONS ARE IN INCHES AND DECIMALS ARE TO THREE UNLESS NOTED OTHERWISE	DATE: 5-20-66 CHK: J. O. G. DESK: J. O. G. INCH ACTIVITY: 0.001 DO NOT SCALE PRINT	Redwood International Corporation Rocketry Division Canoga Park, California CHAMBER LASER ROCKET ASSY OF J 02602 APT-033 SCALE: 1/1 SHEET: 1 PAGE: 1
-----------------------	--	---	--	--

chamber. The electrodes can be easily changed by turning the locking nut by hand. Also the electrode withdrawal distance can be varied for the different distances required for the water-chamber and the uncooled chamber. The ignitor assembly is illustrated in Fig. 95.

10-kw Heat Sink Chamber. The 10-kw heat sink chamber incorporates a thick copper chamber capable of 8-seconds test duration and permits a larger-than-predicted plasma diameter (up to four times larger). In addition, a graphite insert provides the flexibility of altering the gas contour to the contour of the 10-kw water-cooled chamber. The heat sink chamber utilizes the electrode mechanism, injector, and thrust stand designed for the water-cooled chamber.

The assembly drawing of the heat sink chamber with graphite insert is presented in Fig. 96. Chamber details are shown in Fig. 97 through 99.

Details of the graphite insert are shown in Fig. 98. Thermocouple installations for wall temperature monitoring are illustrated in Fig. 97 and 98. Thermocouples installed one-inch from the gas surface were provided at three axial locations (at the throat, and 2.54 and 6.35 cm upstream of the throat). A typical plasma viewing window installation is illustrated in Fig. 99, with a lens window (could be a plane window), and a gaseous purge to prevent external hot gas leakage. Per a verbal agreement with the NASA-LeRC Project Manager, the plasma viewing window was included in the design drawings, but was not fabricated.

Injector

The assembly drawing of the 10-kw chamber injector is shown in Fig. 100. The main propellant, hydrogen, is introduced in a common manifold for the window coolant and the main injector. The flowrate is to be controlled with rigimesh orificing using 0.635 cm (1/4-inch) 100 scfm rigimesh to provide ten percent

H

G

F

E

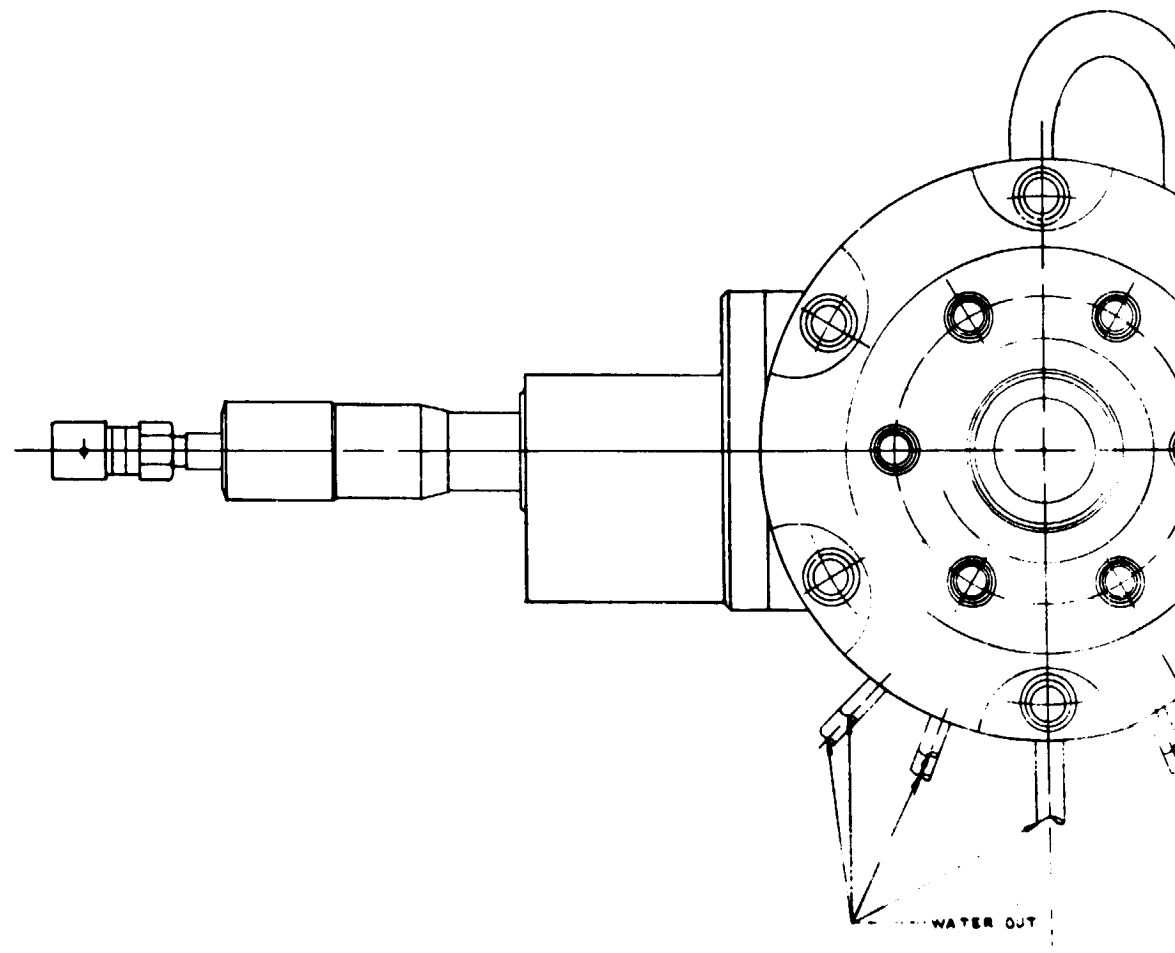
D

C

B

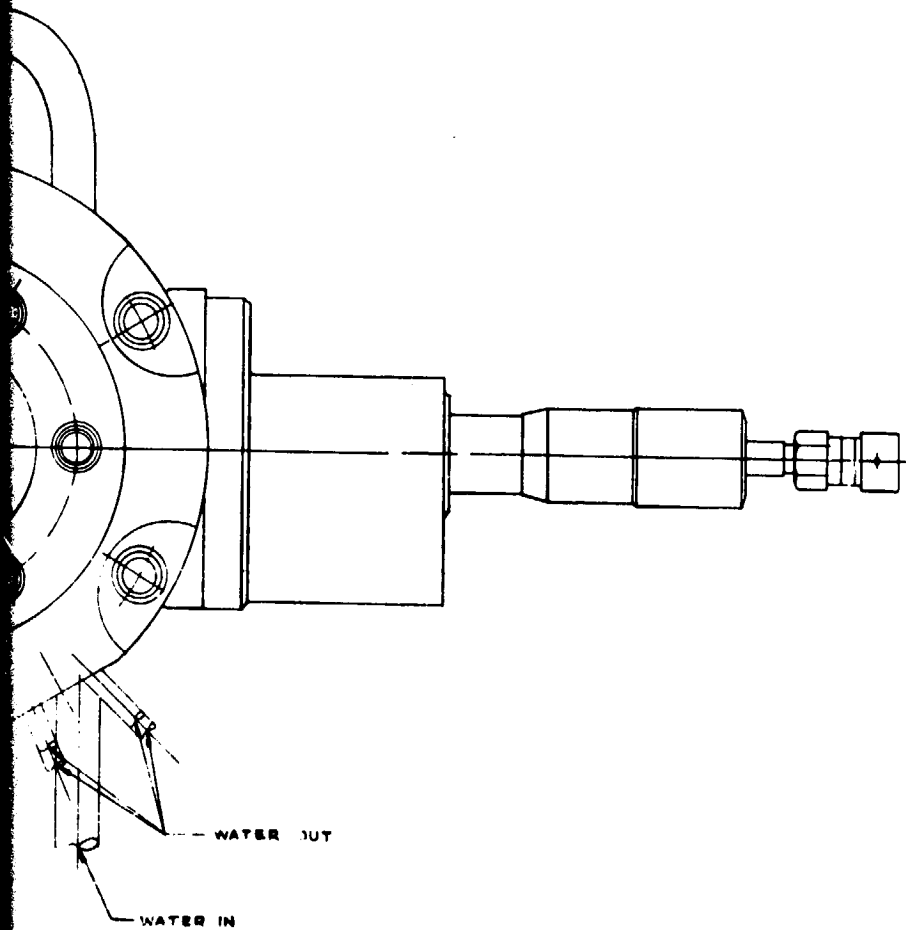
A

FOLDOUT FRAME

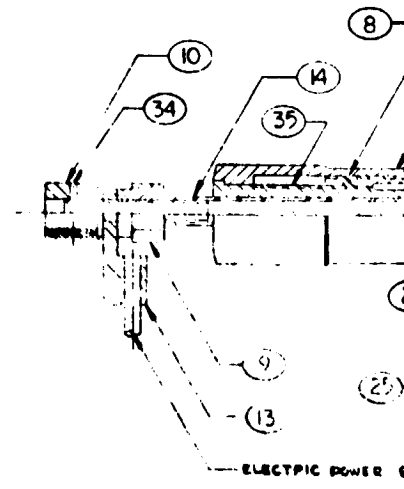


VIEW A - A

A
↓



(PART RO



PISTON ACT
PRESSURE

FOLIOOT FRAME 2

Rolling International Corporation
Rolling International Division
Rolling International Corporation

ROLLING 00007	FRAME	DATE	REV
AP76-035			

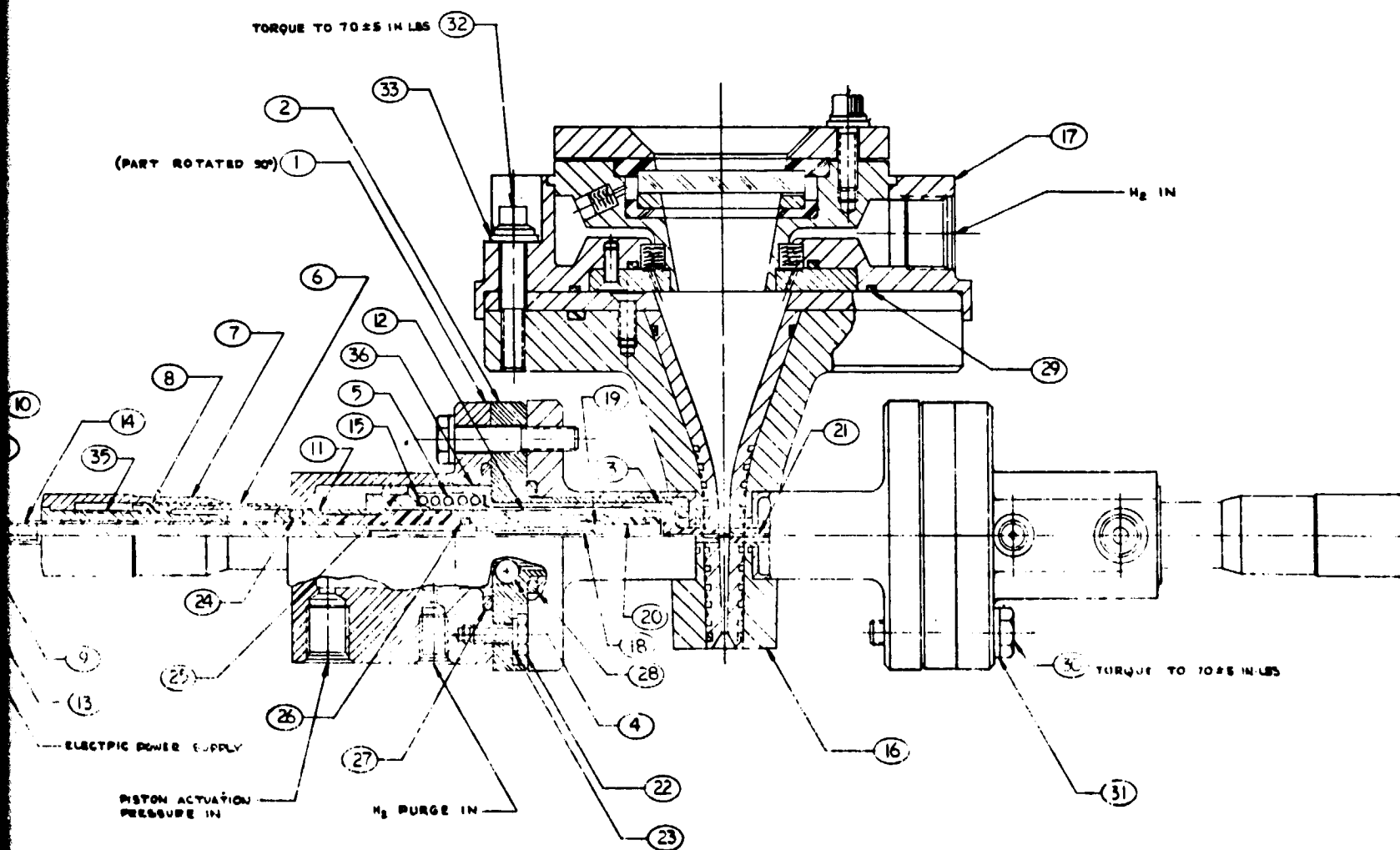
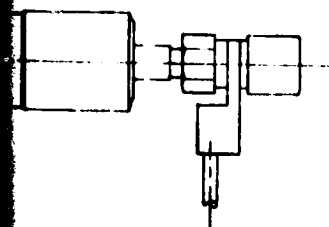


Figure 95. 10-KW Thruster Assembly

BOLT FRAMES
 OUT FRAMEY



ITEM NO	
1	AP76
2	AP76
3	AP76
4	AP76
5	AP76
6	AP76
7	AP76
8	AP76
9	AP76
10	AP76
11	AP76
12	AP76
13	AP76
14	AP76
15	AP76
16	AP76
17	AP76
18	13N2
19	13N2
20	13N00
21	NW-5
22	NA54
23	AN03
24	MS28
25	MS28
26	MS28
27	MS28
28	MS28
29	MS28
30	MS06
31	L0153
32	MS03
33	L0153
34	MS16
35	AP76
36	AP76



EXPLODOUT FRAME

Radford International Corporation
Radford, Virginia
25601-0001

REV 0001	FRAME 2
AP76-035	DATE 1-11

ITEM NO	PART NO	NO REQD	VENDOR
1	AP76-032-003	2	
2	AP76-032-003	2	
3	AP76-032-007	2	
4	AP76-032-009	2	
5	AP76-032-013	2	
6	AP76-032-015	2	
7	AP76-032-017	2	
8	AP76-032-019	2	
9	AP76-032-023	2	
10	AP76-032-025	2	
11	AP76-032-027	2	
12	AP76-032-031	2	
13	AP76-032-033	2	
14	AP76-032-011	2	
15	AP76-032-037	4	
16	AP76-033-001	1	
17	AP76-034-001	1	
18	13N21	2	UNION CARBIDE
19	13N26	2	UNION CARBIDE
20	13N08	2	UNION CARBIDE
21	HW-20 ELECTRODE 3.00 LONG	2	UNION CARBIDE
22	MS464-3	3	
23	AN935-10	3	
24	MS20775-110	2	
25	MS20775-211	2	
26	MS20775-010	2	
27	MS20775-224	2	
28	MS20775-212	2	
29	MS20775-040	2	
30	MS9490-20	6	
31	L0153-0013-0001	6	
32	MS9575-21	6	
33	L0153-0013-0002	6	
34	MS10562-104	2	
35	AP76-032-039	2	
36	AP76-032-045	2	

REVISIONS		DATE	APPROVED
1	NEW RE ASSIGNED		
2	REWORK RE ASSIGNED		
3	NEW RE ASSIGNED		
4	NEW RE ASSIGNED		
5	NEW RE ASSIGNED		

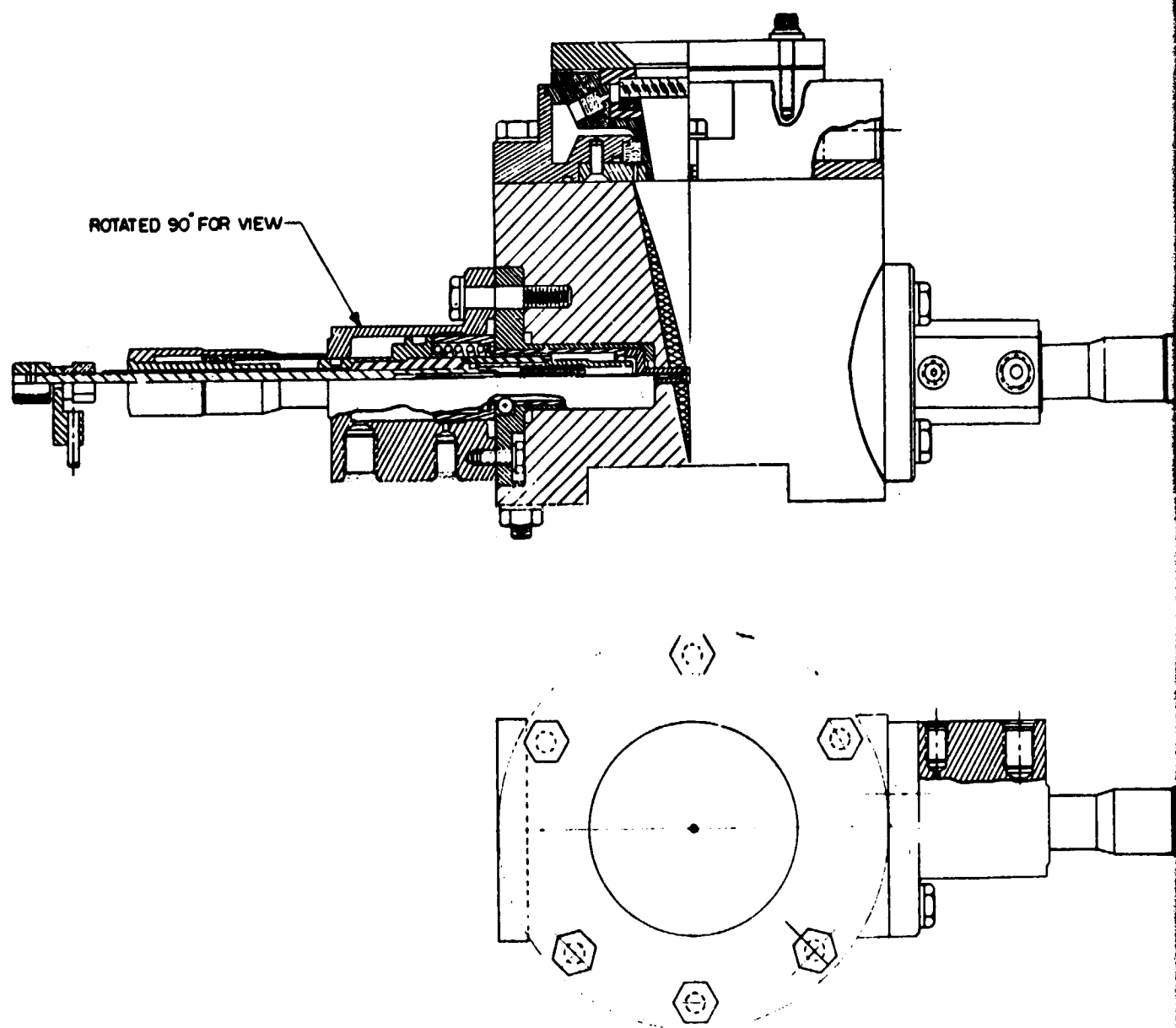
001
NO.

153/154

ASSEMBLE PER ENG INSTRUCTIONS
USE CRANE ATTACHED TO PUMP

NATIONAL INTERNATIONAL CORPORATION Engineering Division Control File Control	
THRUSTER - ASSY OF	
02602 AP76-035	02602 AP76-035

Figure 96 . Uncoo

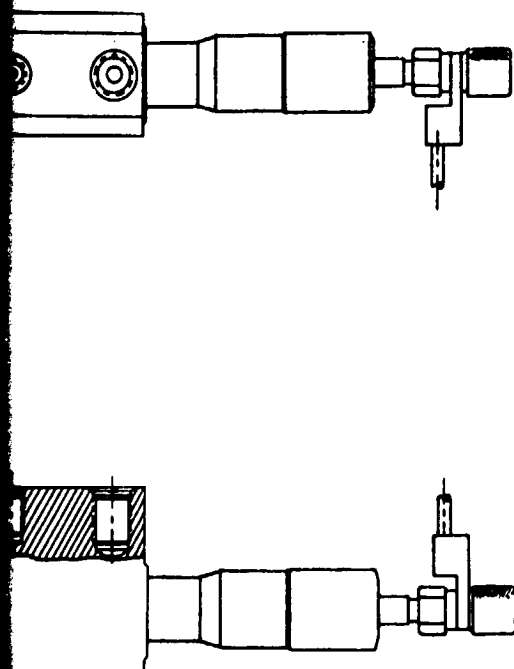


FOLDOUT FRAME

NOTE: UNLESS OTHERWISE SPECIFIED

Figure 96 . Uncooled Chamber Assembly

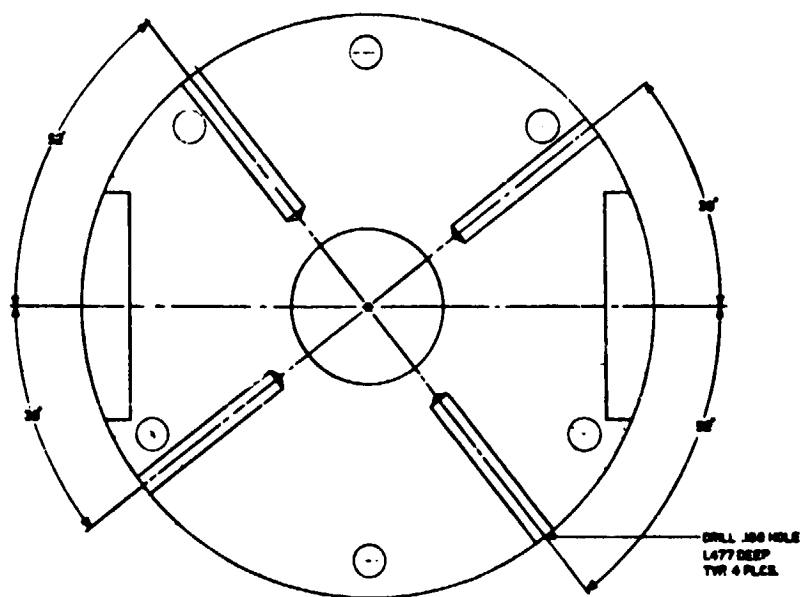
REVISIONS		
LTR	DESCRIPTION	DATE
	1. MAY BE REMOVED 2. CANNOT BE REMOVED 3. RECORD CHANGE 4. NOW SHOP PRACTICE 5. PARTS MADE OK	



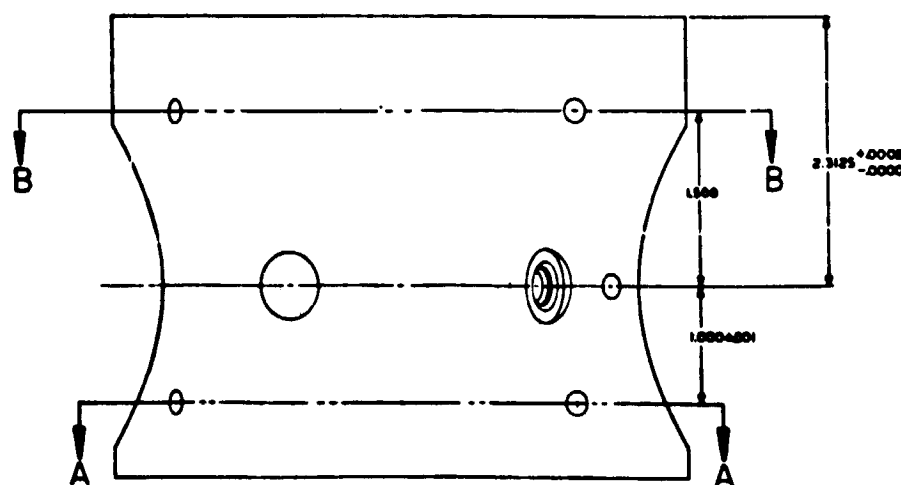
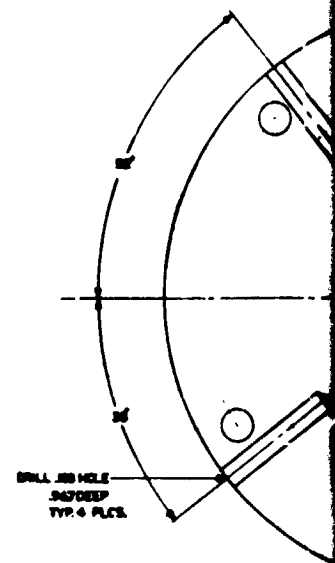
155/156

FINISH NONE	UNLESS OTHERWISE SPECIFIED, DIMENSIONS ARE IN INCHES AND APPLY PRIOR TO FINISH. 250/ MACH SURF. ROUGHNESS TOLERANCES ON ANGLES \pm 30° DECIMALS \pm .01 .001 \pm .005 HOLES NOTED "DRILL"	OWN	KW SPIEGEL	DATE	Rockwell International Corporation Rockaldyne Division Canoga Park, California								
		CHK	KW SPIEGEL	DATE									
FINISH NONE	OVER THRU TOLERANCE +.000 .000 +.005 -.000 .000 .000 +.005 -.000 .000 .000 +.005 -.000 .000 .000 +.005 -.000 .000 .000 +.005 -.000 .000 .000 +.005 -.000 1.000 2.000 +.005 -.000	DESIGN	KW SPIEGEL		WORKHORSE LASER ROCKET ASSY OF								
		MAYL											
DRILL	DO NOT SCALE PRINT	DESIGN AUTHORITY	AP06	DATE	<table border="1"> <tr> <td>SIZE</td> <td>CODE</td> <td>IDENT. NO.</td> <td>REVISION NO.</td> </tr> <tr> <td>D</td> <td>02602</td> <td>AP76-098-021</td> <td></td> </tr> </table>	SIZE	CODE	IDENT. NO.	REVISION NO.	D	02602	AP76-098-021	
SIZE	CODE	IDENT. NO.	REVISION NO.										
D	02602	AP76-098-021											

Fig.97. 10-kw Heat SI
Thermocouple



SECTION A-A



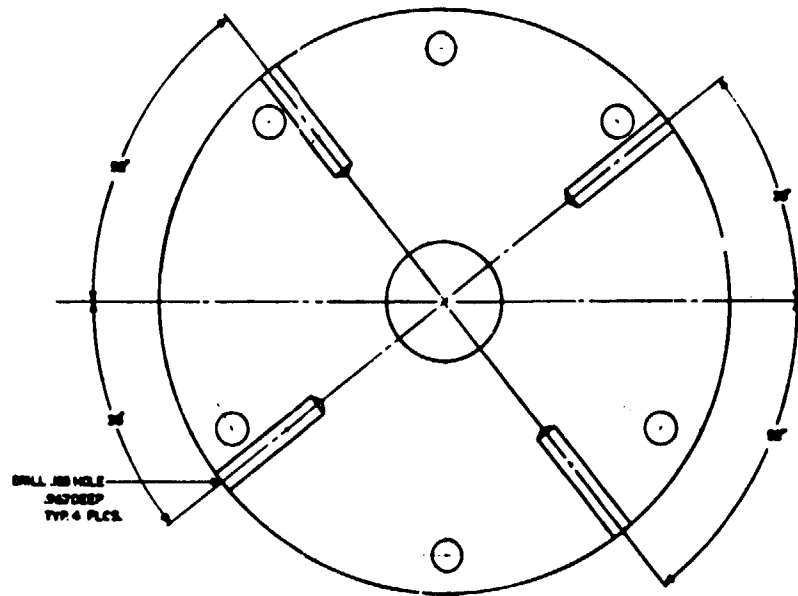
FOLDOUT FRAME
10-47000-01

3 CLEAN PER ENGINEERING INSTRUCTION
2 MACHINE PER RADIO-CODE
1 IDENTIFY BY TAG ONLY

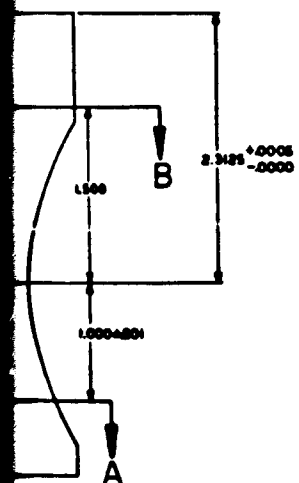
SEE DRAWING 10-47000-01

Fig.97. 10-kw Heat Sink Chamber
Thermocouple Installation

REVISIONS	
NO.	DESCRIPTION
1	REV. BY ENGINEER
2	REV. BY DESIGNER
3	REV. BY FABRICATOR
4	REV. BY INSPECTOR
5	REV. BY USER



SECTION B-B



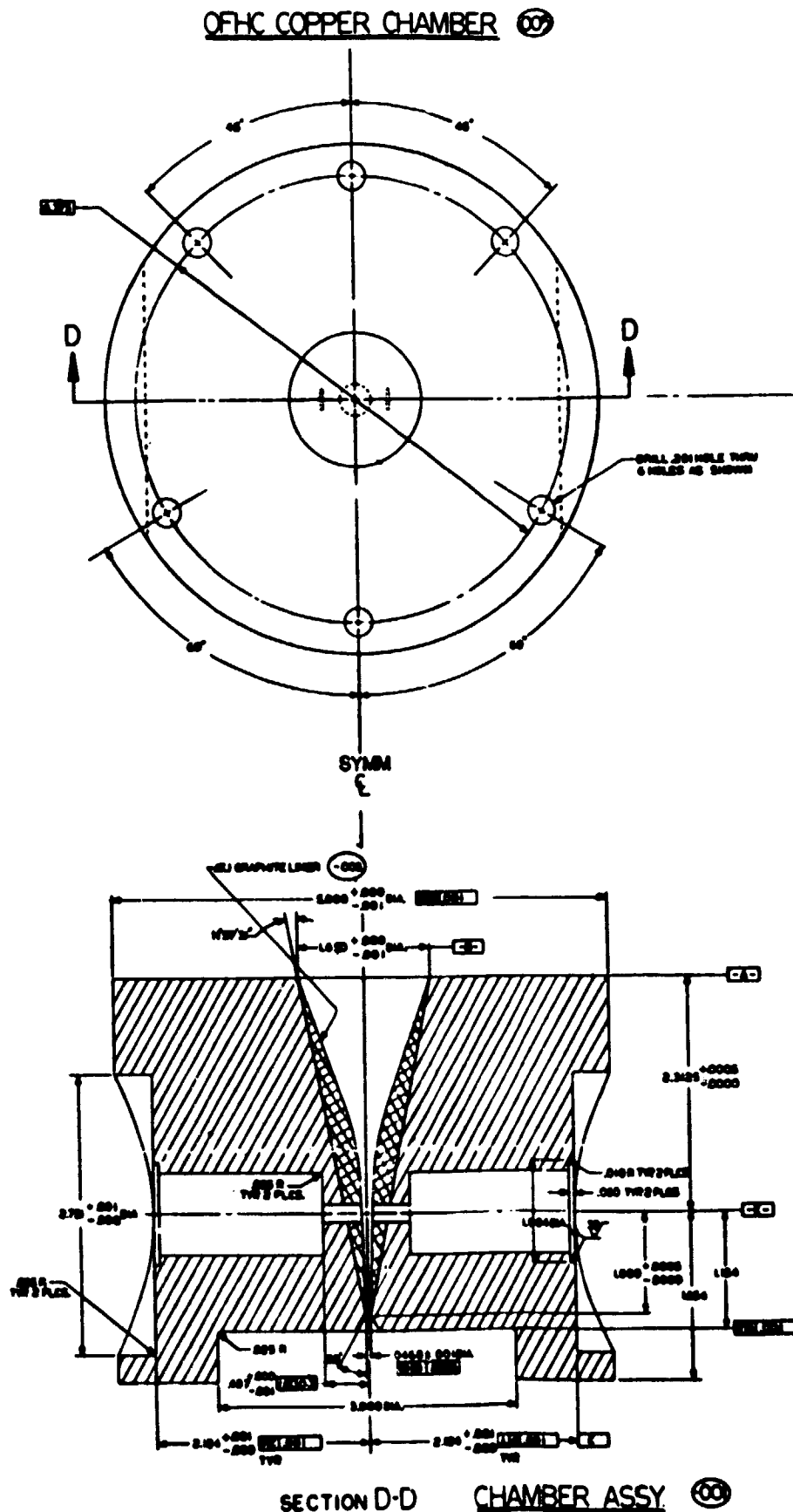
157/158

3 CLEAN PER ENGINEERING INSTRUCTIONS
3 MACHINE PER RADIO-008
1 IDENTIFY BY TAG ONLY

FOLDOUT

WORKHORSE LASER ROCKET COMBUSTION CHAMBER	
8 02402	AP76-098-005

Fig. 98. 10-kw Heat Sink Chamber
Graphite Ins

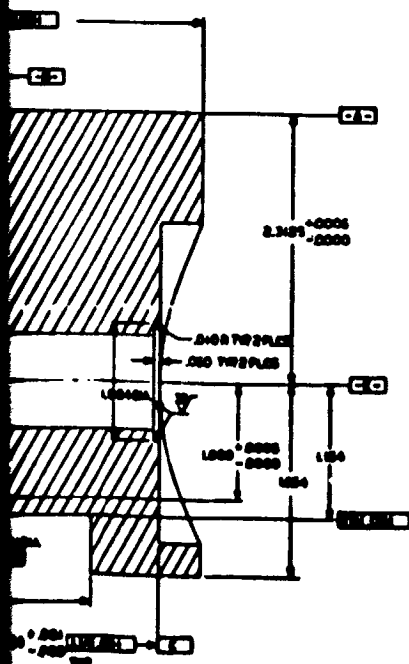
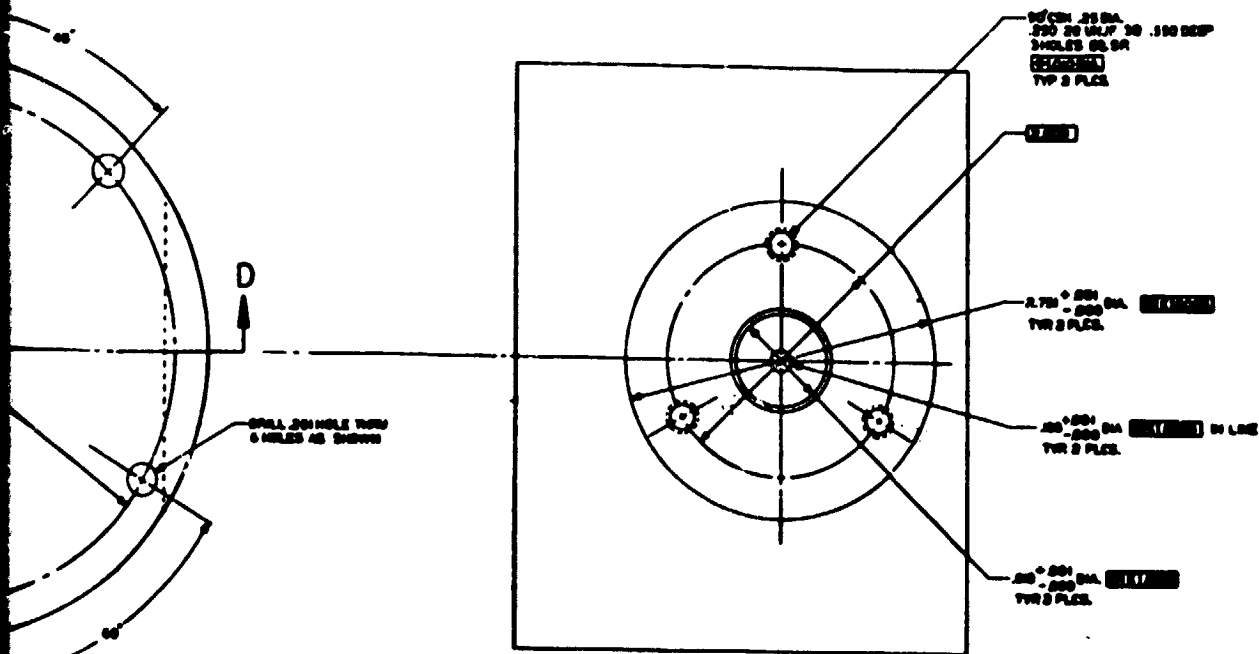


3. CLEAN PER ENGINEERING INSTRUCTIONS
2. MACHINE PER RA-003-000
1. IDENTIFY BY TAG ONLY

END OF DRAWING

Fig. 98. 10-kw Heat Sink Chamber - Graphite
Graphite Insert

CHAMBER ①



CHAMBER ASSY ②

3. CLEAN PER ENGINEERING INSTRUCTIONS
3. MACHINE PER RA-000-000
1. IDENTIFY BY TAG ONLY

000	GRAPHITE		1
000	GRAPHITE		2
QTY	MATERIAL	SPECIFICATION	REMARKS

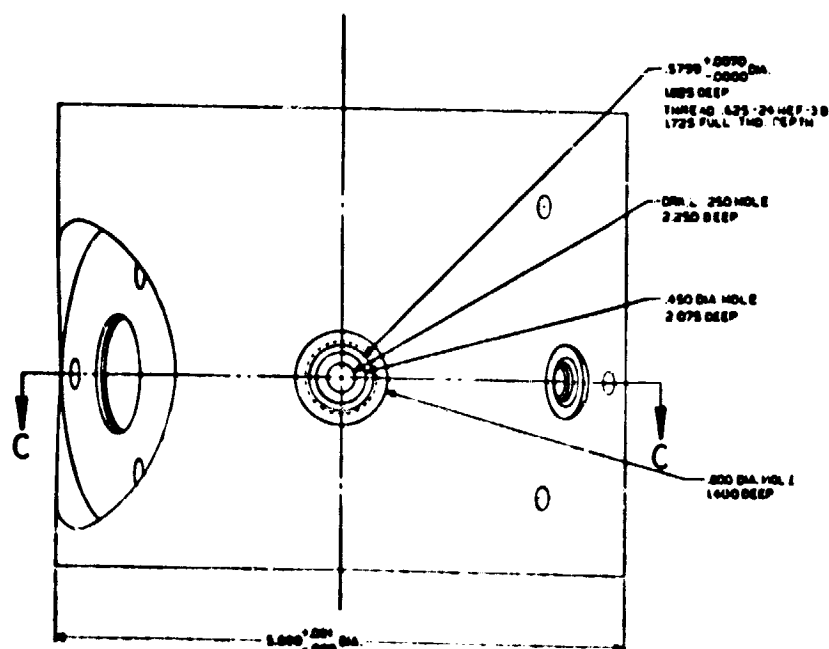
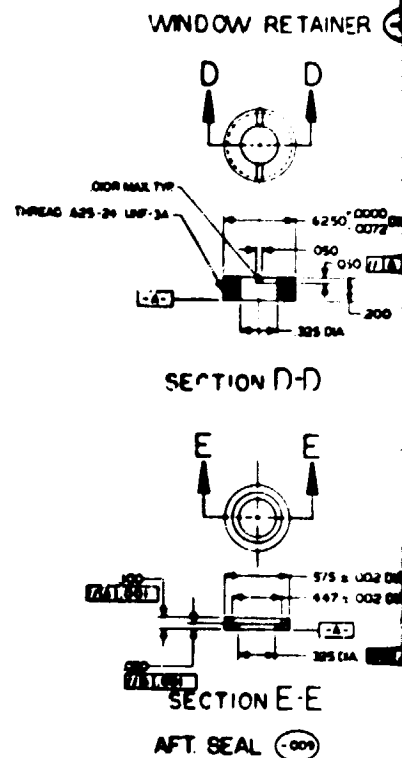
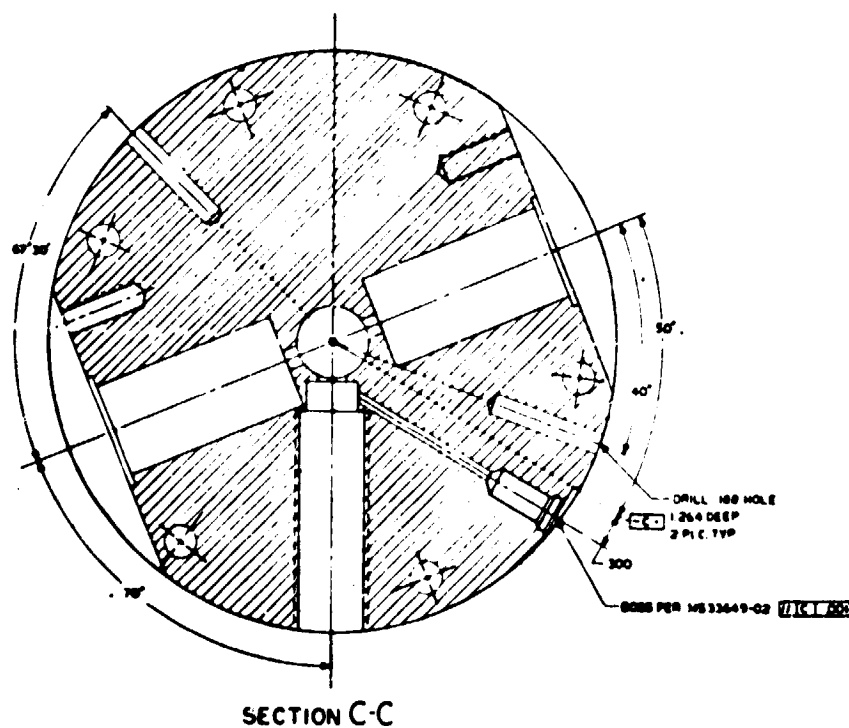
159/160

NAME	DATE	APPROVED	REVISION
NAME	DATE	APPROVED	REVISION
NAME	DATE	APPROVED	REVISION

W. K. HOLE LASER ROCKET,
COMBUSTION CHAMBER

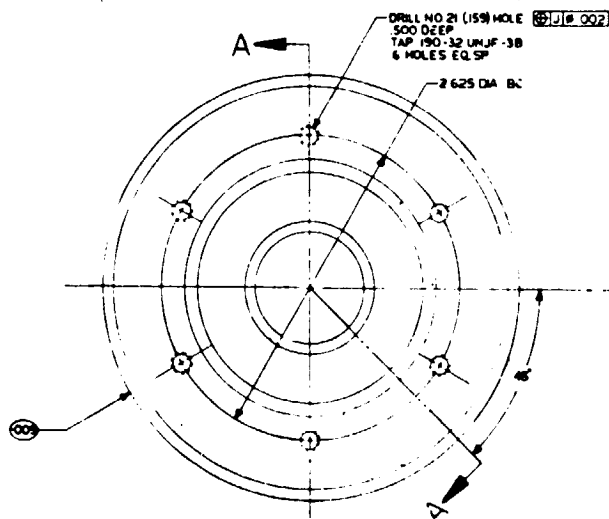
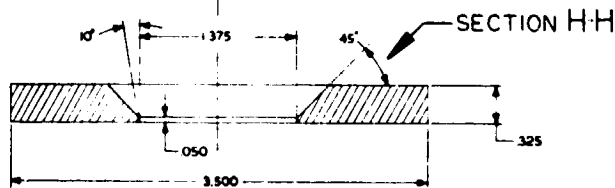
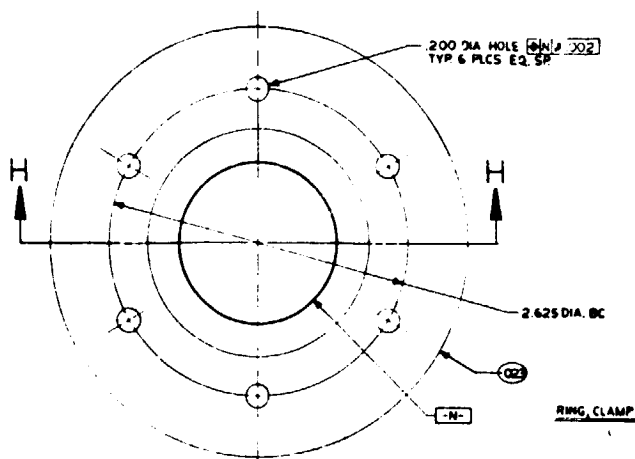
00002/AP 76-098

Fig. 99. 10-kw Heat Sink Ch
Plasma Viewing Win

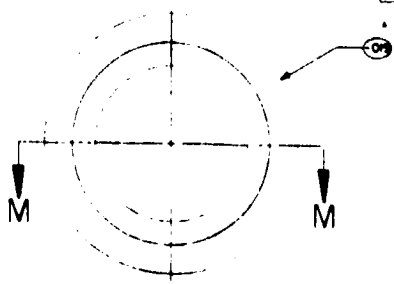
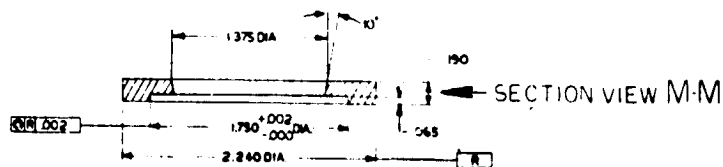


(-023) WINDOW RETAINER-

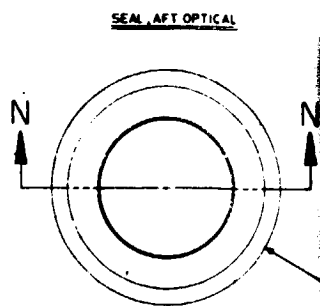
2 CLEAN FOR GUN M714
2 MAGAZINES FOR SA 4103-032
1 MORTAR BY THE GUN
AND OTHER SMALL ARMS



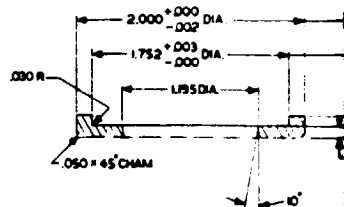
HOUSING, MANIFOLD



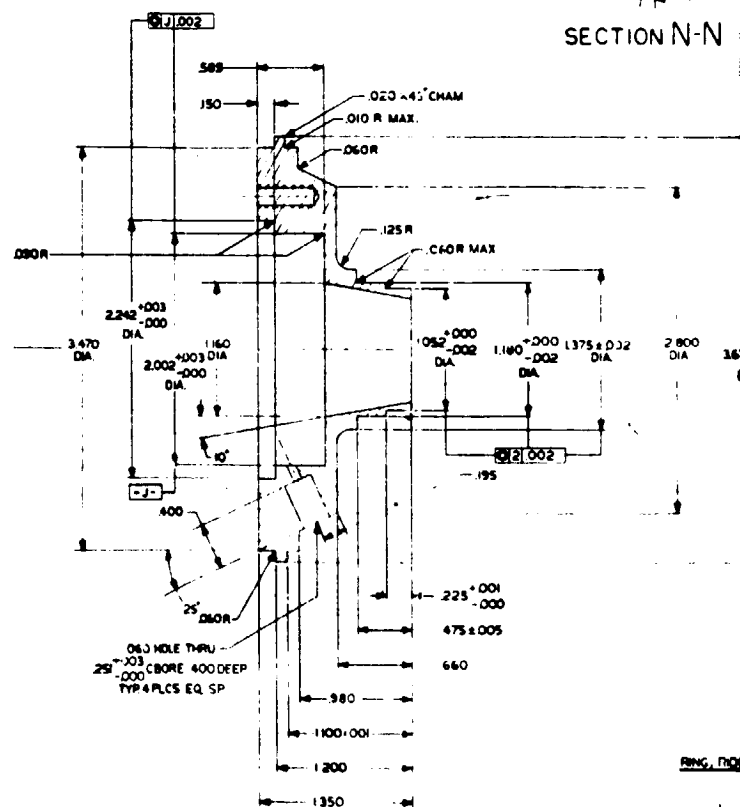
SEAL, FWD OPTICAL



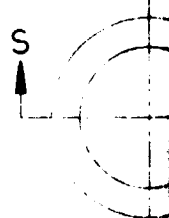
SEAL, AFT OPTICAL



SECTION N-N



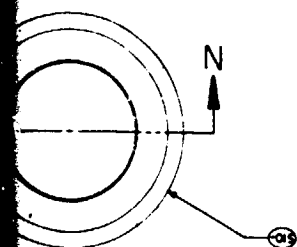
SECTION A-A



SECTION S

FOLDOUT FRAME

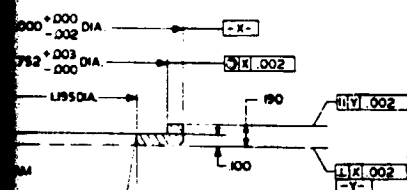
TEAM AFT OPTICAL



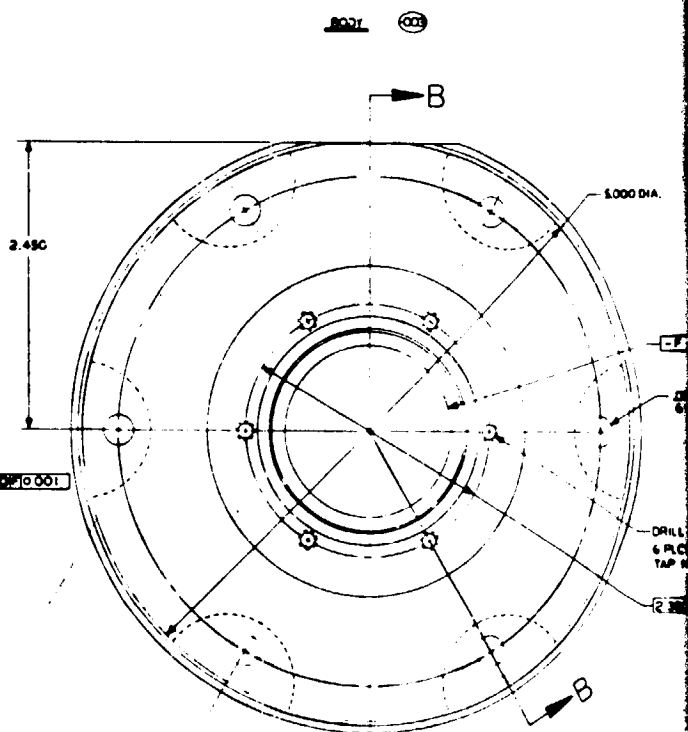
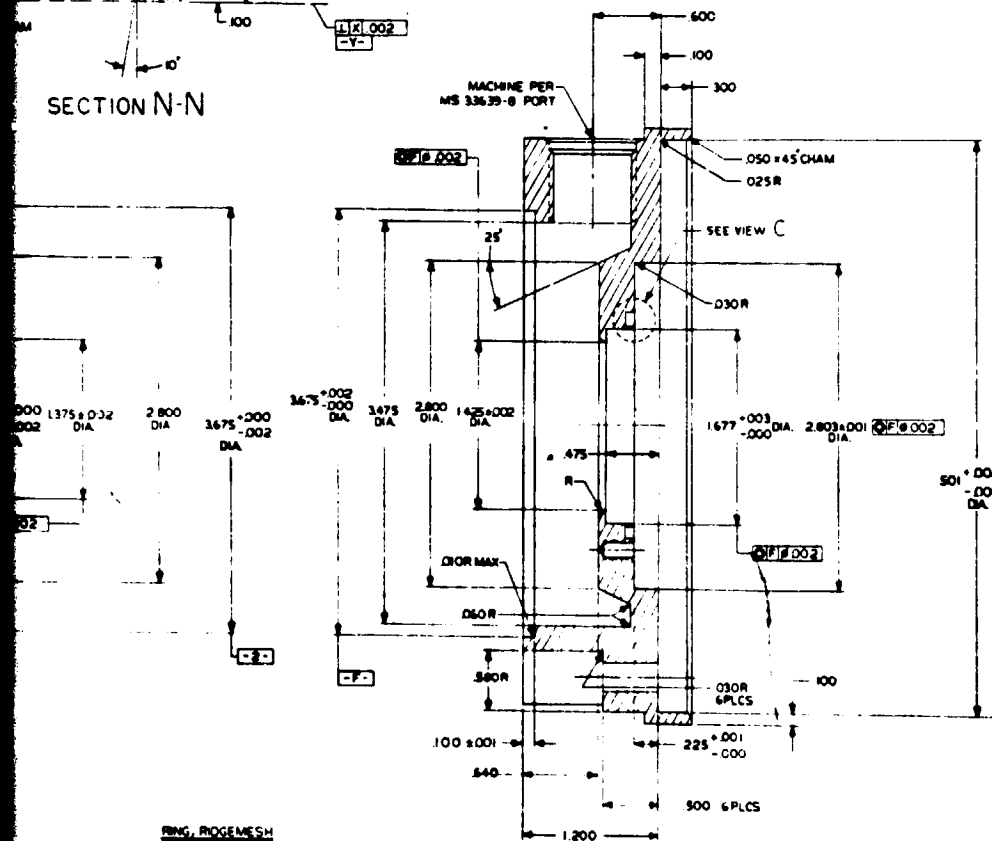
Technical drawing of a mechanical part showing dimensions and tolerances:

- $\frac{3}{2}$
- $.077 \pm .003$
- BREAK EDGES .005 R 1 TP 2 PLCS.
- $1'9'' \pm .002$
- $\frac{3}{2}$
- $\frac{3}{2}$
- $.010 \pm .005 R$
- $1.78 \pm .005$ DIA.

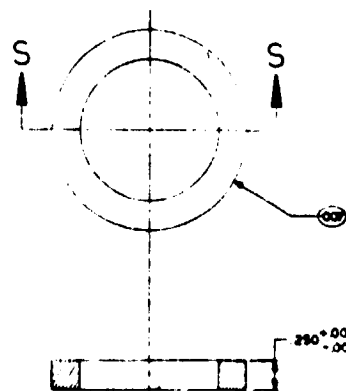
VIEW C
SCALE 4:1



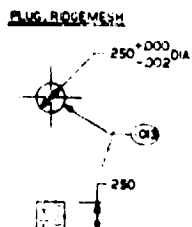
SECTION N-N



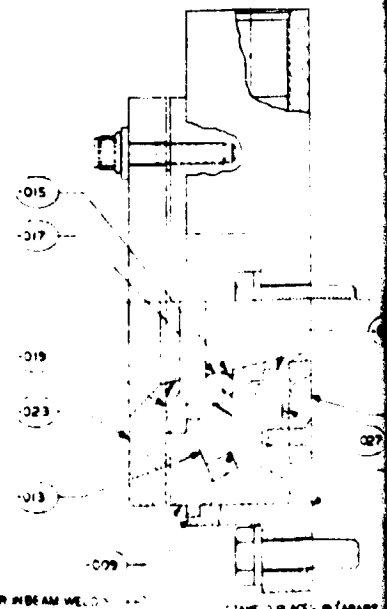
SECTION B-B



SECTION 5-5



WELDOUT FRAME



ELECTR IN BEAM WELD 22 22

STATE 2 PLACES APART

Residual International Corporation
Residuals Division
Garage Park, California

CODE 0000000000	PAGE 1	FORM 10-1
-----------------	--------	-----------

• MICROFILM OVERLAP AREA •

flow for window cooling and the remaining hydrogen flow through the main injector. Also the rigimesh provides the $3.45 \times 10^4 \text{ N/M}^2$ (5 psi) injector pressure drop required (10 percent of chamber pressure) to maintain flow stability. The rigimesh was replaced with an equivalent flow rated felt metal due to long lead times in procuring the rigimesh. Injection velocity of 40 cm/sec (1.3 ft/sec) for the window coolant and 152 cm/sec (5 ft./sec) for the main injection were selected to provide laminar flow across the window and a main propellant injection velocity closely corresponding to an annular velocity of the injector lip annulus (see page 77). The window coolant is fed through 72 slots 0.1016 cm X 0.0508 cm (0.04-inch by 0.02-inch) and the main propellant through 58 holes of 0.1189 cm (0.0468-inch) diameter.

Thrust Stand

The assembly drawing of the 10-kw chamber thrust is presented in Fig. 101. The basic concept employed in designing the thrust stand is a gravity controlled balance beam. The thrust chamber is bolted to the thrust stand through bolt holes in the injector flange. The balance beam has a mechanical stop which prevents any damage to the flextures or load cell during mounting of the thrust chamber. The balance beam is essentially a channel in which the counterbalance weights are placed. The pivot is provided by two Bendix flextures. The main propellant and inlet and outlet water coolant links are flex-lines which originate from a main panel. The procedure for calibrating the thrust stand is to:

1. Install the pressure plate on the thrust chamber exit
2. Pressurize main propellant to rated chamber pressure and water to operational pressure
3. Zero out the measured thrust

24

23

22

21

20

H

G

F

E

D

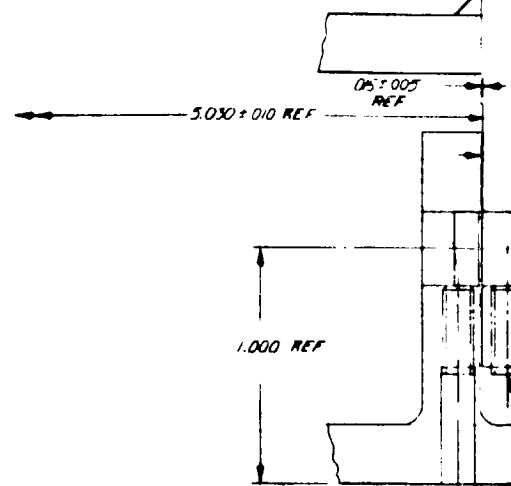
C

B

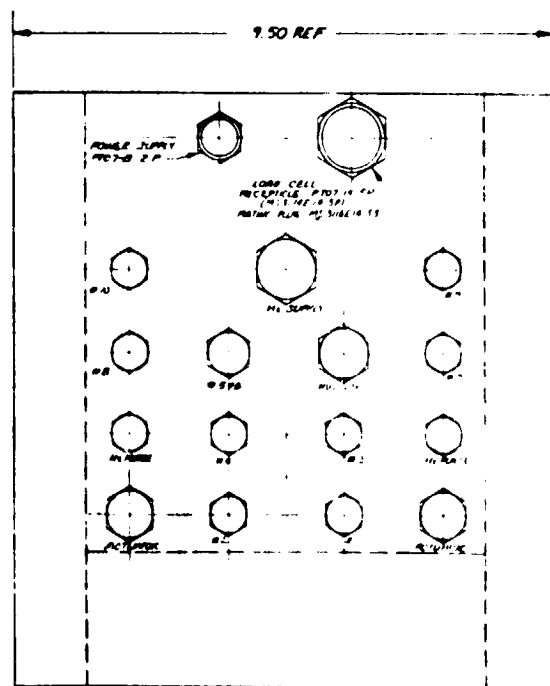
A

GRADE	HOSE	LENGTH	HOSE SIZE	TUBE FITTING
NO.	PART NO.	OVERALL	I.D. O.D.	UPSTN DNSTN
1	ANG270-30 -0134	13.50	.187 .437	ANB15-30/ANB32-30
2		13.50	.187 .437	
3	ANG270-30 -0114	11.50	.187 .437	
4		11.50	.187 .437	ANB15-30/ANB32-30
5	ANG270-40 -0124	12.50	.250 .500	ANB15-40/ANB32-40
6				
7	ANG270-30 -0134	13.50	.187 .437	ANB15-30/ANB32-30
8		13.50	.187 .437	
9	ANG270-30 -0114	11.50	.187 .437	
10		11.50	.187 .437	ANB15-30/ANB32-30
MEET	ANG270-60 -0100	10.00	.375 .625	ANB15-60/ANB32-60
PA IN	ANG270-80 -0110	11.00	.500 .781	ANB15-80/ANB32-80
SLURGE	ANG270-30 -0140	14.00	.187 .437	ANB15-30/ANB32-30
ALTR	ANG270-40 -0150	15.00	.250 .500	ANB15-40/ANB32-40

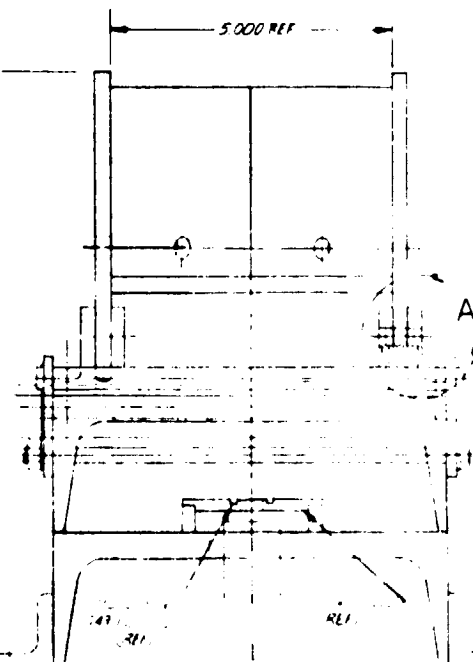
HOSES PER MIL-H 5593



MFG-32-375 SET-SCREEN 6 REGO

VIEW A
SCALE 4

0.04 REF

END VIEW WITH INTER
FROM L. REAR

24

23

22

21

20

20

19

18

17

16

AP 76-125-005
PLATE 1 REGD

AP 76-125-005
GAS

POWER LINE

ELECTRODE PISTON ACTUATION PRESS
LINE 2 REGD

ELECTRODE H₂ PURGE
LINE 2 REGD

H₂O OUTLETS 5/16

VIEW BB

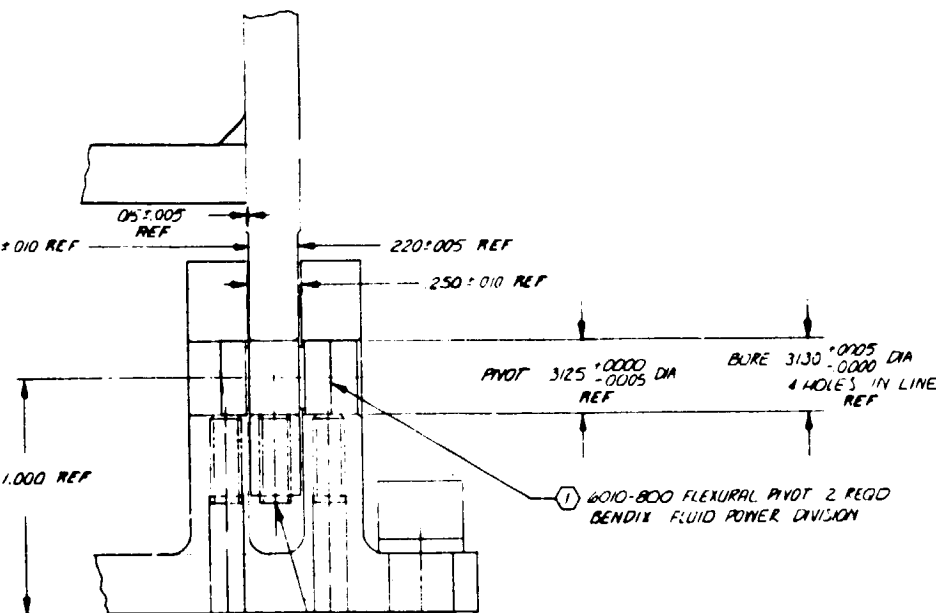
10.00 REF

7.00 REF

Radco International Corporation
Radiation Division
Group Park, California

DATE	BY	REV
0000 0000 0000	0000	0000

M. 125-113 001
REGD



M96.32 ± 0.375 SET SCREW 6 REGD

VIEW A
SCALE 4/1

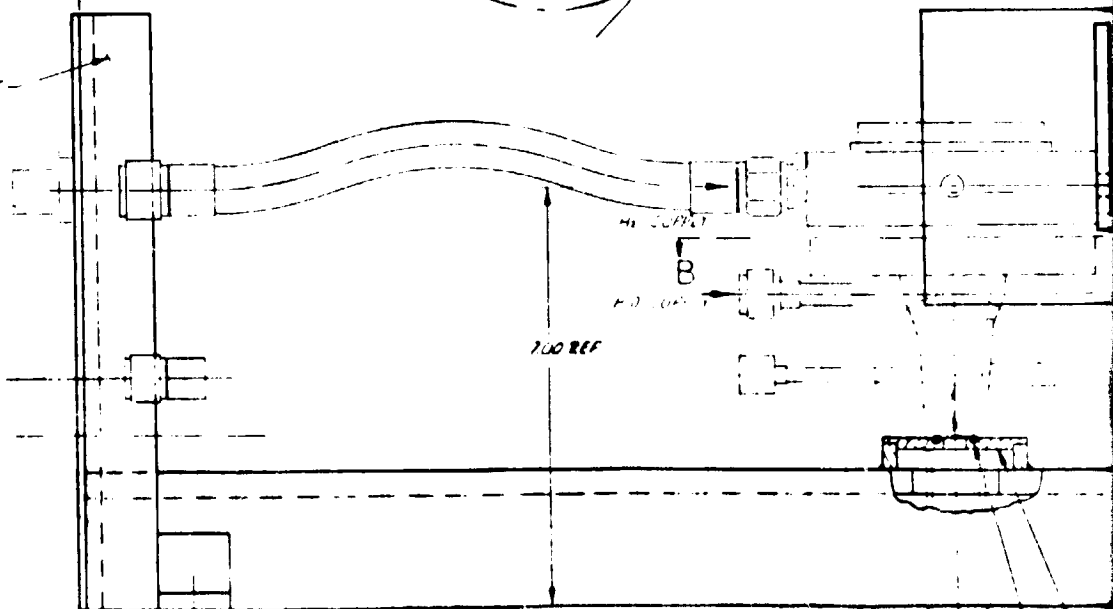
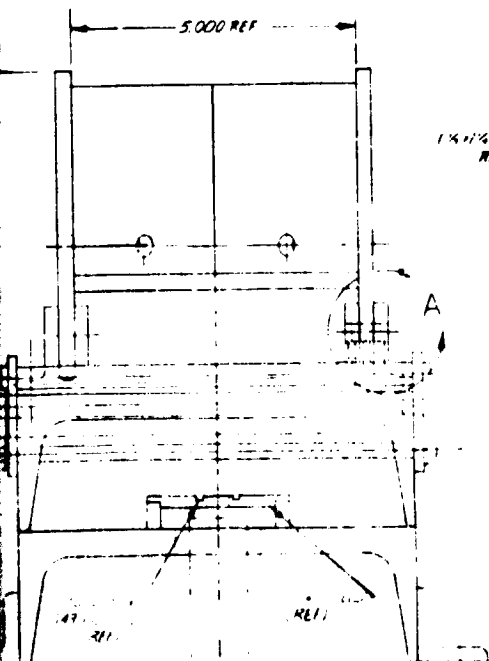
WATER INLET

15.20 REF

1/4 ± 1/4 IN ANGLE
REF

H₂O OUTLET

H₂O OUTLET



20

19

18

17

16

AP76-125-003
GASKET 1 REQD

BALANCE PROCEDURE:

1. INSTALL PRESSURE PLATE AND COUNTER WEIGHT.
2. INSTALL ALL LINES. FILL & PRESSURIZE H₂O LINES WITH H₂O & H₂ LINES WITH G₂.
3. BALANCE SYSTEM WITH LOAD PIN UP AND ASPIRATION SHIELD PLATE AND SEAL OUT. CALIBRATE THE LOAD CELL.
4. ONCE BALANCED DEPRESSURIZE REINSTALL ASPIRATION SHIELD AND SEAL AND REMOVE ITEM 1.
5. ADJUST LOAD CELL PIN SO THAT THE ASPIRATION SHIELD SEAL IS BARELY CONTRACTING THE NOZZLE.

NAS1004-2 BOLT 4 REQD
MS15795-B10 WASHER 4 REQD

AP76-050
PIVOT CLEVIS
2 REQD

AP76-046-001
MOUNT ASSY OF
2 REQD

NAS1010CB 32 SCREW 2 REQD
MS9949-008 WASHER 2 REQD

AP76-151-003 ALUMINUM 1 REQD

200A FORCE TRANSDUCER 1 REQD

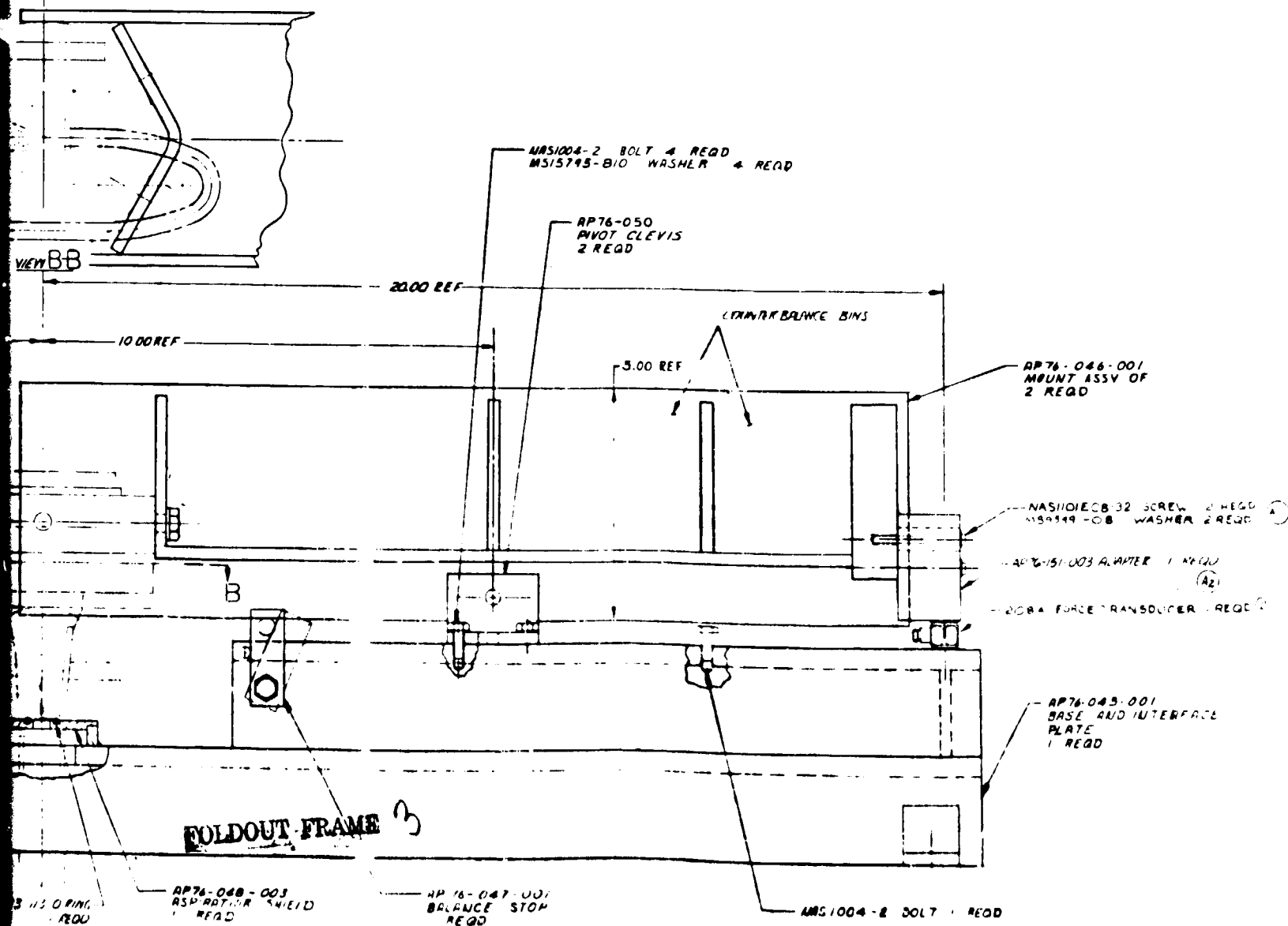
AP76-045-001
BASE AND INTERFACE
PLATE
1 REQD

FOLDOUT FRAME 3

AP76-048-003
ASPIRATION SHIELD
1 REQD

AP76-047-001
BALANCE STOP
1 REQD

NAS1004-2 BOLT 1 REQD



12

11

10

9

8

7

COUNTER WEIGHT.
 PRESSURIZE H₂O LINES
 PIN UP AND ASPIRATION
 CALIBRATE THE LOAD
 REINSTALL ASPIRATION
 ITEM 1.
 AT THE ASPIRATION
 DETRACTING THE NOZZLE.

AP76-046-001
 MOUNT ASSY OF
 2 REQD

NAS1101ECB-32 SCREW 2 REQD (A)
 MS9549-08 WASHER 2 REQD

AP76-151-003 ADAPTER 1 REQD (A2)

208A FORCE TRANSDUCER 1 REQD (2)

AP76-043-001
 BASE AND INTERFACE
 PLATE
 1 REQD

FOLDOUT FRAME

National International Corporation
 Rockledge Station
 Tampa, Florida

FORM 1000-01000	FRONT	1
		A

12

11

10

9

8

7

5000-KW DESIGN CONFIGURATION

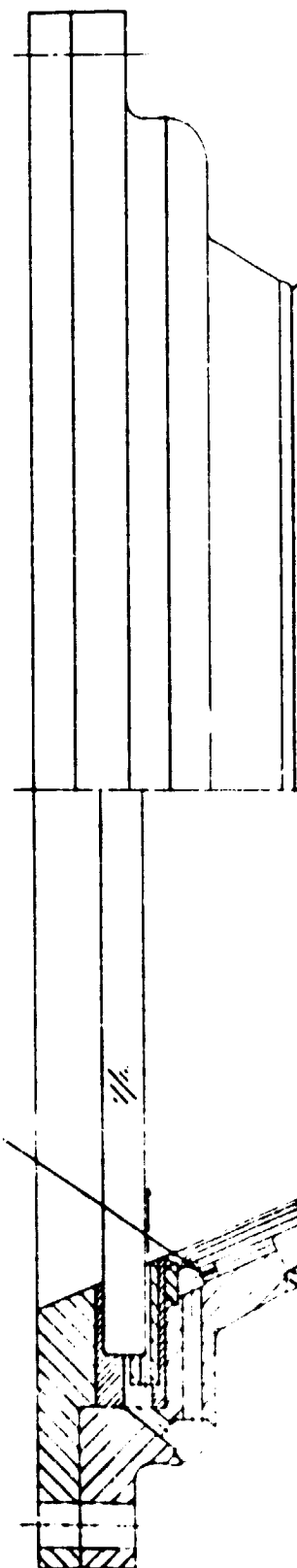
The chamber assembly of the 5000-kw design configuration is shown in Fig. 102 and 103 the two drawings illustrate two methods of injecting the carbon seeded hydrogen flow. In both configurations, a single up-pass circuit is employed with the nozzle ($\epsilon = 10$ to 40) consisting of 80 stainless steel tubes and the combustor of 58 variable depth coolant channels. These coolant channels would be machined in a high thermal conductivity copper alloy and closed out with electro-formed nickel. The channel construction method reduces the wetted surface area exposed to the hot gas by presenting a smooth inner surface and also provides a beneficial "fin conduction" created by the channel lands which reduces the gas-side wall temperature and the wall thermal gradients. In general, the advanced channel wall construction is heavier than the conventional tubular construction. Therefore, a construction technique utilizing channels in the high heat flux, small hot-gas diameter region (subsonic to low supersonic region) and tubes in the low heat flux, large hot-gas diameter and large surface area ratios (supersonic nozzle) provides the best combination thrust chamber with high performance, light weight, and a high cycle life. The plasma arc initiator port is located 2.54 cm (1.0-inch) upstream of the geometric throat.

Single and multi-pane windows were considered and, since the multi-pane window offered no distinct advantages, the single panel window was selected. Since the window coolant eventually flows into the chamber, the coolant pressure must always be higher than chamber pressure $3.45 \times 10^5 \text{ N/M}^2$ (50 psia). Therefore, the concept of using multiple panes having decreasing coolant pressure could not be utilized.

The chamber cooling required a coolant inlet pressure of $1.242 \times 10^6 \text{ N/M}^2$ (180 psia), necessary to maintain reasonable coolant velocities ($M=0.542$). This results in a $1.036 \times 10^6 \text{ N/M}^2$ (150 psia) coolant pressure which must be regulated through a series of orifices prior to injection into the $3.45 \times 10^5 \text{ N/M}^2$ (50 psia), chamber pressure.

In the first configuration (Fig.102) the coolant flow exiting the cooling jacket splits 60 percent to the carbon seeder and the remaining 40-percent to the main hydrogen injection ring (30-percent) and the window cooling (10 percent). In this configuration, the carbon seeded flow is "sandwiched" between streams of hydrogen flow at the main injector.

As discussed in the plasma analysis section, to absorb a major portion of the plasma radiation, the flow velocity of the carbon seeded layer must be low compared to the main propellant flow velocity. Therefore, a second chamber configuration utilizing essentially two axial locations for the injection of the seeded flow was designed as shown in Fig.103. The seeded flow injection ports consist of holes through the land of the coolant channels. This configuration would enable better control of the cooling layer velocity in the region where the plasma exists.

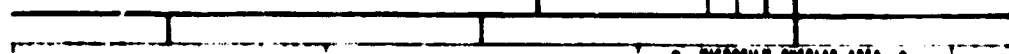


WINDUP COIL MOUNT ON HOLE
0.32 DIA. 6.000

Engineering International Corporation
Engineering Division
Engineering Section

Figure 102

FOLDOUT FRAME 1



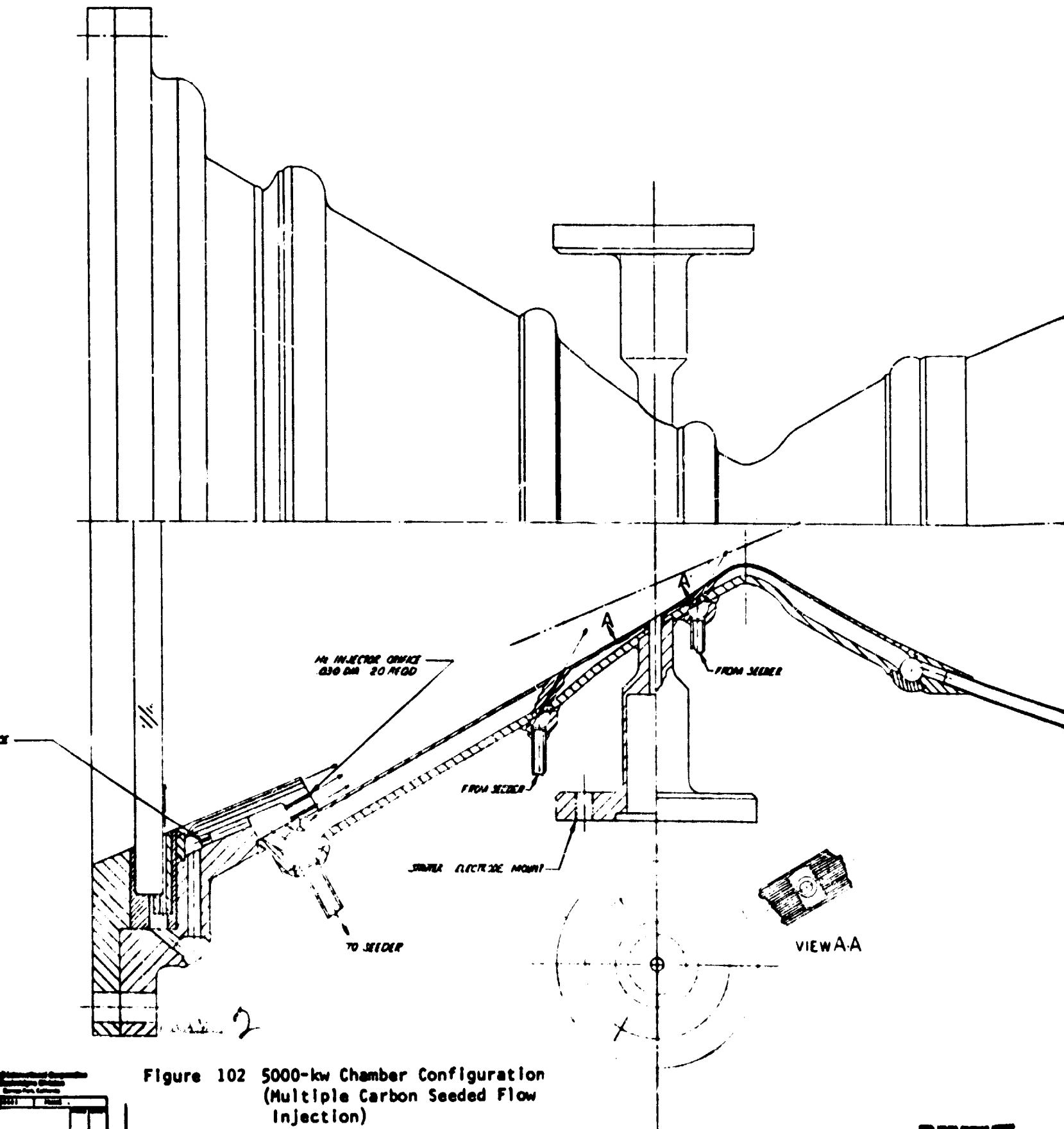
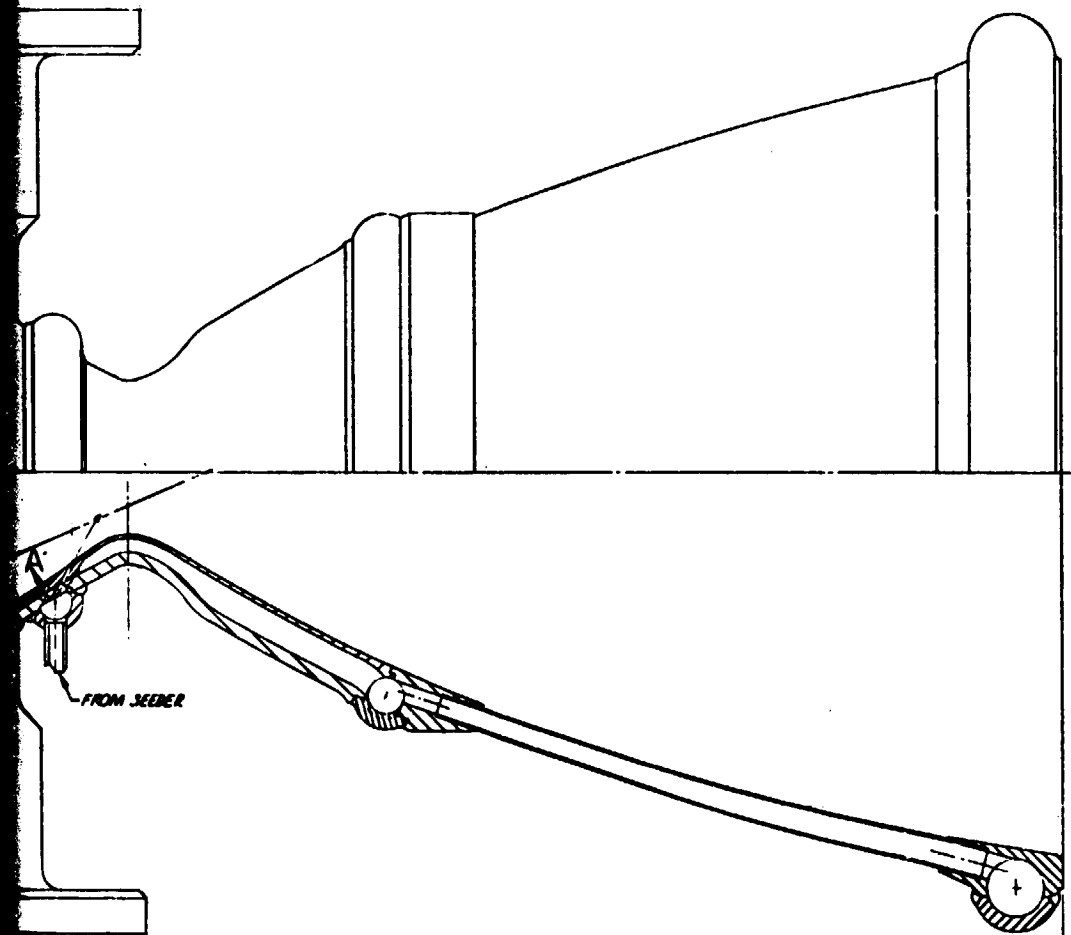


Figure 102 5000-kw Chamber Configuration
(Multiple Carbon Seeded Flow
Injection)

REVISIONS		DATE	BY
1	REVISED TO SHOW		
2	REVISED TO SHOW		
3	REVISED TO SHOW		
4	REVISED TO SHOW		
5	REVISED TO SHOW		

H
G
F
E
D
C
B
A



VIEW A-A

171/172

FOLDOUT FRAME 2
FOLDOUT FRAME

C-3

PROJECT NO. 171/172 DRAWING NO. 171/172 DATE 1/1/74 BY J. J. J.		NATIONAL AERONAUTICS AND SPACE ADMINISTRATION RESEARCH AND DEVELOPMENT DIVISION SPACE SYSTEMS DIVISION	
TITLE SUBTITLE		SCHEMATIC LASER ROCKET CONCEPT B	
1 02602 171/172		APR 76 174	

WINDOW COOLANT ORIFICE
.032 DIA 6 REGD

H₂ INJECTOR ORIFICE
.030 DIA 20 REGD

SEEDED H₂ ORIFICE
.0300 DIA 10 REGD

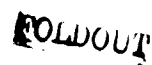
STARTER ELECTRODE MOUNT

FROM SEEDER

TO SEEDER

FOLDOUT FRAME 1

FOLDOUT FRAME 2



Fig

REVISIONS		DATE
1. NEW CHAMBER	2. NEW CHAMBER	
3. NEW CHAMBER	4. NEW CHAMBER	
5. NEW CHAMBER	6. NEW CHAMBER	

H
G
F
E
D
C
B
A

173/174

Figure 103 5000-kw Chamber Configuration
(Single Carbon Seeded Flow
Injection)

5000 KW LASER ROCKET CONCEPT A	
J 02602	A 75-073

OLDOUT FRAME 3

TASK II: FABRICATION

10-KW THRUSTER

All components of the 10-kw thruster were fabricated using conventional manufacturing techniques currently using in fabricating rocket engines.

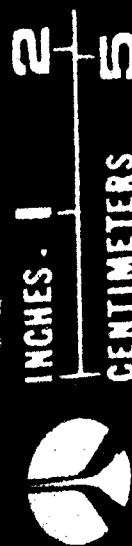
Water-Cooled Chamber

The water-cooled thruster component (copper liner, structural shell, and ignitor flanges) machining was performed by Tri-Models and the brazing and welding were performed at Rocketdyne.

The OFHC copper liner, the stainless structural shell, and the ignitor flanges were machined in the first stage of the water-cooled chamber fabrication. These components are shown in Fig 104. In the first braze cycle the copper liner and the outer structural shell were brazed together. Subsequent to this braze cycle the chamber coolant channels were leak tested. This test revealed only minor inter-passage leakage and no leakage into the electrode region and no external leakage. In the next step of the fabrication process, the ignitor flanges were brazed to the chamber assembly. Next the coolant inlet manifold cover plate and inlet line were TIG orazed to the chamber. The internal chamber contour was then machined and the ignitor ports final machined. Next the nine coolant outlet lines were welded to the chamber assembly.

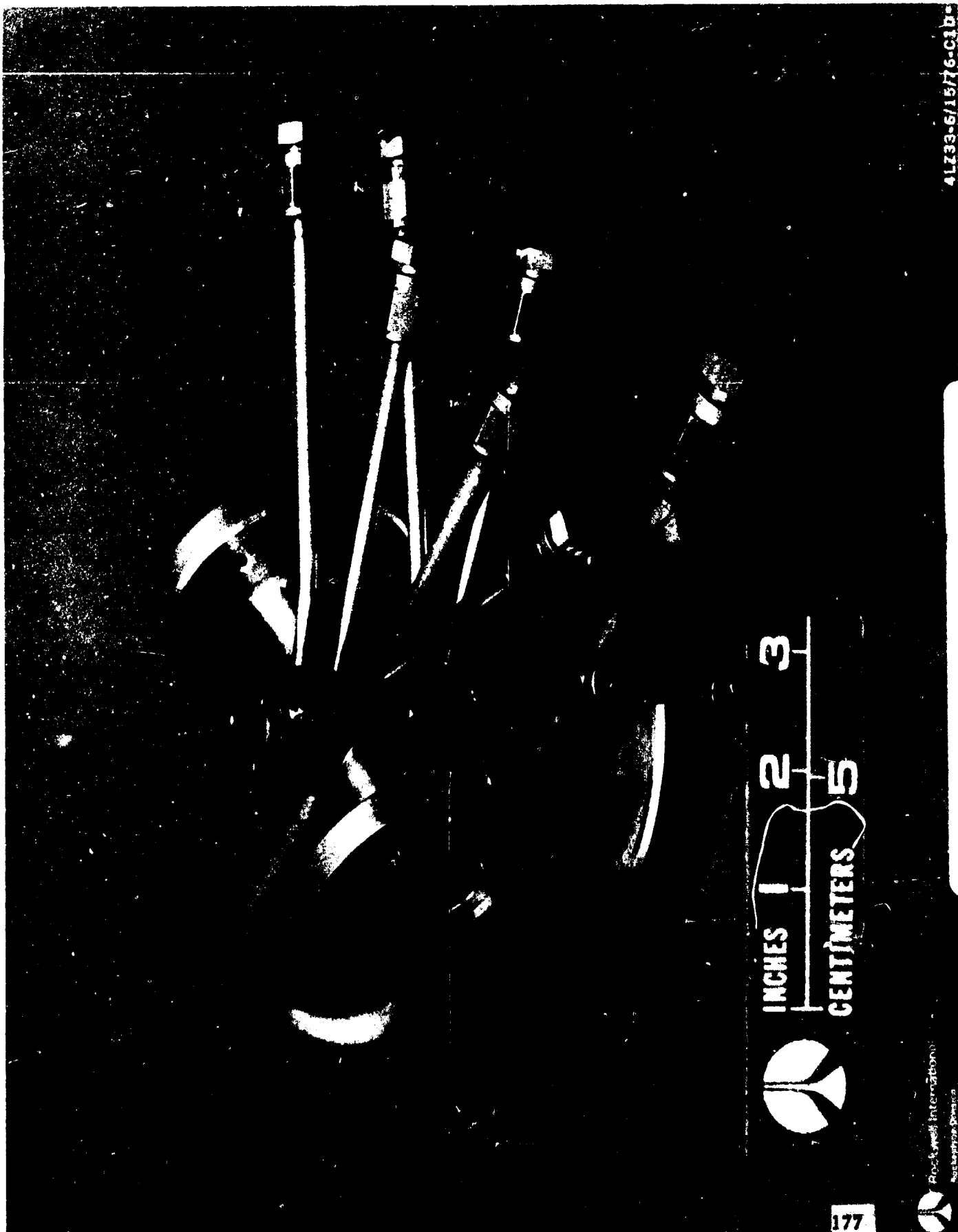
A thermocouple was installed approximately 6.35 cm (2.5 inch) from the chamber throat and 0.508 cm (0.20 inch) from the gas-side surface in the uncooled section of the chamber. This thermocouple will provide an indication of chamber overheating in this region.

Upon completion of the thruster assembly (Fig.105) coolant channels, inlet manifold, and coolant outlet lines were successfully hydrostatically tested to $3.45 \times 10^6 \text{ N/M}^2$ (500 psig) without leakage.



4LZ333-5/10/75-CIA

Figure 104. 10-KW Water-Cooled Chamber-Liners,
Structural Shell and Ignitor Flanges



ALZ33-6/15/16-C1b

Figure 105 10-kw Water-cooled Chamber



Rockwell International
Rockwell Design

177

ORIGINAL PAGE IS
OF POOR QUALITY

Once the ignitors were assembled the fit with chamber ignitor ports were checked and the ports were honed to provide a correct fit. The complete water-cooled chamber assembly with injector and ignitors is shown in Fig. 106.

Ignitors (Plasma ARC Electrode Mechanism)

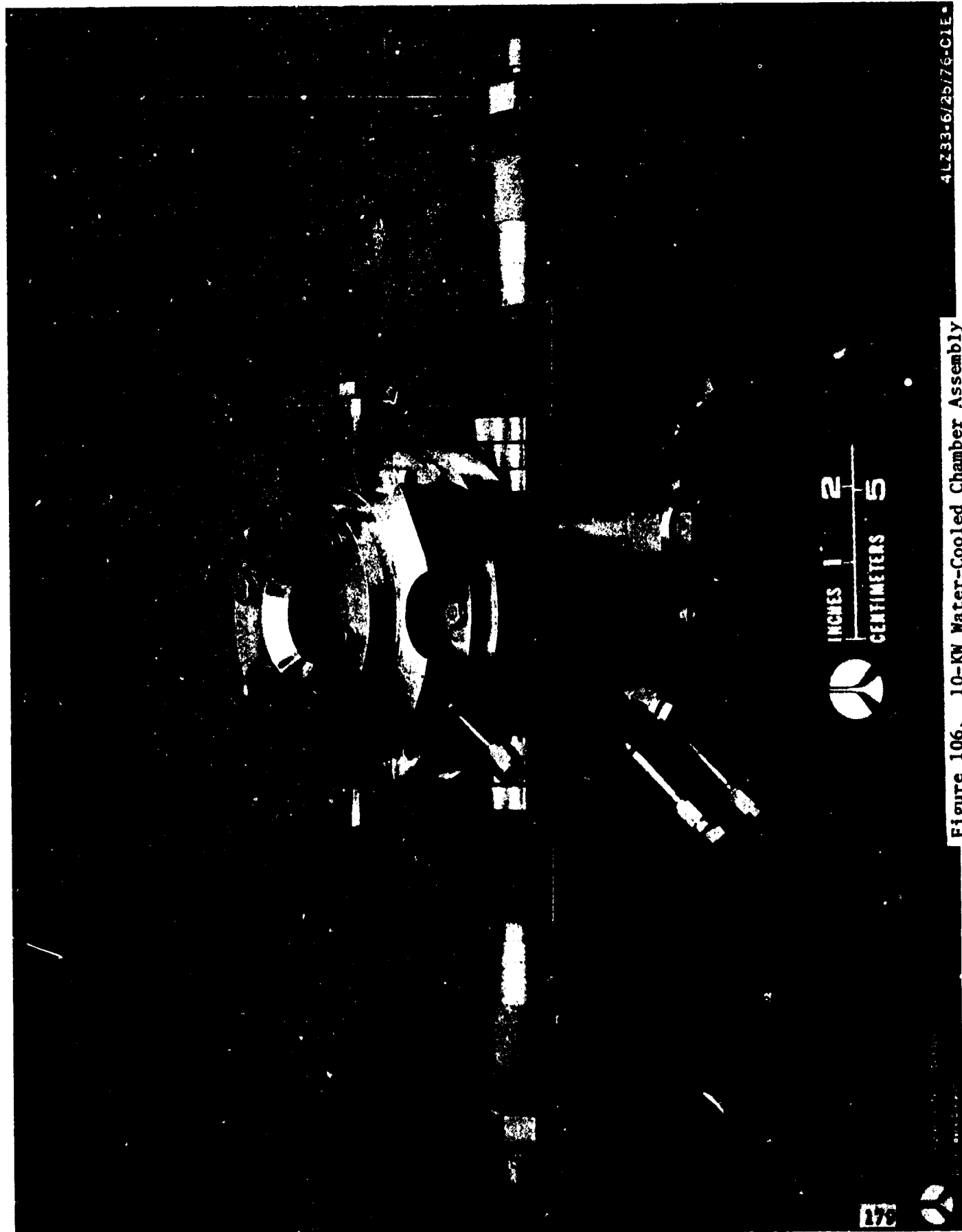
The ignitor components which included the ignitor housing, electrode key, retracting spring, conductor rod and insulator, nut wrench, micrometer housing sleeve, and piston (Fig. 107) were fabricated by Acro-Tech. These components were assembled at Rocketdyne and the one of the final assemblies is shown in Fig. 108. The electrode locking mechanism was checked functionally to lock and retain the tungsten electrode and unlock. The pneumatic piston actuation of the ignitors were checked using approximate $1.034 \times 10^6 \text{ N/M}^2$ (150 PSIG) Argon. Although the specified actuation pressure was $3.45 \times 10^6 \text{ N/M}^2$ (500 PSIA) gaseous nitrogen, these actuation tests indicated that a lower gaseous nitrogen perhaps 1.379×10^6 to $2.068 \times 10^6 \text{ N/M}^2$ (200 to 300 PSIG) would be sufficient. A lower gaseous nitrogen pressure would reduce the electrode retracting time.

Uncooled Chamber

The uncooled OFHC copper chamber and the ATJS graphite insert were fabricated by Tri-Models. The uncooled chamber was machined from a solid copper billet. The ten thermocouples on the uncooled chamber were installed at Rocketdyne. The ignitors, spacers and chamber were assembled for an assembly check as shown in Fig. 109. The uncooled chamber assembly complete with ignitors and injector is shown in Fig. 110. The cooled and uncooled chamber injector orifice plates are shown in Fig. 110.

Injector

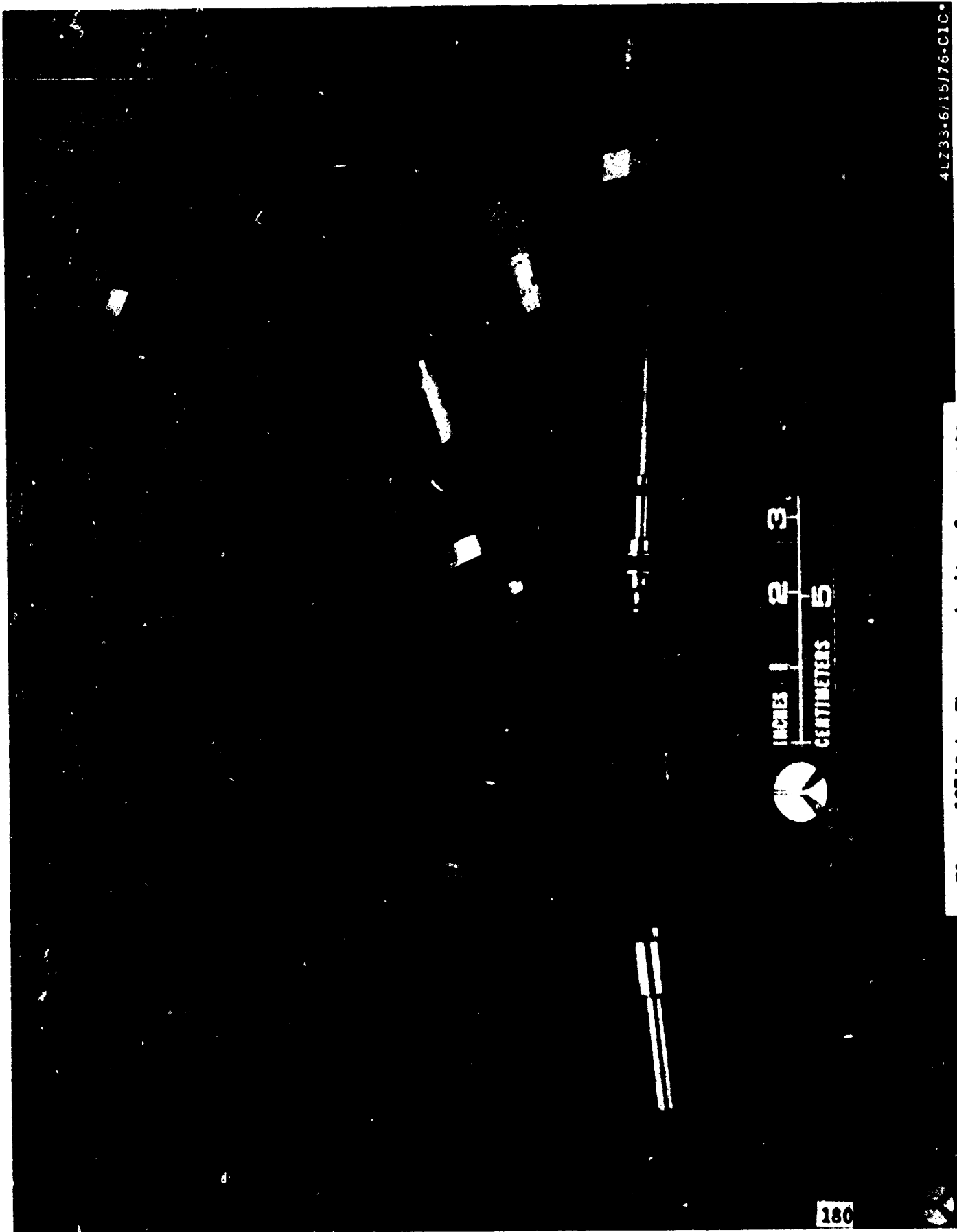
The injector components (Fig. 111) which include the injector body, orifice plates, felt metal ring, window seals, window coolant ring, and window cover



4L233-6/25/76-C1E

Figure 106. 10-KW Water-Cooled Chamber Assembly

ORIGINAL PAGE 1
OF POOR QUALITY



4LZ33-6/16/76-C10

Figure 107,10-kw Thruster Ignitor Components

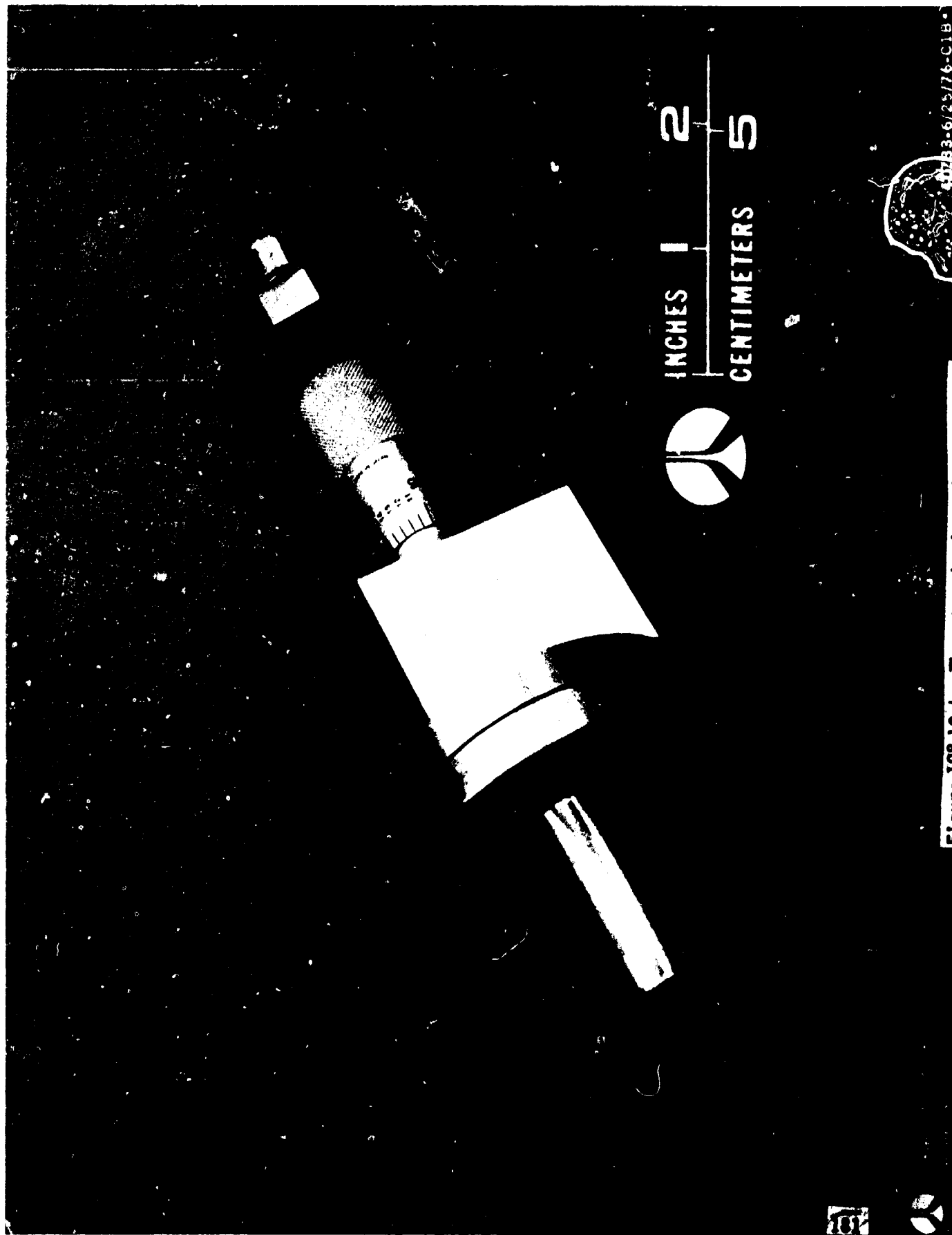
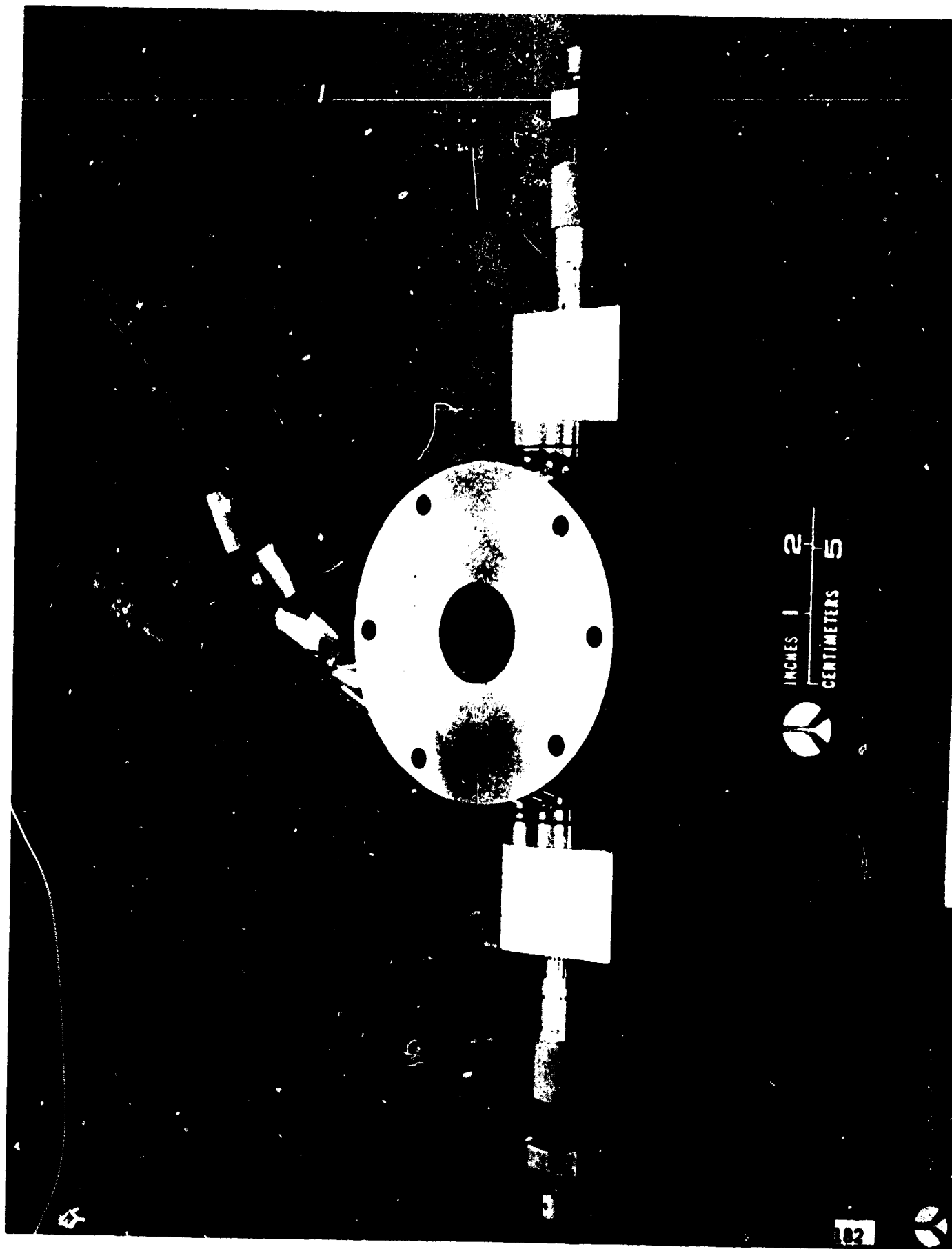


Figure 108-10-kw Thruster Ignitor Assembly

40783-6/25/76-C1B



4L233-6/25/76-C1A

Figure 109.10kw Uncooled Chamber

INCHES 1 2
CENTIMETERS 5

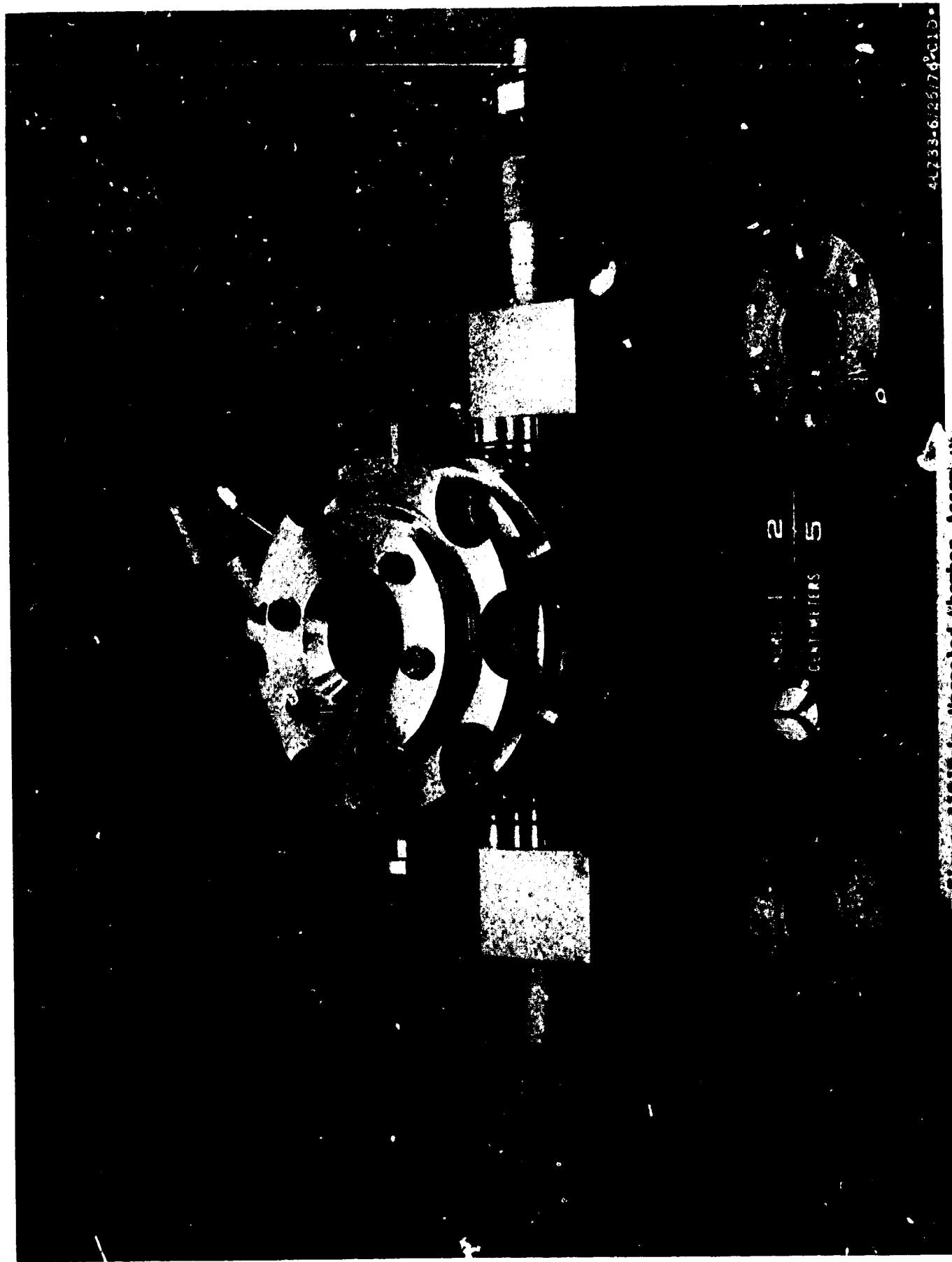


Figure 31010-10 Uncooled Chamber Assembly

41733-6125/74 CID



10-KV Thimster Injector Component

ORIGINAL PAGE IS
POOR QUALITY

plate were fabricated by Acro-Tech. Assembly of the injector and installation of the chamber pressure measuring tap was performed at Rocketdyne. The injector assembly is shown in Fig. 110.

10-KW THRUST STAND

The 10-kw thrust stand components including the balance beam, base, interface panel, pitot clevis, and thruster pressure plate were fabricated by Tri-Models. A check on the chamber fit on the thrust stand indicated that the thrust stand was not to print and therefore required a modification so that the chamber would fit. The thrust stand assembly is shown in Fig. 112.

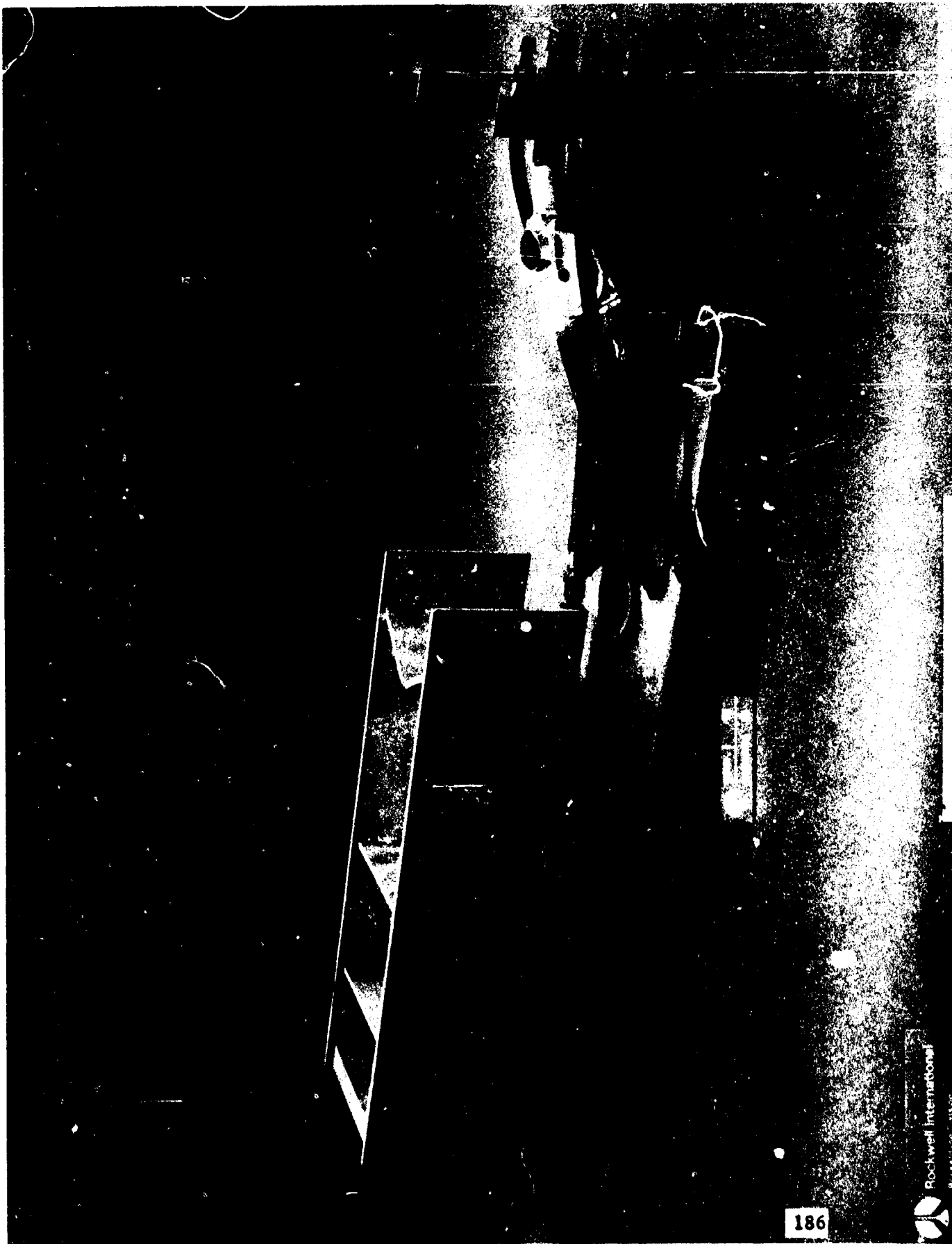


Figure 112J0-kw Thrust Stand

REFERENCES

1. Caledonia, G. E., R. G. Root, P.K.S. Wu, N.H. Kemp, and A. N. Pirri, "Plasma Studies for Laser-Heated Rocket Thruster - Final Report", Physical Sciences Inc., March 1, 1976.
2. Jackson, J. P. and P. E. Nielsen, "Role of Radiative Transport in Propagation of Laser Supported Combustion Waves", AIAA Journal, Vol. 12, No. 11, November 1974, pp. 1498-1501.
3. Bottger, P., and H. Krempf, Spectrochimica Acta, Vol. 26B, 1971, pp. 445-450.